PROCESSING, MODELING AND INTERPRETATION OF WIDE-ANGLE SEISMIC DATA OF AN ACTIVE PLATE BOUNDARY, SOUTH OF CYPRUS

By

© Ayda Rahimi

A thesis submitted to the

School of Graduate Studies

in partial fulfillment of the requirements for the degree of

Master of Science

Department of Earth Sciences

Memorial University of Newfoundland and Labrador

April, 2016

St. John's Newfoundland and Labrador

Abstract

Cyprus lies at the southern edge of the Aegean-Anatolian microplate, caught in the convergence of Africa and Eurasia. Subduction of the African plate below Cyprus has probably ceased and this has been attributed to the docking of the Eratosthenes Seamount microcontinental fragment on the northern edge of the African plat in the subduction zone. In early 2010, on R.V. Maria S. Merian, we conducted a wide-angle seismic survey to test the hypothesis that the Hecataeus Ridge, another possible microcontinental block lying immediately offshore SE Cyprus, might be related to an earlier docking event. The upper crust of southern Cyprus is dominated by ophiolites, with seismic velocities of up to 7 km s^{-1}. A wide-angle seismic profile along Hecataeus Ridge was populated with 15 Canadian and German ocean-bottom seismometers at 5 km intervals and these recorded shots from a 6000 cu. in. air gun array, fired approximately every 100 m. Rough topography of the seabed has made picking of phases and their modeling a demanding task. Bandpass and coherency filtering have enabled us to pick phases out to around 80 km. Tomographic inversion of short-range first arrivals provided an initial model of the shallow sub-seabed structure. Forward modeling by ray-tracing, using the code of Zelt and Smith, was then used to model crustal structure down to depths of around 25 km, with no evidence of reflections from Moho. Modeling results provide good control on P-wave velocities in the top 20 km and some indications of deeper events. There is no evidence of true velocities approaching 7 $km.s^{-1}$ in the top 20 km below the Ridge that might indicate the presence of ophiolitic rocks. Regional gravity and magnetic field data tend to support this proposition. We thus conclude that Hecataeus Ridge is not composed of characteristically ophiolitic, Cyprus (upper plate) crust, and most likely it might be derived from the African (lower) plate.

Acknowledgements

I would like to thank all people who helped and supported me throughout my master's program. Especially my wonderful supervisor, Dr. Jeremy Hall. His determination, focus and pure desire made my thesis an extremely enjoyable experience. I can only thank you so many times in one lifetime. I would have been lost without his guidance. I also would like to thank Dr. Kim Welford, my great co-supervisor. She played a huge role in the completion of my thesis. Her patience and constant support made this program and thesis writing a joy. From the beginning to the end, Dr. Welford was present every stage of the way and for this I offer my deepest gratitude.

I would like to extend my deepest thanks to Dr. Charles Hurich, my dear co-supervisor who also offered his kindest support throughout my master's program.

I would like to now offer my deepest thanks to the Natural Sciences and Engineering Research Council of Canada (NSERC), for providing the founding for this project. The officers and crew of RV Maria S. Marian, research group and the Geological Survey of Canada also got a huge thank-you.

Thanks a million to Mr. Peter Bruce, for helping so much with my figures and maps.

I also would like to thank all my friends especially Hormoz Javaheri.

I thank my mom and dad for always being so supportive and loving. At the end I would like to thank my dearest husband, Farid, for his unconditionally love, support and kindness,

Table of Contents

List of figures

List of tables

CHAPTER 1

Introduction

1.1 Outline of problem

The Cyprus Arc represents part of the surface boundary between rocks belonging to the African and Anatolian plates in the eastern Mediterranean (Figure 1.1, Schattner, 2010). Cyprus lies at the southern edge of the Aegean-Anatolian microplate, caught in the convergence of Africa and Eurasia. Subduction of the African plate below Cyprus has probably ceased (Ben-Avraham *et al.,* 1988) and this has been attributed to the docking of the Eratosthenes Seamount microcontinental fragment on the northern edge of the African plate, in the subduction zone (Robertson, 1998a).

An international team of researchers, from Germany and Canada (Memorial University of Newfoundland and Dalhousie University) combined in 2010 to collect around 1550 km of wide angle seismic refraction profiles from the area of the plate boundary, south of Cyprus. This thesis is focused on one profile, approximately 80 km long, on the Hecataeus Ridge (Figure 1.2) to test the hypothesis that it might be another microcontinental block from the African Plate now docked in the subduction zone.

1.2 Geological setting and study area

1.2.1 Plate configuration and history of plate convergence

The Eastern Mediterranean region has a tectonically complex history involving several major plates and microplates (Figure 1.1). The Mediterranean Sea is the remnant of a much larger Tethys Ocean that evolved during the Mesozoic (Moores *et al.,* 1984; Robertson, 1998a).

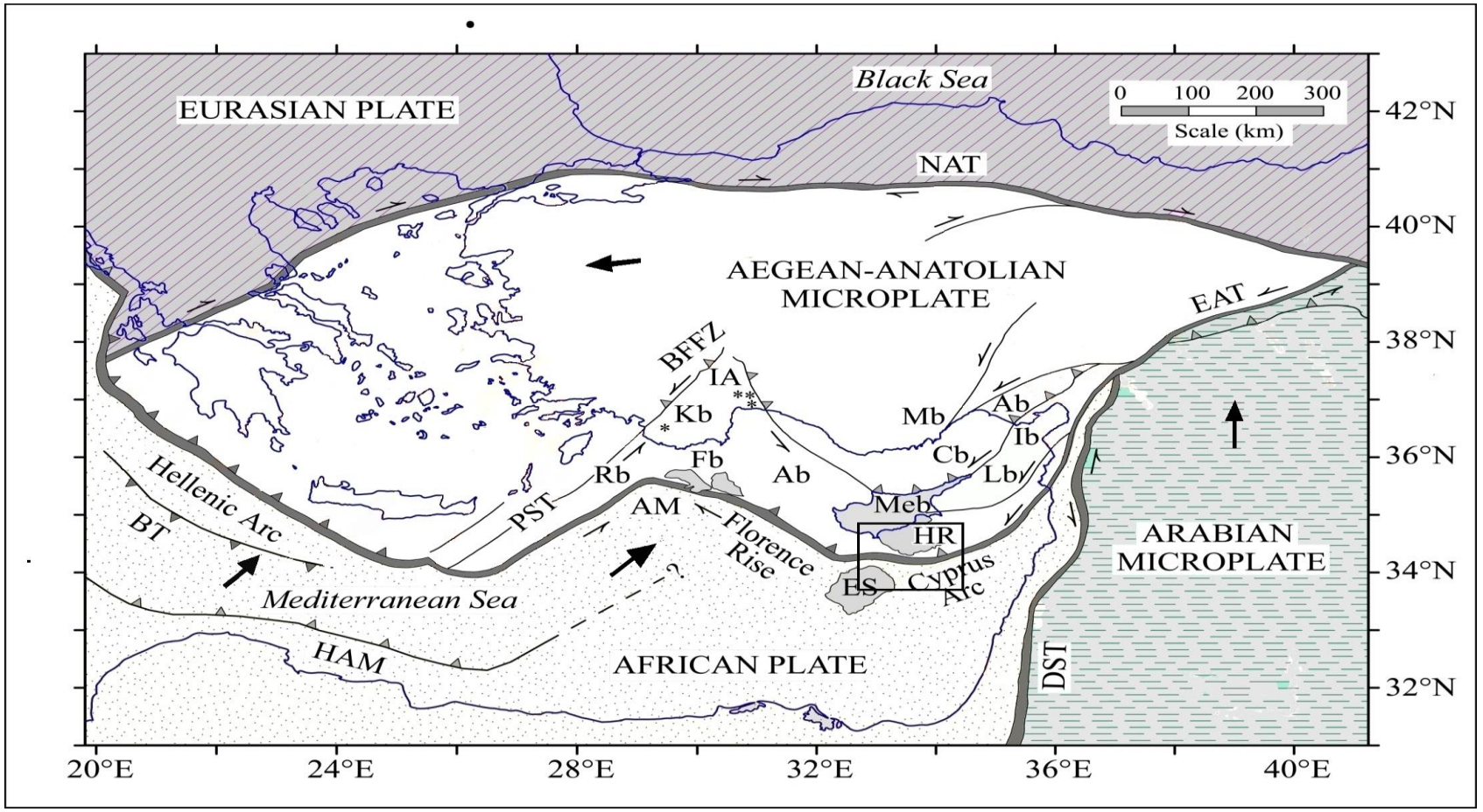

Figure 1.1 Map o f the Eastern Mediterranean basin showing the convergence (subduction/collision) between Africa-Sinai–Arabia and Eurasia–Study area highlighted in rectangle. Large black arrows indicate the sense of plate motion relative to the fixed Eurasian plate; half black arrows indicate transform/strike-slip faults. (ES =Eratosthenes Seamount, HR = Hecataeus Ridge, Mb = Mesaoria Basin, Cb=Cyprus Basin, DST = Dead Sea Transform Fault, EAT =East Anatolian Transform Fault, Lb= Latakia basin, Ib= Iskenderun Basin, BT= Burdur Trench) (Compiled from Şengör and Yilmaz (1981), Hancock and Barka (1981), Dewey *et al.* (1986), Hall *et al.* (2005a) and (2005b)

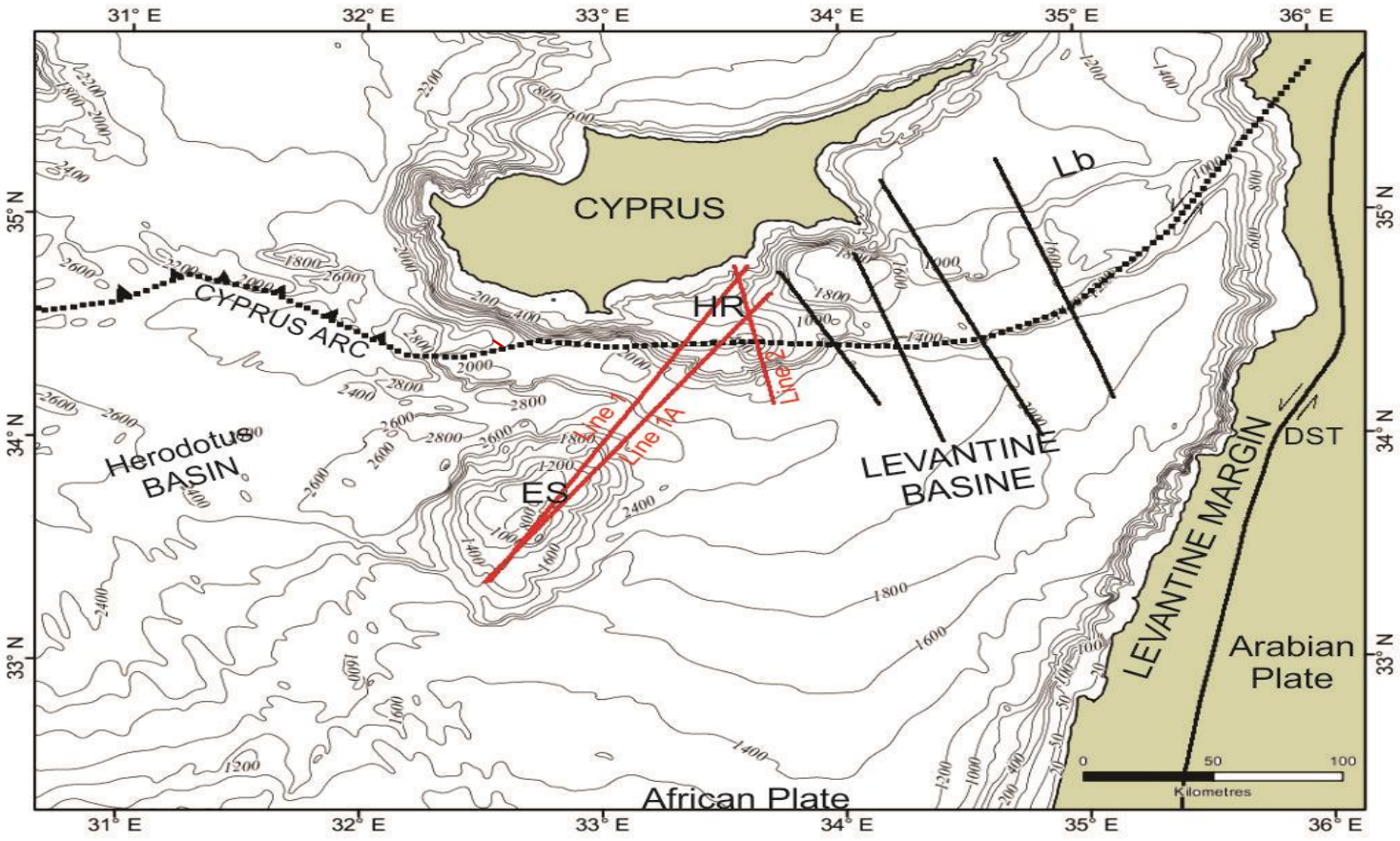

Figure 1.2 Bathymetric map of the eastern Mediterranean. Black lines indicate the seismic reflection profiles acquired by Vidal *et al.* (2000b), Line 1 and 1A represent the seismic refraction surveys interpreted by Welford *et al.* (2015) and line 2 shows the location of seismic refraction profile that is the focus of this thesis (ES =Eratosthenes Seamount, HR = Hecataeus Ridge, Lb= Latakia basin, DST = Dead Sea Transform Fault). Contours with the number represent depth below sea level in metres.

The present day tectonic processes in the eastern Mediterranean region are characterized by convergence of the African, Arabian and Eurasian plates (McClusky *et al.,* 2000). One result of the complexities of these motions is the westwards movement and anticlockwise rotation of the Aegean-Anatolian Microplate (Figure 1.1, Dewey *et al.,* 1986). The North Anatolian Transform Fault indicates the boundary between the Eurasian Plate and Aegean-Anatolian microplate in a dextral strike slip movement, where the East Anatolian Transform Fault shows a sinistral strike slip motion (Figure 1.1, Şengör and Yilmaz, 1981). The convergent boundary between the African and Aegean-Anatolian plates to the west, occurs at the Hellenic Arc where the subduction is still active and the subduction zone is rolling back to produce extension in the Aegean Sea back arc basin (Figure 1.1, McKenzie and Yilmaz, 1991; Schattner, 2010). The current active plate boundary between the African and Aegean-Anatolian plates to the east, occurs at the Florence Rise- Cyprus Arc (Figure 1.1, Nur and Ben-Avraham, 1978; Schattner, 2010). Some previous studies suggested that the present plate boundary between the African and Aegean-Anatolian plates (Cyprus Arc) was located north of Cyprus and transferred to south of Cyprus, between the Cyprus Island and the Eratosthenes Seamount in pre-Miocene (Nur and Bn-Avraham, 1978; Rotstein and Ben-Avraham, 1985; Robertson *et al.,* 1995a; 1995b). Earthquake studies (Papazachos and Papaioannou, 1999) suggest that the Cyprus Arc to the west connects with the Hellenic Arc (Kempler and Ben-Avraham 1987; Ben-Avraham *et al.,* 1988) and to the east, the plate boundary extends from south Cyprus to the Iskenderun Bay, toward the East Anatolian Fault junction (Ben-Avraham *et al.,* 1988; Rotstein and Ben-Avraham, 1985).

Due to the initiation of collision of microcontinental blocks on the north end of the subducting African plate, subduction has essentially stopped along the Cyprus Arc (Ben-Avraham *et al.,* 1988; 1995). In the east of the Cyprus Arc, the Dead Sea- East Anatolian Transform Fault

systems delineate the boundary between the Arabian and African plates (Vidal *et al.*, 2000a) and, across the central part of the Cyprus Arc, the Levantine Basin is slowly converging with the Aegean-Anatolian microplate to the north and results in the incipient collision of the Eratosthenes Seamount with the Island of Cyprus across the intervening trench (Figure 1.1, Kempler, 1996; Robertson, 1998b; Hall *et al.*, 2005b).

1.2.2 Study area

The Eratosthenes Seamount to the south of Cyprus, which lies 50 km SW of the Hecataeus Rise (Figure 1.2, Vidal *et al.*, 2000b), is a microcontinental block on the north end of the African plate which has become trapped in the subduction zone and locked it, consequently thrusting has jumped to the south of the seamount to the edge of the Nile delta cone (Schattner, 2010). The transition from subduction of oceanic crust to the collision of continental lithosphere is accompanied by downthrusting of continental lithosphere resistant to subduction, overthrusting and uplift of the overriding lithosphere, and complex shunting of continental blocks in the broadening subduction/collisional zone. In the late Miocene, the Seamount underwent inferred extensional faulting and broke up, followed by rapid subsidence (Robertson, 1998a) as it docked into the subduction zone.

It is believed that the arrival of the Eratosthenes Seamount at the Cyprus Arc interrupted the convergence between the African–Arabian and the Eurasian–Anatolian plates during the early Pleistocene (Figure 1.3; Schattner, 2010). On the verge of subduction, tectonic subsidence of Eratosthenes accelerated and the Eratosthenes Seamount and its surrounding area were at water depths ranging from 700 to 2000 m (Robertson, 1998b), while to the south, there was no subduction-related flexural uplift (Schattner, 2010). Microfossils of early Pliocene age that were

already of deep-marine type, indicates that much of the subsidence took place rapidly (Robertson, 1998b).

During the collision and underthrusting of the Eratosthenes Seamount with Cyprus, the northern margin of the seamount was tilted down from a depth of approximately 800 to 2000 m over a distance of about 50 km (Figure 1.3; Robertson and Xenophontos, 1993; Robertson *et al.*, 1995a). The plateau area was also undergoing active extensional faulting possibly related to crustal flexure associated with the downward bending.

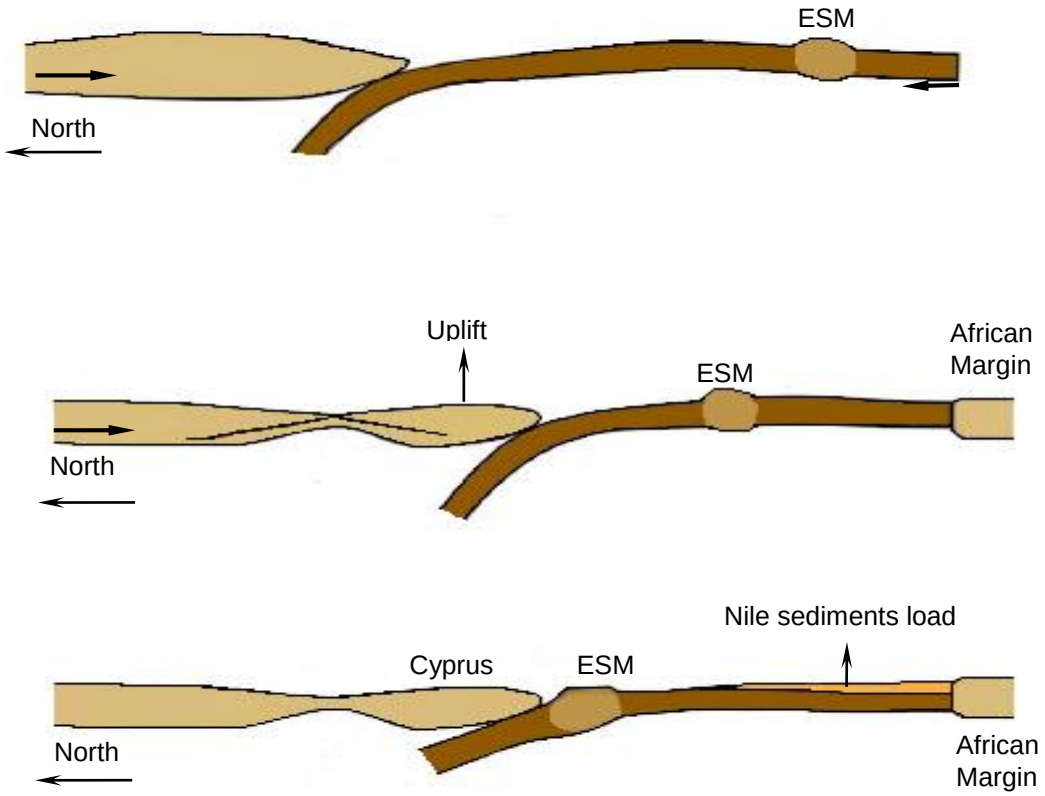

Figure 1.3 Subduction along the Cyprus Arc changed into the underthrusting of continental crust. This process is interrupted by the approach of the Eratosthenes Seamount (ESM) to its location south of Cyprus, which has caused the incipient continental collision (modified after Schattner, 2010).

Incipient collision of the Eratosthenes continental fragment caused the uplift of Cyprus in the eastern Mediterranean (Figure 1.3, Robertson, 1998b). Uplift to near sea level took place onshore southern Cyprus in early Miocene (e.g. the Maroni basin of southern Cyprus) (Robertson *et al.*, 1998b). The uplift of the Troodos Massif on Cyprus happened gradually, but markedly accelerated during, and after, the late Pliocene (Robertson, 1998b; Schattner, 2010). It is hypothesized that the increase in subsidence of Eratosthenes Seamount in late Pliocene is coincident with the rapid uplift of southern Cyprus. The uplift of southern Cyprus probably was not only because of underthrusting of Eratosthenes, but coupled with diapiric protrusion of serpentinite (Robertson *et al.*, 1995a; Robertson, 1998b). This serpentinite was hydrated, expanded and then rose diapirically and represented ultramafic oceanic mantle under Cyprus (Robertson, 1998b). The collision of Eratosthenes Seamount acted as a cause for the diapiric protrusion of serpentinite. In summary, the serpentinite diapirism combined with the underthrusting of the Eratosthenes Seamount, are seen as collaborating to the uplift of Cyprus (Robertson, 1995a; Robertson, 1998b). Deformation across Cyprus and below the sea to the east is characterized by multiple 'principal deformation zones' on structural highs.

The Hecataeus Ridge is located directly south of Cyprus (Figure 1.1) and has a steep southern slope rising around 1800 m from the floor of the Levantine Basin (Hall *et al.*, 2005b). The Hecataeus Rise is separated to the northeast from the Island of Cyprus by the Cyprus Basin and consist of highs in its central, shallowest part (Kempler *et al.*, 1994). Seismic studies reveal that the southern side of the Hecataeus Ridge is folded and cut by southward dipping steep faults (Robertson. 1998b). A weak positive magnetic anomaly over the Rise indicates that the Hecataeus Ridge may be part of an ophiolitic suite (Robertson, 1998b) perhaps an extension of the Troodos Ophiolite on Cyprus.

The area offshore from southeastern Cyprus and northeast of Hecataeus Rise is characterized by the Cyprus Basin, about 50 km wide and 2 km deep, which contains about 1km of post-Miocene sediments (Ben-Avraham *et al.,* 1995). Seismic studies suggest that this feature is likely to be a large Pliocene–Pleistocene half graben (Robertson, 1998b).

East of Hecataeus Rise, the Latakia Ridge is a prominent northeast trending narrow structure that emerges gradually from the eastern lower slope of the Hecataeus Rise, and connects the Hecataeus Rise with the Latakia region of the northern Levantine coast (Hall *et al.,* 2005b).

The Levantine Basin, the south of the Cyprus Arc, is characterized by the last remnants of the oceanic and transitional lithosphere of the Mesozoic Neotethys Ocean (Vidal *et al.,* 2000a) and together with the rifted continental crust of the Levantine continental margin (Netzeband *et al.,* 2006b; Gardosh and Druckman, 2006) forms an arcuate depression in the southeastern Mediterranean Sea. The Levantine Basin is converging slowly with the Aegean-Anatolian Microplate across the Cyprus Arc and, causing the incipient collision of the Eratosthenes Seamount with the Cyprus Island (Figure 1.1, Robertson, 1998a; 1998b).

The subsidence of Eratosthenes in the post Miocene, was rapid, and corresponded to acceleration in the uplift of Cyprus. Robertson (1998b), while suggesting that the Hecataeus Ridge may have ophiolitic associations linking it to Cyprus as cited above, also points to the possibility that the Ridge may be part of the African plate that already docked in the subduction zone, prior to the collision of Eratosthenes. This thesis aims to test these alternative hypotheses, by seeking seismological evidence for the presence of ophiolites in the upper crust of the Hecataeus Ridge (Figure 1.4).

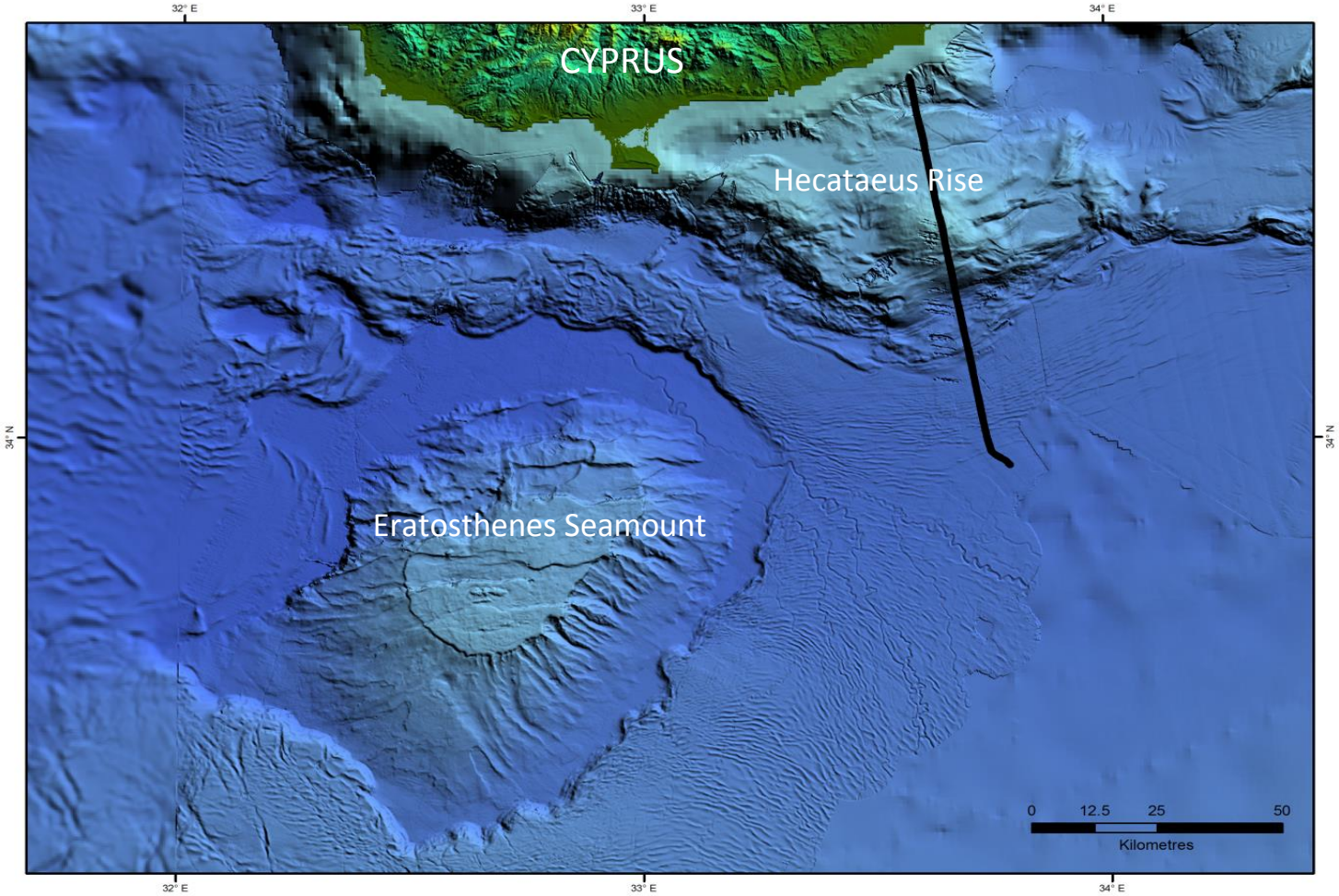

Figure 1.4 Location map of line2, southeast of Cyprus. Thick black line is the seismic data from 2010 that is used in this thesis. The map derived from the EMODNet Bathymetry portal- http://www.emodnet-bathymetry.eu.

1.3 Previous geophysical studies

The complexity of the Eastern Mediterranean has resulted in numerous tectonic models for this region (e.g. Nur and Ben-Avaraham, 1978; Robertson, 1998a; 1998b; MacKenzie *et al.*, 2006; Le Pichon and Kreemer, 2010; Welford *et al.*, 2015) but there is a lack of agreement on the geometry and crustal structure in this region. Several geophysical studies of varying type and scale have been done in the Eastern Mediterranean, but in general the structure and complex interaction of the study area south of Cyprus had rarely been studied through wide-angle seismic reflection/refraction experiments. However gravity, aeromagnetic and geomagnetic surveys have all contributed to our knowledge of crustal structure of the region and seismic experiments in the vicinity of the profile provides complementary evidence for velocity structure and crustal characteristics of the study area (e.g. Ben-Avraham *et al.*, 1995; Vidal *et al.*,2000b; Hübscher *et al.*, 2012; Klimke and Ehrhardt, 2014). Generally, the lateral change in the mode of convergence along the Cyprus Arc, and differences in the crustal structure of the underthrusting plate, resulted in compression and diffuse deformation in the eastern segment of the Cyprus Arc (Ben-Avraham *et al.*, 1995b; Reiche *et al.*, 2015).

1.3.1 The crust of Cyprus

Interpretation of gravity surveys across the Cyprus Island by Gass and Masson-Smith (1963), conducted in 1946, by Mace, and 1958 by Overseas Geological Surveys (O.G.S.), indicated a strong positive anomaly mainly between 100 and 250 mgal over the Troodos massif of Cyprus that falls off to less than 100 mgal all around Cyprus (see Figure 4.8 for original gravity anomalies). Gass and Masson-Smith (1963) believed that the strong anomaly over Troodos massif was because of an extensive slab of high density rock, at least 11 km thick, which underlies the Cyprus area at shallow depth. Gass and Masson-Smith (1963) noted that this slab was part of the

upper mantle underlying an oceanic crust between the African and Eurasian plates and was underthrust by the edge of the African plate due to east-west tensional stress and raised to its present level in the upper part of the crust when the continental plates approached each other during the Alpine orogeny.

Khan *et al.* (1972) conducted a 20 km long seismic refraction experiment in the north area of the ophiolite belt and suggested a three-layer velocity model for this region. Khan *et al.* (1972) interpreted the model as a thin (0.5 km) layer of pillow lavas with the velocity 3.25 km s^{-1}, overlying a basal layer with the velocity of 5.2 km s^{-1}, above a layer of the diabase or sheeted dyke with the velocity of 6.38 km s^{-1} at a depth of approximately 1.5–2.0 km. Khan *et al.* (1972) considered the Troodos Massif as an upthrust slice of oceanic crust.

Lort and Matthews (1972) conducted 16 short (200–1300 m) seismic refraction surveys across the ophiolite complex, each survey conducted in a single constituent rock type to specify velocities within that lithology. Lort and Matthews (1972) compared their obtained results with velocities of oceanic crust achieved from marine refraction experiments. Their obtained velocities were in the range of 2.8 km s^{-1} for the pillow lavas, 5.5 km s^{-1} for the gabbros and 3.8 km s^{-1} for the ultramafic rocks, which were lower than expected. Lort and Matthews (1972) proposed that the relatively low velocities were due to the modification and high fracturing of the Troodos rocks. Lort and Matthews (1972) further suggested that the boundary between oceanic seismic layers may represent a bulk porosity reduction caused by closure of cracks by overburden pressure instead of a petrological or metamorphic boundary.

Vine *et al.* (1973) using aeromagnetic data, observed that the amplitude of aeromagnetic anomalies over Troodos ophiolite of Cyprus were around +/-300 nT at a flying height of 1.5 km above terrain.

Makris *et al.* (1983) conducted a N–S seismic refraction experiment between Israel and Cyprus, combined with nine onshore stations in the west of the ophiolite. They concluded that Cyprus is characterized by a thick continental crust of about 35 km underneath, thinning southward of approximately 25 km below Eratosthenes and then changing to an oceanic nature crust with the thickness of 8 km below the Levantine Basin. The crust of Levantine Basin is covered by 12-14 km of sedimentary rocks.

Ergün *et al.* (2005) modeled four Bouguer gravity profiles across the Cyprus Arc. One of the profiles crosses the Troodos ophiolite and the Eratosthenes Seamount (Figure 1.5, profile C). They observed that the boundary between the African and Aegean-Anatolian plates at basement level is marked by a central gravity low. Ergün *et al.* (2005) interpreted this gravity low and the low one between Eratosthenes and Cyprus as being caused by thick sediments that are the remnants of an accretionary wedge sitting in the former trench, and that the gravity high on Cyprus was caused by the Troodos ophiolite combination (modeled with the thickness of 2 km and the density of 3.0 $g.cm^{-3}$) and a thinning of the sedimentary section.

Mackenzie *et al.* (2006) conducted 160 km combined wide-angle seismic reflection/refraction and gravity profiles (IANGASS 1995 project) across the north of the Troodos ophiolite complex and eastward into the circum-Troodos sedimentary succession and suggested a tectonic structure model with five layers consisting of sediments, pillow lavas, sheeted dykes and a gabbroic layer for the profile. They presented velocities of around 7 km/s at depths of 5-10 km for ophiolites across the Troodos ophiolite in Cyprus. Mackenzie *et al.* (2006) interpreted several syn-volcanic growth normal faults downthrown to the west of the profile that displaced both the lava/dyke and dyke/gabbro boundaries. Mackenzie *et al.* (2006) also suggested a depth reflector

at ~55 km deep beneath the ophiolite which originated from the subduction of the Sinai microplate beneath Cyprus to the north.

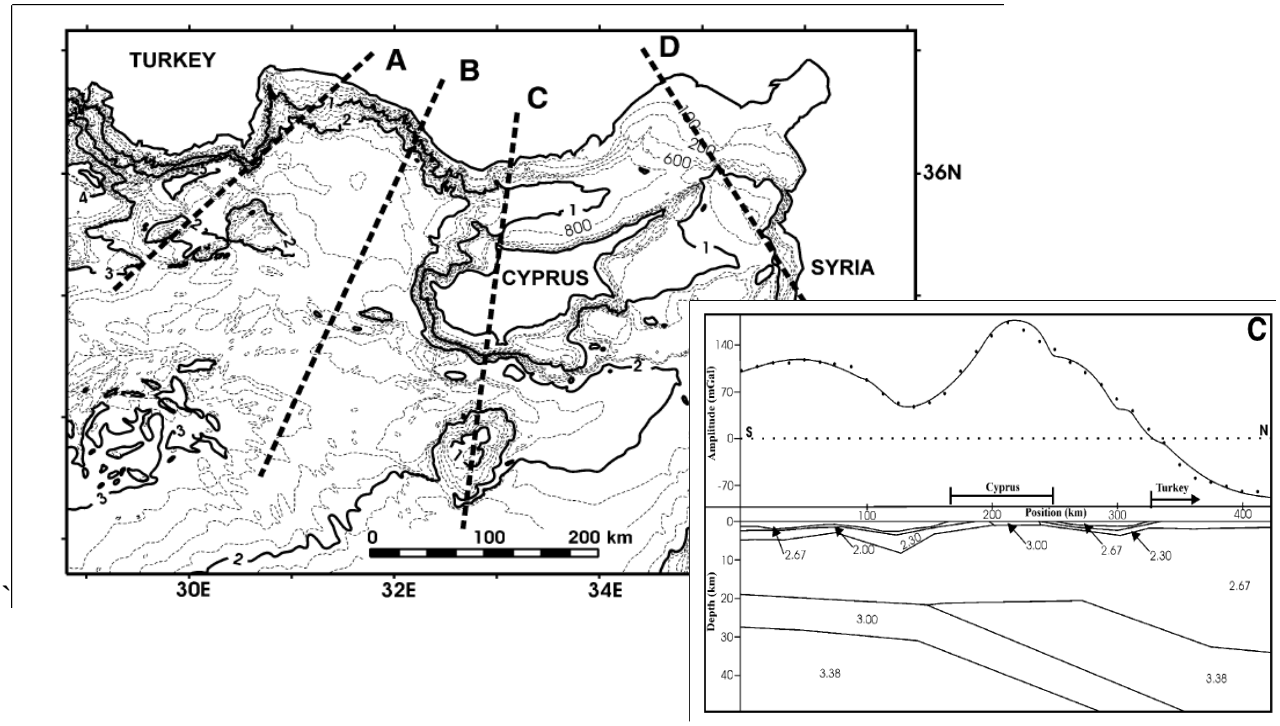

Figure 1.5 Bathymetric map of the eastern Mediterranean with location of modeled gravity profiles A-D, Bouguer gravity profile and 2D model of profile C. Dots are observed gravity, full line shows model values, Densities of layers given in g cm^{-3} (Ergün *et al.*, 2005)

1.3.2 The Mediterranean Sea and the eastern segment of the Cyprus Arc and vicinity of study area

Woodside (1977) studied the tectonic components and crust of the Eastern Mediterranean Sea from combined seismic reflection and gravity data and suggested that the crust of the Eastern Mediterranean has characteristics of either continental and oceanic crust and probably represents the marginal extension of the African continental plate. He suggested that the Eastern Mediterranean is dominated by two major thrust belts; the Kyrenia-Misis-Bitlis Thrust located in the northwest between Cyprus and southeast of Turkey, and convergence of the southeastern of

the Mediterranean Ridge and the Strabo Trench in the south of the Florence Rise. He indicated that the south Florence Rise fault continuous to the east and marks the steep (6 ~) slope of the south of Cyprus. Woodside (1977) denoted that northeast-southwest-trending large structural elements in the Levantine basin continue northeastward into structures onshore Lebanon and Syria. He suggested that a complex deformation structure along old faults and zones of weakness has affected the subduction of the Eurasian and African plates in the thinned continuation African continental crust between Egypt and the Cyprus Arc. Woodside (1977) further noted that due to contact of the African plate with the Turkish plate, shallow underthrusting of the African plate across the Cyprus Arc cause taken up of only a small part of the plate convergence.

As mentioned a N–S seismic refraction survey between Israel and Cyprus by Makris *et al.* (1983) interpreted a sedimentary section with a velocity of 2.5 $km.s^{-1}$ that probably corresponds to Miocene shales to the east of Eratosthenes Seamount that thicken northward. The next layer, with a velocity of 4.5 - 5 $km.s^{-1}$, was interpreted as Tertiary evaporites and Cretaceous to Jurassic carbonates. The next layer, with a velocity of 6 $km.s^{-1}$, was interreted as crystalline upper crust overlying crystalline lower crust with a velocity of 6.7 $km.s^{-1}$. Makris *et al.* (1983) suggested 8 $km.s^{-1}$ for the velocity of the upper mantle. Their model does not cross south of the Hecataeus Ridge. But it crosses the Cyprus Arc where it does not show any evidence of the complex crustal velocity structure.

Rotstein and Ben-Avraham (1985) considered that the Hellenic and Cyprus Arcs were part of one subduction arc in which normal subduction took place. The collision of a large oceanic plateau created the present two arc systems. To explain the unusual complexity of the bathymetric and seismic patterns of subduction zones in the eastern Mediterranean, Rotstein and Ben-Avraham (1985) suggested a tectonic model in which the Hecataeus Ridge and Eratosthenes Seamount are

oceanic plateaus in various stages of collision and accretion. They believed that the process of collision and accretion of these structures was associated with the emplacement of ophiolites which are found in Cyprus.

Kempler (1994) and Kempler and Garfunkel (1994) in their study of tectonic evolution and plate boundaries of the northeastern Mediterranean suggested irregularity in Cyprus crust toward Lebanon and Syria. They suggested the existence of compressional structures along the convergent plate boundary which have been reshaped in a transtensional regime since the middle Miocene. Kempler (1994) denoted that the Hecataeus Ridge is an example of a positive superposed structure which reflects partial reactivation of original boundaries of the lithosphere in the eastern Mediterranean during the post-middle Miocene.

Sage and Letouzey (1990) collected about 6500 km of seismic reflection data over the area east of the island of Rhodes to the Nile delta and suggested that the most southerly topographic expression of the convergence of the African-Eurasian plate is made up of the Cyprus Arc, the Florence Ridge, and the Mediterranean Ridge which extends to south and southwest of the Florence Rise. These structures separate the thrust belts in the north, which are part of the Alpine orogenic arc and usually involve lower Cretaceous ophiolite material originating in the Tethyan Ocean, and thesouth Levantine basin, Eratosthenes plateau and Nile cone basins in the south which are more tectonically stable and developed on a passive continental margin. Sage and Letouzey (1990) noted that the existence of a thrust front of late Cretaceous age in the north of Eratosthenes Seamount indicates that the Seamount resulted from a bulge of the African plate plunging beneath the Cyprus Arc. Sage and Letouzey (1990) further suggested that the Miocene-Pliocene deformation front of the Cyprus Arc between Eratosthenes and the Levantine Basin shows an en-

echelon organization with flower structures along the easternmost Cyprus Arc and Syrian margin which indicates a transcurrent movement along this front.

Ben-Avraham *et al.* (1995) collected 1300 km of seismic reflection, gravity and magnetic profiles in the east of the Cyprus Arc and noted that the structural features in the eastern part of the Cyprus Arc are all tilted to the north. They noted shallow deformation and different crustal units along the present plate boundary of the eastern Cyprus Arc which is located along a line that extends from the area between Cyprus and the Eratosthenes Seamount, along the southern flank of the Hecataeus Rise and its eastern continuation and reaches to the bathymetric escarpment west of the Latakia Ridge (Figure 1.6). Ben-Avraham *et al.* (1995) suggested that the evaporites situated north of the Latakia Ridge were affected by strike–slip deformation initiated in the late Miocene. They also suggested that wrench faulting is occurring in the eastern segment of the Cyprus Arc. As a result, a half-graben was formed that resembles a sedimentary basin along transform faults in this region. Ben-Avraham *et al.* (1995) further suggested that the convergence direction in the east Cyprus Arc changed in the late Miocene.

Robertson (1998b) published a paper in which he used evidence from drilling of the adjacent Cyprus margin and the Eratosthenes Seamount during Leg 160 of the Ocean Drilling Program to suggest that the Eratosthenes Seamount, a rifted marginal continental fragment from the north of African plate, is currently in the tectonic collision process with the Cyprus margin to the north. Consequently, the plateau area of Seamount, in response to southward overthrusting of Cyprus, experiences flexural loading and faulting, and the proximal part of Seamount (i.e. the Seamount's lower slope northwards) is undergoing compression. He used the geophysical log data (ODP, site 967) to indicate that the tectonic compression at the base of the north of Eratosthenes

Seamount caused the fold of structural high and a small sedimentary basin development in this region.

Vidal *et al.* (2000b) conducted a seismic reflection survey at the convergence zone from south of Cyprus to the Syrian coast, and from the interpretation of seismic data of line1, which passes the Hecataeus Rise, and line 2, which contains the eastern flank of the Hecataeus Rise, (Figure 1.2), Vidal *et al.* (2000b) suggested that the intersection of the Hecataeus Rise and the Levantine Basin, to the east, is a wide zone of deformation consisting of three major sinistral strike-slip faults. Vidal *et al.* (2000b) believed that the oblique convergence of the African Plate and escape of the Anatolian plate to the west created major variations in the geometry of the faults across the plate boundary. They further proposed that the northern plate became strongly deformed during the middle-late Eocene, while Eratosthenes Seamount was unaffected. They noted that the Eratosthenes Seamount was uplifted during the Miocene and emerged during the Messinian salinity crisis, as it started the initial collision with Cyprus. The authors suggested that Eratosthenes Seamount was thrust beneath the Troodos ophiolite after its load-induced subsidence occurred in response to collision with the active margin of the Anatolian plate in the Pliocene. A set of faults which are the result of flexure-induced faulting (Robertson *et al.*, 1995a; 1995b; Vidal *et al.*, 2000b), cut the uppermost Pliocene-Pleistocene sedimentary cover of the plateau area of the Eratosthenes Seamount.

Hall *et al.* (2005b) acquired ~800 km of multichannel seismic reflection profiles to study the stratigraphy and structural evolution of the eastern segment of the Cyprus Arc and the Cyprus Basin and identified four stratigraphic units bounded by major basin-wide unconformities for the active deformation front between the African and Anatolian Plates. Hall *et al.* (2005b) noted that the structural history of the deformation front is characterized by a compressional regime during

the Miocene and a strike-slip regime during Pliocene-Quaternary. Hall *et al.* (2005b) suggested that the deformation front of the Cyprus Arc is dominated by the Latakia Ridge which merges with the Hecataeus Rise in the west and continues till the north of Levantine coast in the east where the expression changes to a number of narrow, northeast-trending Ridges and basins.

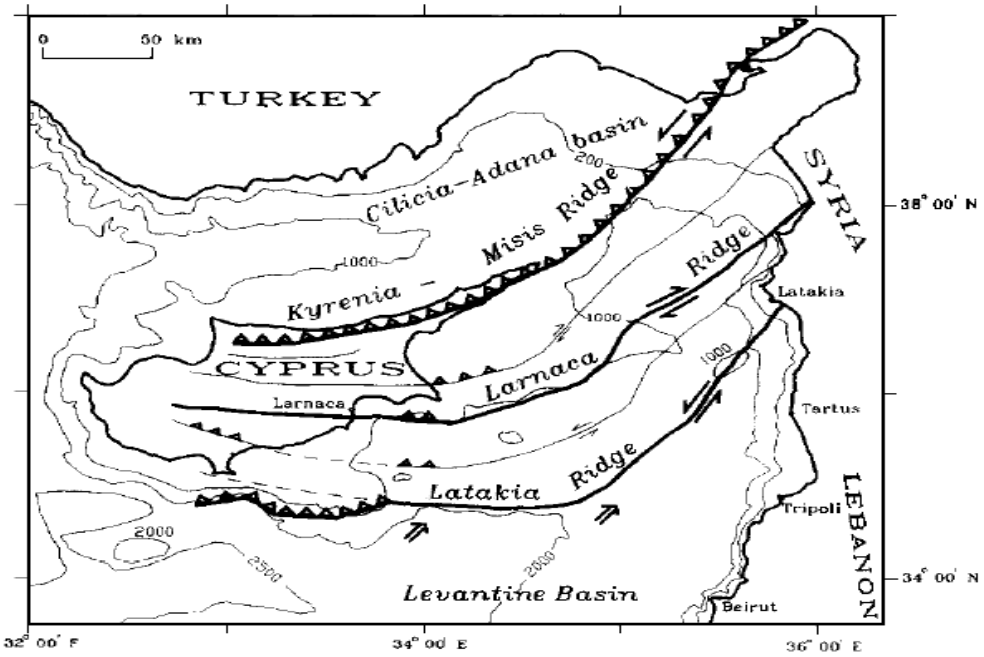

Figure 1.6 Main morphological and structural elements in the east Cyprus Arc (Ben-Avraham *et al.,* 1995). The present plate boundary along the eastern Cyprus Arc extends from the area between Cyprus and the Eratosthenes Seamount, along the southern flank of the Hecataeus Rise and its eastern continuation reaches to the bathymetric escarpment west of the Latakia Ridge

Netzeband *et al.* (2006a) in their study of structural evolution of the Levantine Basin, using high resolution seismic data, suggested five evaporitic sequences, separated with four internal reflections for the Messinian evaporite succession. They noted that each of the internal reflection bands indicate a change of evaporite facies, possibly interbedded clastic sediments, which were deposited during temporal sea level rises. Netzeband *et al.* (2006a) suggested a layer of Plio-Quaternary sediments with a velocity of 1.9-2.1 $km.s^{-1}$ above a layer with older sediments from

Jurassic to Miocene age of average velocity 3.7-4.4 km.s^{-1} and a sediment layer of velocity 4.5-4.6 km/s. They interpreted the next layer as marine carbonates, with the velocity of 4.6-4.9 km.s^{-1}. They interpreted two crustal layers throughout the model; an upper crust with a P-wave velocity of 5.7- 6.4 km.s^{-1} and the lower crust with a P-wave velocity of 6.6- 6.9 km.s^{-1}. They suggested 7.8 km.s^{-1} for the velocity of the uppermost mantle. In the south they interpreted a similar velocity model but with lower velocities than the north profile. They further noted that all of the internal reflections are differently folded and distorted, proving that the deformation was syn-depositional. Netzeband *et al.* (2006a) suggested that salt tectonics of the Levantine Basin are mainly driven by the sediment load of the Nile Cone. Netzeband *et al.* (2006a) further suggested that deep-rooted compression heavily deformed the base of the evaporites of the convergence zone of the African and the Anatolian plates in the eastern Cyprus Arc, whereas the Eratosthenes Seamount mainly experienced superficial compression affecting the post-Messinian sediments and the top of the evaporites is observable.

Hübscher *et al.* (2012) investigated tectonic processes of Eratosthenes Seamount and Hecataeus Rise from four wide-angle reflection/refraction seismic profiles (WARRPS) and suggested a compressional regime in the crustal lithosphere in the eastern Mediterranean which resulted in flexure of Eratosthenes Seamount, uplift of Turkey and Cyprus and therefore an increase in slope inclination. Hübscher *et al.* (2012) noted that the Mesozoic fault lineaments was reactivated by collision in the Levantine basin (like the Baltin-Hecataeus-Line) and created the Hecataeus Rise. The authors further noted that shortening of the Messinian to Holocene sediment succession between Eratosthenes Seamount and Cyprus has resulted in compressional salt diapirism, folding and faulting.

Klimke and Ehrhardt (2014) hypothesized an undeformed crustal structure below and south of the Hecataeus Ridge. They interpreted a sediment succession of approximately 10 km with several key horizons of Cretaceous to Plio-Quaternary age and Early Mesozoic basement in about 13 km depth in the western Levantine Basin. Klimke and Ehrhardt (2014) depicted that the sediments in the west of the Levantine basin and south of the Hecataeus Rise are undeformed and show no deformation that could be associated with subduction or collision. They believed that onlapping of the Middle Miocene reflector pinches out the Base Miocene reflector in the Levantine Basin, which is evidence of the uplift of Eratosthenes Seamount and the Hecataeus Ridge. But Messinian Evaporites north of the Eratosthenes Seamount and Levantine basin near the Hecataeus Ridge are tectonically undeformed. Klimke and Ehrhardt (2014) proposed that the Hecataeus Ridge is linked to west of the Levantine Basin and northeast of the Eratosthenes seamount by an extensive zone of thinned continental crust that acts as one tectonic unit. This may imply that the collision front is located north of this unit and that the Hecataeus Ridge covers and protects the sediments to the south from the collision between the African and Anatolian plates. However, compression regime may located south of this unit in the west and central part of Levantine Basin.

Welford *et al.* (2015) through a wide-angle refraction/reflection study of Cyprus Arc, from Eratosthenes Seamount to the Hecataeus Ridge, supported the idea of continental crust for Hecataeus Ridge. Despite poorly constrained velocity structure below the Hecataeus Ridge, Welford *et al.* (2015) did not find high velocity ophiolites in the upper to middle crust of Hecataeus comparable to the Troodos ophiolite in Cyprus (Mackenzie *et al.*, 2006) and modeled velocities of less than 5 $km.s^{-1}$ for the upper 10 km of crust below Hecataeus Ridge in agreement with this study. They denoted that the north part of the Eratosthenes Seamount has been deformed due to the collision with the Cyprus margin. They further suggested that the Hecataeus Ridge is probably

separated from Eratosthenes Seamount by oceanic crust, therefore they may not have a similar origin or history.

1.3.3 Hecataeus Ridge; a microcontinental block from the African plate docked in the subduction zone

There are no previous studies focused solely on the Hecataeus Rise and for a long time it has been thought that the Eratosthenes Seamount, a microcontinental block from the northern edge of the African plate, caused subduction along the Cyprus Arc to change into the underthrusting of continental crust (Robertson, 1998b) and the onset of collision.

Geological interpretation of seismic profiles of the Hecataeus Ridge by Robertson *et al.* (1998a; 1998b) revealed a relatively thin, nearly transparent Pliocene–Pleistocene succession, underlain by a relatively steeply dipping, folded lower unit in this area. Absence of Messinian evaporites in the Hecataeus Ridge suggested that these areas were raised, emergent features during the Messinian salinity crisis. Robertson (1998b) believed that the Hecataeus Rise experienced corresponding flexural uplift (of the upper plate margin) in the Messinian time. He suggested that the Hecataeus Rise is a microcontinental block from the northern edge of the African plate that resulted from an earlier collision than Eratosthenes Seamount and that has been transferred to the northerly upper plate.

The same author also considered that the Hecataeus Ridge might include ophiolitic material, linking its genesis to Cyprus, based on the magnetic anomaly of the Rise that merges with the larger regional anomaly characteristic of the Troodos ophiolite.

Rotstein and Ben-Avraham (1985) proposed that the elevated blocks in the eastern Mediterranean (Anaximander Seamount, Eratosthenes Seamount, etc) are oceanic plateaus in

different stages of collision and accretion that disrupted the normal subduction of African and Aegean -Anatolian plates. Rotstein and Ben-Avraham (1985) and Vidal *et al.* (2000b) considered the Hecataeus Ridge as one of the structures that had collided along the Cyprus Arc and that caused the fragmented pattern of the subduction zone and that are now attached to the southern coast of Cyprus. Vidal *et al.* (2000b) noted compression and incipient diapirism in the Pliocene-Quaternary and upper Miocene sedimentary deformation at the junction of the Levantine Basin and Hecataeus Ridge. Vidal *et al.* (2000b) further noted active faulting and deformation of evaporite units along the Hecataeus Rise. They observed an abrupt change and discontinuity in sedimentary layers from south to north of Hecataeus Rise and suggested the existence of a strike-slip boundary here. From the comparison of previous studies on Eratosthenes Seamount and interpretation of seismic data over the Hecataeus Rise, Vidal *et al.* (2000b) interpreted the Hecataeus Rise as the southern expression of the Anatolian plate SE of Cyprus. This conclusion is consistent with the interpretation of magnetic field results by Makris *et al.* (1994). The positive magnetic anomaly associated with Cyprus extends to the south of Cyprus including the Hecataeus Ridge. So the Hecataeus Ridge is considered as a continental fragment belonging to south of Cyprus continental crust (Makris *et al.*, 1994; Vidal *et al.*, 2000b). However, the amplitude of aeromagnetic anomalies over the Troodos ophiolite of Cyprus is around +/-300 nT at flying height of 1.5 km above terrain (Vine *et al.*, 1973). The same source would have to be buried by several kilometers more to produce the low anomalies observed below Hecataeus Ridge.

1.4 Scientific objectives

The specific objectives of studying the marine seismic refraction data that are the focus of this thesis are:

1) To analyse the seismic data and identify characteristic phase arrivals and apply ray tracing techniques to construct a cross-section velocity model of the Hecataeus Ridge that conforms to the travel time picks.

2) Use the velocity model to interpret the crustal structure and composition of the Hecataeus Ridge

3) Use interpreted results to determine if the Hecataeus Ridge might be a microcontinental block from the northern edge of the African plate or, alternatively, to determine if it is a part of the Aegean-Anatolian microplate carrying an ophiolitic shallow basement, as found immediately to the north.

CHAPTER 2

Data acquisition and processing

Memorial University of Newfoundland in collaboration with Dalhousie University and the University of Hamburg conducted seismic refraction surveys in 2010 using Dalhousie, Geological Survey of Canada (GSC) and German Ocean Bottom Seismometers (OBS) aboard the German research vessel Maria S. Merian (Figure 2.1) south of Cyprus, in the Eastern Mediterranean Sea. Four main refraction profiles (Figure 2.2) were acquired. Line 2, the focus of this thesis, is 80 km long and was designed to determine the velocity structure of the crust of the Hecataeus Ridge to the south of Cyprus.

Figure 2.1 German research vessel Maria S. Merian.

2.1 Data acquisition

The survey consisted of recording four wide-angle profiles (Figure 2.2) across the subduction/collision zone in the eastern Mediterranean. It was undertaken from March to April, 2010. For line 2, OBSs were deployed on March 23rd, 2010 and shots fired on March 23rd and 24th, 2010. A total of 15 OBSs, comprising hydrophones and three-component 4.5 Hz geophones, were used along the 80 km profile, with a spacing of approximately 5 km between OBSs. 10 of the instruments were owned by Dalhousie University and the Geological Survey of Canada and 5 by Hamburg University. Shots were fired approximately every 100 m along the profile. To navigate, synchronize and calculate OBS and shot locations and shot timing, the Global Positioning System (GPS) was used.

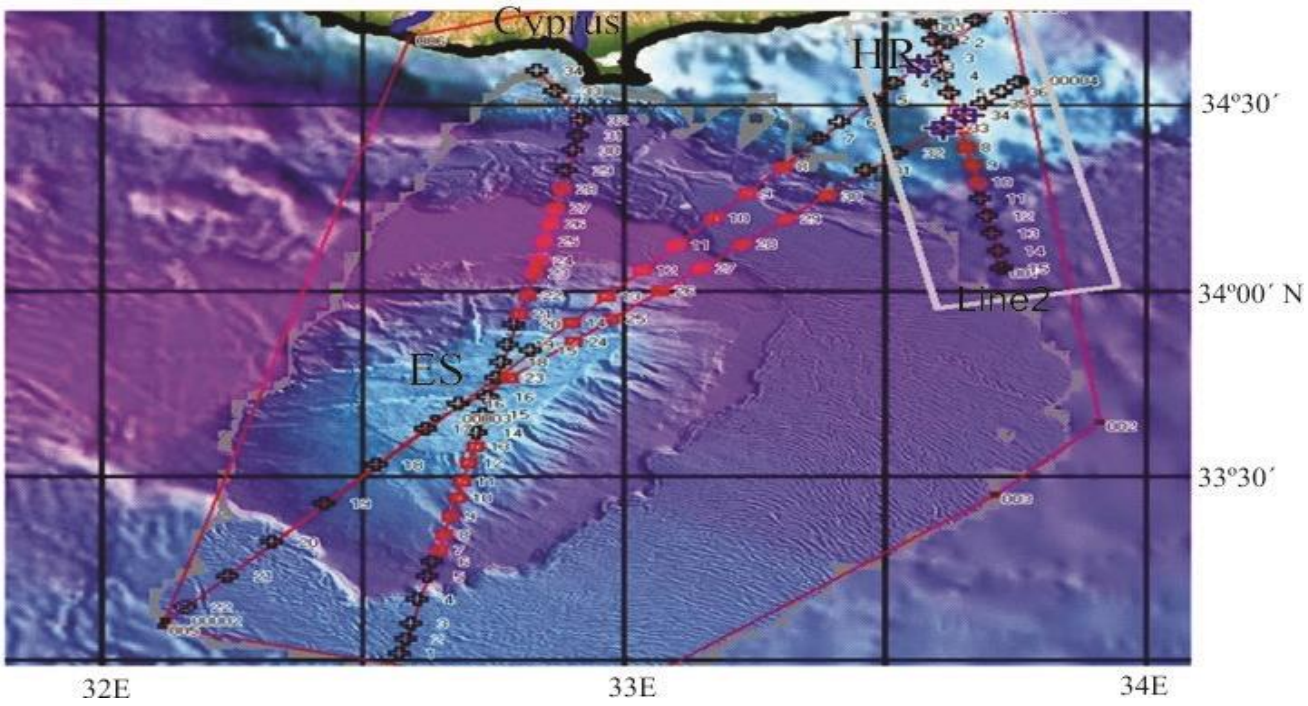

Figure 2.2 Wide-angle seismic experiment locations, south of Cyprus. Line 2 is highlighted with the white rectangle (ES-Eratosthenes Seamount, HR- Hecataeus Ridge). Black symbols indicate the instruments owned by Dalhousie University and the Geological Survey of Canada and red symbols show the instruments owned by Hamburg University. The bathymetric metadata and Digital Terrain Model data is derived from the EMODNet Bathymetry portal- http://www.emodnet-bathymetry.eu.

2.1.1 Shot and recording instruments

The air gun array provided by the Canadian group for this experiment consisted of two steel beams (Figure 2.3), each supporting one 1000 cu. in. (16.4 l) gun and one 700 cu. in. (11.5 l) gun. The guns were suspended by chains from the 5 m steel beam, itself hung from buoys to lie at 10 m depth. Thus the total volume of the array was 3400 cu. in. (56 l). The array was towed astern, and connected to the- ship by an umbilical cable with air lines and electrical lines. The 15 OBS were deployed along the profile (Figure 2.4), including five DAL OBS (E, F, I, K, N) for Stations 1-5 in shallow water, at 519-822 m depth; 5 Hamburg OBS deployed at stations 6-10 and five GSC OBS (A, C, E, F, H) for Stations 11-15 in deeper water of 1930-2175 m (Figure 2.5).

Table 2.1 indicates more details about the Canadian ocean-bottom seismometers and Table 2.2 shows basic information about the German OBSs.

Figure 2.3 Canadian gun beam on stern deck of Maria S. Marian, with two guns mounted.

Item	Specification
Housing/Platform	Uses existing design of BIO-OBS (6 km max water depth). Weight in air: instrument (82 kg); anchor (55 kg) Size: 1.1 m high, 1.2 m long, 0.6 m wide
Release	12.5 kHz Acoustic command + timed backup
Duration of recording	23 days @ 2ms sampling on 8 Gb flash card
Sampling rates / dynamic range	up to 5 kHz / 16 bit SAR ADC
Anti-alias filter	software selectable 8th order low-pass digital filter (LTC1164-7)
Gain	Variable settings software selectable: geophones (0-40 or 53-93 dB); hydrophone (0-40 or 34-74 dB)
Max electrical noise	< 125 nVrms on geophone input < 1u Vrms on hydrophone input
Clock	Seascan precision clock, (4 MHz, drift<1 msec/day)
Data storage	Persistor CF2 data logger with variable length files stored on 8 Gb flash card; optional use of 2.5" HD up to 80 Gb
Sensors	3-component deployed geophone package (oil filled), deployed on bottom with corrosible link: 4.5 Hz (Mark L-15B or L-28; 380 Ohm coil w/ 0.7 damping) hydrophone (OAS E-2SD)

Table 2.1 Canadian OBS specifications taken from http:\\seismic.ocean.dal.ca/obs.php

(b)

(a)

Figure 2.4 a) Canadian OBSs on the deck of RV Maria S. Merian, b) Ocean Bottom seismometer ready for deployment

item	**specifications**
Data logger	MLS10 sample rate 50Hz MLS14 sample rate 200Hz
Hydrophones	HTI-04-PCA/ULF
Matching of hydrophones to MLS	by pre-amplifier LOWN21/ input sensitivity 1,25Vss in MLS-logger
Seismometer	LE-1D/V 223-0035
Releaser	KUMQUAT K/MT 562 IXSEA (MORS)

Table 2.2 German OBS specifications

2.1.2 OBS locations

OBS launch and shot positions were obtained using the Global Positioning System (GPS) and water depths were calculated using the ships echo sounder responses and reflection profile over the Hecataeus Ridge. OBS locations along the colocated Hecataeus reflection seismic profile are indicated in Figure 2.5. No data was collected from station 2 (OBS F).

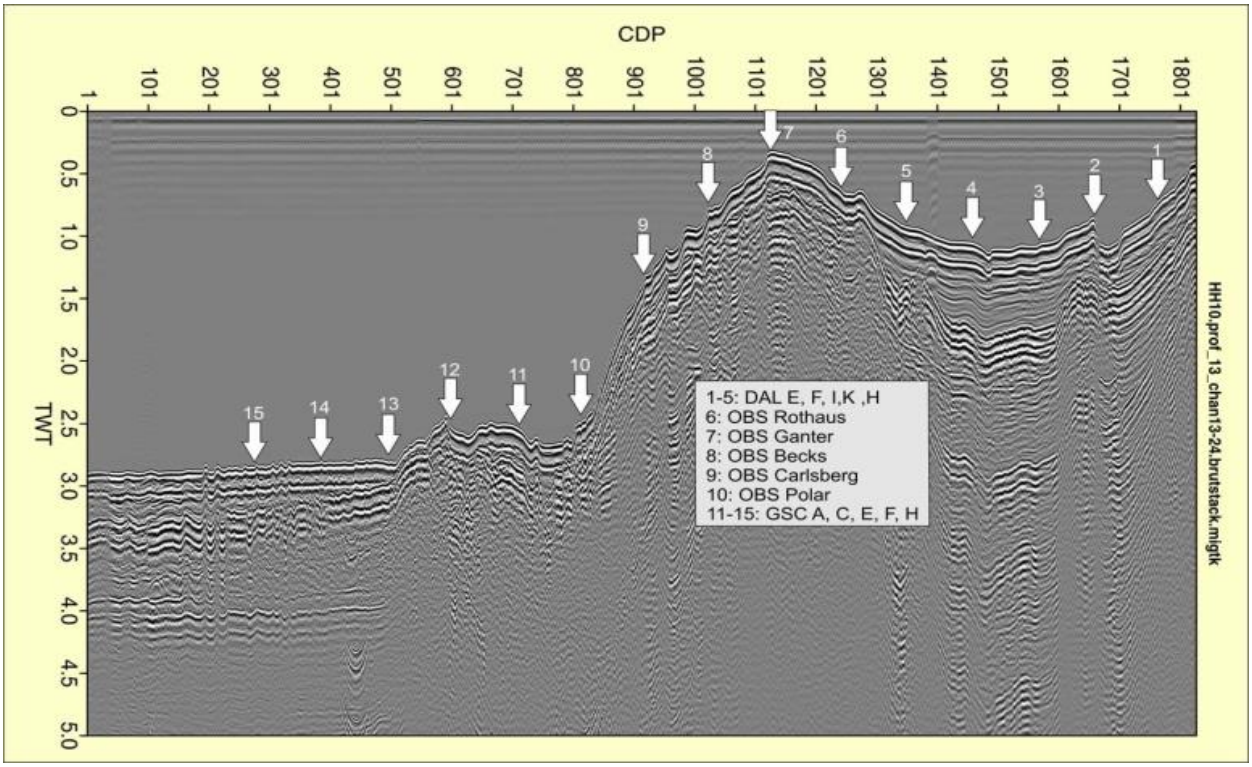

Figure 2.5 Brute stack of reflection data collected using the air gun shots on a short streamer. White arrows indicate the OBS locations along Hecataeus reflection seismic profile (line 2).

Table 2.3 shows the model distances for OBSs along the profile. These were computed using GMT (Generic Mapping Tool, Wessel and Smith, 1988) by projecting the OBS locations onto a great circle from OBS1 to OBS15 and Table 2.4 shows the longitudes and latitudes for the located OBSs.

OBS #	OBS Name	Model distance (x, in km)	OBS depth (z. in m)
1	DALE	0	551
3	DALI	10.43	819
4	DALK	15.67	798
5	DALN	21.19	685
6	Rothaus	26.43	36
7	Ganter	31.63	278
8	Becks	37.02	664
9	Keo	42.33	1054
10	Polar	47.63	1891
11	GSCA	52.96	1919
12	GSCC	58.40	1872
z13	GSCE	63.69	2138
14	GSCF	68.97	2153
15	GSCH	74.43	2176

Table 2.3 Distance and depth of OBSs along the Hecataeus seismic profile, line2.

Once deployment was completed, the shots were detonated, and finally the OBSs were recovered. After OBS recovery, the raw OBS data were converted to SEGY format.

OBS#	OBS Name	longitudes (˚E)	latitudes (˚N)
1	DALE	33.5842	34.717
3	DALI	33.6045	34.6246
4	DALK	33.6147	34.5783
5	DALN	33.6254	34.5294
6	Rothaus	33.6355	34.4831
7	Ganter	33.6456	34.437
8	Becks	33.656	34.3894
9	Keo	33.6662	34.3424
10	Polar	33.6765	34.2955
11	GSCA	33.6867	34.2483
12	GSCC	33.6972	34.2001
13	GSCE	33.7073	34.1533
14	GSCF	33.7175	34.1065
15	GSCH	33.7279	34.0582

Table 2.4 Latitude and longitude of OBSs along the line 2.

2.2 Preparation of data

2.2.1 Time correction

To account for the clock shift, the width of the pulse, electronic recording delay, and the guns mechanical delay, timing corrections were applied to each OBS record (Welford *et al.*, 2015). The data were already time corrected before doing any further process for this thesis. For the

Canadian OBSs an average total time correction of -139 ms has been applied and for the German OBSs an average total time correction of -69 ms has been applied.

After the time corrections, a Matlab code from Dalhousie University was used to recalculate the OBS locations using the near-offset picks of the direct arrival, the original OBS locations and a water column velocity. The water column velocities are calculated considering the temperature and salinity of the region and are indicated in appendix A.

2.2.2 Processing routine

Once the time corrections were applied to the data, the SEGY file headers were updated with survey geometry and timing information for input into the PLOTSEC (Amor, 1996) seismic processing program. The PLOTSEC package contains routines that allow the user to merge different data sets according to time and/or offset, update parameters in the SEG-Y header file, stack data, interactively pick phase arrivals, apply different reducing velocities and plot data sections to the screen or on hardcopy according to time and/or offset. For the initial step, the data were read into the system using the plotsec_rsegy option with the reducing velocity of 8 $km.s^{-1}$. The recorded direct wave for each OBS was used to recalculate the OBS position on the sea floor and then the shot-receiver offsets were recalculated relative to the corrected OBS positions. To pick the first breaks at near offsets (~10-15 km) all shots were band-pass filtered from 4.0 to 10 Hz using the plotsec_filt routine. Figure 2.6 indicates one of the stations as an example before and after applying band-pass filter. For other stations see Appendix D.

For picking the events, the data were plotted with true amplitudes in different offset ranges with different scales dependent on the quality of the data of that particular station, using the plotsec_plot routine. To account for the decrease in amplitude with increasing offset caused by spherical spreading and attenuation, the traces were scaled and individually multiplied by their

(a)

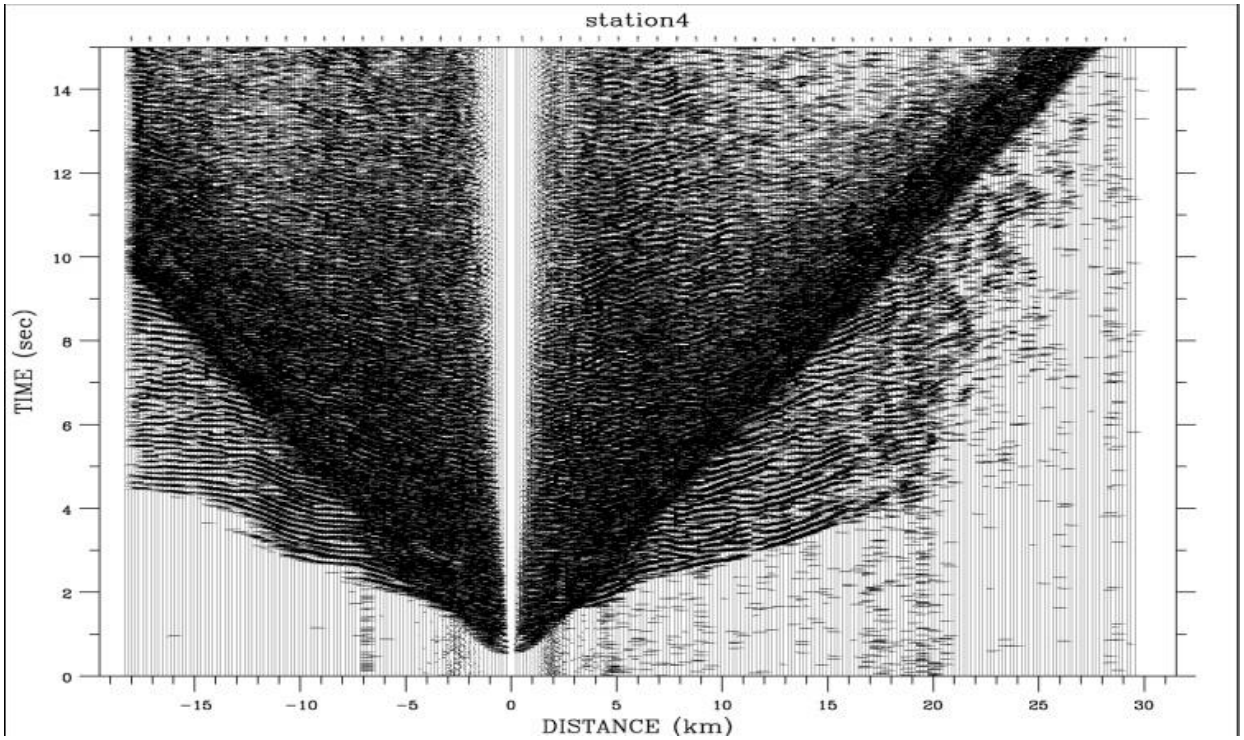

(b)

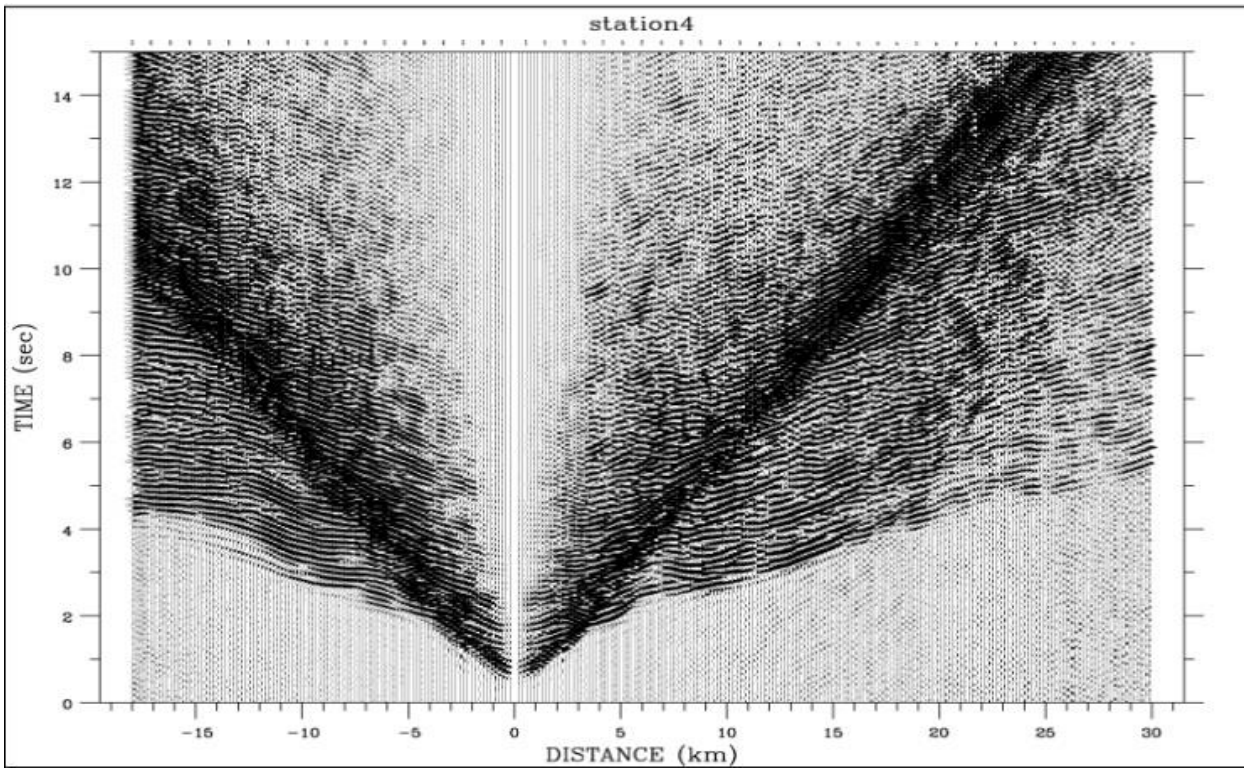

Figure 2.6 Hydrophone component receiver gather for OBS 4. a) SEGY format of the data with applied time correction, b) With applied band pass -filter from 4-10 Hz.

source-receiver distance in the true relative amplitude plots. Different choices of scaling were determined based on visual examination and improvement of the far offset arrivals.

The data for most of the OBSs had a good signal-to-noise (S/N) ratio. Due to the sparsity of shear wave data, only the P-wave arrivals were analyzed in this thesis.

2.2.3 Coherency filter

After primary picking of near offset arrivals was done and the shallow structure velocity model was developed (see next chapter), the data were coherency filtered to enhance the visibility of coherent events and enhance arrivals at longer offsets. Appendix D, Figures D1b, D4b..., D40b indicate the data plots after applying coherency filter.

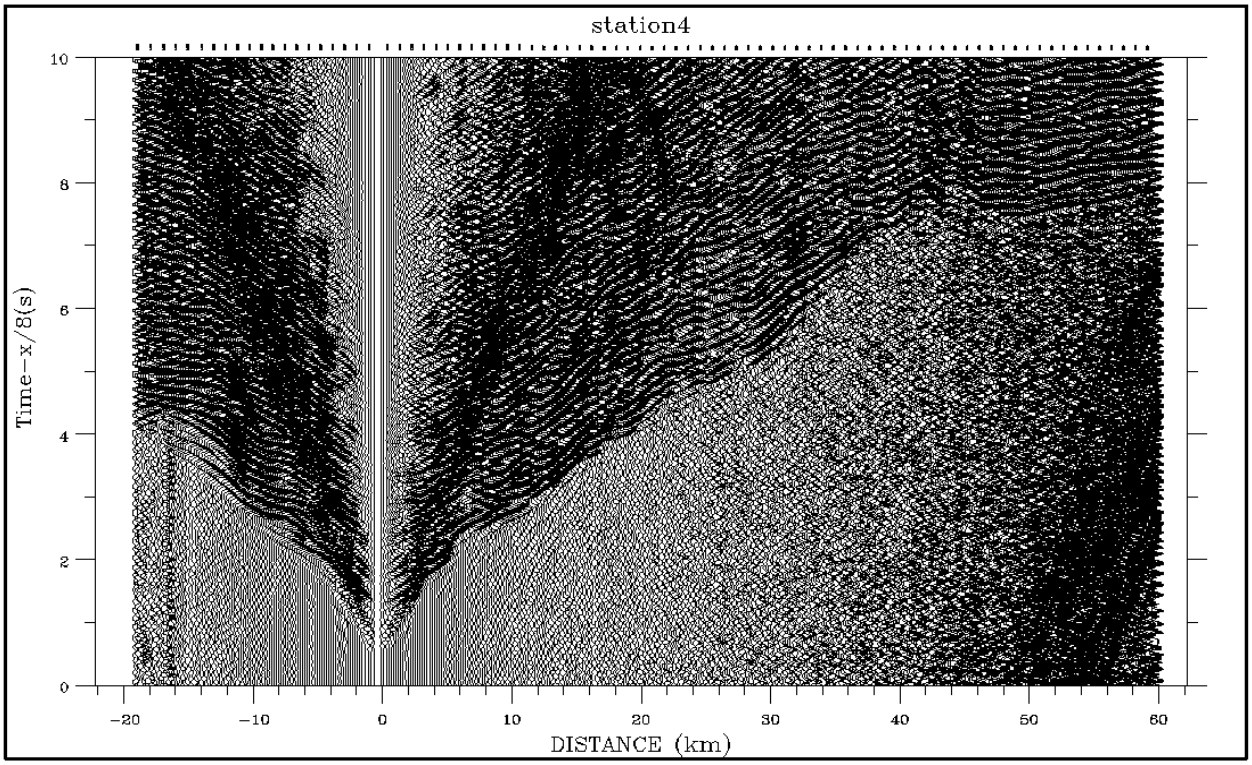

Figure 2.7 Hydrophone component receiver gather for OBS 4, after band pass filtered (4-10Hz) and applying coherency filter.

In general, for crustal seismic data, events may be present on seismograms over long offset range; but often they are hidden under noise. As such, local coherency is usually more relevant to the interpreter than is global continuity. The SEMBSMOOTH software (written by Bernd Milkereit and further modified by Lithoprobe staff, Mark Lane, Rolf Maier and Kris Vasudevan) that was used to filter the data takes advantage of this local coherency, using a sliding window algorithm to compute the minimum semblance of traces within a range of apparent velocities.

The SEMBSMOOTH process module is a post-stack coherency filter.

The fundamental steps of the algorithm are:

1. Compute semblances over a lateral window of traces.

Local semblances are computed using a slant-stack method. A lateral window is centred on a given input trace. Then, over the range of the window, semblances are computed along dipping straight lines, centred on the input trace. The semblance, in this context, is the slant stack sum squared, divided by the total input power along the slant path. This lies between 0 and 1 inclusive, with 0 representing total incoherence and 1 complete coherence. In order to stabilise the estimate near the zero crossings of wavelets, the semblances are conditioned with a short median filter. The result of this process is a semblance value for each dip, at each input data point. For each input point, the maximum semblance over all dips is chosen as the output of the process. Thus a map of semblances is derived, one semblance for each input point.

2. Compute coherencies from these semblances.

Coherencies are calculated as the semblance raised to an exponent, the exponent being dependent on the estimated noise to signal ratio of the data. This has the effect of pushing low

semblances lower while minimally decreasing high semblances; the larger the exponent, the more the incoherent noise is reduced. (Although, of course, so are the less coherent events.)

3. Smooth the data in the direction of the maximum semblance.

The input data are smoothed by taking the average value in the direction of maximum semblance, over the lateral window

4. Filter the smoothed data using the coherency.

The filter is applied by scalar multiplication of the smoothed data with the coherency on a point by point basis.

SEMBSMOOTH is similar in operation to the other coherency processors but with the differences that SEMBSMOOTH:

- produces cleaner output, particularly at the near surface
- runs about five times faster than other processors with similar parameters
- produces output with non-linear amplitudes (anomalously low numbers of samples with near-zero amplitude).

The parameters that are used for coherency filtering of the data are explained in Appendix B.

CHAPTER 3

Data analysis and modeling

3.1 Data interpretation and modeling procedure

3.1.1 Quality of data after processing

The data quality is variable, ranging from high signal to noise (S/N) ratio to noisy and poor quality in far offsets for some stations. Band-pass and coherency filtering improved the quality of data. Some stations like OBSs 1-4 still show low signal to noise ratio but still best given the coherency filtering. Primary phases are observable for most of the seismographs. Although some stations still are noisy and do not show clear arrivals, this might be due in part to recording the data in one of the busiest seas in the world.

Data plots and related results after applying band-pass filter, and coherency filter are presented in Appendix D. Figures D1a, D4a... D40a display the raw data, Figures D1b, D4b... D40b display the processed (bandpass and coherency filtered) data and Figures D3, D6...D42 display the plots with the picked phases.

3.1.2 Approach to modeling

The sequence of steps in the modeling is described later (section 3.3) and illustrated in Table 3.1. For the first step after processing the data, the clearest first breaks of OBS records were used to construct a shallow velocity model for each OBS using the forward modeling component of RAYINVR program from Zelt and Smith (1992) (Appendix D, Figures D2b, D5b…D41b). The information obtained from modeling of each OBS were used with the tomographic code tomo-2D from Korenaga *et al.* (2000; 2001) to construct an initial velocity model for the profile. “The tomo-

2D code uses a hybrid ray tracing method based on the shortest path method and the ray bending method" (e.g. as illustrated in Welford *et al.,* 2015). A simple linearly increasing velocity model with a water layer and accurate seabed geometry was constructed for the shallow part of the profile. This velocity model was used as a starting input model to develop final velocity structural model by forward modeling and constructing layer by layer from the top of the model to the bottom and fitting the observed travel times at near offsets first and then further to larger offsets (Welford *et al.,* 2015). The detailed explanation about parameters and the resulting final model from tomo-2D and RAYINVR is explained later.

3.2 Picking of phases

3.2.1 First arrivals

3.2.1.1 Water wave arrivals (P_w)

The first arrival in marine refraction seismograms at short offset, as indicated in Appendix C, is the water wave. This arrival has a very large amplitude and it has a velocity of ~1.5 km.s^{-1}. Figure 3.1 shows a couple of stations with picked water arrivals.

Water wave arrivals are the reference point of correlating the seismograms with each other (Figure 3.2) using the reciprocity of total travel time for the same phase (for more details see Appendix C).

3.2.1.2 Near offset arrivals

As the seismic waves propagate through the different layers of the Earth, a change from a relatively low velocity layer to a high velocity layer causes the rays to turn and the upcoming ray is refracted to each OBS (Fowler, 2004; McClymont, 2004).

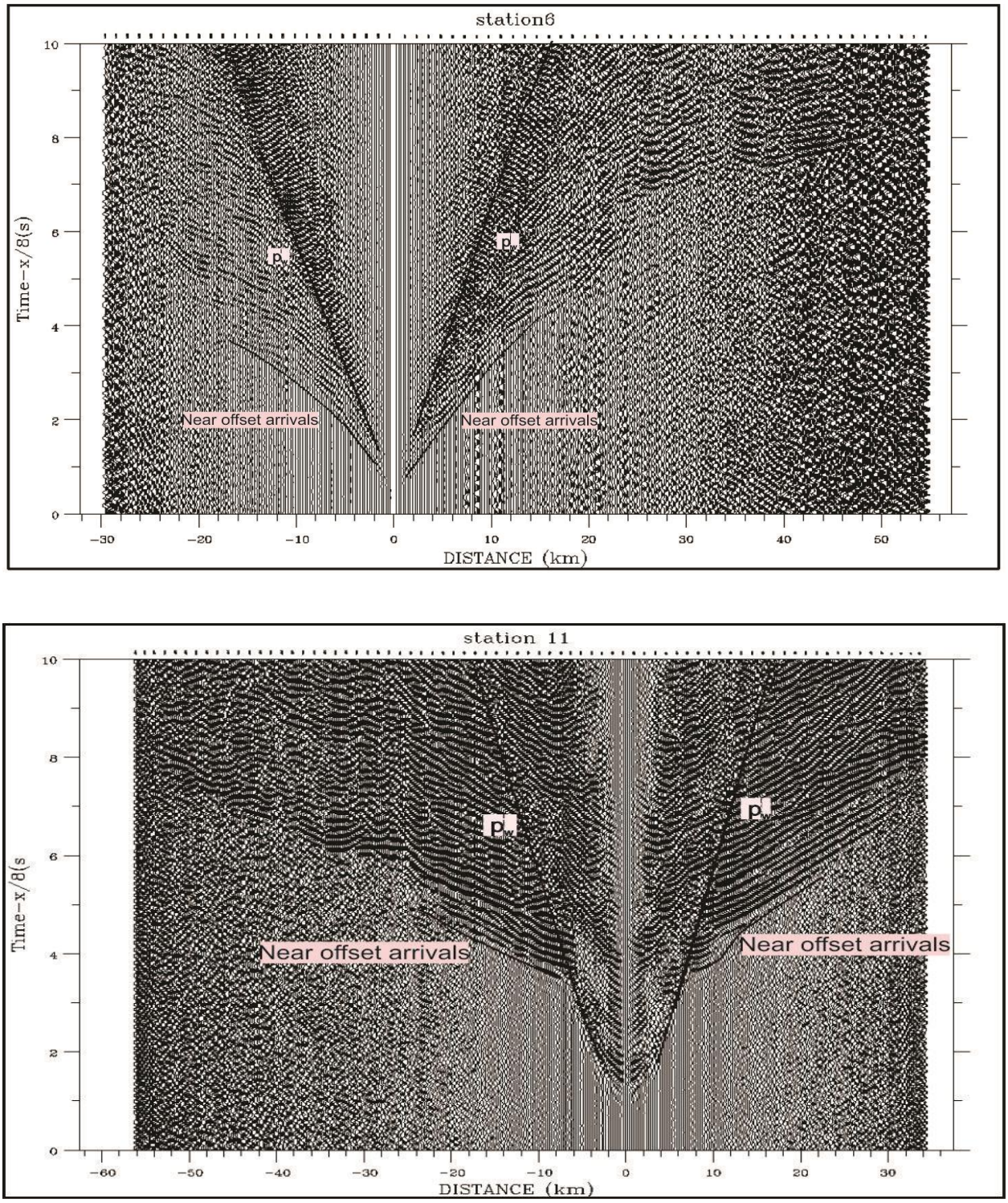

Figure 3.1 Hydrophone component receiver gathers for OBS 6 from shallow part of the profile and OBS 11 from deep part of the profile with water wave arrivals (P_w), velocity of ~ 1.5 km.s^{-1}, and near offset~15 km picking arrival times. Near offset arrivals delineate near surface layers with laterally variable velocities ranging from 1.5 km.s^{-1} to 3.6 km.s^{-1}.

The near offset arrivals represent rays turning in the shallow sub-seabed layers. These arrival times provide insight into the velocity and velocity gradient distributions within the shallow layers along the profile. This phase is easy to pick for near offsets (~10-15 km, Appendix D, Figures D2a. D5a…D41a) where the trace is relatively free from noise and has high amplitude. The apparent velocity of near offset arrivals lies in the range of 1.5 km.s^{-1} to 3.6 km.s^{-1}. Figure 3.1 shows a selection of OBS records with picked near offset arrivals.

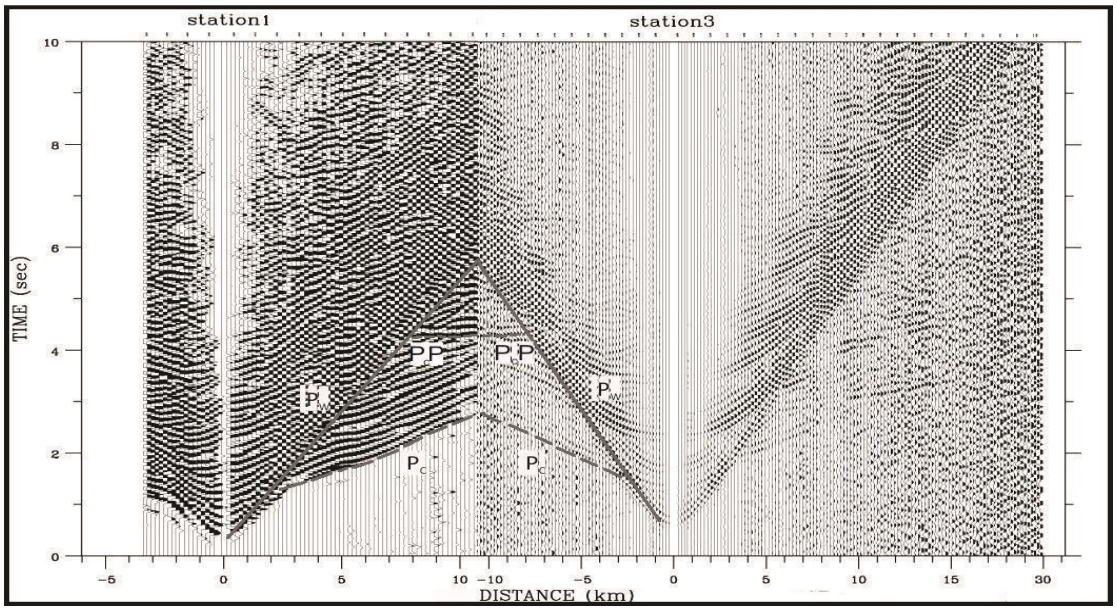

Figure 3.2 Correlation of record section of OBS 1 and OBS 3. OBS 1 is located at x=0 and OBS 3 is located at x=10.43 km along the profile. The depth difference for these two stations is (Z_1= 0.55 km, Z_2= 0.81 km) ~0.26 km, Water wave velocity is specified as 1.5 km.s^{-1} and is the first arrival of each record section. So the time difference would be 0.26/ 1.5= 57ms. With shifting of OBS 3, 57 ms relative to OBS 1 and matching the water wave arrival, other phase arrivals can be correlated too. (P_c= refraction arrival, P_w= water wave arrival, P_cP= reflection arrival).

3.2.1.3 Wide offset arrivals (P_c)

The limited size of the source, surrounding noise and the complicated velocity structure of area might be the reasons for the poor energy propagation in far offsets for many OBSs (Welford

et al., 2015). Because of these factors not many phases could be observed for each OBS record section. The most dominant refracted arrival, P_c, (Figure 3.3, Appendix D) was observed for all OBS records and indicates the crustal refractions. This phase continues from near-offset arrivals with change in apparent velocity.

Picking of P_c arrivals can be continued out to a range of 60-70 km for most stations (Figure 3.3; appendix D). However for offsets greater than 15-20 km, where noise is more of a problem, records must be picked carefully. The data quality for both vertical and hydrophone components of the OBSs are generally good after processing and picked arrivals were verified on both components. The noisiest data along the profile are from stations 3 and 13 (Figures D3 and D23) where the P_c phase can be picked up to no more than 40 km. These arrivals show a broad range of apparent velocities from 3.2 km.s^{-1} to 6.2 km.s^{-1}.

3.2.2 Secondary arrivals

3.2.2.1 Crustal reflection arrivals (P_cP)

Wide angle crustal reflections are second arrivals after the P_c phase in receiver gathers. When this phase is observed consistently over at least a few stations, it can provide information about the geometry of a subsurface boundary and the velocity contrast across it. The data set from line 2 exhibits a few consistent crustal reflections (Figure 3.4).

Also there are a few short reflectors, observed sporadically in some stations which have relatively poor amplitude. These reflectors are less informative but still can be helpful in the modeling process (Welford, 1999).

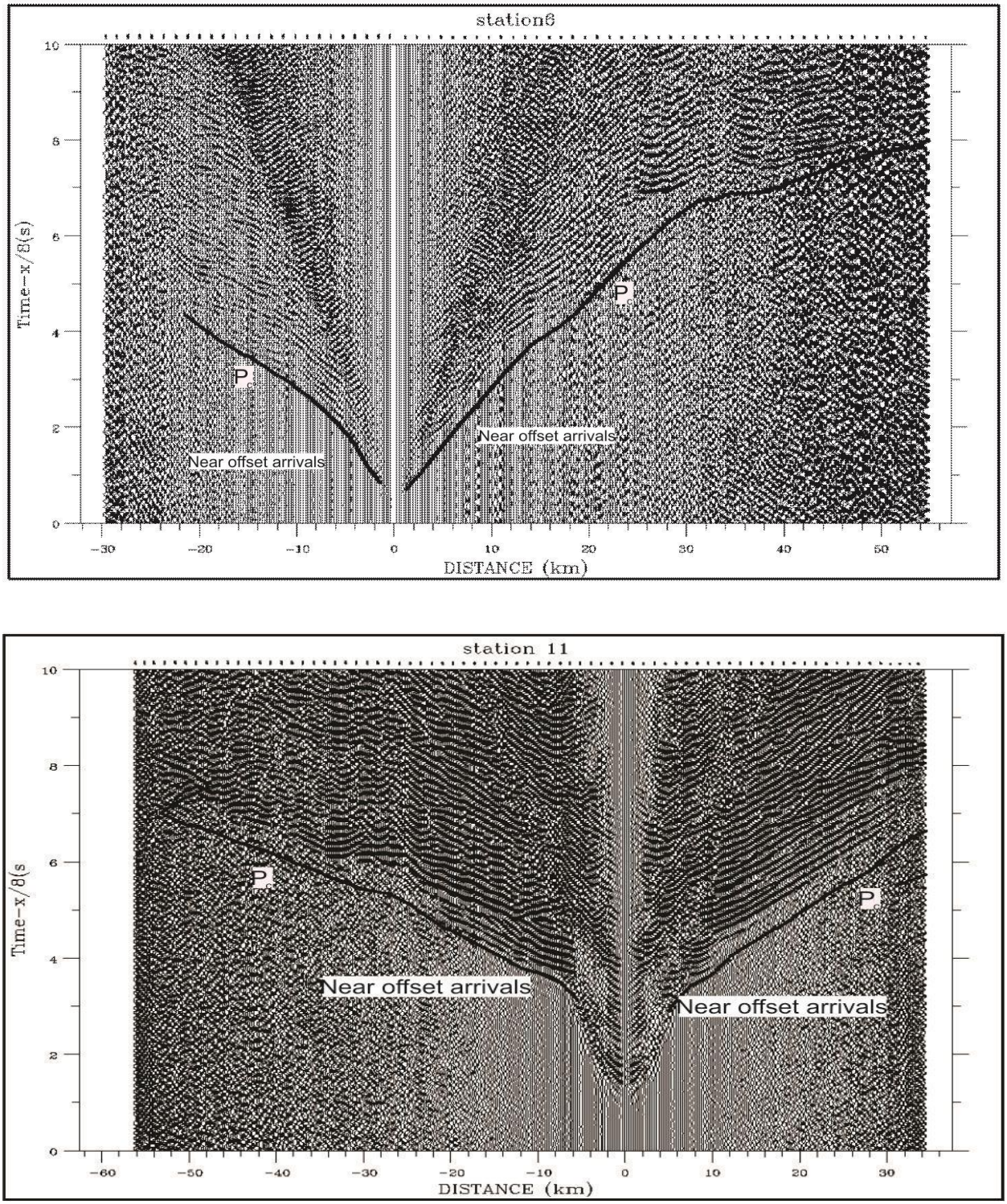

Figure 3.3 Hydrophone component receiver gathers for OBS 6 from shallow part of the profile and OBS 11 from deep part of the profile with far offset arrivals (P_c), this phase is observable for all OBS record sections (appendix D) and represents a broad range of velocities from 3.2 km.s^{-1} to 6.2 km.s^{-1}.

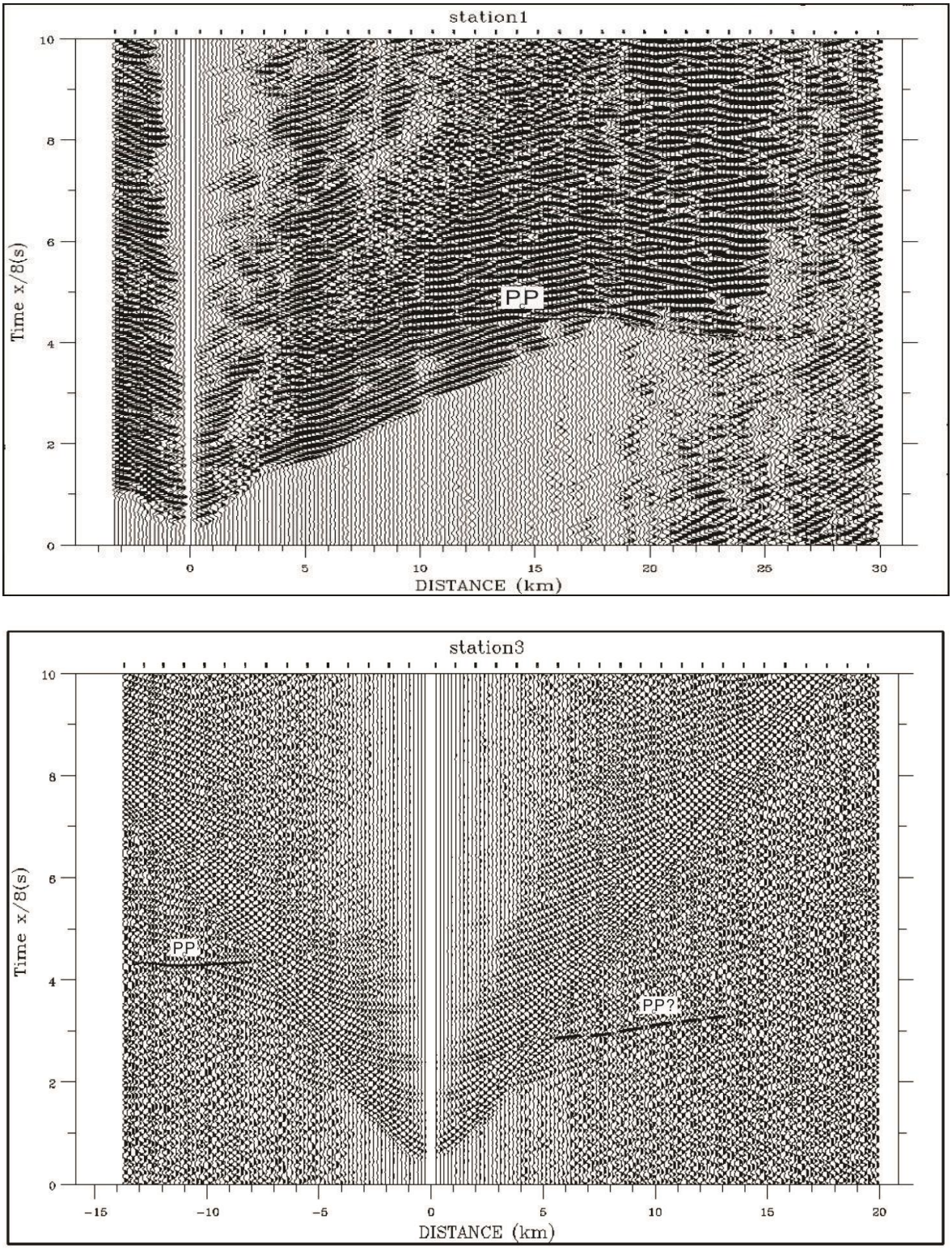

3.4 Hydrophone component receiver gathers for OBS 1 and OBS 3 showing examples of the consistent crustal reflection arrivals.

3.3 Approach to interpretation

The sequence of modeling the data followed the path shown in Table 3.1. Once the data set for each instrument has been processed, short offset arrivals at ranges of < 15 km were picked (Appendix D, Figures D2a, D5a…D41a). An initial velocity model was constructed for each OBS based on the short offset picks (Appendix D, Figures D2b, D5b…D41b). Then a shallow crustal structure tomography model was developed using the merged results of each OBS individual modeling. Then further offset arrivals > 60 km were picked using the data correlation from large paper plots and reciprocity among a number of different source receiver pairs and the interactive plotsec-pick routine (Amor, 1996) (Appendix D, Figures D3, D6…, D42). The travel times calculated for the constructed model are based on the reliable picked travel times, but the data were of modest quality for some stations, suffering from noise and incoherent events. Even with strong filtering, no P_c phase could be picked further than 40 km for some stations (stations 3 and 13). Also no clear Moho reflection was identified throughout the transect. Therefore the following analysis focuses mostly on the modeling of refracted arrivals.

The uncertainty of each pick was calculated using the plotsec_amppk routine (Amor, 1996) that estimates the uncertainty value by comparing the energy before and after the pick over a time window of 0.1 s. Generally the uncertainty of picks increases with shot offset. The picks with large uncertainties can be highlighted during the modeling process and viewed after modeling.

The wide-angle experiment along line 2 resulted in 1500 traces recorded by each Canadian instrument and 1376 traces recorded by each German instrument. From these traces, for each OBS approximately 1000 traces provided usable travel time picks for rays turning in the layers beneath the seafloor.

The recorded traces for each ocean bottom seismometer and also number of picks and corresponding average uncertainties are displayed in Table 3.2.

Step	Process	Notes
1	Pick data	Described in section 3.2
2	Forward model short offset data from individual OBS	Using RAYINVR forward modeling
3	Create initial model for shallow structure for whole	Smooth interpretation of results from step 2, by 'hand'
4	Apply TOMO2D inversion	Good shallow velocity model for whole line
5	Create mode for overall structure on whole line	Based on Step 4 formatted for RAYINVR forward modeling
6	Apply RAYINVR forward modeling for overall structure of whole line	Iterate until satisfactory fit
7	Final velocity model	Derived from final interaction in Step 6

Table 3.1 Sequence of modeling the data

3.4 Modeling algorithms and techniques

Analysis, modeling and interpretation of crustal seismic refraction data mostly involves using a trial-and-error forward two-dimensional ray tracing model such as those developed or used, by Spence *et al.* (1984), Mereu *et al.* (1977), Zelt and Ellis (1989), Funck *et al.* (2004), Welford *et*

al. (2015). Forward modeling ray tracing algorithms that incorporate inversion techniques are a more efficient way of ray tracing because they reduce the misfit of the resolved velocity model. Although by combining user controlled forward modeling and computer controlled inversion, the required time to develop a velocity model is reduced (Welford, 1999), applying inversion is beyond the scope of this thesis and only forward modeling component of RAYINVR program is used to develop the velocity model and interpret the crustal structure of focused area.

OBS No.	Recorded traces No.	Picked traces No. (Near offset and P_c)	Estimated uncertainty(ms)
1	1500	1040	127
2	–	–	–
3	1500	945	109
4	1500	1170	155
5	1500	1302	150
6	1376	1165	136
7	1376	1182	107
8	1376	1175	127
9	1376	1065	134
10	1376	1106	109
11	1500	1098	121
12	1500	1131	136
13	1500	1326	143
14	1500	1177	106
15	1500	1187	108

Tables 3.2 Number of traces recorded for each OBS and number of observations (from travel time picks) with corresponding average travel time uncertainties (in milliseconds).

As mentioned before, the shallow subsurface information obtained from the modeling of each OBS was used with the tomographic code tomo-2D from Korenaga *et al.* (2000; 2001) to generate an initial velocity model for the shallow part (~ top 10 km) of the profile. From the initial generated velocity model, seabed velocities and the 3, 4 and 5 $km.s^{-1}$ velocity contours were used to build a starting model for use with the RAYINVR ray tracing forward modeling and inversion

program from Zelt and Smith (1992). The details about the RAYINVR program and tomo-2D code parameters and their application in modeling procedure are explained below.

3.4.1 RAYINVR modeling

For the modeling of refraction data from line 2, the RAYINVR software package was chosen. RAYINVR is a forward modeling and inversion program of ray tracing of reflection and refraction travel times. This program is able to provide geologically reasonable models for a typical crustal refraction data set in laterally varying media (Zelt and Ellis, 1989).

3.4.1.1 RAYINVR forward modeling and velocity model parameterization

The forward modeling of the RAYINVR program is based on asymptotic ray theory in two-dimensional media (Zelt and Ellis, 1989). The velocity model in RAYINVR consists of layers. These layers are separated by boundaries which are made up of straight-line segments that cross the model from left to right without crossing another boundary. To model pinch-outs or isolated bodies, the thickness of layer may be reduced to zero. The velocity in each layer is defined by specifying a single velocity value for the top and bottom of each straight-line segment of the layer. This velocity pair may change laterally within the layer. Whenever a velocity or a boundary node is assigned along the top of a given model layer, vertical boundaries are automatically emplaced by the routine as a requirement of the model parameterization (Zelt and Smith, 1992). Vertical boundaries divide each layer into large blocks (Zelt and Ellis, 1989). In other words, each layer consists of a series of large trapezoidal blocks with vertical left and right sides and upper and lower boundaries of arbitrary dip. The velocity structure within each trapezoid is specified with a single upper and lower velocity and changes linearly from upper to lower boundary in a vertical path (Figure 3.5) (Zelt and Ellis, 1989). Undefined node values on each layer boundary are specified by linear interpolation between defined node parameters. So each trapezoid is defined by 4 nodes with

x and z coordinates and a P-wave velocity. The velocity of any point in a trapezoid is specified by linear interpolation between the upper and lower boundary in vertical path.

The P-wave velocity, v_0, at any point (x_0, z_0) in the trapezoid determined by:

$$v_0 = \frac{[(v_1 m_2 - v_2 m_1)x_0 + (v_2 - v_1)z_0 + (v_1 b_2 - v_2 b_1)]}{[(m_2 - m_1)x_0 + (b_2 - b_1)]}$$

Where x_0 and z_0 represent horizontal and vertical coordinates, v_1 and v_2 are the velocities at the top and bottom of the segments of the trapezoid respectively and m_1, b_1, m_2 and b_2 are constants related to the gradients and intercepts of the upper and lower boundaries of the trapezoid, pre-calculated for all trapezoids in the velocity model prior to ray tracing (Figure 3.5, Zelt and Ellis, 1989).

3.4.1.2 RAYINVR ray tracing algorithm

The path of the propagating ray through the two-dimensional velocity model is defined by equations:

$$\frac{\partial z}{\partial x} = \frac{1}{\tan\theta} \quad , \quad \frac{\partial \theta}{\partial x} = \frac{\left(v_z - v_x \frac{1}{\tan\theta}\right)}{v}$$

$$\frac{\partial x}{\partial z} = \tan\theta \quad , \quad \frac{\partial \theta}{\partial z} = \frac{(v_x \tan\theta - v_x)}{v}$$

With initial conditions

$$x = x_0, z = z_0, \theta = \theta_0$$

θ is the angle between the tangent to the ray and the z-axis, v is velocity, v_x is the partial derivative of v in the x direction and v_z is the partial derivative of v in the z direction [Zelt and Ellis, 1989;

Sheriff and Geldart, 1995]. Snell's law is also applied to the point of intersection of a ray with a model boundary to complete the ray tracing path (Sheriff and Geldart, 1995).

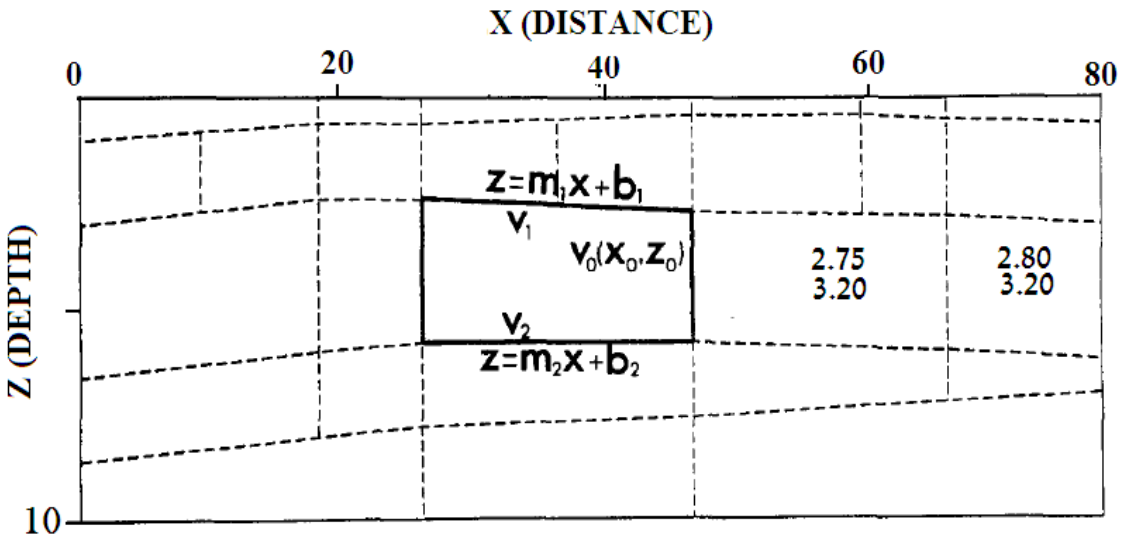

Figure 3.5 Block-model representation of the velocity model of a shallow part of profile to the depth of 10 km. The velocity distribution, $v_0(x_0, z_0)$, inside a model trapezoid is given by equation described in the text (v_1 and v_2 are the velocities at the top and bottom of the trapezoid segment, m_1, b_1, m_2 and b_2 are constants that pre-calculated for all trapezoids in the velocity model prior to ray tracing in the $x - z$ plane). The upper and lower boundary's velocities are represented in km.s^{-1} in two trapezoids. Modified from Zelt and Smith (1992).

Blocky model parameterization with velocity gradients and velocity discontinuities have the disadvantage of causing scattering and focusing of ray paths (Zelt and Ellis, 1989). RAYINVR performs a boundary smoothing simulation during ray tracing to reduce this problem. The smoothing simulation has little effect on take-off angles at the smoothed boundary, but it ensures more rays will reach the surface to provide more travel time data.

To ensure that the ray is appropriately sampled, the ray tracing algorithm in RAYINVR employs a variable step length, Δ, during ray tracing. The step length is defined as

$$\Delta = \frac{\alpha v}{|v_x| + |v_z|}$$

where α is specified by the user. If α would be considered a value between 0.025 and 0.1, total travel time errors for ray paths can be as low as ±0.002- 0.01s (Zelt and Ellis, 1989). A varying step length ensures that bending rays in velocity fields with gradients are sampled more often than straight rays traveling through trapezoids of constant velocity.

Depending on user selection, refracted, reflected and head waves may be traced through the velocity model. Also ray paths may include converted phases or multiple reflections. The user may specify rays with certain take-off angles to be traced through the model (Zelt and Ellis, 1989).

The sources may be positioned anywhere within the model but receivers are assumed to be located on top of the model. As a result the required configuration for a marine seismic refraction survey where multiple shots at the sea surface are fired into one receiver at the seabed can not be achieved. To overcome this problem, the shots are specified as receivers and OBSs are considered as shots and rays are traced in reverse.

3.4.2 Tomo-2D modeling

To generate an initial velocity model for the shallow part of the profile from the clearest first break picks the tomographic code tomo-2D (Korenaga *et al.,* 2000; 2001) was used. Tomo-2D code uses a hybrid ray tracing scheme based on the graph method and local ray bending refinement to build an accurate compressional velocity model (Korenaga *et al.,* 2000).

3.4.2.1 Tomo-2D model parameterization and forward problem

The two-dimensional velocity model in tomo-2D is parameterized as a sheared mesh hanging under the seafloor [Toomey *et al.,* 1994; Van Avendonk *et al.,* 1998] (Figure 3.6). By representing the velocity model as sheared mesh it is possible to calculate the accurate travel time in divergent topographic environment. Because of using of bilinear interpolation, the velocity field

is constant everywhere in the model (Korenaga *et al.,* 2000). To avoid any bias introduced by a coarse parameterization, the space of nodes in the vertical and horizontal directions are considered variable. A reflector in the model is represented as an array of linear segments with fixed horizontal node coordinates. The node spacing is independent of that used in the velocity grid. Each node in the reflector has only one degree of freedom in the vertical direction (Korenaga *et al.,* 2000). In seismic tomography, accurate and efficient calculation of travel times and ray paths is essential. To calculate forward travel times a hybrid method is used, followed by a graph-theoretical method for global optimization and ray-bending refinement to achieve the desired accuracy (Korenaga *et al.,* 2000). Hybrid method takes less memory and computation time and the graph method can calculate the shortest connection from an origin node to all other nodes and it is the shortest path method in the network theory [e.g. Gallo and Pallottino, 1986]. To obtain an accuracy of 1 ms in travel times and 100 m in ray path positions, a sampling rate of 10 ms and an average spacing of a few hundred meters in a velocity grid are usually considered. Seismic travel time between nodes is used as a nodal distance to generate a set of first arrival travel times and corresponding ray paths (Korenaga *et al.,* 2000). The calculation of later arrivals such as reflection phases can be formulated as a two step application of the graph method. Because the water column is outside the sheared mesh representation of the velocity model, graph solution is supplied with connections between marine sources and seafloor nodes (Korenaga *et al.,* 2000). All seafloor nodes are searched for a connection with the minimum travel time to find an entry point for a ray starting from a particular marine source (Fermat's principle) (e.g. Toomey *et al.,* 1994). Then the ray bending procedure developed by Moser *et al.* (1992) is applied to minimize the travel time along the ray paths.

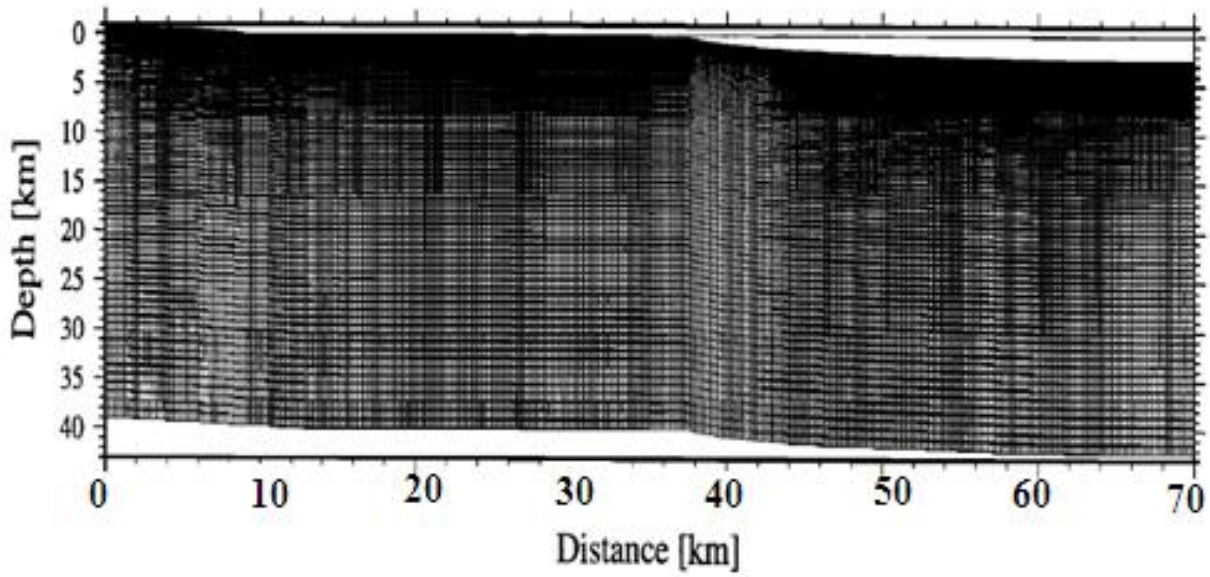

Figure 3.6 tomo-2D velocity model sheared mesh, hanging beneath seafloor. Modified from Korenaga *et al.* (2000).

3.4.2.2 Tomo-2D inverse problem

According to Korenaga *et al.* (2000) the travel time tomography velocity model is generated based on the matrix equation:

$$\boldsymbol{d} = \boldsymbol{G}\ \delta m$$

where **d** is the refraction/reflection travel time residual vector, **G** is the Fréchet derivative matrix, and δm is the unknown model disturbance vector. This matrix equation mostly depends on the velocity which is a path length distributed to the relevant velocity node and the depth which is pointed to the incident angle upon reflection, the slope of the reflector and the velocity at the reflecting point (Korenaga *et al.*, 2000).

The above inversion equation must be applied iteratively to the initial velocity model until an appropriate travel time fit is achieved.

3.5 Modeling applications

3.5.1 RAYINVR modeling of each OBS

As the first step and to obtain accurate information of sub-seasurface gathered by each OBS, the clearest first breaks from each OBS record were used to construct a near offset velocity model for each OBS using the forward modeling component of the RAYINVR Program (Zelt and Smith, 1992) (Appendix D, Figures D2b, D5b…, D41b). Figure 3.7 shows a couple of near offset modeled stations.

3.5.2 Developing initial velocity model using tomo-2D

After construction of a simple velocity model of near-offset arrival picks for each OBS, to obtain an initial 2-D model as an input for RAYINVR, seismic travel times were inverted to a two-dimensional velocity structure and a tomographic model was developed for shallow crustal structure (Figure 3.8) using tomographic code tomo-2D from Korenaga *et al.* (2000; 2001).

The model domain, obtained from the near offset travel times of 14 wide-angle data sets, is 80 km wide and 25 km deep from sea surface. But only the top 6-10 km is constrained by the near offset data used.

The horizontal grid spacing resulting from the tomo-2D model is ~200 m on average and the vertical grid spacing increases gradually from 27 m at the seafloor to ~3 km at the top of layer 5, amounting to over 481 velocity nodes for modeling the 4 layers in the shallow part of the profile. Velocities ranged from 1.5 $km.s^{-1}$ to 4 $km.s^{-1}$ for the top 4 layers of the velocity model.

To regularize the inversion, smoothness constraints were employed on both velocity and reflector node**s** and the final result is shown in Figure 3.8.

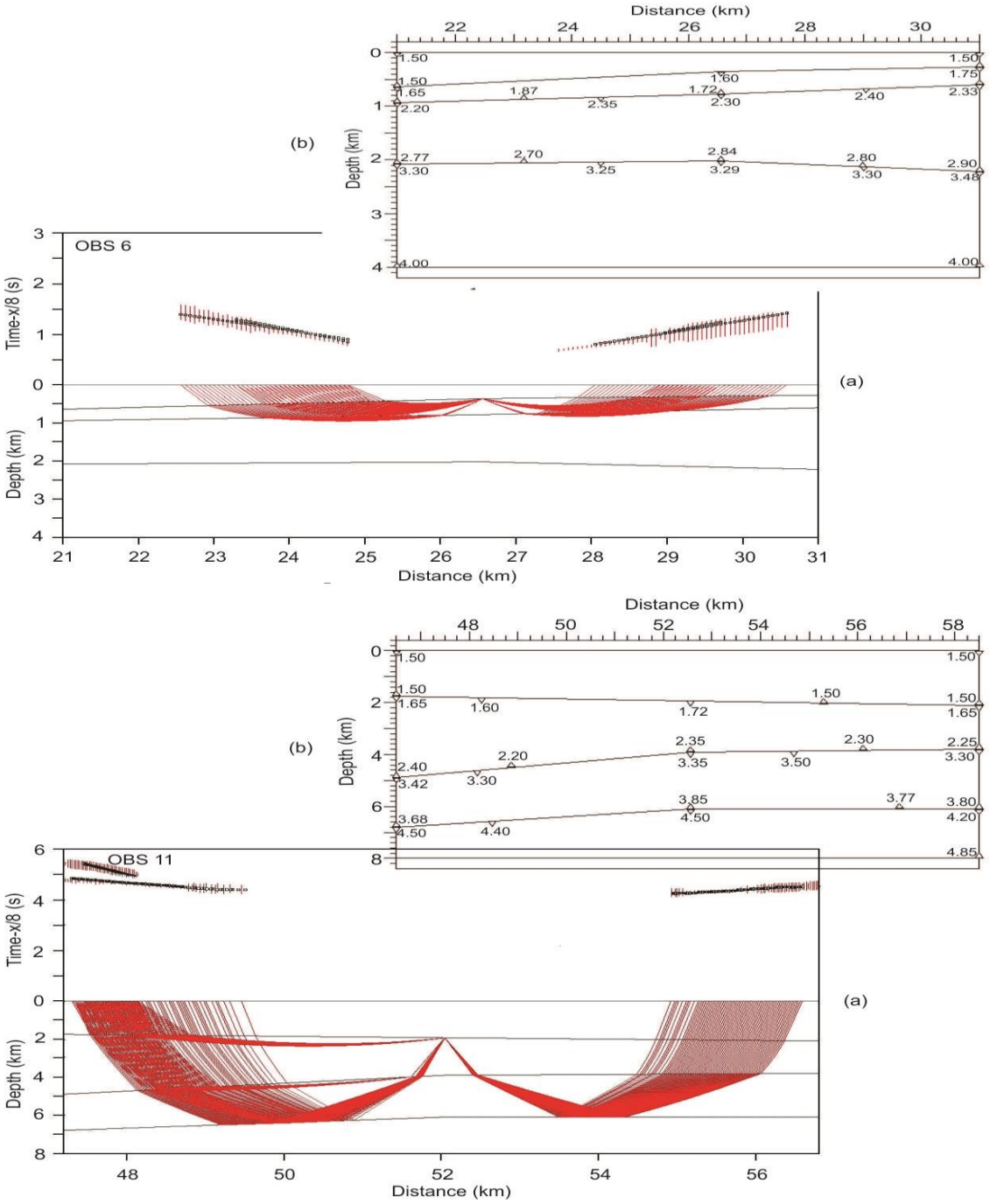

Figure 3.7 a) Plots of fit between observed and calculated travel times and corresponding ray path for OBS 6 from the shallow part of the profile and OBS11 from the deep part of the profile, OBS 6 is located at x=22.56 and OBS 11 is located at x=45.12 along the profile, observed picks are shown as vertical bars, heights of bars are proportional to pick uncertainty. The calculated travel times are shown as black squares. The data are plotted with a reducing velocity of 8 km.s^{-1}, b) RAYINVR velocity model at near offset for each station. Triangles indicate points where velocity nodes are specified.

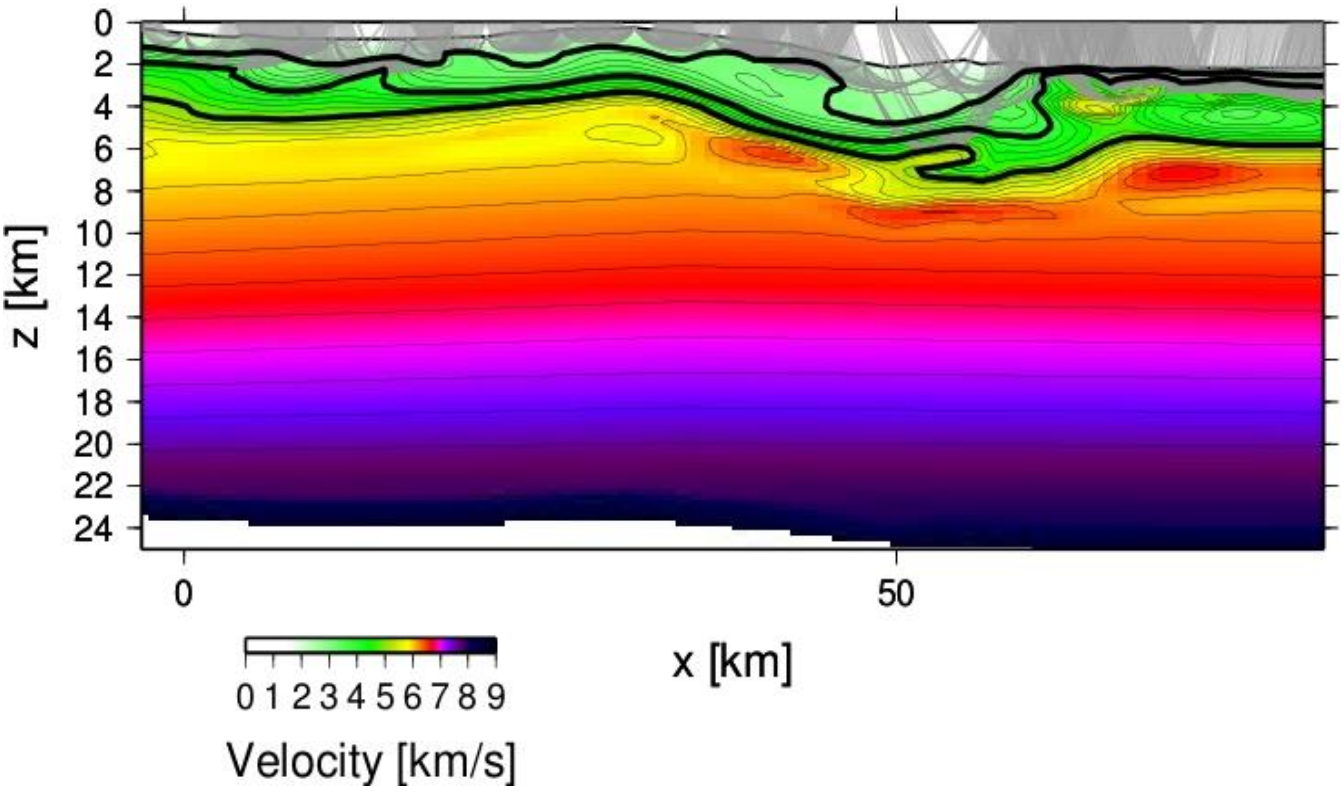

Figure 3.8 Tomographic model of shallow section of the profile, thick black lines indicate three velocity contours and grey lines show the modeled ray paths.

3.5.3 Developing final 2D velocity model using RAYINVR

Modeling of refraction data using RAYINVR requires the implementation of a number of key steps. First OBS positions are projected onto a 2D great circle arc. OBS 1 defines approximately the origin of the horizontal axis (x=0 km) and the southernmost instrument (OBS 15) was located at the range of approximately 75 km. A preliminary 2D velocity model was constructed based on the results from preliminary modeling of each station and results of the tomography model for the shallow part of the profile. The preliminary model is then developed layer by layer from top to bottom and model was characterized according to the RAYINVR required parameterization and geometry of layer horizons. This characterization involves dividing

the 2D model into layers, each layer defined by boundary nodes and assigned velocities at points along the top and bottom of each layer, based on a smoothed version of the velocity model for the tomo-2D inversion.

After parameterization of the preliminary model, the RAYINVR procedure is to attempt to adjust the geometry of the shallowest layer by adding or removing boundary and/or velocity nodes or by changing their resolved values manually, and calculating travel times for rays traced through that layer until the satisfactory fit to observed travel times is achieved. Then the first layer is kept fixed and the next deepest layer is adjusted to fit the later observed arrivals. This routine is repeated for each layer all the way down to the base of the model. Through this procedure reflected arrivals can be significantly affected by the upper crustal velocity distribution and must be well resolved before deeper velocities and layers are added to the model (Welford, 1999). The model parameterization of the final model is shown in Figure 3.9.

The results from RAYINVR depend on the picked travel times, so when the modeling has advanced and all picks from all shots put together, a pick reassessment was often required, since information from neighboring shots could reveal inaccuracies in the original picks.

3.6 Final model parameterization interpretation and detailed modeling results

The modeling of seismic refraction data is rarely unambiguous and generally requires some interpretation choices. Although the results from the final velocity structural model fit the observed data to a satisfactory degree, it is important to note that the final model does not represent a unique solution. The non-uniqueness of the model arises from its dependence on the parameterization chosen and also on the inevitable uncertainty of the travel time picks for the data being modeled.

In the RAYINVR modeling program to indicate the lateral and vertical change of the velocity gradient, it is required to divide the 2D model into layers, each layer defined by boundary nodes and assigned velocities at points along the top and bottom of each layer. Layered velocity model parameterizations with velocity gradient and velocity discontinuities have the disadvantage of having extra boundaries which may not be indicative of a geological boundary. Also the evidence for distinct layering of crust is often a matter of interpretation too. For example the scatter in the travel time and noise in the data make it difficult to distinguish a gradual increase in velocity with depth from a series of step increases indicative of distinct geological layer. Generally, a change in the slope of travel time arrivals is interpreted as a new layer with a different velocity (Figure 3.10).

In the final velocity model the uppermost layer of the model (Figure 3.9) is the water layer with a velocity of 1.5 $km.s^{-1}$. The thickness of this layer varies between 300 m in the shallow part of the profile (northern part) and 2.2 km in the deep southern part of the profile. The bottom of layer 1 was assigned 31 boundary nodes to model the bathymetry.

The second layer of the model has varying thickness between 100 m in the northern part of the profile to 1.2 km in the southern part. This layer consists of 35 velocity nodes at the top and 2 velocity nodes at the bottom and 92 boundary nodes along the bottom of the layer. Final modeling results of this layer, based on travel time fits of near-offset phases, indicate that the layer is laterally homogeneous with a range of subsurface velocities from 1.5 $km.s^{-1}$ to 3.0 $km.s^{-1}$.

Below layer 2, layer 3 comprises 27 velocity nodes at the top of the layer and 11 velocity nodes and 62 boundary nodes at the bottom of the layer. Thickness of this layer varies between 500 m and 2 km and velocities vary from 3.1 $km.s^{-1}$ to 3.9 $km.s^{-1}$.

Layer 4 of the velocity model is made of 12 velocity nodes at the top and 11 velocity nodes and 41 boundary nodes at the bottom of the layer. The thickness of this layer is between 2 to 6 km and velocities vary between 4 km.s^{-1} to 4.5 km.s^{-1}.

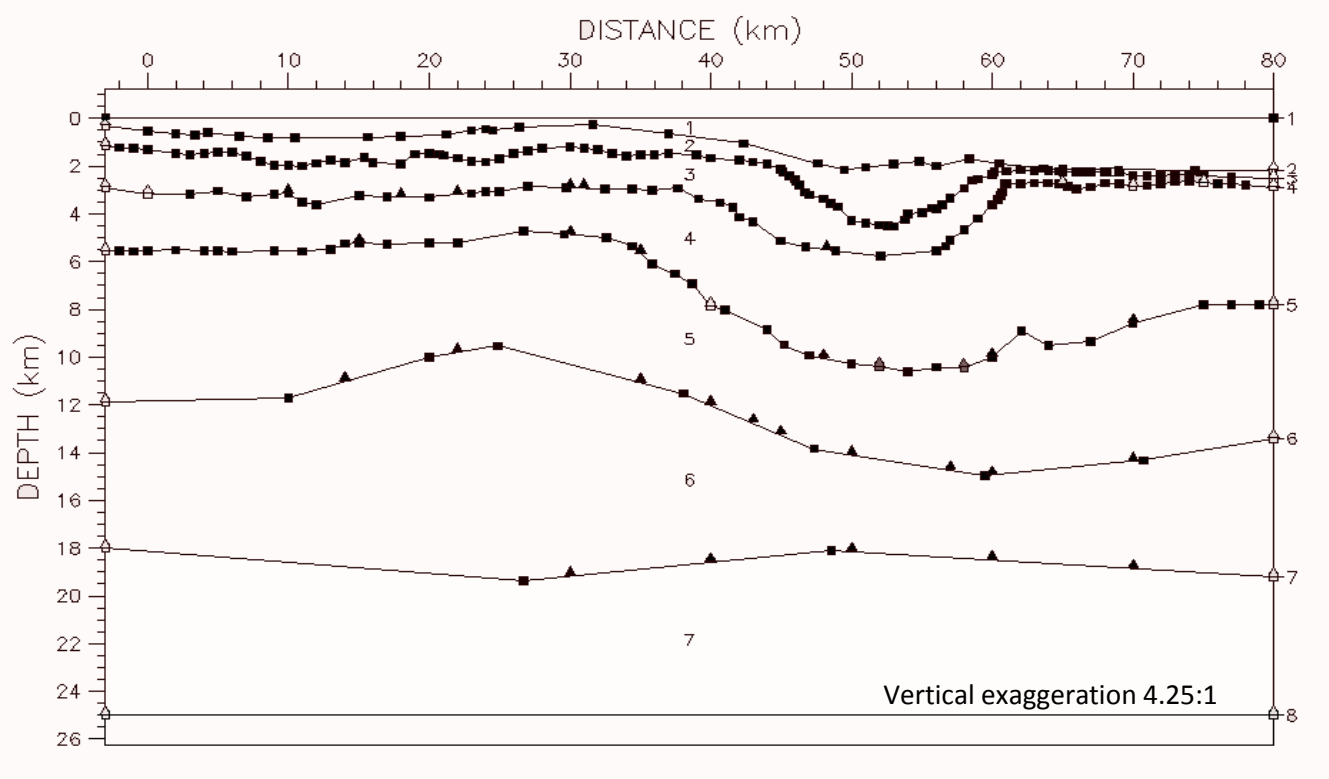

Figure 3.9 Nodal parameterization of final velocity model for line 2. Boundary nodes are designated by darkened squares and velocity nodes appear as black triangle. White triangle-squares indicates points where both boundary and velocity nodes are specified. Layers are indicated with numbers from top to the base of the model. Solid lines denote the horizontal layer boundaries which connect the boundary nodes in RAYINVR.

Layer 5 consists of 18 velocity nodes at the top and 12 velocity nodes and 9 boundary nodes at the bottom of the layer. The thickness of this layer is around 6 km and velocity varies from 4.6 km.s^{-1} to 5.1 km.s^{-1}.

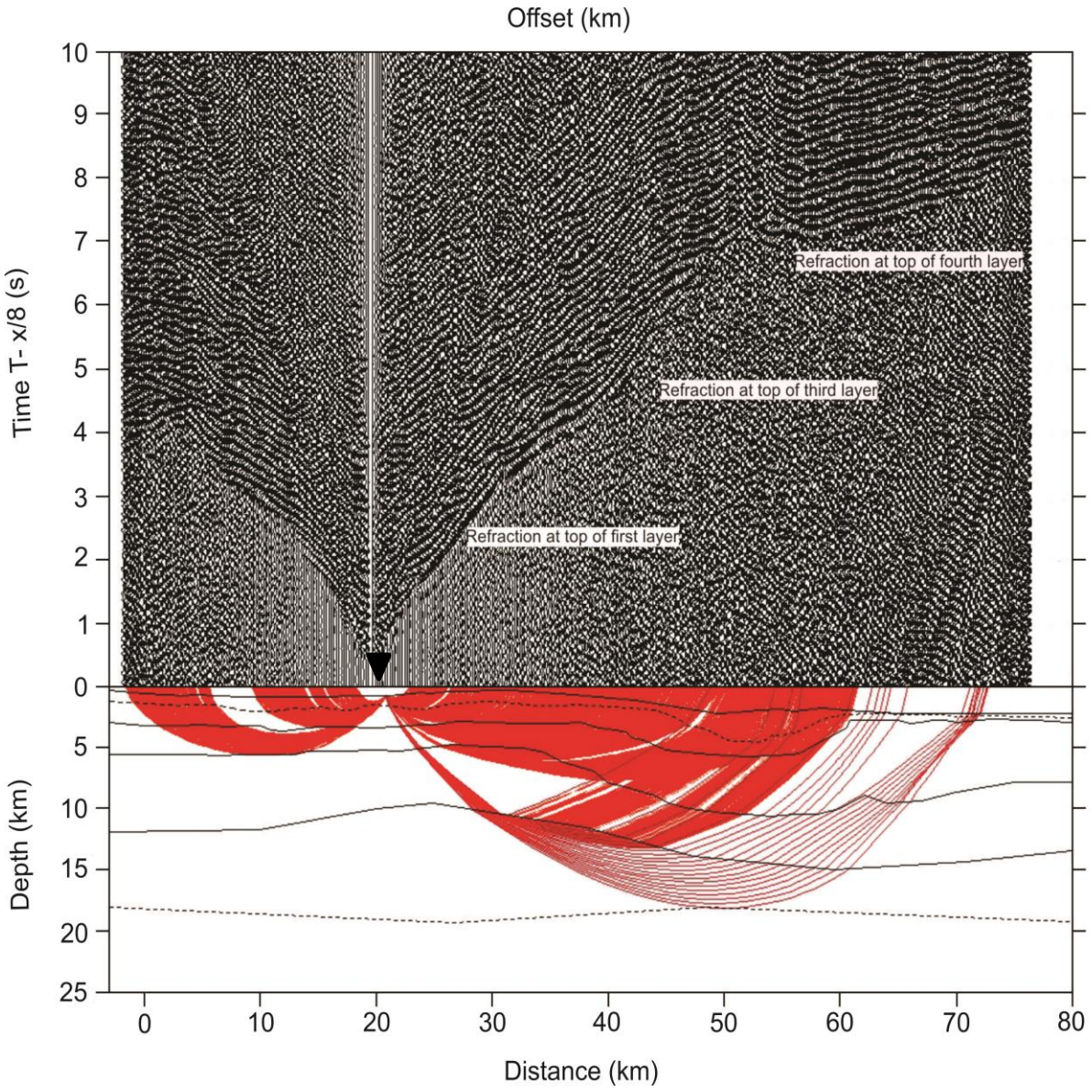

Figure 3.10 Vertical component record section for OBS 5. Interpreted arrival times (top Panel) and corresponding ray path diagram (bottom panel). The seismic data are plotted with a reducing velocity of 8 km.s^{-1}. The black triangle indicates the position of the OBS relative to the ray path diagram. Labeled phases in the diagram correspond to different layers in the model. The geologic boundaries in the model corresponding to arrivals with a certain velocity are shown by solid lines and the boundaries to show velocity gradients are indicated by dashed lines in the model.

Layer 6 comprises 4 velocity nodes at the top and 7 velocity nodes and 4 boundary nodes at the bottom. Thickness of this layer varies between 3.5 km to 9.5 km and velocity is in the range of 5.1 km.s^{-1} to 5.7 km.s^{-1}. Last layer of the model (7), which is not particularly well constrained

by data, comprises 3 velocity nodes at the top and 2 velocity nodes at the bottom of the layer. The thickness of this layer is around 7 km and velocity varies between 6 km.s^{-1} to 6.7 km.s^{-1}. Table 3.3 shows the summary of characteristics of velocity and boundary nodes for each layer.

Layer	B	V_1	V_2	z	V_{1ave}	V_{2ave}
1	31	2	2	0.3 - 2.2	1.50	1.
2	92	35	2	0.1 – 1.2	1.50	3.
3	62	27	11	0.5 – 2.0	3.10	3.
4	41	12	11	2.0 – 6.0	4.00	4.
5	9	18	12	~ 6	4.6	5.
6	4	4	7	3.5 – 9.5	5.1	5.
7	2	3	2	~ 7	6.00	7.

Table 3.3 Number of velocity and boundary nodes of each layer. B= Number of boundary nodes, V_1= Number of velocity nodes at the top of the layer, V_2= Number of velocity nodes at the bottom of the layer, z= layer depth variation range (km), V_{1ave}= Velocity average at the top of the layer(km.s^{-1}), V_{2ave}= Velocity average at to bottom of the layer (km.s^{-1}).

3.7 Model resolutions and uncertainty

The final velocity model was obtained first using the tomo-2D code to generate the primary velocity model from the clearest near offset refracted phases and then developing the model using forward modeling of RAYINVR and all picked phases (Figure 3.11). The resulting fits of the calculated to the observed travel times for all 14 OBSs are illustrated in Figure 3.12. The final velocity model is shown in Figure 3.13. To provide an estimate of the parts of the model that are best constrained the model is shown with color intensity scaled by ray density. As shown in the Figure 3.11, picked phases covered the upper to middle part of the crustal velocity structure. To calculate the resolution and uncertainty of the final model a formal error analysis is applied for each phase of the model (Welford *et al.*, 2015).

Ray tracing statistics, travel time residuals, number of observations, and normalized X^2 for individual phases and for all phases are summarized in Table 3.4. Despite lots of attempts, the lowest X^2 value achieved for line 2 for all phase arrivals, wax 2.07. This might have been due to mispicking of a phase due to the background noise or due to complexity of the region.

Phase	n	t_{rms}, ms	X^2
Near offset arrivals	6396	137	1.776
P_c	8916	136	1.535
$p_m p$	1190	181	2.618
All phases	10106	1.88	2.076

Table 3.4 Number of observations (n), RMS misfit between calculated and picked travel times (t_{rms},), and normalized (X^2) for individual and for whole phases

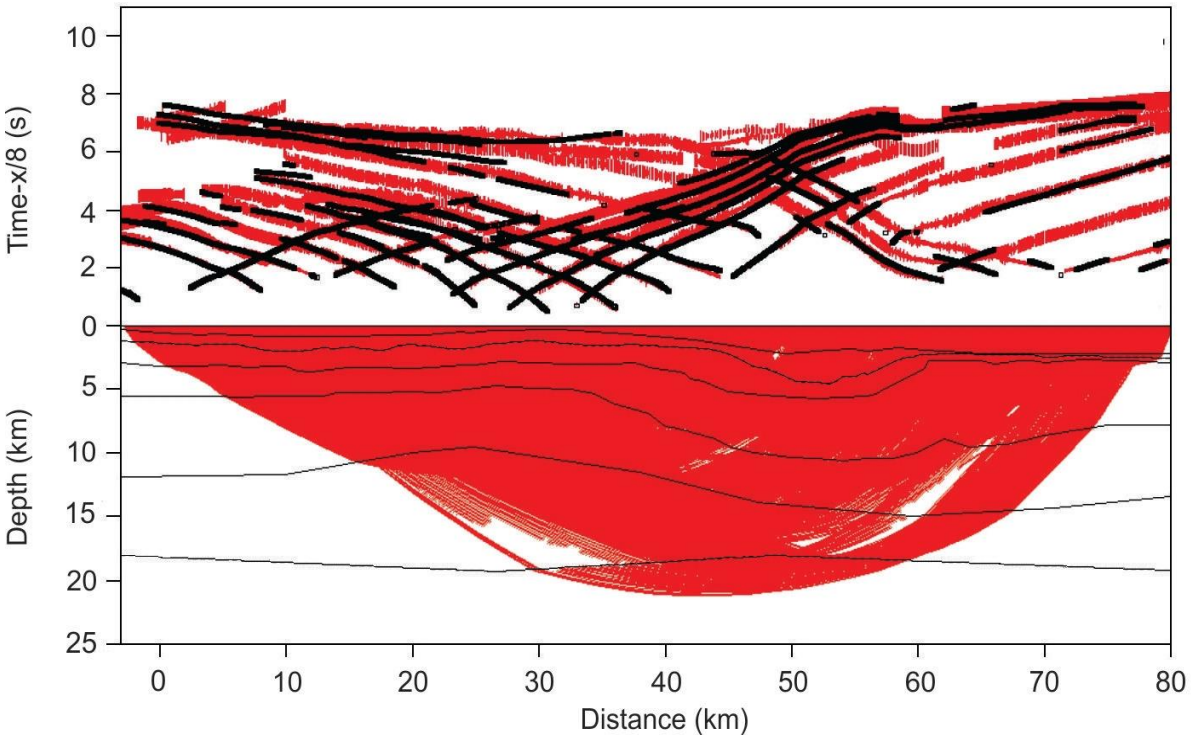

Figure 3.11 Fit between observed and calculated travel times for all OBSs with corresponding ray paths. Observed picks are indicated by red colour and vertical bars. Heights of bars are proportional to pick uncertainty. The calculated travel times are represented by black squares. The travel times are plotted with a reducing velocity of 8 km s^{-1}.

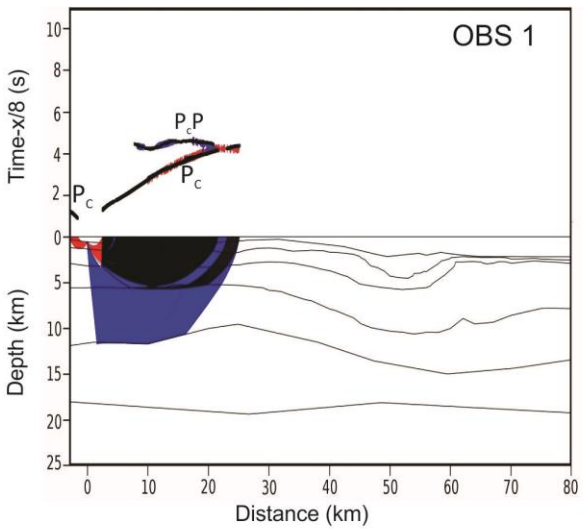
OBS 1
Time-x/8 (s)
Depth (km)
Distance (km)
P_cP
P_c
P_c

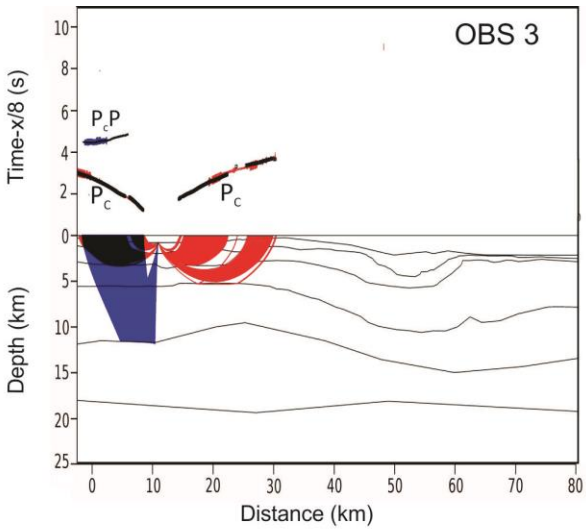
OBS 3
Time-x/8 (s)
Depth (km)
Distance (km)
P_cP
P_c
P_c

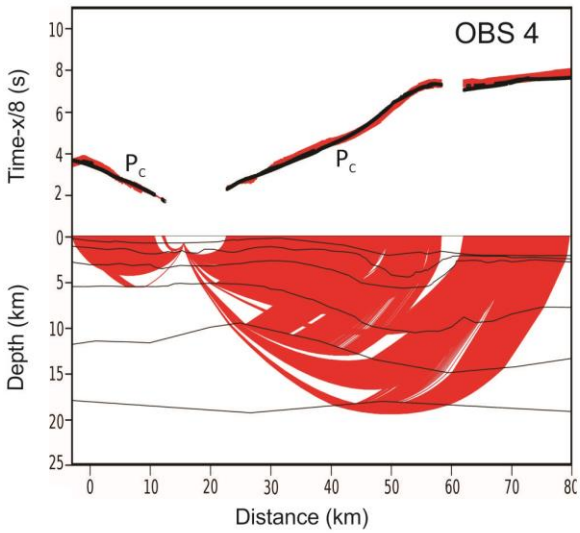
OBS 4
Time-x/8 (s)
Depth (km)
Distance (km)
P_c
P_c

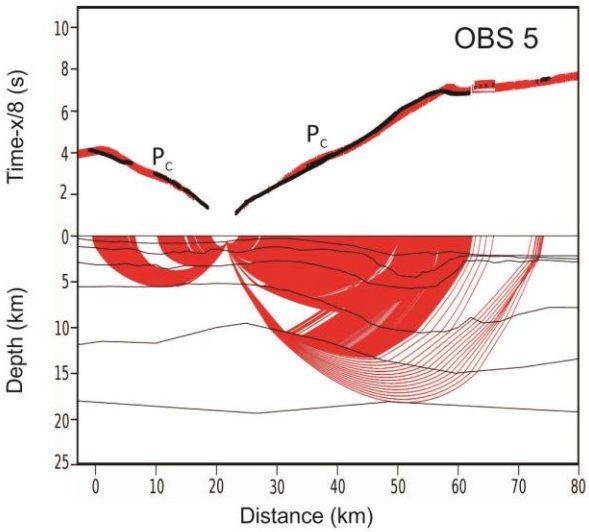
OBS 5
Time-x/8 (s)
Depth (km)
Distance (km)
P_c
P_c

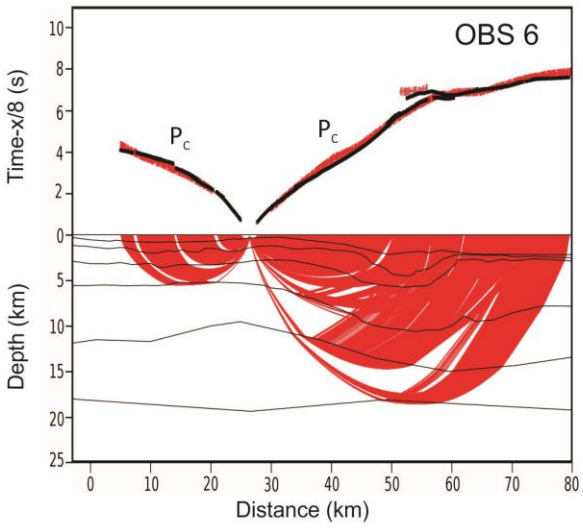
OBS 6
Time-x/8 (s)
Depth (km)
Distance (km)
P_c
P_c

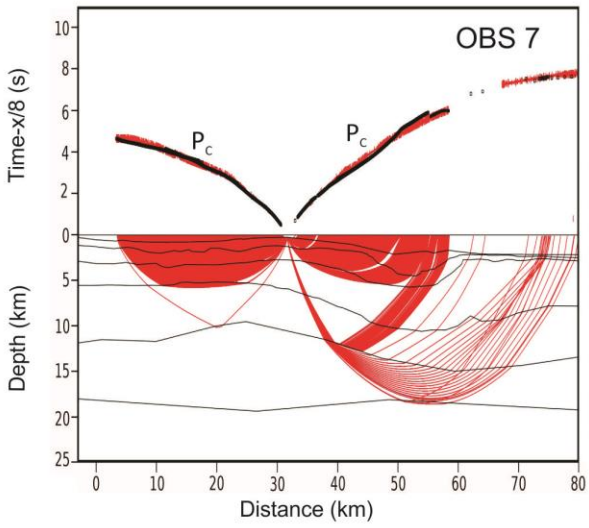
OBS 7
Time-x/8 (s)
Depth (km)
Distance (km)
P_c
P_c

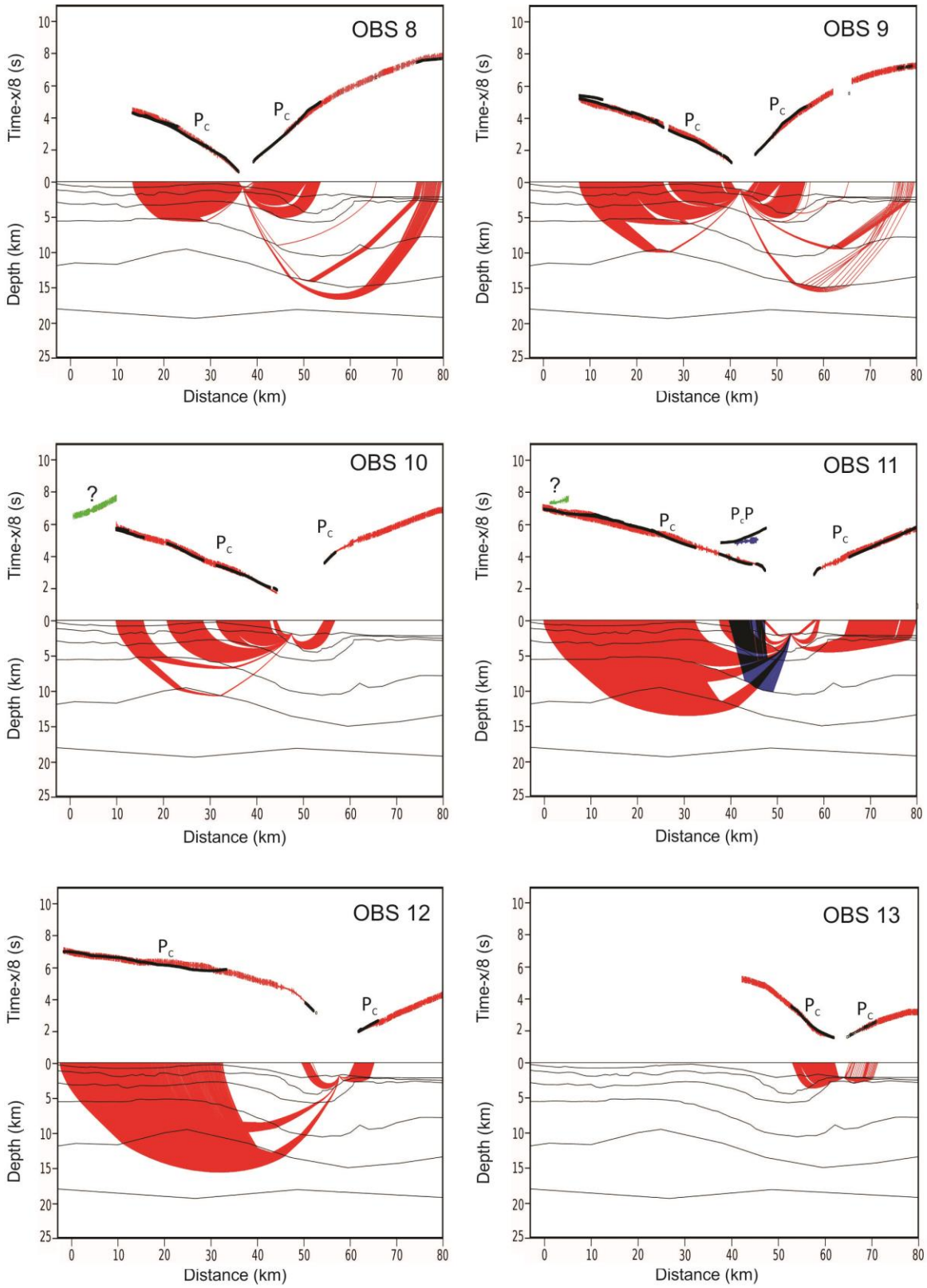
OBS 8
OBS 9
OBS 10
OBS 11
OBS 12
OBS 13
Time-x/8 (s)
Depth (km)
Distance (km)
P_c
P_cP
?

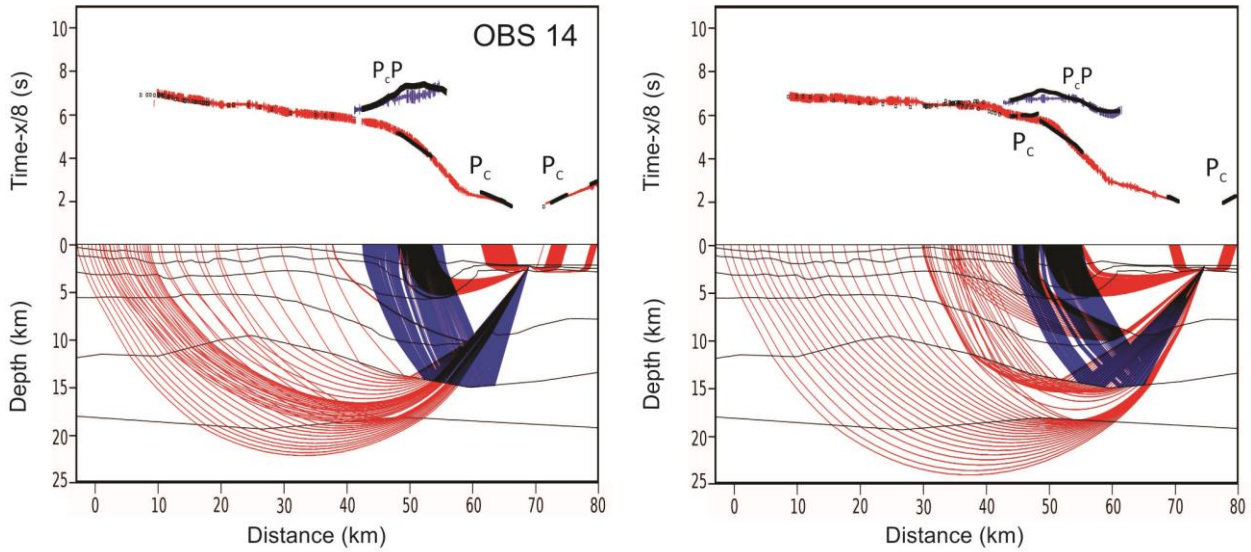

Figure 3.12 Comparison of observed and calculated travel times (top) and corresponding ray paths (bottom) for OBS 1-15 along line. Observed picks are shown as vertical bars and are colour-coded to match the corresponding rays, bar heights are proportional to pick uncertainty. The calculated travel times are shown by black dots. The travel times are plotted with a reducing velocity of 8 km.s^{-1}. *P_cP* labeled phase indicates observed reflection arrivals of some boundaries and P_c labeled phase indicates far offset refraction arrivals.

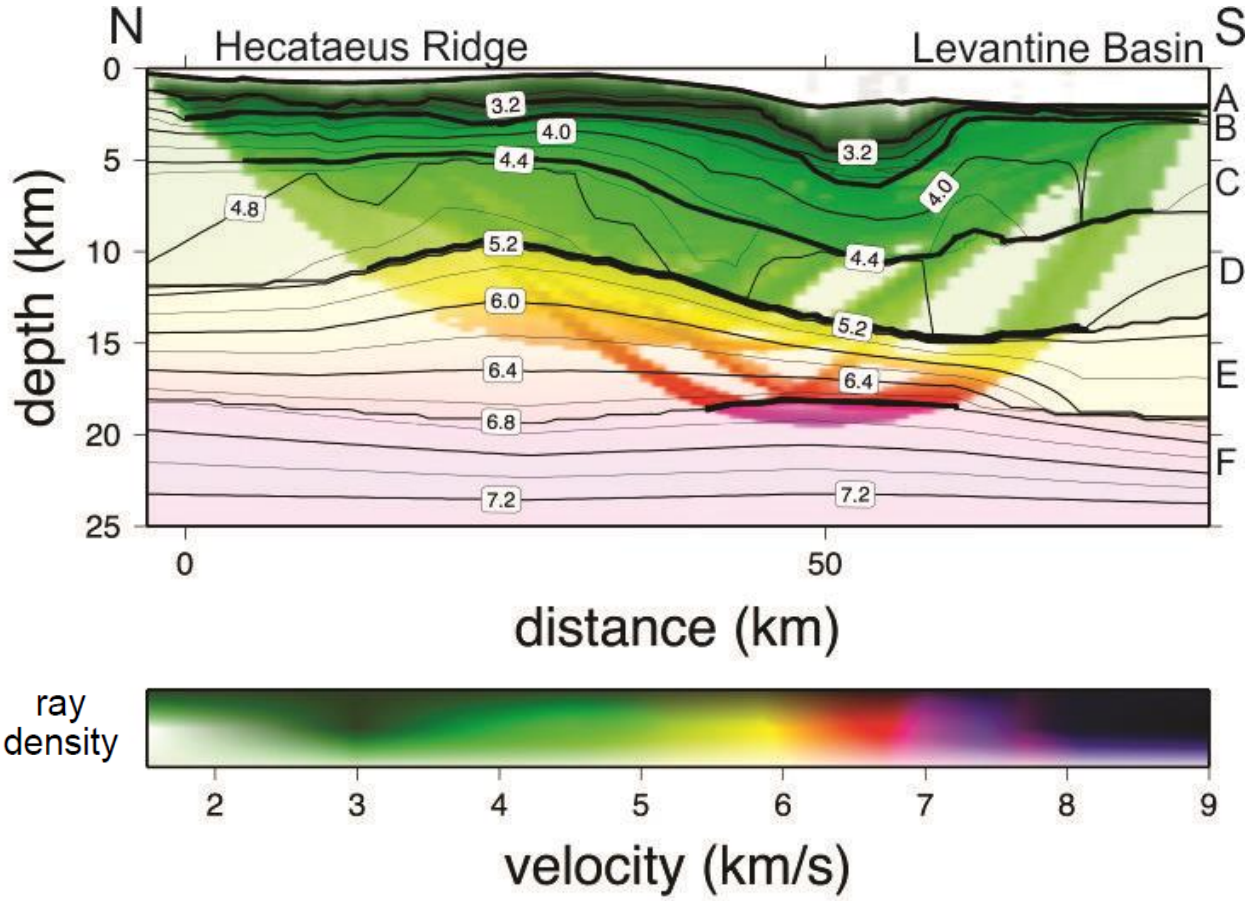

Figure 3.13 Final velocity model (no vertical exaggeration) with color intensity as a function of ray density (full color represents 80 rays or more while white area has no ray coverage). Black thin lines indicate velocity contours while thick black lines illustrate the model layers used in the parameterization.

CHAPTER 4

Discussion

4.1 Final velocity model

The final velocity model of the study area described in Chapter 3 (Figure 4.1), reveals a laterally variable velocity distribution for the profile across the Hecataeus Ridge and its southerly margin, north of the Levantine Basin.

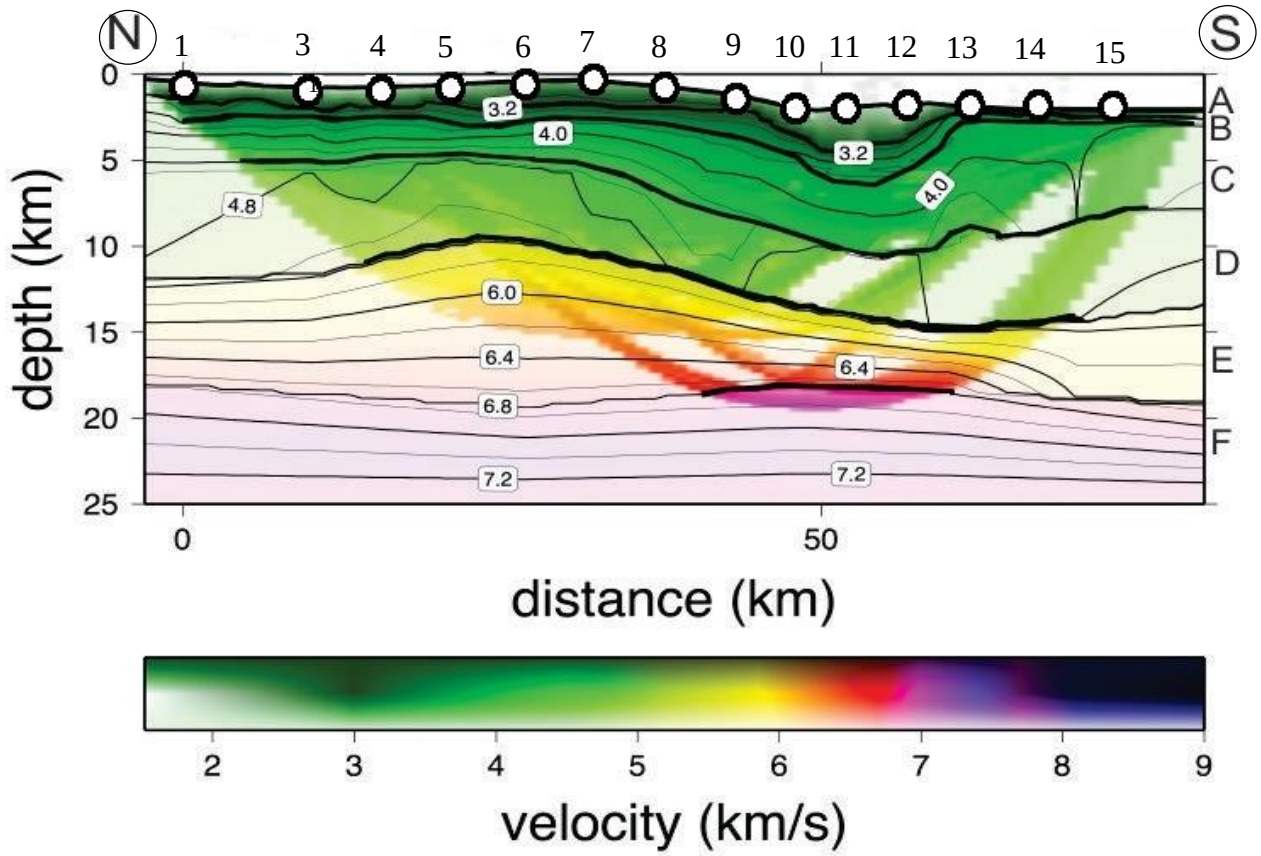

Figure 4.1 Final velocity model with colour ray coverage as a function of velocity values. Black thick lines indicate model boundaries while labeled gray lines show the velocity contours throughout the model. Numbered circles show OBS locations. Unconstrained parts of the model have been marked in white. Numbers show the velocity values along velocity contours. Contour interval of velocity is 0.2 km.s^{-1}

The P-wave seismic velocity model, including six separate layers, is determined to a depth of ~25 km. Of the 80 km line length, approximately 40 km beneath and south of the Hecataeus Ridge are well resolved to a depth of 15 - 20 km. The upper layer below the seabed has an average velocity of 2.6 $km.s^{-1}$ and is modeled with a variable thickness between 100 m to 1.2 km, significantly thinning toward the south of profile in the Levantine Basin. The second layer, has an average velocity of 3.5 $km.s^{-1}$ and thickness of 2 km, thins to 500 m toward the south of the profile. The third layer, of average velocity 4.1 $km.s^{-1}$, thickens southward from 2 km to 6 km. Beneath these layers, there is a layer roughly 6 km thick with an average velocity of 4.9 $km.s^{-1}$. This layer thickens slightly to the southern end of the profile (Figure 4.2a). The basement of the model consists of two layers; the upper layer consists of an average P-wave velocity of 5.4 $km.s^{-1}$ and variable thickness between 3.5 – 9.5 km and the lower layer has an average velocity of 6.3 $km.s^{-1}$ and a thickness of roughly 7 km (Figure 4.2b). Generally the south of the profile (between OBS 10 to OBS 12) is characterized by thicker velocity layers than the other parts of the profile. A slightly high velocity zone is modeled in Layer 6 (Layer F), in the depth of approximately 18 km below seabed, between OBS 9 and OBS 13 with velocities more than 6.5 $km.s^{-1}$.The boundaries between layers of the velocity model indicate the lateral and vertical change of the velocity. These boundaries may not represent the real geological boundaries. Figures 4.1, 4.2a and 4,2b suggest that the boundary between layers D and E (DE) and the boundary between layers E and F (EF) may be real boundaries (significant steps in velocity), but others may just be representative of a change in velocity gradient since there is only a very small change in velocity across these boundaries.

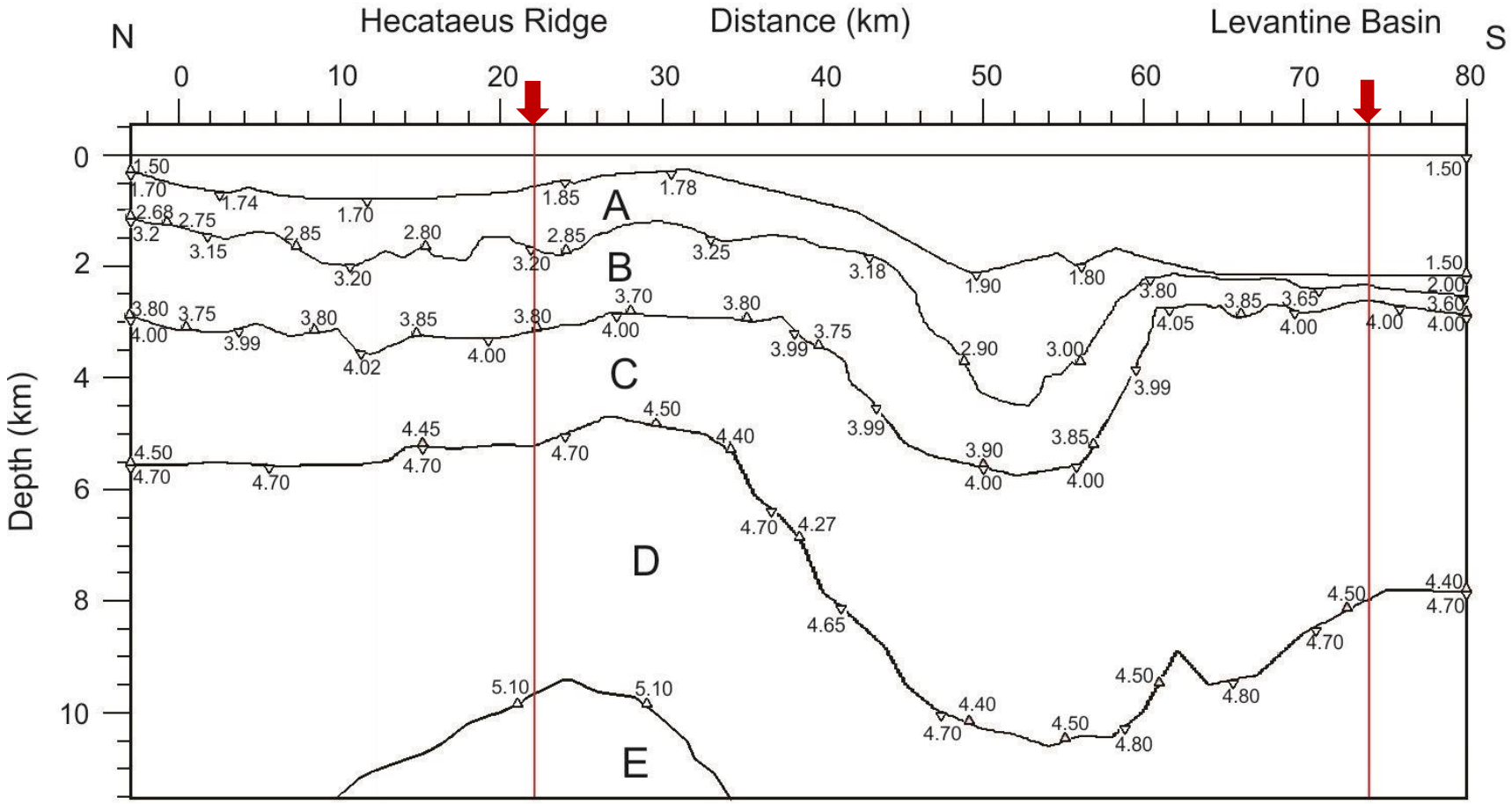

Figure 4.2a final structural velocity model of the top 11 km of the profile. Some selected velocity nodes with assigned values along each boundary are indicated with white triangles. Red arrows on the velocity model show the model distances, x, from which 1-D velocity profiles were extracted for Figure 4.6.

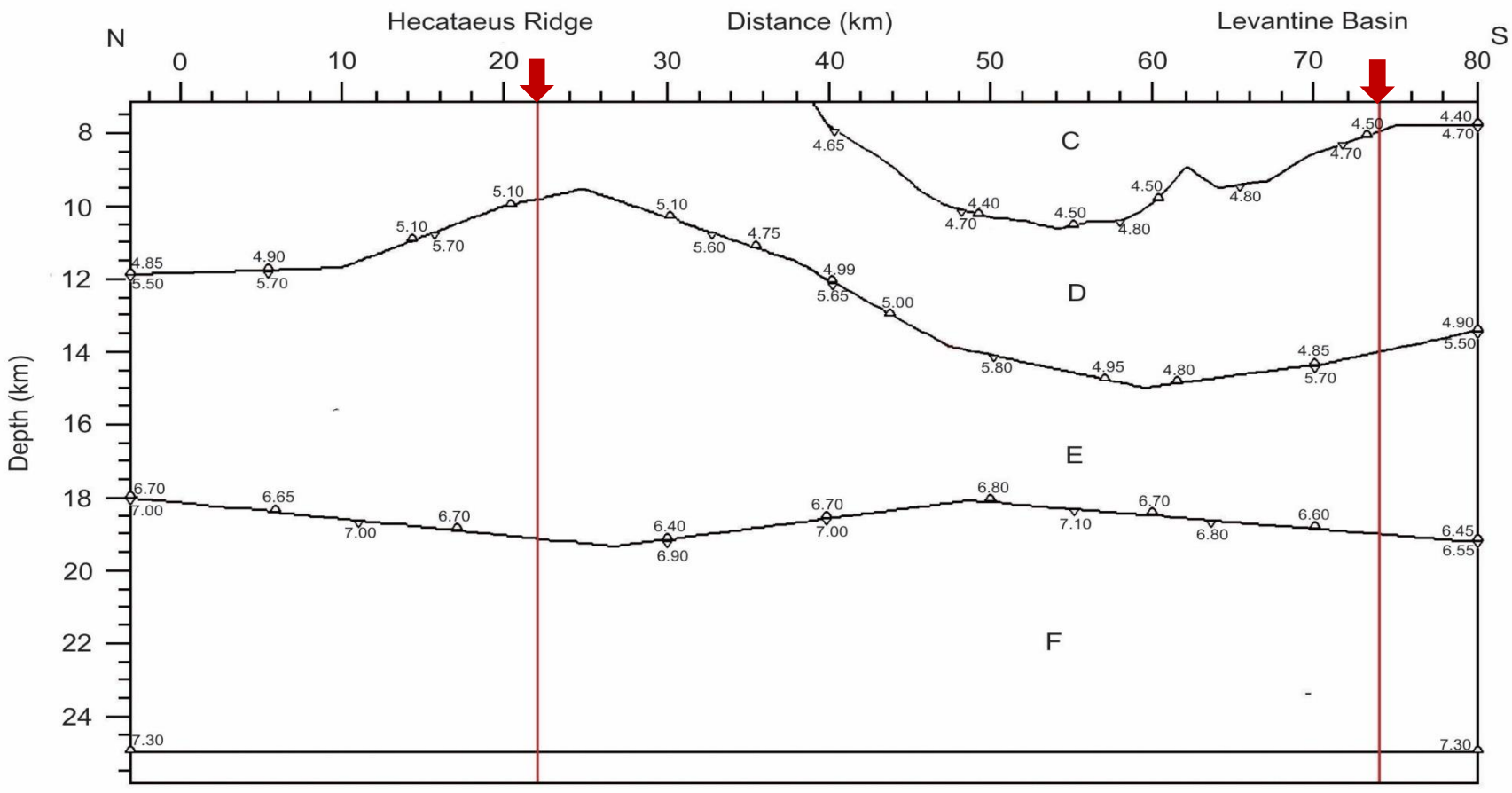

Figure 4.2b final structural velocity model of the basement of the profile. Some selected velocity nodes with assigned values along each boundary are indicated with white triangles. Red arrows on the velocity model show the model distances, x, from which 1-D velocity profiles were extracted for Figure 4.6.

4.2 Context of the local geology

Before interpreting the final velocity model, in the next sections, it is appropriate to review local geology, and to characterise the seismic velocities of the anticipated geological layers that might be expected along this seismic line. The nature of the Levantine basin, the remnant of the Neotethys Ocean in the north of the African plate and east of the Hecataeus Ridge as a continental crust or transitional oceanic crust, is a matter of debate. Netzeband *et al.* (2006a) suggested a continental lithosphere for the Levantine Basin covered by thick Mesozoic sediments on the top, whereas Ben-Avraham *et al.* (2002) earlier confirmed thick sediments above an oceanic crust.

The western Levantine basin is filled with approximately 10 km of sediments of Early Mesozoic (probably Jurassic) to Plio-Quaternary age with only a localized deformation affecting the Miocene–Oligocene rock units. These sediments onlap directly against the southern flank of the Hecataeus Ridge to the north (Klimke and Ehrhardt, 2014). The southwestern flank of the Hecataeus Ridge is characterised by inflated, autochthonous evaporites. The area between the Hecataeus Ridge and the Eratosthenes Seamount is occupied by evaporites of up 3.2 km thickness (Reiche *et al.,* 2015) and high velocity basement blocks (7.2 $km.s^{-1}$) in deep water (Welford *et al.,* 2015). These high velocity basement blocks, parallel to the margin of Hecataeus Ridge, are interpreted as a deformed Tethyan oceanic crust fragment or mafic intrusives and separated and bounded by deep low-velocity troughs (Welford *et al.,* 2015). Irregular seafloor topography and thrust faults involving Pliocene-Quaternary sediments indicate that this area is in the active accretion stage (Reiche *et al.,* 2015). The area west of the Hecataeus Ridge is characterised by significant lateral shortening and allochthonous salt. Densely stacked thrust faults indicate the presence of accreted sediments of post-Messinian age in this area (Reiche *et al.,* 2015). Cyprus is characterized by a 35 km thick continental crust which continues to the south (Makris *et al.,* 1983).

The Troodos ophiolite of Cyprus, a fragment of a fully developed oceanic crust and consisting of plutonic, intrusive and volcanic rocks and sediments, has velocities of approximately 7 $km.s^{-1}$ at depths of 5-10 km (Mackenzie *et al.,* 2006).

4.3 Detailed local velocity structure

4.3.1 Shallow velocity structure

4.3.1.1 Velocities in Pliocene-Quaternary sediments

Velocity analysis of seismic reflection data of various basins (Cilicia Basin, Antalya Basin, and Finike Basin) indicate that the velocity in the Pliocene-Quaternary (PQ) sediments starts at the seabed from ~1.5 kms^{-1} and goes as high as 3.0 kms^{-1} at the bottom of the layer (Figure 4.3). The vertical velocity gradient is around 1.7 s^{-1} in PQ sediments (Figure 4.3).

4.3.1.2 Velocities of Miocene and later sediments

Samples from DSDP Leg 42a (sites 375 and 376) drill cores and downhole logging results (Hsu *et al.,* 1978; Erickson, 1978) indicate Messinian evaporites, gypsum and marls of late-Miocene age with velocities of 4.4 $km.s^{-1}$ to 4.9 $km.s^{-1}$ below Plio-Quaternary sediments and are underlain by limestones of early-Miocene with velocities of 5.5 $km.s^{-1}$. Velocity of 3.64 $km.s^{-1}$ were measured through marlstones of Tortonian, Late-Miocene age.

4.3.1.3 Seismic stratigraphy of study area using reflection data

High quality seismic reflection data were gathered across the study area as part of the wide-angle reflection/refraction seismic profiles (WARRP) during which line 2 was obtained (Hübscher, 2012) and indicated that the Hecataeus Ridge was widely subject to erosion during the Messinian (Reiche and Hübscher, 2015).

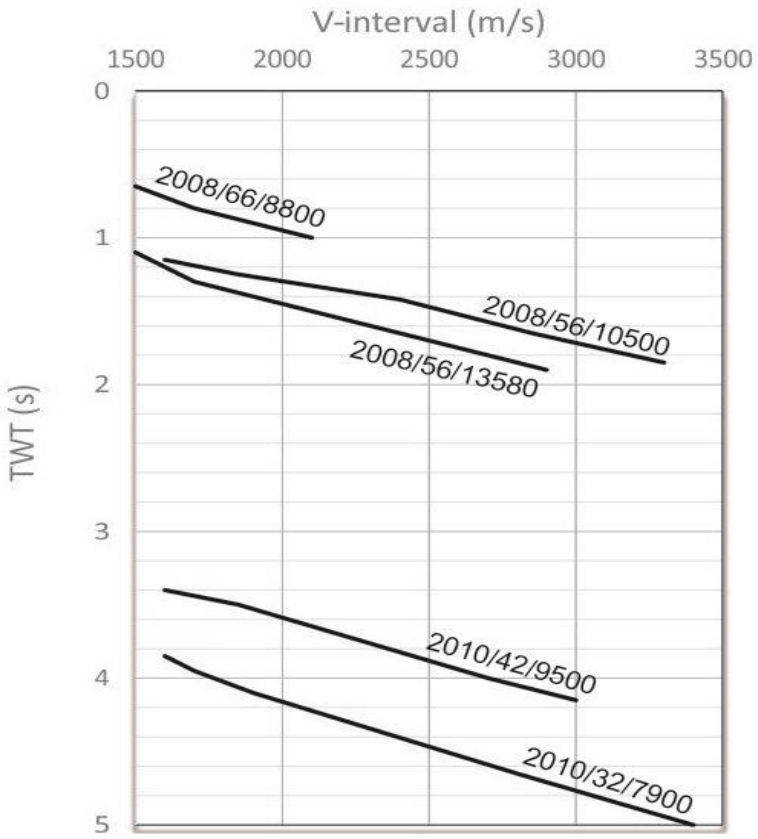

Figure 4.3 Interval velocity versus two way traveltime (TWT) of Pliocene-Quaternary sediments of Cilicia Basin, Antalya Basin, and Finike Basin in the Eastern Mediterranean (obtained using semblance analysis of seismic reflection data; J. Hall, personal communication). The velocity in PQ at the seabed is ~1.5 kms^{-1} and reaches to 3.0 ms^{-1} at the bottom of the PQ sediments. Velocity gradient in PQ is ~1.7 s^{-1}. The numbers refer to the year that the data were obtained, line number and CDP respectively.

Reiche and Hübscher (2015) through the interpretation of seismic reflection data subdivided the sedimentary succession of the Hecataeus Ridge into four stratigraphic units (Figure 4.4 shows an example of seismic section of reflection data by Reiche and Hübscher, 2015);

The uppermost unit, post-Messinian sedimentary section, is observed within the entire study area. This unit is divided into three subunits, the lower and middle subunits were correlated with the lower and middle-upper Pliocene, respectively, while the upper subunit corresponded to

the Quaternary deposits in the region (Reiche and Hübscher, 2015; Hall *et al.*, 2005b). The post-Messinian sedimentary unit (PQ) is characterized by parallel to divergent, wavy and laterally

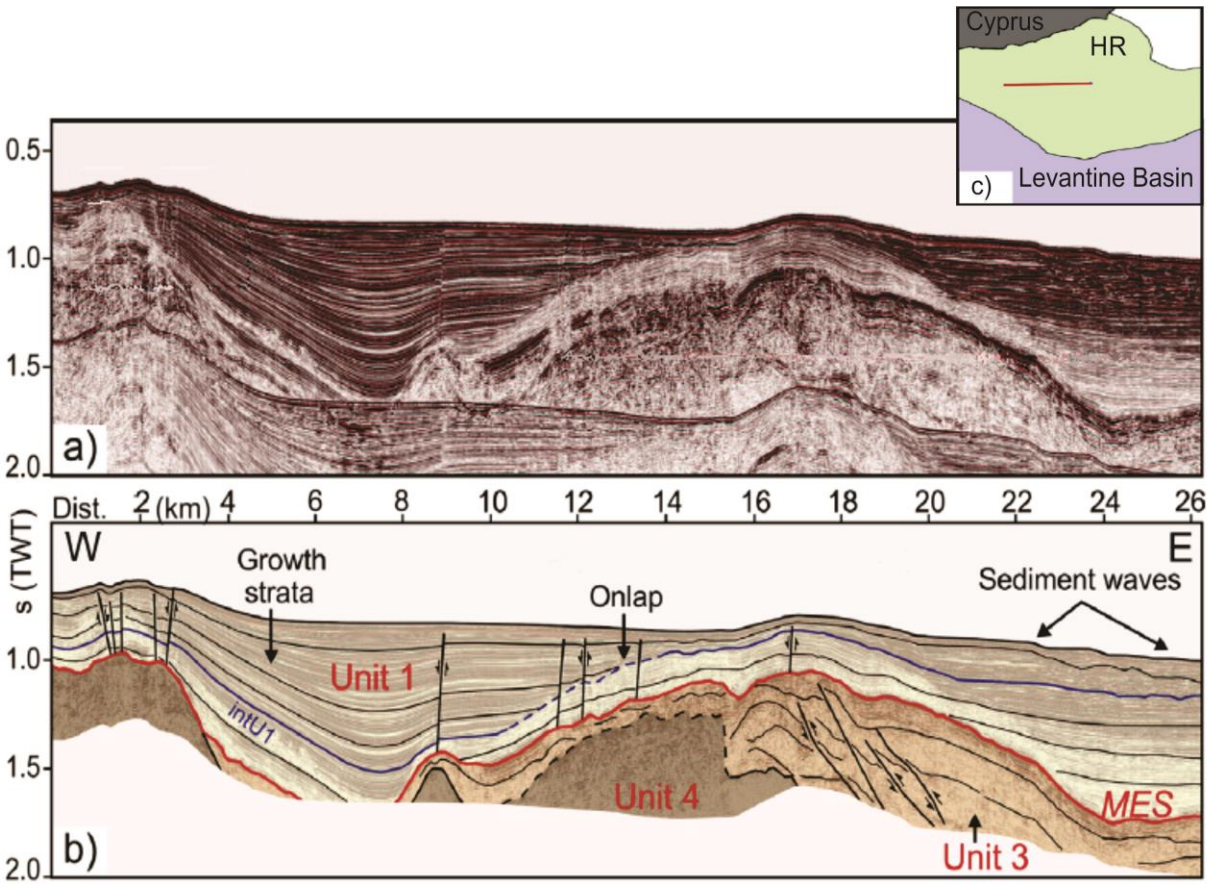

Figure 4.4 (a) Composite seismic profile over the Hecataeus Ridge conducted by Reiche and Hübscher (2015) during RV MARIA S. MERIAN (MSM) research cruises MSM 14/2 and MSM 14/3 in 2010, b) its interpreted version. The uppermost unit 1, interpreted as a post-Messinian sedimentary section, is observed within the entire study area, Unit 3 interpreted as Eocene-Miocene carbonates, Unit 4 is interpreted as the continuation of the Cretaceous Moni Melange. (For more details see Reiche and Hübscher, 2015, MES-reflection= significant high in the central part of the profile, HR=Hecataeus Ridge), c) location map of the profile. This profile crosses the northern part of the Hecataeus Ridge in E-W direction (modified after Reiche and Hübscher, 2015)

continuous reflections. The thickness of post-Messinian sediments reaches more than 1000 ms (TWT) within the northwestern part of the Hecataeus Ridge. This thickness reaches to 950 ms (TWT) further east. The thickness of post-Messinian sediments in the other parts of the Hecataeus

Ridge reach mostly less than 300 ms (TWT). Unit 2, the Messinian evaporites unit, exists within isolated sub-basins on the Hecataeus Ridge. The thickness of evaporites on onshore southern Cyprus is more limited compared to the Hecataeus Ridge (around tens of metres compared to hundreds of metres). The top Messinian unconformity occurs at approximately 1500 ms TWT and corresponds to a high amplitude reflector with significant topographic variation. Unit 3 exists across the entire study area and is characterized by low to high amplitude semi-continuous reflections. Reiche and Hübscher (2015) correlated this stratigraphic unit with Eocene-Miocene carbonates of the onshore Cyprus. The base and so the thickness of unit 3 is not clear in some parts of the Hecataeus Ridge, but it has a minimum thickness of 400-600 ms (TWT). The lowermost seismic unit, unit 4, is characterized by a chaotic and occasionally transparent reflection event. This stratigraphic unit is mostly observed in the northwest part of the Hecataeus Ridge. The base of this unit cannot clearly be identified but it has a high amplitude reflection on the top. Reiche and Hübscher (2015) interpreted this unit as the offshore continuation of the Cretaceous Moni Melange.

Hecataeus Ridge has experienced a NW directed convergence of African-Anatolian plates of Miocene phase evidenced by pre-Messinian deformation in the southern and western segment of the Hecataeus Ridge and NE-SW trending anticlinal structures in the Latakia basin (Hall *et al.*, 2005b; Reiche and Hübscher, 2015). This resulted in constructing of anticlinal structures in the north of the nplate boundary and south of Hecataeus Ridge.

Reiche and Hübscher (2015) proposed that the late Pliocene/Early Pleistocene collision between the Eratosthenes Seamount (ESM) and Cyprus caused the vertical separation between Cyprus and the Hecataeus Ridge where steepening of slopes cause the wavy sediment deposition. They further suggested that the collision of Cyprus with the ESM caused the change of direction

of plate convergence from NW to NE and the deformation of the southeastern flank of the Hecataeus Ridge.

The reflection data further indicated that the pre-Messinian compressional deformation exists more widely in the western half of the Hecataeus Ridge compared to the eastern half and Reiche and Hübscher (2015) suggested that may be because of the presence of structural heterogeneities and variation in shortening accommodation along the plate boundary. Due to continuity of pre-Messinian structures from Hecataeus Ridge to Cyprus, a Miocene structural link is suggested by Reiche and Hübscher (2015) between Cyprus and the Hecataeus Ridge.

A heterogeneous structure is observed between Hecataeus Ridge and the Levantine basin further east (Reiche and Hübscher, 2015). Figure 4.5 shows a brute stack reflection profile, crossing the central part of Hecataeus Ridge from northwest to southeast by Hübscher (2012). A thick package of parallel reflections are observable in the uppermost part, 700 to 1500 ms (TWT), of the profile. Hübscher (2012) interpreted the package as a Pliocene to recent laminated sediment deposits. The exhumation of Cyprus has caused the bottom current circulation change which is observable by wavy reflections in the sediment package of the top 100 ms (TWT). The high amplitude reflection at 1500 ms (TWT) represents the top Messinian unconformity, marked by a thrust fault in the central part of the profile (Hübscher, 2012). The Messinian unconformity is overlain by chaotic reflections. As the thrust fault is a potential pathway for vertical migration of mud, these chaotic reflections may represent mud extrusions (Hübscher, 2012).

4.4 Detailed velocity structure and interpretation of the velocity model

4.4.1 Shallow sub-seabed velocity structure

The uppermost layer of the velocity model below seabed (layer A) is modeled with variable thickness starting approximately 800 m in the northern part of the profile. This thickness continues

roughly into the southern area of Hecataeus Ridge and then thickens to ~1.2 km in the south of the Ridge before significant thinning to a few hundred metres in the last 20 km of the profile toward the north of the Levantine Basin (Figure 4.2a).

The velocity in layer A starts with 1.5 km.s^{-1} on the top of the layer and reaches to 3 km.s^{-1} at the bottom of the layer. The velocity and gradient of layer (A) corresponds well with Pliocene-Quaternary (PQ) sediments (Figure 4.3).

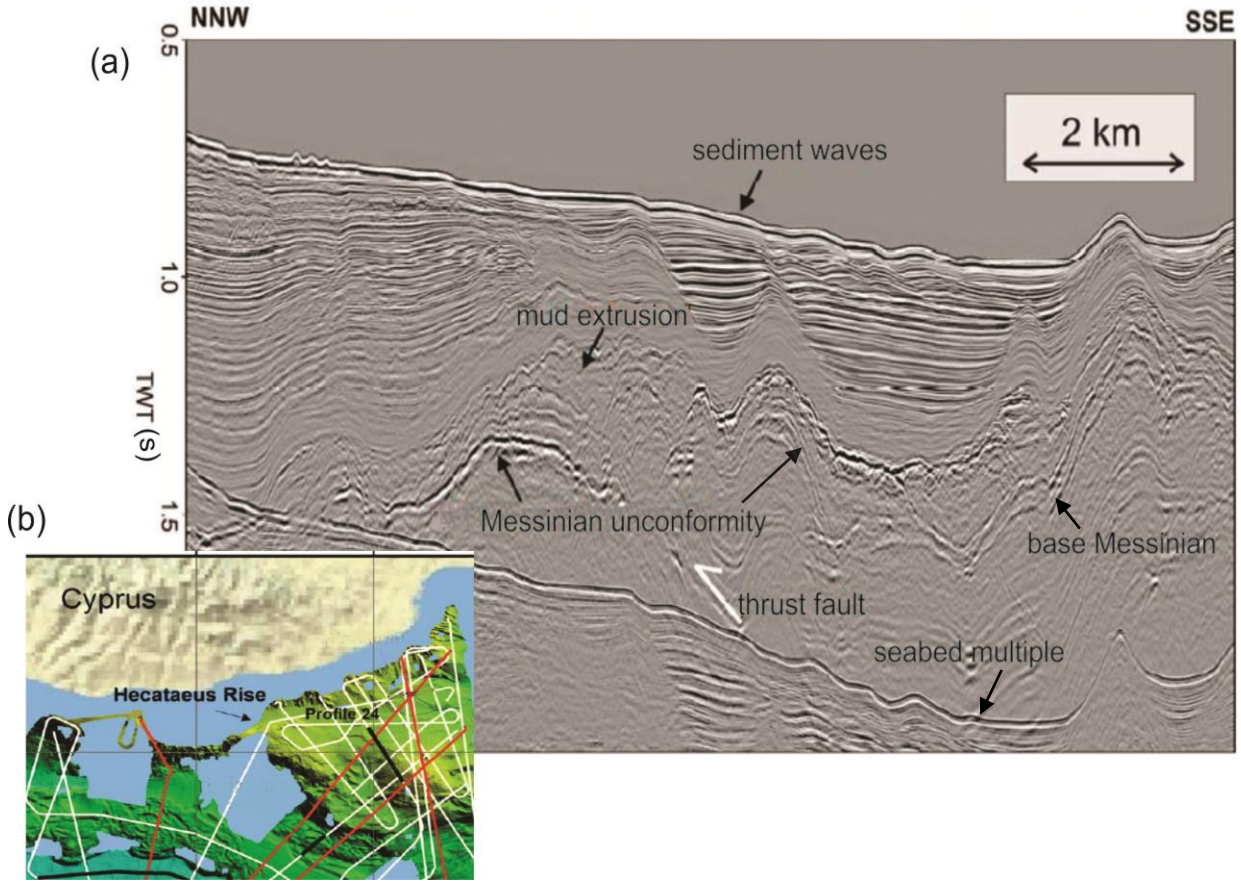

Figure 4.5 a) Brute stack of reflection data of central part of the Hecataeus Ridge. Thick package of parallel reflections in the shallow part, interpreted as a Pliocene to recent laminated sediment deposits, overlie a body of chaotic reflections interpreted as mud extrusions. The high amplitude reflection at 1500 ms (TWT) represents the top of Messinian unconformity, offset by a thrust fault b) Inset map showing the location of reflection profile (profile 24) in the central part of the Hecataeus Ridge (modified after Hübscher, 2012).

The next layer (B) is modeled with variable thickness between 500 m to 2 km and velocity of 3.1 km.s^{-1} to 3.9 km.s^{-1}. The vertical velocity gradient in layer B varies between 0.02 s^{-1} to 0.35 s^{-1}. Based on corresponding velocities of drill core and analysis of reflection data, layer B may represent deeper Pliocene-Quaternary sedimentary rocks. Note that there is no significant step in velocity across the A-B boundary

Following layer (C) is modeled with a thickness of roughly 2 km for the first 45 km in the northern section of the profile and then thickens to 6 km in the south of the Hecataeus Ridge. This layer is characterized by P-wave velocities of 4.0 km.s^{-1} to 4.5 km.s^{-1} and modest vertical velocity gradients between 0.04 s^{-1} and 0.25 s^{-1} (Figure 4.2a). Layer C has characteristics similar to the late Miocene sedimentary rocks perhaps including Messinian evaporites.

The sedimentary shallow layers are underlain by layer (D) with a constant thickness of roughly 6 km and velocities of 4.6 km.s^{-1} to 5.1 km.s^{-1}, perhaps representative of either Miocene carbonates or rather well-indurated clastic sediments or volcanics. Vertical velocity gradients within this layer are very low.

Figure 4.6 show the brute stack of reflection data along the profile collected using the air gun shots on a short streamer. The reflection boundary on top of the Messinian unconformity (M reflector) is shown in green across the profile and the top of the Messinian evaporites in the velocity model is shown in red. There is a good correspondence between these two boundaries toward the south of the profile. Meanwhile, the area between the Hecataeus Ridge and the Levantine Basin (area between OBS 6 - OBS11) associated with the Cyprus Arc, has a complex structure and is highly deformed which makes it difficult to track the M reflector in this area (Figure 4.6, dashed red/green line). It is suggested that this area is a mixture of deformed PQ sedimentary rocks and interthrust deep rocks including Messinian evaporites. It should be noted

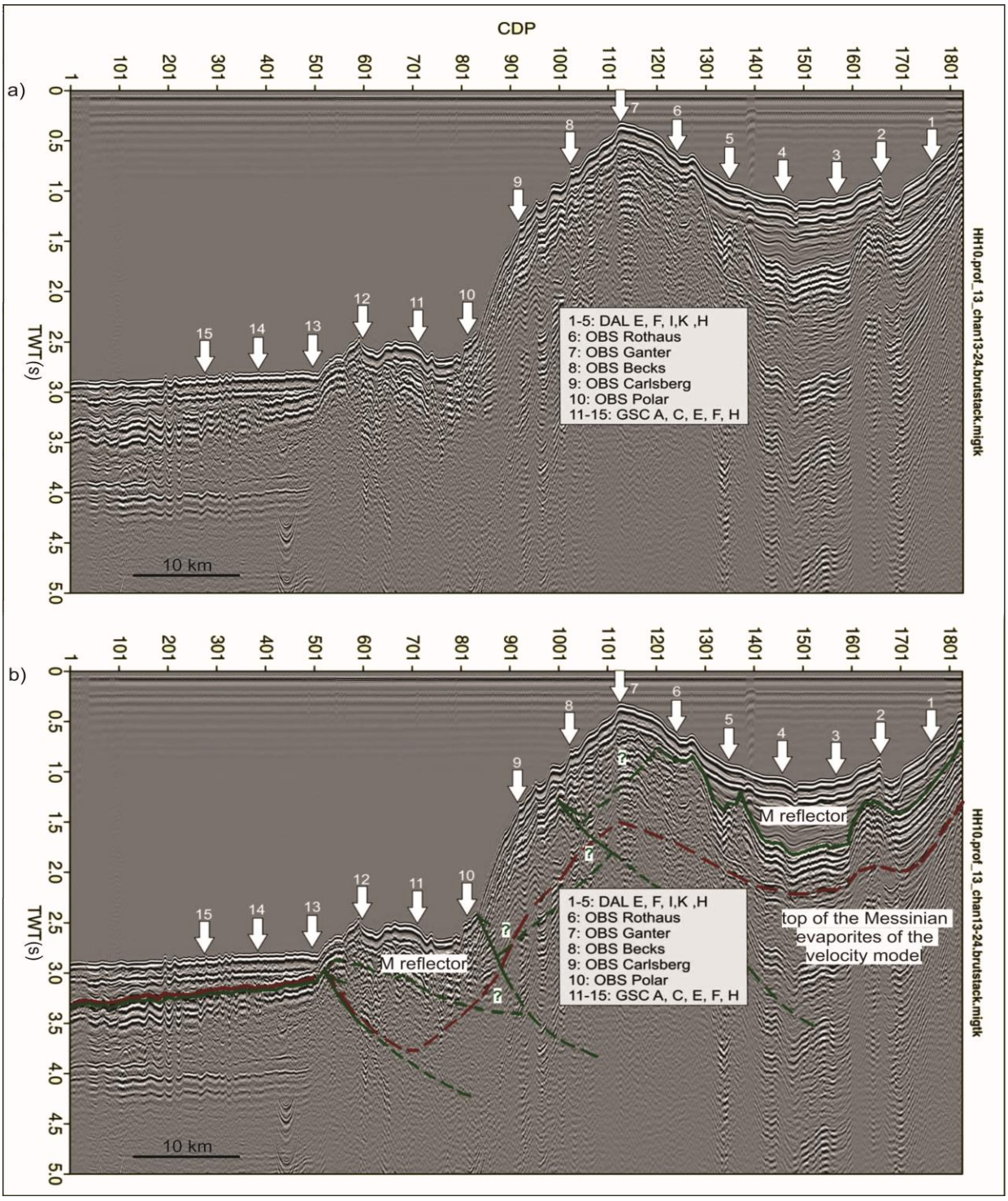

Figure 4.6 a) uninterpreted, b) interpreted brute stack of reflection data along the profile collected using the air gun shots on a short streamer. Top of the Messinian unconformity (M-reflector) is shown by green color and estimated top of the Messinian evaporites of the velocity model is shown by red color across the profile. Question marks indicate the uncertain picks. White arrows with number show the positions of OBS along line 2.

that the velocity model is an averaged and simplified version of what may be a very complex structure interleaving of Miocene and Pliocene- Quaternary rocks.

4.4.2 Basement

The layers described in the previous section overlie two basement crustal layers (E and F). Upper basement layer thickness varies between 3.5 km and 9.5 km and the P-wave velocity varies between 5.5 km.s^{-1} and 6.7 km.s^{-1}. The vertical velocity gradients vary between 0.05 s^{-1} and 0.25 s^{-1} in layer E. The lower basement layer with the constant thickness of approximately 7 km has a varying P-wave velocity over 6.7 km.s^{-1}. The vertical velocity gradients within this layer are very low (< 0.1 s^{-1}). A high velocity zone is modeled in the bottom of layer E and top of Layer F toward the south of Hecataeus Ridge, between distances of 45 km to 60 km along the line. Velocities in this region is more than 6.5 km.s^{-1}. Because of limited ray coverage in deeper part of the profile, it cannot say certainly that the high velocity region is representing either a high velocity block in the southern part of the Hecataeus Ridge, similar to the blocks modeled by Welford *et al.* (2015) in southeast of Ridge and interpreted as remnant of Tethyan oceanic crust, or rather is representing a constant high velocity layer along the whole profile.

4.4.3 Comparison of the velocity model with the continental and oceanic crust

The base of the crust was not detected clearly in the final velocity model. Thus the model only penetrates the upper parts of the crustal basement. Nevertheless it is of value to test whether or not the basement velocity information in the final model more nearly matches continental or oceanic crust.

Two vertical velocity profiles were extracted through the model (Figure 4.7); one below Hecataeus Ridge and the other below the southern margin of the model, at the northern edge of the Levantine Basin (the location of the profiles along the line are indicated by red lines in Figures

4.2a and 4.2b). The Moho and lower crust of the profile are not well constrained in the model, but upper and middle crust are compared against normal oceanic and continental crusts in Figure 4.8.

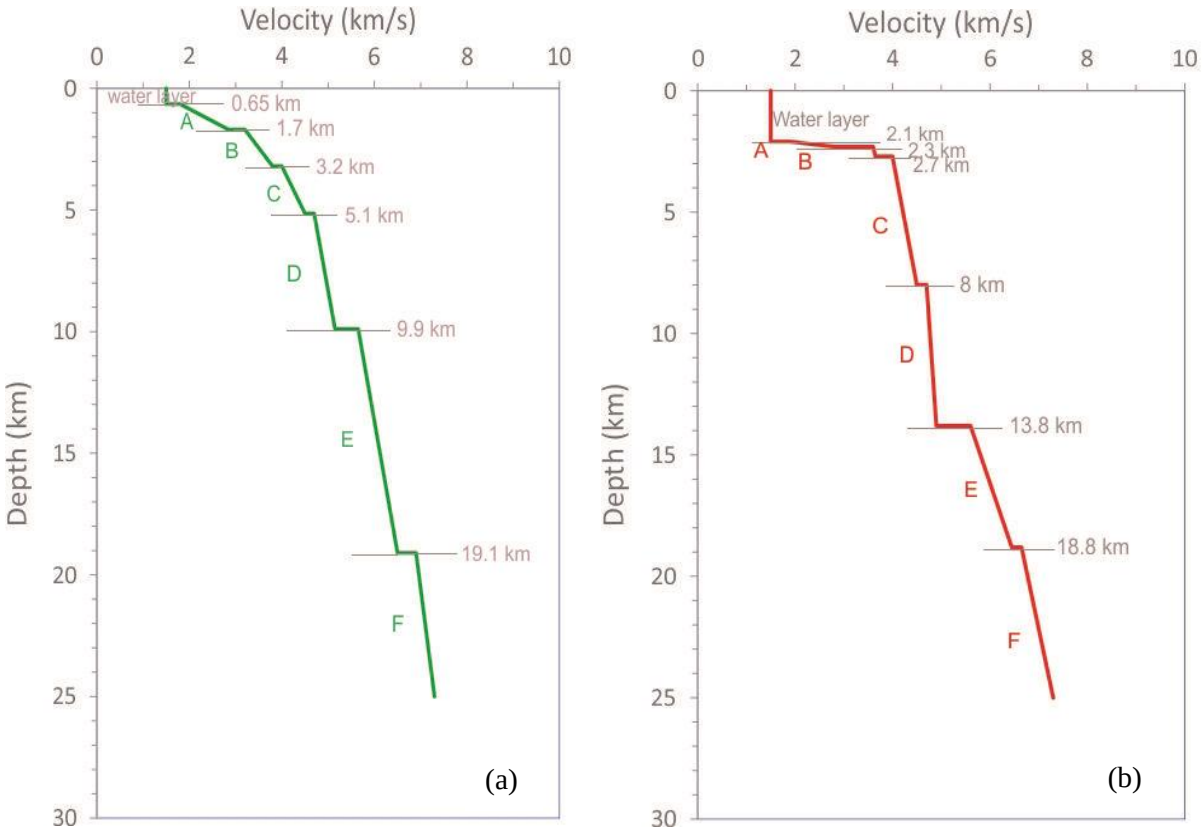

Figure 4.7 (a) Vertical velocity profile at x=22 km along the profile, below Hecataeus Ridge and (b) at x=74 km below the southern margin and the northern edge of the Levantine Basin, the location of the profiles along the line are indicated by red lines in Figures 4.2a and 4.2b.

The Hecataeus Ridge and the southern end of the profile, down to approximately 10 km is characterized by velocities less than 5 km.s^{-1} (Figure 4.2a). As mentioned the velocity of the uppermost layers below seabed (A and B) with velocities between 1.5 km.s^{-1} and 3.9 km.s^{-1} is consistent with the observed velocities in the Pliocene-Quaternary sediments (section 4.3.1). The velocities of the next layer (C) vary in the range of 3.9 km.s^{-1} to 4.5 km.s^{-1} and correspond to the Late Miocene sediments, including the Messinian evaporites (DSDP, Leg 42a, sites 375 and 376).

Next layer (layer D) with the constant thickness of roughly 6 km and velocity of 4.6-5.1 km.s^{-1} is difficult to interpret. The velocity could indicate either well indurated clastic sediments, carbonates or volcanics.

The boundary below layer D and top of Layer E, with a big velocity jump ~ 0.5- 0.6 km.s^{-1}, is interpreted as the base of the sedimentary section and top of the basement. The velocities of layer E and F approach the velocity profile for continental crust (Figure4.8) once adjusted for the thickness of overlying sediment and most likely represent upper and lower crystalline continental basement respectively.

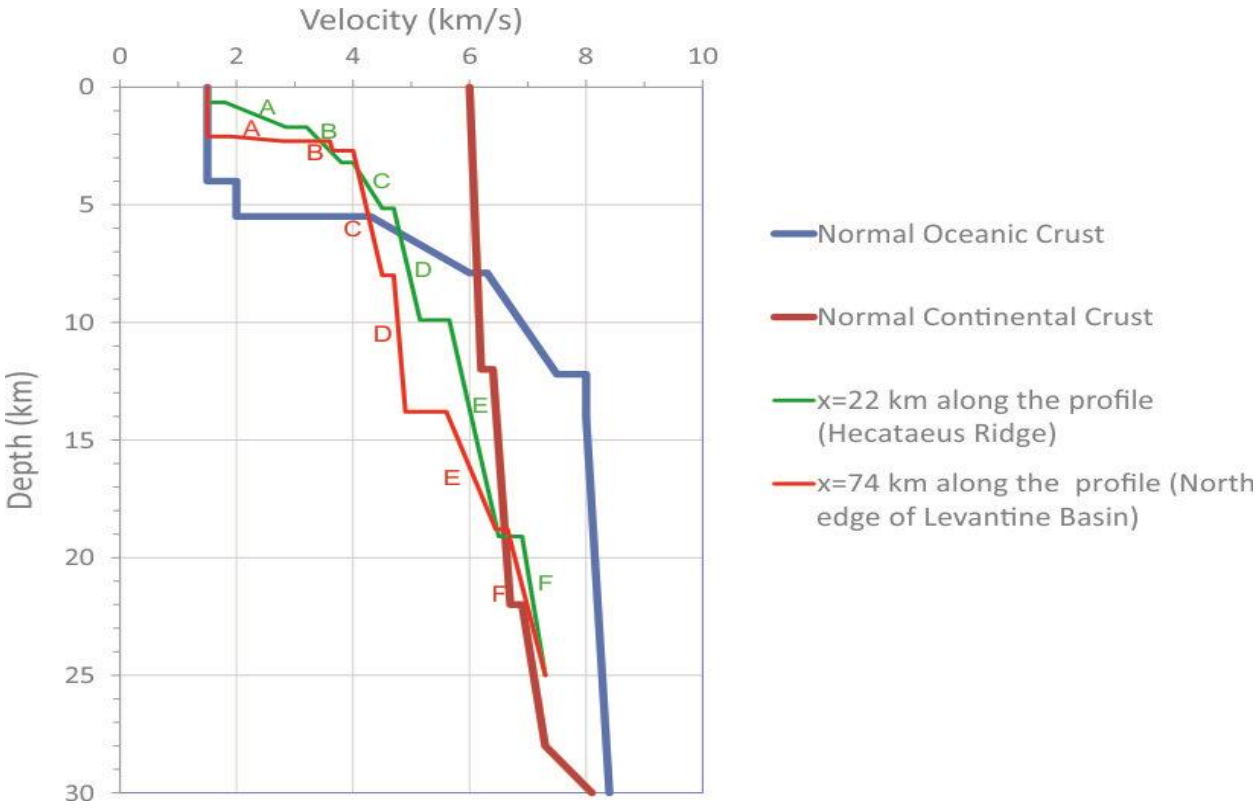

Figure 4.8 1D vertical velocity profiles from particular points along the refraction profile; one below the Hecataeus Ridge (denoted by green) and one below the southern margin of model, at the northern edge of the Levantine Basin (denoted by red). The velocity profiles are compared with the velocity profiles for continental crust (Holbrook *et al.*, 1992) shown in brown, and normal oceanic crust (White *et al.*, 1992) shown in blue. The reference normal oceanic crust is generated away from the influence of fracture zones which are typically anomalously thin (White *et al.*, 1984). The main velocity jumps occur at the interface between sediments and igneous basement and the interface between base of the crust and the mantle.

In addition, the P-wave velocity in the upper oceanic crust has a large velocity gradient of 2.0 s^{-1} -3.3 s^{-1} (White at al., 1992) and the total thickness of the oceanic crust is around 6.2- 7.4 km (Figure 4.5) followed by a crust-mantle transition layer with a large velocity gradient (Oikawa *et al.*, 2010). The vertical velocity gradients for basement layers of the velocity model vary between 0.05 s^{-1} and 0.25 s^{-1} which would be remarkably low for oceanic crust. This further suggests that layer E and F represent continental basement.

4.4.4 Are there ophiolites in the shallow crust of the Hecataeus Ridge?

Mackenzie *et al.* (2006), through velocity and density modelling of the seismic and gravity data sets, presented velocities of around 7 km/s at depths of 5-10 km for ophiolites across the Troodos ophiolite in Cyprus (Figure 4.9). Based on the results of this study there is no clear evidence of similar velocities of ophiolites in the shallow crust below Hecataeus Ridge. If there are any ophiolites present below the profile they are buried deep in the crust (lower crust) or in the adjacent high velocity blocks (Welford *et al*., 2015).

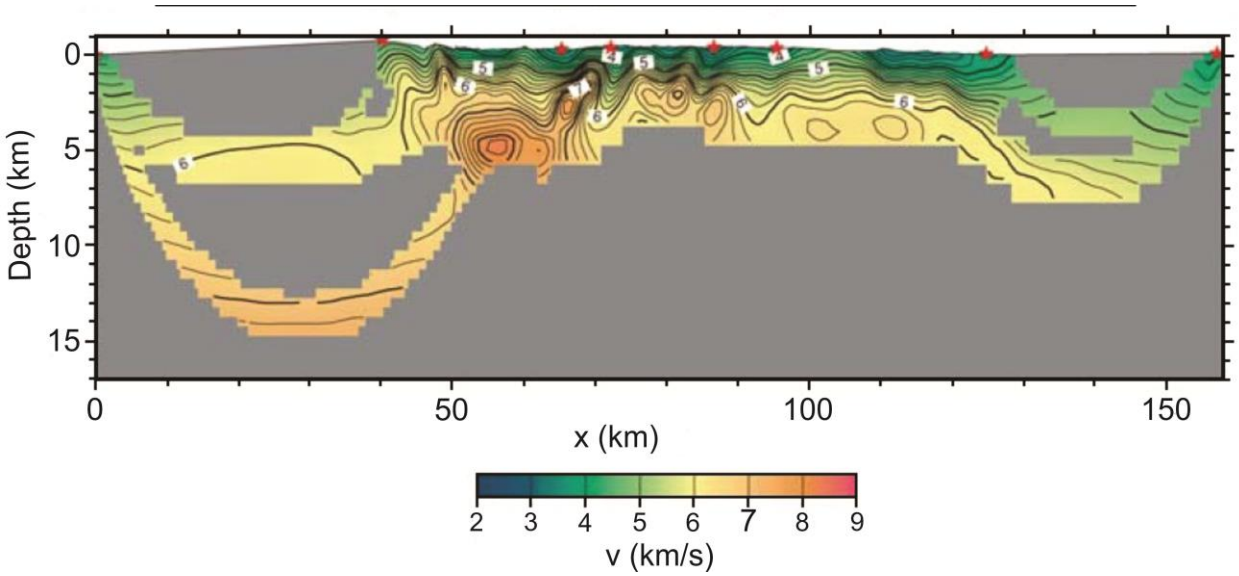

Figure 4.9 2-D tomographic velocity model of the Troodos ophilolite by Mackenzie *et al.* (2006) Areas with no ray coverage have been masked with grey color. Velocity contours are shown every 0.2 km s^{-1}. Modified after Makenzie *et al*. (2006).

4.5 Gravity and magnetic data

While the P-wave velocities of the final velocity structural model reveal some information about the rock types of the field area, using other geophysical information such as gravity and magnetic data can improve the interpretation by providing extra constraints on other physical parameters of the crust. Regional scale gravity anomalies are largely associated with the nature of the crust, whereas magnetic anomalies are associated with local magnetic features (Rybakov *et al.,* 1997). In this respect, free-air gravity and magnetic anomaly data were used to reveal the additional crustal and structural features of the survey area.

4.5.1 Gravity model

Free air gravity data for gravity modeling over the survey area were obtained from Satellite Altimetry data maintained by the Scripps Institution of Oceanography, University of California San Diego (Sandwell *et al.,* 2014; Sandwell and Smith, 1997). This gravity data is extracted from global 1-minute (~ 1.8 km) grids in ASCII XYZ format. Each gravity observation made by satellite has a location (X, Y) and a gravity value (Z). The XYZ data is gridded using a GMT algorithm (Wessel and Smith, 2015). The process of gridding takes XYZ data and interpolates the value of Z at the nodes of a grid. The resolution of the grid data is dependent on both the spacing between grid

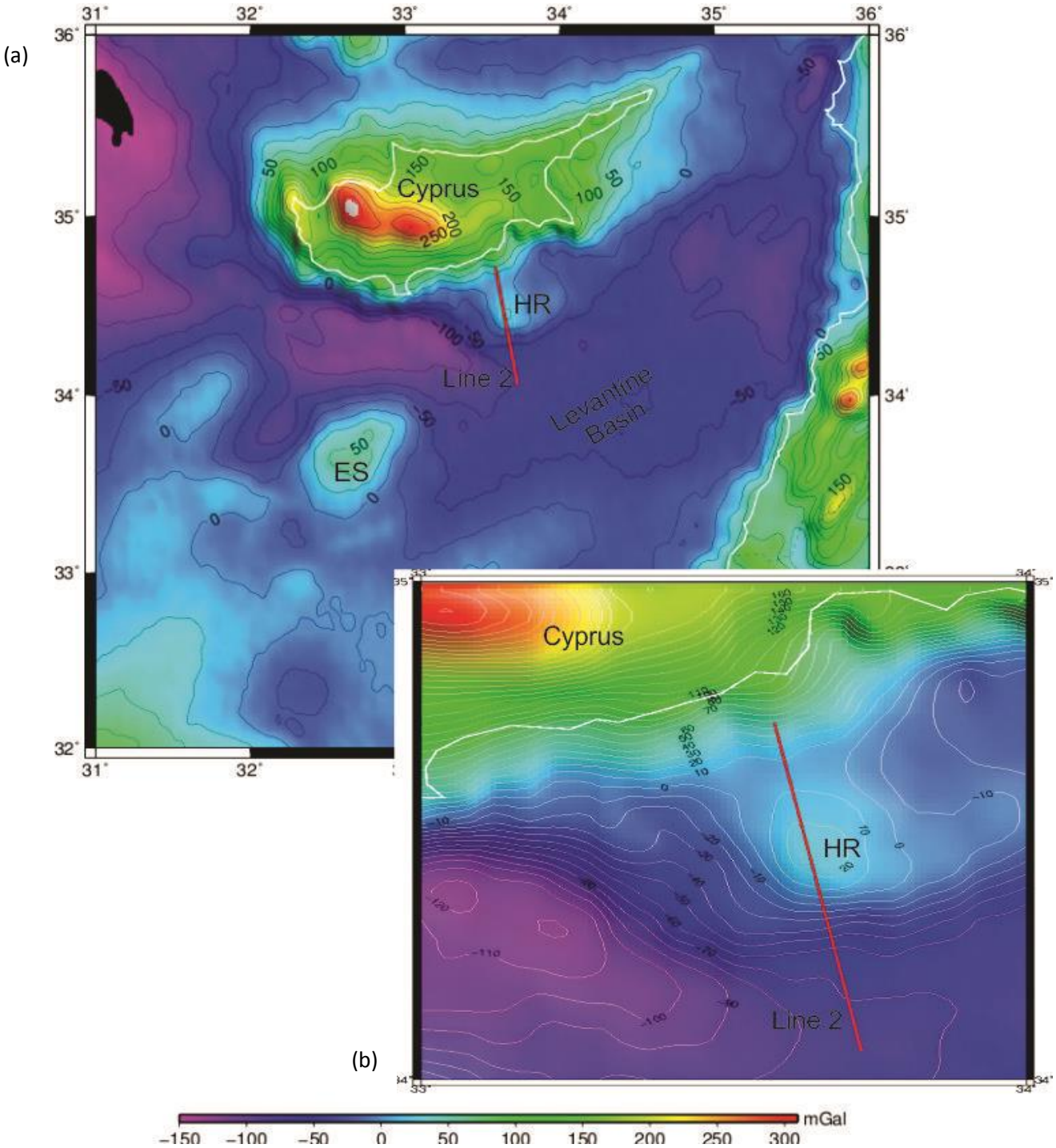

Figure 4.10 2D gravity map over Hecataeus Rise (HR), Eratosthenes Seamount (ES), Cyprus and the Levantine Basin. White lines show the coastlines and political boundaries. The contour interval is 50 mGal in Figure 4.10(a) and 10 mGal in Figure 4.10(b). The free air gravity data were achieved from the Satellite Altimetry maintained by the Scripps Institution of Oceanography, University of California San Diego (Sandwell *et al.*, 2014).

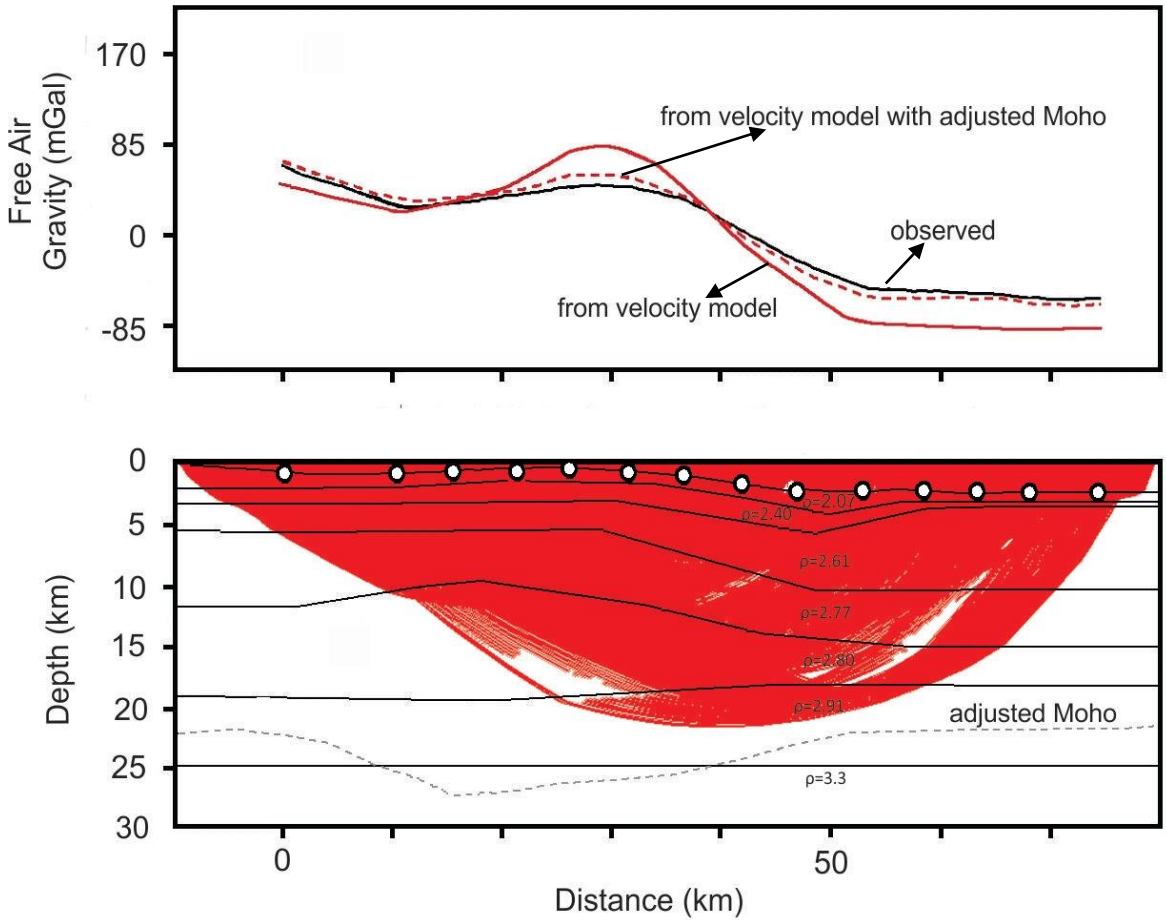

Figure 4.11 Free air gravity modeling results for the line2 refraction profile. The average velocity of each layer of velocity model converted into the density using the Nafe and Drake curve (1963) and the P-wave and density relationship from and Ludwig *et al.*, (1970) and the density model constructed using Potent forward and inversion software from Geophysical Software solutions (Potent v4.09.11, 2007). Numbers on the model show the density values for each layer ($gr.cm^{-3}$). The free air gravity data were achieved from the Satellite Altimetry maintained by the Scripps Institution of Oceanography, University of California San Diego. Above the density model, the observed free air gravity anomaly is indicated by the black solid line and calculated gravity anomaly generated nased on the density model is indicated by red solid line. The best fit between observed and calculated gravity anomalies (dashed red line) was obtained by adjusting the Moho depth (dashed grey line in density model). Constrained parts of the model are shown by red ray coverage in the density mode. White circles show OBS locations along the profile.

nodes and the density of the original gravity observations. If the node interval is large relative to the observations, the grid data would be subject to spatial aliasing. The altimeter-derived

gravity field has an accuracy of about 2 mGal (one mGal is about one millionth the normal pull of gravity, 9.8 m/s^2). The gravity anomaly map for Cyprus and offshore south of Cyprus is shown in Figure 4.10.

Gravity modeling along the refraction profile (Figure 4.11) was conducted using the 2D gravity and magnetic forward modeling and inversion Potent software package from Geophysical Software Solutions (Potent v4.09.11, 2007). A primary 2D density model was built using the base seismic velocity model. An average velocity was calculated for each layer and that velocity was converted into density using the Nafe and Drake curve (Nafe and Drake, 1963) and P-wave and density relationship from Ludwig *et al.* (1970).

The maximum depth of the constructed density model is 30 km (Figure 4.11) and the model was considered ±100 km further the limits of the seismic profile to reduce edge effects. The initial density model was refined to obtain a model giving a theoretical anomaly which matches with the observed one. A deeper Moho to approximately 27 km below the Hecataeus Ridge and a shallower Moho to approximately 22 km toward northern and southern limit of the profile is required in order to best fit between the calculated and observed gravity anomalies (dashed line in Figure 4.11). Since ray coverage is not well constrained at the deep parts of the profile, changing the Moho depth is consistent with the velocity model. Welford *et al.* (20145) also estimated a depth of 22 km for the Moho beneath the Hecataeus Ridge.

The free air gravity anomaly profile shows a positive anomaly associated with the Hecataeus Ridge, reduced to a negative gravity anomaly across the Cyprus Arc and the northern part of the Levantine Basin to the south. It is considered that the decrease in free air gravity anomalies from north to south may correspond to the increase in water depth and sediment

thickness. South of Hecataeus Ridge corresponds to the Cyprus Arc marked by a trench occupied by thick sediments and so associated with negative gravity anomalies (Figure 4.10 and 4.11).

4.5.2 Magnetic data modeling

The magnetic anomaly data were obtained from the EMAC2 data base from the National Geophysical Data Center (NGDC) of the National Oceanic and Atmospheric Administration (NOAA). EMAG2 is an updated version of their first global magnetic anomaly grid, EMAG3, which provides the base grid for the World Digital Magnetic Anomaly Map of the Commission of the World Geological Map (Maus *et al.,* 2007; Mens *et al.,* 2007). The 2D magnetic anomaly map of the survey area and magnetic anomaly data along the line are shown in Figures 4.11(a) and 4.11(b) respectively. Grid spacing of ECMAG 2 is 2 arc-minutes (~3.7 km).

As indicated on the map, the northern part of the profile is associated with a low magnetic anomaly whereas the southern part of the profile toward the Cyprus Arc is associated with a high magnetic anomaly as it transitions to a postulated strike-slip system (Welford *et al.,* 2015). The magnetic anomaly highs immediately south of Hecataeus Ridge may represent deeply buried oceanic crust of the subduction zone.

(a)

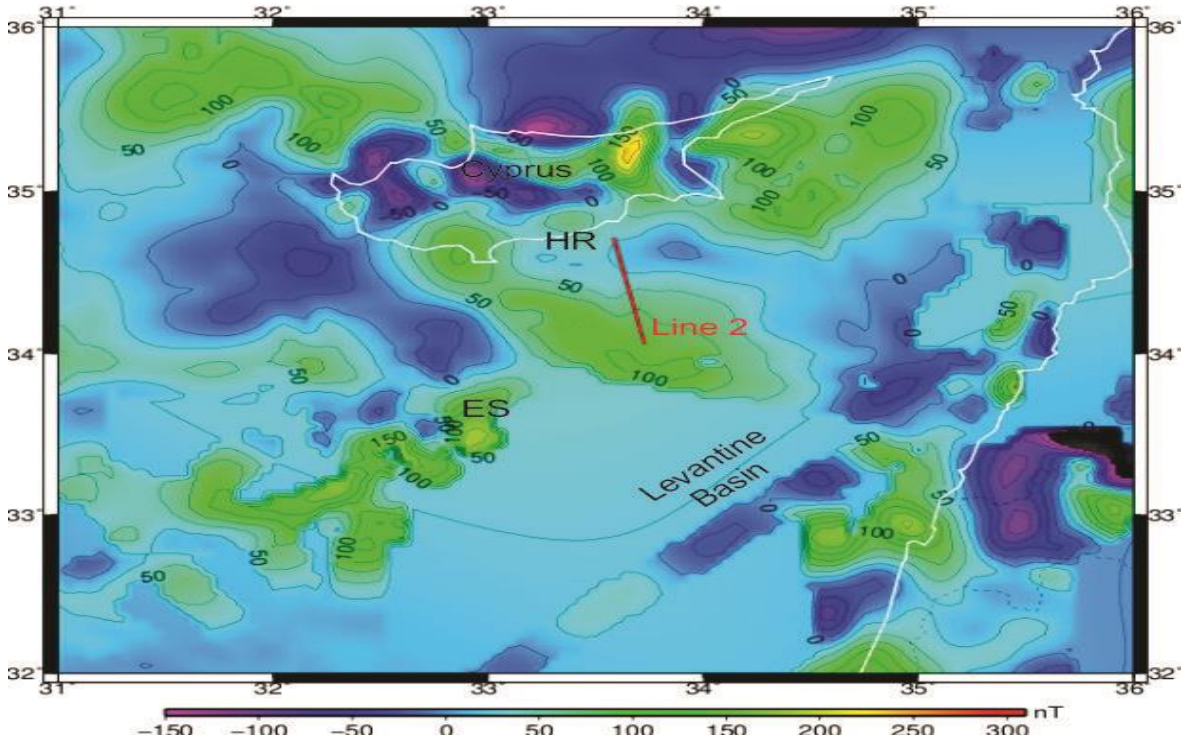

(b)

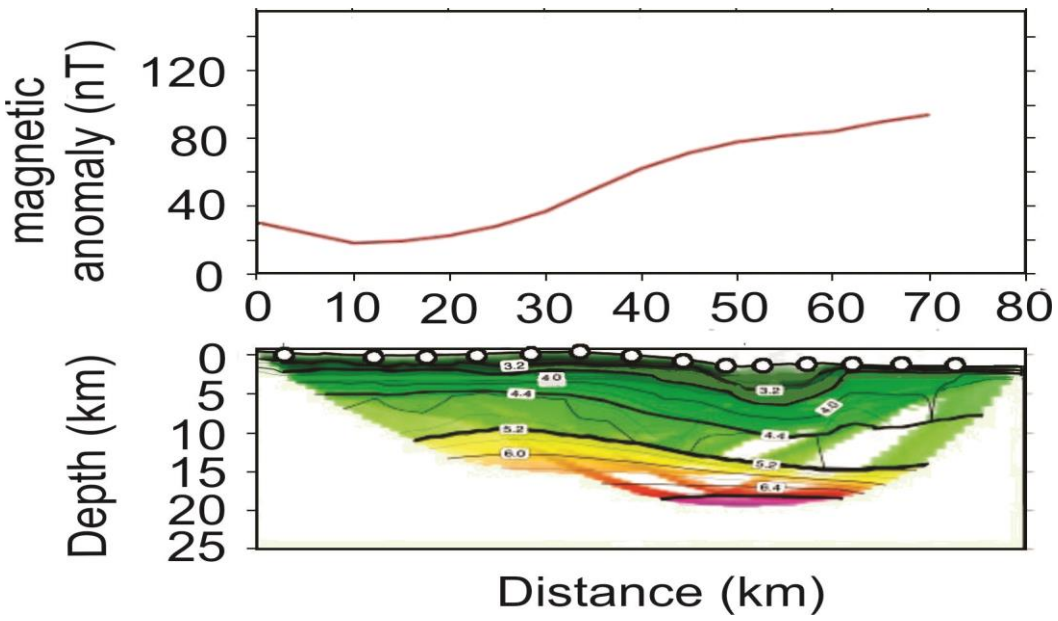

Figure 4.12 a) Magnetic anomaly map of the survey area obtained from the EMAG2 data set (Maus *et al.*, 2007) from the NGDC of NOAA, grid spacing of ECMAG 2 is 2 arc-minutes (~3.7 km), HR: Hecataeus Ridge, ES: Eratosthenes Seamount b) Extracted magnetic anomaly data over the profile (top), velocity model of the profile is plotted beneath the EMAG2. White circles indicate OBS locations along the profiles and white area shows the unconstrained parts of the velocity model.

4.6 Summary and tectonic model

The velocity model obtained for Line 2 (presented in this study) indicates similar velocity structure to those obtained for lines 1 and 1A from the same 2010 cruise (Welford *et al.,* 2015) with a thick sedimentary cover on the upper crust. Figure 4.13 indicates the location of line 2, 1 and 1A and their intersection points. The top 10 km of the velocity model of the Hecataeus Ridge contains velocities less than 5 $km.s^{-1}$.The velocities and their gradients are similar to those for sedimentary rocks overlying continental crust and there is no evidence of high velocity material (~7 $km.s^{-1}$) similar to the velocity of ophiolite (Makenzie *et al.,* 2006) under the Hecataeus Ridge. A high velocity area is modeled beneath the southern edge of the Hecataeus Ridge which might be a high velocity block or continuous high velocity layer. Welford *et al.* (2015) modeled high velocity blocks along line 1 and 1A in the southeast of Hecataeus Ridge. These high velocity lower crustal areas probably represent either a deformed remnant Tethyan oceanic crust (Welford *et al.,* 2015) or mafic intrusives, though they might also be high-velocity lower continental crust. The region outboard of Hecataeus Ridge toward the south appears to have irregular velocity structure with thicker sedimentary sections and correlates with the deformation zone linked with the Cyprus Arc (Welford *et al.,* 2015). Similar structure is imaged along the coincident seismic reflection lines (Reiche and Hübscher, 2015; Reiche el al., 2015) and it might be an accretionary wedge caused by either strike-slip motion or direction change of convergence (Welford *et al.,* 2015). The structure of southeast of velocity model, northern edge of the Levantine Basin, is a homogeneous velocity structure. It is similar to the velocity models obtained for the Levantine Basin in earlier studies (Ben-Avraham *et al.,* 2012; Netzeband *et al.,* 2006a) which probably represents a regionally content shallow velocity structure in the Levantine Basin (Welford *et al.,* 2015). A shallow 4 $km.s^{-1}$ velocity contour represent the top of the Messinian evaporate in the Levantine

Basin. This layer broadly does not exist under the Hecataeus Ridge. Based on the 9 km thickness modeled structure and velocities comparable to oceanic crust (White *et al.,* 1992), Ben-Avraham *et al.* (2002) interpreted the nature of the Levantine basin as oceanic. However Netzeband *et al.* (2006a) used a denser sampling of receivers later and suggested a highly thinned continental crust for the Levantine Basin evidenced by low-velocity gradients.

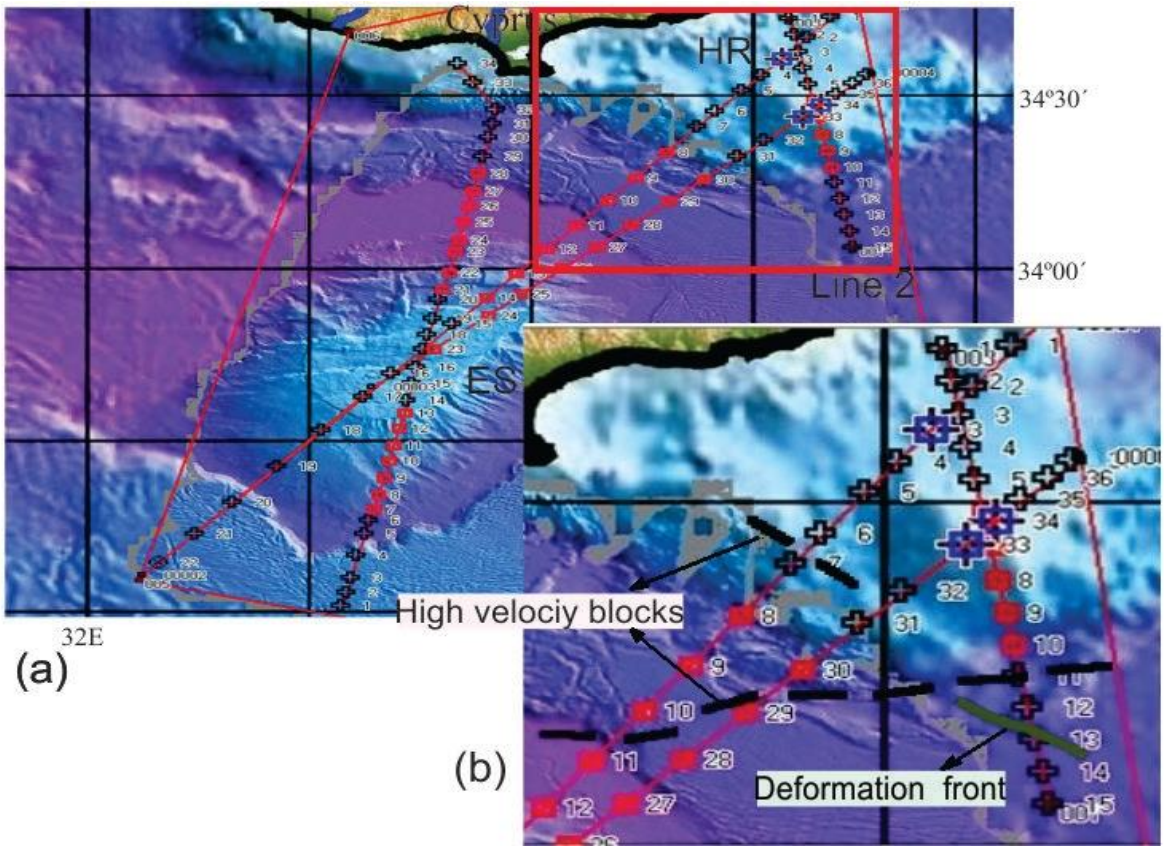

Figure 4.13 a) Bathymetric map of the survey area showing relative locations of WARRP profiles including line 2, 1 and 1A, from 2010 cruise. HR: Hecataeus Ridge, ES: Eratosthenes Seamount, b) Close-up Figure (red rectangle area in Figure 4.13b) showing the deformation front for line 2 and the location of high velocity blocks modeled along lines 1, 1A and 2. The bathymetric metadata and Digital Terrain Model data products is derived from the EMODnet Bathymetry portal - http://www.emodnet-bathymetry.eu.

4.7 Origin of the Hecataeus Ridge

The results of our analysis suggest that there is no evidence of high velocity ophiolites in the shallow crust of the Hecataeus Ridge. So if this structure is an extension of Cyprus crust, from the overlying Aegean-Anatolian plate, the ophiolite material must be deeply buried or perhaps does not extend as far as the Ridge, as agrees with magnetic observations. Furthermore, if Hecataeus Ridge is part of the Aegean-Anatolian microplate then the plate boundary sits at the southern edge of the Ridge.

If Hecataeus Ridge is a northward extension of the African continental margin then the boundary was originally north of Hecataeus Ridge, but with the onset of collision, it might have wedged into the subduction zone, so the deformation front migrated to the south of the Hecataeus Ridge, thus giving a more complex wider plate boundary zone.

The high-velocity area modeled in the velocity model in the southern part of the profile) may be oceanic crust of the African plate, a remnant of Neotothys Ocean. Hecataeus Ridge is separated from Eratosthenes by oceanic crust in either case.

CHAPTER 5

Conclusions and future work

5.1 Conclusions

Velocity modeling of the Hecataeus Ridge and its southerly margin, north of the Levantine Basin has been completed using the seismic data acquired in 2010 on the German research ship R.V. MARIA S. MARIAN. The velocity model reveals a laterally variable velocity distribution over the profile. The results of this modeling are as follows:

i. The Hecataeus Ridge consists of Pliocene-Quaternary and Miocene sedimentary rock cover on the top (approximately 10 km) overlying basement crust that is consistent with the characteristics of a continental crust.

ii. The top 10 km of the velocity model of the Hecataeus Ridge contains sediments with the velocities less than 5 $km.s^{-1}$ and there is no evidence of high velocity material similar to velocity of ophiolite (Makenzie *et al.*, 2006) in shallow depth as is characteristic of southern Cyprus.

iii. The Moho beneath the Hecataeus Ridge is constrained to 25-27 km depth based on the gravity data but reaches to shallower depth, 22 km, in the north of the Levantine Basin, southeast of the profile. Both the Hecataeus Ridge and Levantine Basin are likely thinned continental crust.

iv. A high velocity area is modeled in the crustal layer beneath the southern edge of the Hecataeus Ridge. This high velocity area might be representative of a high velocity block, similar to blocks modeled by Welford *et al.* (2015) in the southeast of Hecataeus Ridge and is interpreted either a remnant Tethyan oceanic crust or mafic intrusives (Welford *et al.*, 2015), or might be representative of a high velocity layer across the whole region.

v. Hecataeus Ridge is separated from the Levantine Basin by a sharp boundary associated with the deformation zone. The deformation zone also marks the plate boundary.

vi. Outboard of Hecataeus Ridge toward the south is modeled with thick sedimentary sections with low velocities. This area is coincident with the deformation region combined with the Cyprus Arc and is likely a highly-deformed accretionary wedge.

vii. The Levantine Basin in the southeast of the profile has a homogenous velocity structure and is consistent with the velocity models obtained for the Levantine Basin in previous studies (Ben-Avraham *et al.*, 2002; Netzeband *et al.*, 2006a) which probably suggests a regionally constant shallow velocity structure in the Levantine Basin (Welford *et al.*, 2015).

viii. Hecataeus Ridge may represent an extension of Cyprus crust. However there is no evidence of high velocity ophiolite material in the shallow crust of Ridge. So either the ophiolite material is buried deep under the Ridge or does not extend as far as the Ridge.

ix. If Hecataeus Ridge is a northward extension of the African continental margin, it suggests the original location of the plate boundary lies to the north of Hecataeus Ridge. Due to the collision of the African plate with the Aegean-Anatolian plate, the Hecataeus Ridge may have wedged into the subduction zone resulting in a spreading of the deformation front to the south of Ridge, giving a more complex wider plate boundary zone.

5.2 Future work

The Hecataeus Ridge and eastern segment of Cyprus Arc represent a natural laboratory with lots of complexities that allow for fundamental Earth processes study. The refraction data revealed some aspects of the evolution and structure within the study area, south of Cyprus. However, the Hecataeus Ridge and adjacent area including deformation front require to be better imaged to better determine the region evolution and development on a crustal scale. Further more some parts of the

study area are not well constrained by these data. So to answer some lingering questions especially about the deeper structure a wide-angle survey with larger aperture~120 km should be performed.

References

Amor, J., 1996. PLOTSEC: Generalized Software for Seismic Refraction Data, LSPF, Newsletter, 23, 1039-1043.

Ben-Avraham, Z., Ginzburg, A., Makris, J., Eppelbaum, L., 2002. Crustal structure of the Levant Basin, eastern Mediterranean, Tectonophysics 346(1–2), 23–43.

Ben-Avraham, Z., Kempler, D., Ginzburg, A., 1988. Plate convergence in the Cyprean Arc.Tectonophysics 146, 231–240.

Ben-Avraham, Z., Tibor, G., Limanov, A., Leyboy, M., Ivanov, M., Tokarev, M.Y., Woodside, J., 1995. Structure and tectonics of the eastern Cyprean Arc, Marine and Petroleum Geology, 12(3), 263–270.

Dewey, J.F., Hempton, M.R., Kidd, W.S.F., Şaroğlu, F., Şengör, A.M.C., 1986. Shortening of continental lithosphere: the neotectonics of eastern Anatolia—a young collision zone. In: Coward, M.P., Ries, A.C. (Eds.), Collision Tectonics, Geological Society Special Publication, Vol. 19, 3– 36.

EMODNet, European Marine Observation and Data Network, 2009, - http://www.emodnet-bathymetry.eu.

Ergün, M., Okay, S., Sari, C., Oral, E. Z., Ash, M., 2005. Gravity anomalies of the Cyprus Arc and their tectonic implications, Marine Geology 221, 349– 358.

Erickson, A. J., 1978. Leg 42A physical properties data, Deep Sea Drilling Project, V. XLII Part 2, doi: 10.2973/dsdp.proc.42-2.

Fowler, C.M.R., 2004. The solid Earth: An introduction to Global Geophysics, 2nd edition, Cambridge University Press, ISBN:9780521893077.

Funck, T., Jackson, R., Louden, K.E., Dehler, S.A., Wu, Y., 2004. Crustal structure of the northern Nova Scotia rifted continental margin (Eastern Canada). Journal Geophysics 109. doi:10.1029/ 2004JB00300.

Gallo, G., Pallottino, S., 1986. Shortest path methods: A unifying approach, Math, Program, Study, Vol. 26, 38-64.

Gardosh, M.A., Druckman, Y., 2006. Seismic stratigraphy, structure and tectonic evolution of the Levantine Basin, offshore Israel. In: Robertson, A.H.F., Mountrakis, D. (Eds.), Tectonic Development of the Eastern Mediterranean Region. Geological Society of London, Special Publications, 260, 201–227.

Gass, I.G., Masson-Smith, D., 1963. The geology and gravity anomalies of the Troodos massif, Cyprus, Phil. Trans. R. Soc. Lond., 1060(255), 417–467.

Hall, J., Aksu, A., Calon, T., Yasar, D., 2005a. Varying tectonic control on basin development at an active microplate margin: Latakia Basin, Eastern Mediterranean, Marine Geology 221, 15–60.

Hall, J., Calon, T., Aksu, A., Meade, S., 2005b. Structural evolution of the Latakia Ridge and Cyprus Basin at the front of the Cyprus Arc, Eastern Mediterranean Sea, Marine Geology 221, 261–297.

Hancock, P.L., Barka, A.A., 1981. Opposed shear senses inferred from neotectonic mesofractures systems in the North Anatolian fault zone. Journal of Structural Geology 3, 383– 392.

Holbrook, W.s., Mooney, W.D., Christensen,N.I., 1992. The seismic velocity of the deep continental crust, in lower Continental Crust, edited by fountain, D.M., Arculus, R., Kay, R., 1-43.

Hsu, K. J., Montadert, L., Bernouilli, D., Bizon, G., Cita, M, B., Eriksn, A., Fabricius, F., Garrison, R. E., Kidd, R.B., Melieres, F., Muller, C., Wright, R. C., 1978. Sites 375 and 376: Florence Rise, in Hsu, K. J., Montadent, L., *et al.*, initial Reports of the Deep Sea Drilling Project, Vol. 43, 219- 304.

Hübscher, C., 2012. Eratosthenes Seamount/Eastern Mediterranean Sea: Cruise No. MSM14/3 - March 12 - April 05, 2010 - Limassol (Cyprus) - Limassol Cyprus). MARIA S. MERIAN-Berichte, MSM14.3, Report, DFG-Senatskommission fur Ozeanographie, doi:10.2312/cr_msm14_3.

Kearey, P., Brooks, M., 2002, An Introduction to Geophysical Exploration, 3rd Edition, Blackwell Scientific Publications, ISBN-13: 978-0632049295.

Kempler, D., Ben-Avraham, Z., 1987. The tectonic evolution of the Cyprus Arc. Tectonophysics 1, 58–71.

Kempler, D., Garfunkel, Z., 1994. Structures and kinematics in the northeastern Mediterranean: A study of an unusual plate boundary. Tectonophysics 234(1–2), 19–32.

Kempler, D., 1994. An outline of the Northeastern Mediterranean tectonics in view of Cruise 5 of the Akademik Nikolaj Strakhov. In: Krasheninnikov, V.A., Hall, J.K. (Eds.), Geological Structure of the Northeastern Mediterranean: (Cruise 5 of the Research Vessel Akademik Nikolaj Strakhov). Historical Productions- Hall Ltd, Jerusalem, 277– 293.

Kempler, D., 1996. Eratosthenes Seamount: The possible spearhead of incipient continental collision in the Eastern Mediterranean, Proceedings of the Ocean Drilling Project, Scientific Results, Vol. 160, 709–722.

Khan M.A., Summers, C., Bamford, S.A.D., Chroston, P.N., Poster, C.K., Vine, F., 1972. Reversed seismic refraction line on the Troodos Massif, Cyprus, Nature, 238, 134–136.

Klimke, J., Ehrhardt, A., 2014. Impact and implications of the Afro-Eurasian collision south of Cyprus from reflection seismic data, Tectonophysics 626, 105–119.

Korenaga, J., Holbrook, W., Detrick, R., Kelemen, P., 2001. Gravity anomalies and crustal structure at the southeast Greenland margin, Journal of Geophysical Research, Vol. 106(B5), 8853–8870.

Korenaga, J., Holbrook, W., Kent, G., Kelemen, P., Detrick, R., Larsen, H.- C., Hopper, J. Dahl-Jensen, T., 2000. Crustal structure of the southeast Greenland margin from joint refraction and reflection seismic tomography, Journal of Geophysical Research, Vol. 105(B9), 21591–21614.

Le Pichon, X. Kreemer, C., 2010. The Miocene-to-present kinematic evolution of the Eastern Mediterranean and Middle East and its implications for dynamics, Annu. Rev. Earth Planet Sciences 38, 323–351.

Lort, J.M., Matthews, D.H., 1972. Seismic velocities measured in rocks of the Troodos igneous complex, Journal of Geophysical Researches. Astron. Soc., 27. 383–392.

Ludwig, W., Nafe, J., Drake, C., 1970. Seismic refraction, in The Sea, in New Concepts of Sea Floor Evolution, Part I, vol. 4, 5–84.

Mackenzie, G., Maguire, P., Coogan, L., Khan, M., Eaton, M., Petrides, G., 2006. Geophysical constraints on the crustal architecture of the Troodos ophiolite: results from the IANGASS project, Geophysical Journal International, 167, 1385– 1401, doi: 10.1111/j.1365-246X.2006. 03144.x.

Mackenzie, K.V., 1981. Discussion of sea-water sound-speed determinations, Journal of the Acoustical Society of America, Vol. 70(3), 801–806.

Makris, J., Ben-Avraham, Z., Behle, A., Ginzburg, A., Giesse, P., Steinmetz, L., Whitmarsh, R.B., Eleftheriou, S., 1983. Seismic refraction profiles between Cyprus and Israel and their interpretation. Geophysical Journal of the Royal Astronomical Society, Vol. 75, 575–591.

Makris, J., Wang, J., Odintsov, S.D., Udintsev, G.B., 1994. The magnetic field of eastern Mediterranean Sea, In: Krasheninnikov, V.A., Hall, J.K. (Eds.), Geological Structure of the Northeastern Mediterranean. Historical Productions-Hall, Jerusalem, 75-86 (Cruise 5 of the Research Vessel `Akademik Nikolaj Strakhov').

Maus, S., Sazonova, T., Hemant, K., Fairhead, J., Ravat, D., 2007. National Geophysical Data Center candidate for the World Digital Magnetic Anomaly Map, Geochemistry Geophysics Geosystems, Vol. 8(6), doi:10.1029/ 2007GC001643.

McClusky, S., Balassanian, S., Barka, A., Demir, C., Ergintav, S., Georgiev, I., Gurkan, O., Hamburger, M., Hurst, K., Kahle, H., Kastens, K., Kekelidze, G., King, R., Kotzev, V., Lenk, O., Mahmoud, S., Mishin, A., Naderiyan, M., Ouzounis, A., Paradissis, D., Peter, Y., Prilepin, M., Reilinger, R., Sanli, I., Seeger, H., Tealeb, A., Toksoz, N., Vels, G., 2000. Global Positioning System constraints on plate kinematics and dynamics in the eastern Mediterranean and Caucasus, Journal of Geophysical Researches, Vol. 105(B3), 5695–5719.

McClymont, A. F. 2004, Crustal structure of the northern Juan De Fuca plate (M.Sc. Thesis) University of British Columbia.

McKenzie, D., Yilmaz, Y., 1991. Deformation and volcanism in western Turkey and the Aegean, Bulletin of the Istanbul Technical University, 345-373.

Mens, S., Sazonova, T., Hemant, K., Fairhead, J. D., Ravavt, D., 2007. National Geophysical Data Center candidate for the Worldm Digital Magnetic Anomaly Map, Geochemistry geophysics geosystems E-jouyrnal of the Earth Sciences, Vol. 6, Q06017, doi:10.1029/2007GC001643, ISSN: 1525-2027.

Mereu, R.F., Majumdar, S.C., White, R.E., 1977. The structure of the crust and upper mantle under the highest ranges of the Canadian Rockies from a seismic refraction survey, Canadian Journal of Earth Sciences, Vol. 30, 209-230.

Milkereit, B., Spencer, C., 1989. Noise suppression and coherency enhancement of seismic data, in Statistical application in the Earth Sciences, pp. 243–248, eds Agterberg, F., Bonham-Carter, G., Geological Survey of Canada, Paper 89–9.

Moores, E.M., Robertson, P.T., Malpas, J., Xenophontos, C., 1984. Model for the origin of the Troodos massif, Cyprus and other Mideast ophiolites, Geology, vol. 12, 223-226.

Moser, T.J., Nolet, G., Snieder, R., 1992. Ray bending revisited, Bulletin of the Seismological Society of America, Vol. 82, 259-288.

Nafe, J.E., Drake, C.I., 1963. Physical properties of marine sediments, in the sea, edited by M.N., Hill, Interscience, Vol. 3, 794-815.

Netzeband, G.L., Gohl, K., Hübscher, C., Ben-Avraham, Z., Dehghani, A., Gajewski, D., Liersch, P., 2006a. The Levantine Basin—crustal structure and origin, Tectonophysics 418 (3–4), 178–188.

Netzeband, G.L., Hübscher, C.P., Gajewski, D., 2006b. The structural evolution of the Messinian evaporites in the Levantine Basin, Marine Geology, 230, pp 249-273.

Nur, A., Ben-Avraham, Z., 1978. The Eastern Mediterranean and the Levan tine: Tectonics of continental collision, Tectonophysics 46, 297- 311.

Oikawa, M., Kaneda, K., Nishiziwa, A., 2010. Seismic structures of the 154-160 Ma oceanic crust and uppermost mantle in the Northwest Pacific Basin, Earth Planets Space, 62, e13-e16

Papazachos, B.C., Papaioannou, C.A., 1999. Lithospheric boundaries and plate motions in the Cyprus area. Tectonophysics 308(1–2), 193–204.

Potent v4.09.11, 2007. Forward and inversion software, Geophysical software solutions Pty. Ltd., http://www.geoss.com.au.

Reiche, S., H¨ubscher, C., 2015. The Hecataeus Rise, easternmost Mediterranean: a structural record of Miocene-Quaternary convergence and incipient continent-collision at the African-Anatolian plate boundary, Marine and Petroleum Geology, Vol. 67, 368–388.

Reiche, S., H¨ubscher, C., Ehrhardt, A., 2015. The impact of salt on the late Messinian to recent tectonostratigraphic evolution of the Cyprus subduction zone, Marine and Petroleum Geology, Vol. 1(29), doi:10.1111/bre.12122.

Robertson, A.H.F., Emeis, K.C., Richter, C., Blanc-Valleron, M.M., Bouloubassi, I., Brumsack, H.J., Cramp, A., De Lange, G.J., Di Stefano, E., Flecker, R., Frankel, E., Howell, M.W.,

Janecek, T.R., Jurado, M.J., Kemp, A.E.S., Koizumi, I., Kopf, A., Major, C.O., Mart, Y., Pribnow, D.F.C., Rabaute, A., Roberts, A.P., RuÈllkotter, J.H., Sakamoto, T., Spezzaferri, S., Starker, T.S., Stoner, J.S., Whiting, B.M., Woodside, J.M., 1995a. Evidence of collisional processes associated with ophiolite obduction in the eastern Mediterranean. Results from ocean drilling program leg 160. GSA 5, 11.

Robertson, A.H.F., Kidd, R.B., Ivanov, M.K., Limonov, A.F., Woodside, J.M., Galindo-Zaldivar, J., Nieto, L., 1995b. Eratosthenes Seamount: collisional processes in the easternmost Mediterranean in relation to the Plio– Quaternary uplift of southern Cyprus. Terra Nova 7, 254– 264.

Robertson, A.H.F., Xenophontos, C., 1993. Development of concepts concerning the Troodos ophiolite and adjacent units in Cyprus, in Magmatic Processes and Plate Tectonics, Geological Society Special Publications, Vol. 76, 85–119.

Robertson, A., 1998a. Tectonic significance of the Eratosthenes Seamount: a continental fragment in the process of collision with a subduction zone in the eastern Mediterranean (Ocean Drilling Program Leg 160), Tectonophysics, 298(1–3), 63–82.

Robertson, A.H.F., 1998b. Formation and destruction of the Eratosthenes Seamount, Eastern Mediterranean Sea, and implications for collisional processes. In: Robertson, A.H.F., Emeis, K.C., Richter, C., Camerlenghi, A. (Eds.), Proceedings of the Ocean Drilling Program. Scientific Results, 160, 681–699.

Rotstein, Y., Ben-Avraham, Z., 1985. Accretionary processes at subduction zones in the Eastern Mediterranean. Tectonophysics 112, 551–561.

Rybakov, M., Goldshmidt, V., Rotstein, V., 1997. New regional gravity and magnetic maps of the Levant, geophysical Research Letters, 24(1), 33-36.

Sage, L., Letouzey, J., 1990. Convergence of the African and Eurasian Plates in the eastern Mediterranean. In: Letouzey, J. (Ed.), Petroleum and Tectonics in Mobile Belts, Editions Technip, Paris, 49– 68.

Sandwell, D. T., Müller, R.D., Smith, W. H. F., Garcia, E., Francis, R., 2014. New global marine gravity model from CryoSat-2 and Jason-1 reveals buried tectonic structure, Science, Vol. 346, no. 6205, 65-67.

Sandwell, D.T., Smith, W.H., 1997. Marine gravity anomaly from Geosat and ERS 1 satellite altimetry, Journal of Geophysical Research, Vol. 102(B5), 10 039–10 054.

Schattner, U., 2010. What triggered the early-to-mid Pleistocene tectonic transition across the entire eastern Mediterranean? Earth and Planetary Science Letters 289(3–4), 539–548.

Şengör, A.M.C., Yilmaz, Y., 1981. Tethyan evolution of Turkey: A plate tectonic approach. Tectonophysics 75, 181– 241.

Sheriff, R.E., Geldert, L.P., 1995. Expolation Seismology, 2nd Edition, University of Houston, ISBN: 9780521468268.

Spence, G.D., Whitall, K.P., Clowes, B.M., 1984. Practical synthetic seismograms for laterally varying media calculated by asymptotic ray theory, Bulletin of the Seismological Society of America, Vo. 74, 112209-1223.

Toomey, D.R., Solomon, S.C., Purdy, G.N., 1994. Tomographic imaging of the shallow crustal structure of the East Pacific Rise at 9˚30′ N, Journal of Geophysical Research, Vol. 99, 24135- 24157.

Van Avendonk, H.J.A., Harding, A.J., Orcutt, J.A., 1998. A two-dimensional tomographic study of the Clipperton transform fault, Journal of Geophysical Research, Vol. 103, 17885- 17899

Vidal, N., Alvarez-Marr´on, J., Klaeschen, D., 2000a. Internal configuration of the Levantine Basin from seismic reflection data (eastern Mediterranean), Earth and Planetary Science Letters 180(1–2), 77–89.

Vidal, N., Klaeschen, D., Kopf, A., Docherty, C., von Huene, R., Krasheninnikov, V.A., 2000b. Seismic images at the convergence zone from south of Cyprus to the Syrien coast, eastern Mediterranean. Tectonophysics 329 (1–4), 157–170.

Vine, F.J., Poster, C.K., Gass, I.G., 1973. Aeromagnetic survey of the Troodos igneous massif, Cyprus, Nature Physical Science, Vol. 244.

Wessel, P., Smith, W.H.F., 2015. The Generic Mapping Tool (GMT), Version 4.5.14, School of Ocean and Earth Science and Technology, University of Hawai'I at Mänoaand Laboratury for Satellite Altimetry, NOAA/NESDIS/STAR.

Welford, J.K., Hall, J., Reiche, S., H¨ubscher, C., Louden, K., 2015. Crustal seismic velocity structure from Eratosthenes Seamount to Hecataeus Riseacross the Cyprus Arc, easternMediterranean, Geophysical Journal International, 200, 935– 953.

Welford, J.K., 1999. Lithospheric structure across the Canadian Cordillera of northeastern British Columbia from seismic refraction and potential field data, M.Sc. Thesis, University of British Columbia, Vancouver, British Columbia, Canada, 178pp.

White, R.S., Detrick, R.S., Sinha, M.C., Cormier, M.H., 1984. Anomalous seismic crustal structure of oceanic fracture zones, Journal of Geophysical Research, 79, 779-798 .

White, R., McKenzie, D., O'Nions, R., 1992. Oceanic crustal thickness from seismic measurements and rare earth element inversions, Journal of Geophysical Research, Vol. 97(B13), 19683–19715.

Woodside, J.M., 1977. Tectonic elements and crust of the eastern Mediterranean Sea. Marine Geophysical Researches 3, 317–354.

Zelt, C.A., Ellis, R.M., 1989. Seismic structure of the crust and upper mantle in the Peace River Arc region, Canada, Journal of Geophysical Research, Vol. 94, 5729- 5744.

Zelt, C.A., Smith, R.B., 1992. Seismic traveltime inversion for 2-D crustal velocity structure, Geophysical Journal International, Vol. 108, 16–34.

Appendix A

Table A shows the water velocities that are derived from a general database of temperature and salinity for the region.

A simple empirical equation for the speed of sound in sea water with reasonable accuracy for the world's oceans is due to Mackenzie (1981):

$$c(T,S,z) = a_1 + a_2T + a_3T^2 + a_4T^3 + a_5(S-35) + a_6z + a_7z^2 + a_8T(S-35) + a_9Tz^3$$

where T, S, and z are temperature in degrees Celsius, salinity in parts per thousand and depth in m, respectively. The constants a_1, a_2, ..., a_9 are:

$a_1 = 1448.96, a_2 = 4.591, a_3 = -5.304 \times 10^{-2}, a_4 = 2.374 \times 10^{-4}, \ a_5 = 1.340,$

$a_6 = 1.630 \times 10^{-2}, a_7 = 1.675 \times 10^{-7}, a_8 = -1.025\times 10^{-2}, a_9 = -7.139 \times 10^{-13}$

with check value 1550.744 m/s for T=25 °C, S=35‰, z=1000 m. This equation has a standard error of 0.070 m/s for salinity between 25 and 40 ppt.

Depth (m)	Velocity (m/s)
0	1522.0660502511
10	1521.9091016075
20	1521.7664086414
30	1521.0961883486
50	1520.2540205164
s75	1518.9246944893
100	1518.6124780518
126	1518.5033526162
150	1518.5090471118

200	1518.2259260172
250	1518.0559820164
300	1517.570
400	1516.926
500	1517.1334806588
600	1517.892
700	1519.0346238269
800	1520.407
900	1521.8615479485
1000	1523.390238884
1100	1524.9767277802
1200	1526.6005091714
1300	1528.2555387235
1400	1529.9245995605
1500	1531.588614477
1750	1535.7986575491

Table A The water velocities for eastern Mediterranean area considering the temperature and salinity

Appendix B

The parameters that are used for coherency filtering of the data are:

MODE = unstacked

This parameter is the mode of the data and has two options. 1) Stacked: to process stacked input data 2) unstacked: to process pre-stack CDPs or shot records.

DX = 40

DX is the trace spacing in m. This is used to calculate the angles of the lines in the slant stack. As such it may be artificial, as long as the maximum slowness (PMAX) uses the same (artificial) units.

PMAX = 0.5

PMAX is the absolute value of the dip limits expressed as slownesses, in milliseconds/metre (ms/m). This parameter only is used to calculate the dips and as such may be an artificial number as long as the trace spacing (DX) uses the same (artificial) units. This should avoid spatial aliasing and thus satisfy: PMAX <= 1000 / (2 * Fmax * DX)

where F is the maximum frequency of the data in Hz. The maximum frequency may be identified by carrying out the necessary post-stack spectral analysis.

NTRPANEL = 17

NTRPANEL is the number of traces in the sliding window. This should be odd and must be in the range 3 to 101. The number cannot exceed the total number of traces to process. Even-numbered windows will be increased by one. Events which are significantly shorter than, or non-linear over, NTRPANEL will be highly attenuated. Those which are linear over NTRPANEL will

be enhanced. Thus, a good option would be to set the window to about the length of the shortest linear segment of the event which is considered signal. As the window size becomes shorter, the probability of random alignments being enhanced increases. As the window becomes larger, smaller events become more attenuated. NP = 101

NP is the number of slownesses (dips) to be used. This must be between 3 and 201, inclusive. A guideline is to avoid time aliasing at the far traces. Thus:

NP >= (2 * F * PMAX * DX * (NTRPANEL - 1)) / 1000 + 1

where F is the maximum frequency in the data in Hz. However, in practice, this degree of accuracy is often not needed and NP can be decreased.

SEMEXP = 1.0

SEMEXP is the semblance exponent. Typically this is between 1 and 2. Semblances are raised to this power to form coherencies. This should be roughly equal to the noise to signal ratio of the data, but not less than 1 (Milkereit and Spencer, 1989). This acts as a 'gentle' threshold; low semblances are made lower while high semblances are unchanged. A good starting point is 1.0.

ADDBACK = 0.0

ADDBACK is the amount (0.0 to 1.0) of original trace to add back into the filtered output (default is 0.0).

The run time for SEMBSMOOTH coherency filter is proportional to NTR_PANEL * NSLOW * NSAMPS, where NSAMPS is the number of samples in the input trace.

Appendix C

Refraction Seismology

In refraction seismology, the velocity of different layers should be higher than those of overlying layers for critical refraction to happens (Kearey and Brooks, 2002; Fowler, 2004). Energy from the source can reach the ocean bottom seismometer (OBS) by a variety of paths; directly through the water layer (direct wave, Figure C1), by reflection from the interface between the water layer and subsurface layer, by multiple reflections within the subsurface layers or by traveling along the interface as a critically refracted wave or head-wave. The head wave, which is often called a refraction or refracted wave, has a travel time corresponding to a ray that traveled down to the interface at the critical angle i_c, then along the interface with the velocity of lower layer and then reach to the OBS.

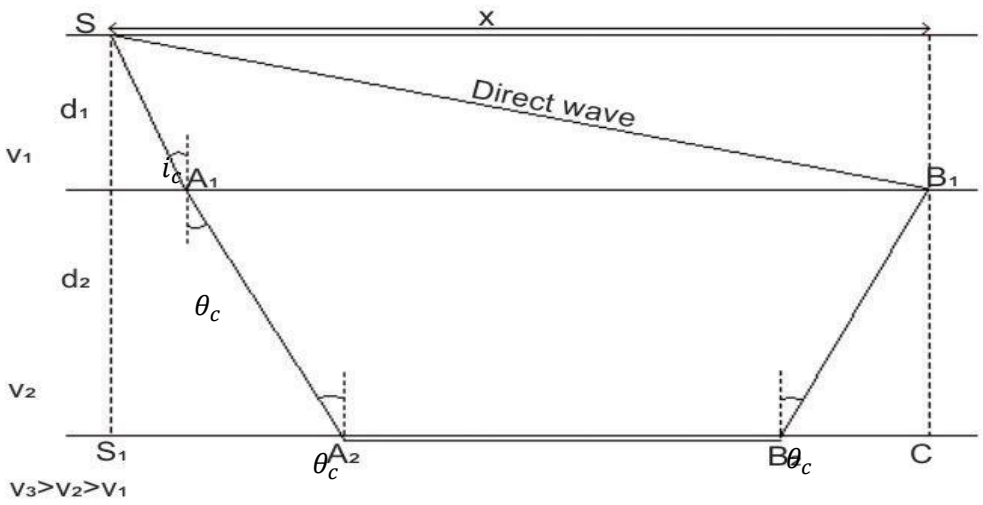

Figure C1 Ray path for seismic energy travelling from source S down to the layer below seabed and come back to receiver located at the sea bed (point B_1). The P-wave velocity is $v_1 \cong 1.5\ km/s$ for the water layer (upper layer) and v_2 for the second layer and v_3 for the lower layer, where $v_3 > v_2 > v_1$. The direct wave takes ray path SB_1 in the water layer. (x= offset of OBS from the source, d_1= depth beneath the seasurface, d_2= thickness of first layer below seabed, i_c= angle of incidence, θ_c=refraction angle)

Direct Wave:

The time taken for energy to reach the OBS directly from source through the water:

$$d_1 = d_w, \;\; v_1 = v_w$$

Direct wave travel time

$$T_{direct} = \frac{\sqrt{(x^2 + d_w^2)}}{v_w}$$

This is the equation for straight line when time is plotted against distance.

Refracted Wave:

For the refracted-ray path, the travel time from the layer below seabed is:

$$sin\,\theta_c = \frac{v_w}{v_3}, \;\; tan\,\theta_c = \frac{S_1A_2}{d_2+d_w} = \frac{CB_2}{d_2}, \;\; cos\,\theta_c = \frac{d_2+d_w}{SA_2}$$

$$A_2B_2 = x - S_1A_2 - B_2C = x - 2d_2\,tan\,\theta_c - d_w\,tan\,i_c$$

In refraction forward modeling for simplicity, we assume the velocity of layer below seabed is equal to water wave velocity (v_w).

$$T_{refraction} = T_{SA_2} + T_{A_1B_2} + T_{B_2B_1} = \frac{d_w + d_2}{v_w\,cos\,\theta_c} + T_{CS_1} - T_{CB_2} - T_{S_1A_2} + \frac{d_2}{v_w\,cos\,\theta_c}$$

$$= \frac{d_w + 2d_2}{v_w\,cos\,\theta_c} + \frac{x}{v_3} - \frac{d_2\,tan\,\theta_c}{v_3} = \frac{x}{v_3} + (d_w + 2d_2)\left\{\frac{1}{v_w\,cos\,\theta_c} - \frac{tan\,\theta_c}{v_3}\right\}$$

$$= \frac{x}{v_3} + \frac{d_w + 2d_2}{v_w}\left\{\frac{1}{cos\,\theta_c} - \frac{v_w\,tan\,\theta_c}{v_3}\right\}$$

$$T_{refraction} = \frac{x}{v_3} + \frac{d_w + 2d_2}{v_w}(cos\,\theta_c)$$

A Multilayer Model

The travel times for a model consisting of n uniform horizontal layers of thickness d_i and P wave velocity v_i are determined the same way as calculated above.

The travel time for a wave refracted along the top of the nth layer is:

$$T_{refraction} = \sum_{j=1}^{n-2}\left(\frac{2d_j}{v_j}\sqrt{1-\frac{v_j^2}{v_n^2}}\right) + \frac{d_w}{v_w cos\theta_c} + \frac{x}{v_n} \quad , n>2$$

Traveltime Curves

Travel time-distance diagram for the two-layer model is indicated in Figure C2.

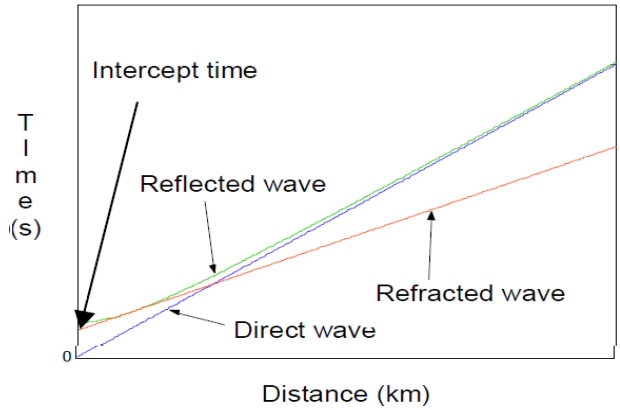

Figure C.2 Travel time-distance plot for two-layer model (Fowler, 2004).

The distance at which the refracted arrival overtakes the direct arrival can be used to determine the layer depth. According to ray theory there is a minimal distance at which the refracted wave can be observed, this is called the critical distance.

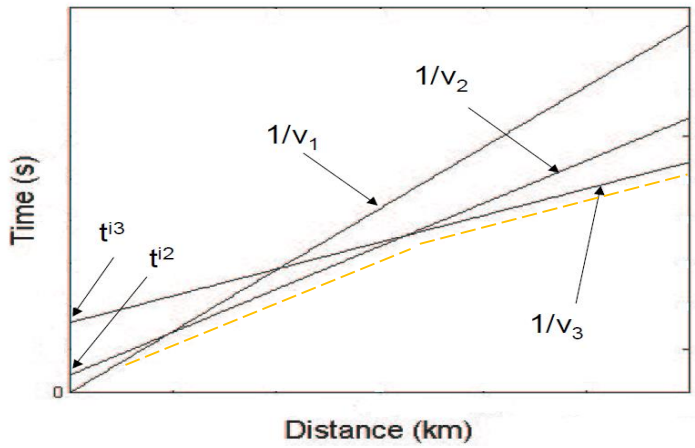

Figure C3 Travel time diagram for multilayer model, Orange dashed line indicates the travel time path for a refraction seismogram (Fowler, 2004).

Figure C3 indicates travel time -distance diagram for a multilayer model.

Reciprocal time

The travel time of seismic energy between two points is independent of the direction traveled. So interchanging the source and receiver will not affect the seismic travel time between the two.

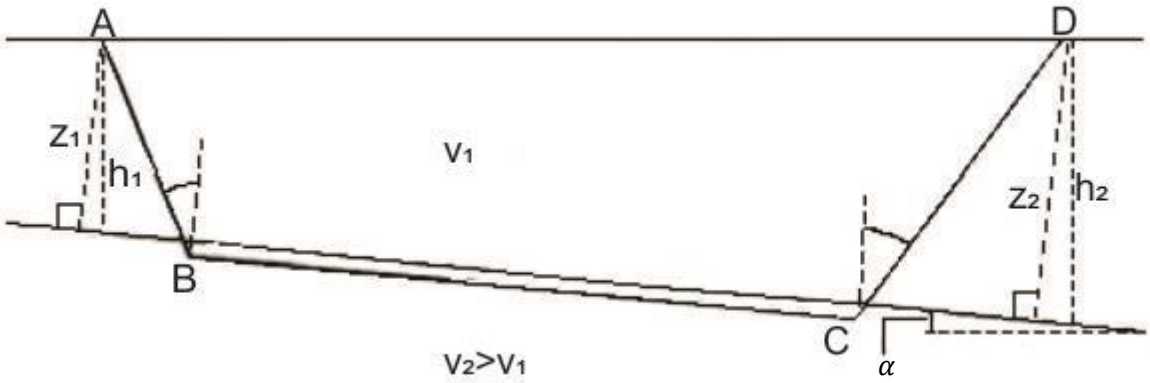

Figure C4 Ray path for seismic energy travelling from source S to receiver R in a two-layer model in which the interface between the two layers dips at an angle α. The P-wave velocity for the upper layer is v_1 and for lower layer is v_2, where $v_2 > v_1$.

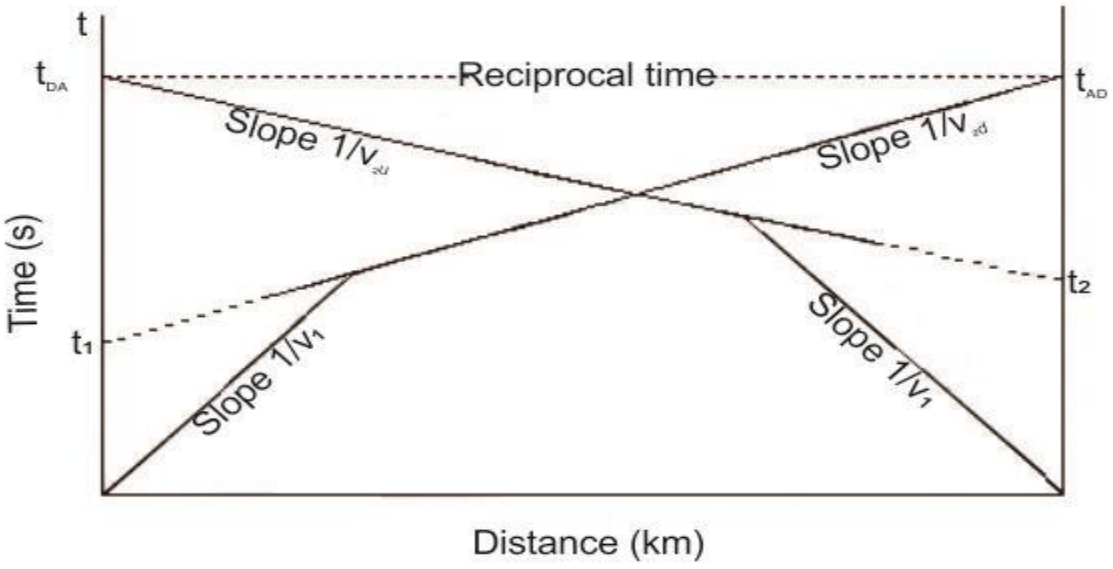

Figure C5 Travel time- distance plot for a wave travelling from source S to receiver R in a two-layer model. Travel times are equal in forward and reverse direction for switched source/receiver positions (reciprocal time)

If we assume the first interface has an angle of α instead of being horizontal ($\alpha = 0$) as in Figure C4, the travel time for the wave to travel from

$$T_{ABCD} = \frac{x \sin(\theta_1 + \alpha)}{v_1} + \frac{2z_1 \cos\theta_1}{v_1}$$

Where z_1 is the perpendicular distance from the shot point (Figure C4, point A) to the interface. Apparent velocity of head wave in the forward direction (ABCD) is

$$v_{2d} = \frac{v_1}{\sin(\theta_c + \alpha)} < v_2$$

The apparent velocity, v_{2d}, is less than v_2 $\left(= {}^{v_1}/_{\sin\theta_c}\right)$ which results in a steeper slope on the travel time curve (Figure C5).

If a second shot was fired at the far end of the receiver array, then the wave will travel up dip. As the refraction travels to larger offsets (x) the final leg in the upper layer will become shorter,

and the refraction will arrive earlier. This effectively increase the apparent velocity and reduce the slope of the travel time curve.

$$T_{DCBA}(\text{reverse}) = \frac{x \sin(\theta_c - \alpha)}{v_1} + \frac{2z_2 \cos\theta_c}{v_1}$$

Apparent velocity in the reverse direction (DCBA) is

$$v_{2u} = \frac{v_1}{\sin(\theta_c - \alpha)}$$

The travel time T_{ABCD}(forward direction) and T_{DCBA} (reverse direction) are the same. This is called reciprocity and can be used for correlation of travel time arrivals of same phase of different receivers

Appendix D

Data and Related Results

Appendix D displays all data plots and related results for line2. Travel time-distance (T-X) plots band-pass filtered from 4 - 10 Hz and coherency filtered. All seismic data have been plotted with a reducing velocity of 8 km s^{-1}.

- Location map of line 2 and OBS profiles, south of Cyprus is displayed in Figure D0.
- The raw data plots are displayed in Figures D1a, D3a... D40a.
- Processed (band-pass and coherency filtered) and gained data are shown in Figures D1b, D3b... D40b.
- Short offset range (~$\pm$20 km) and short range shallow velocity model of OBSs with the numbers indicated the assigned velocity values to each velocity node in the model are indicated in Figures D2a, D5a,…, D41a and D2b, D4b,…, D41b respectively.
- Data with the picked travel times are indicted in Figures D3, D6...D42.

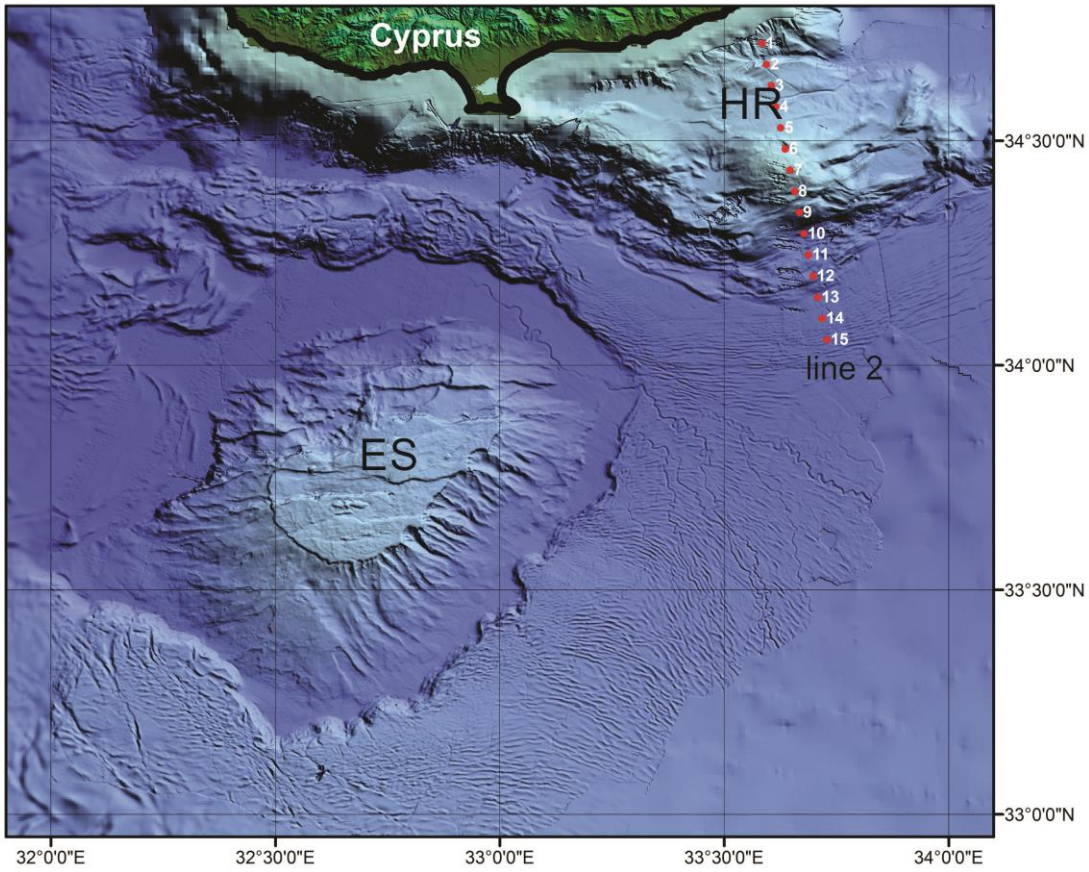

Figure D0 Location map of line 2 and OBS profiles, south of Cyprus. (ES-Eratosthenes Seamount, HR- Hecataeus Ridge). The bathymetric metadata and Digital Terrain Model data is derived from the EMODNet Bathymetry portal- http://www.emodnet-bathymetry.eu.

a)

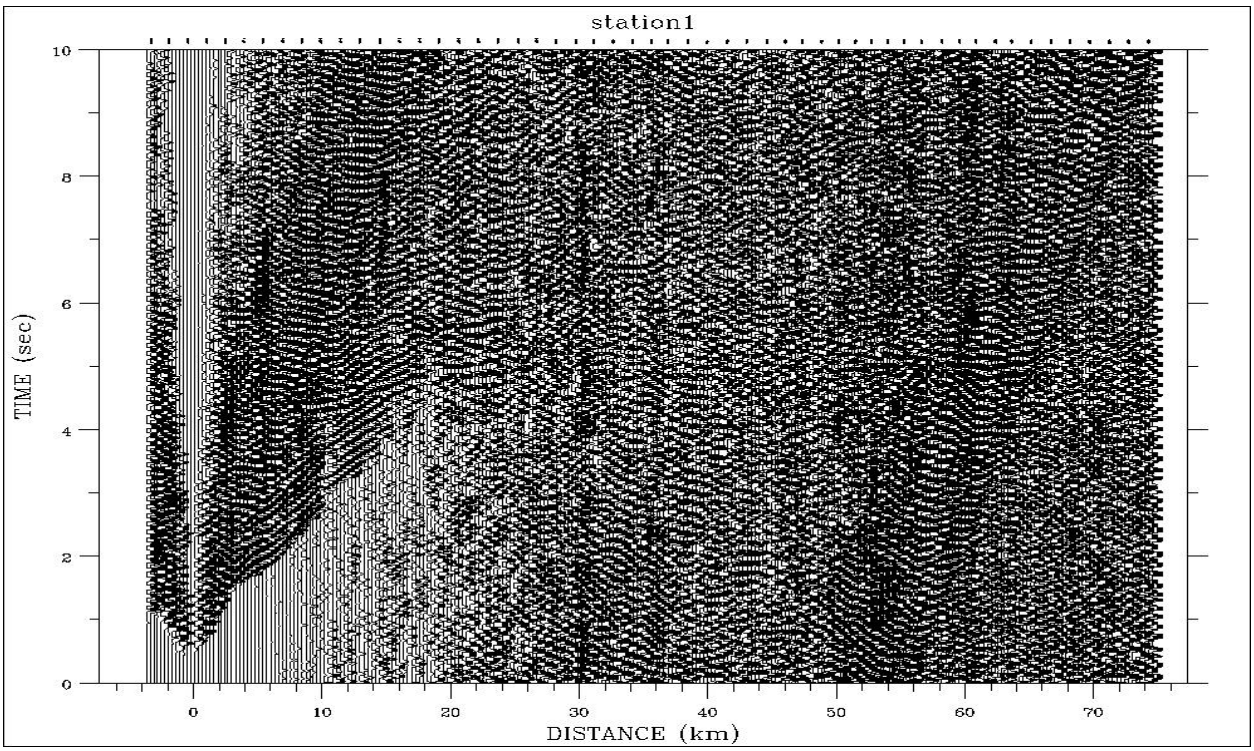

b)

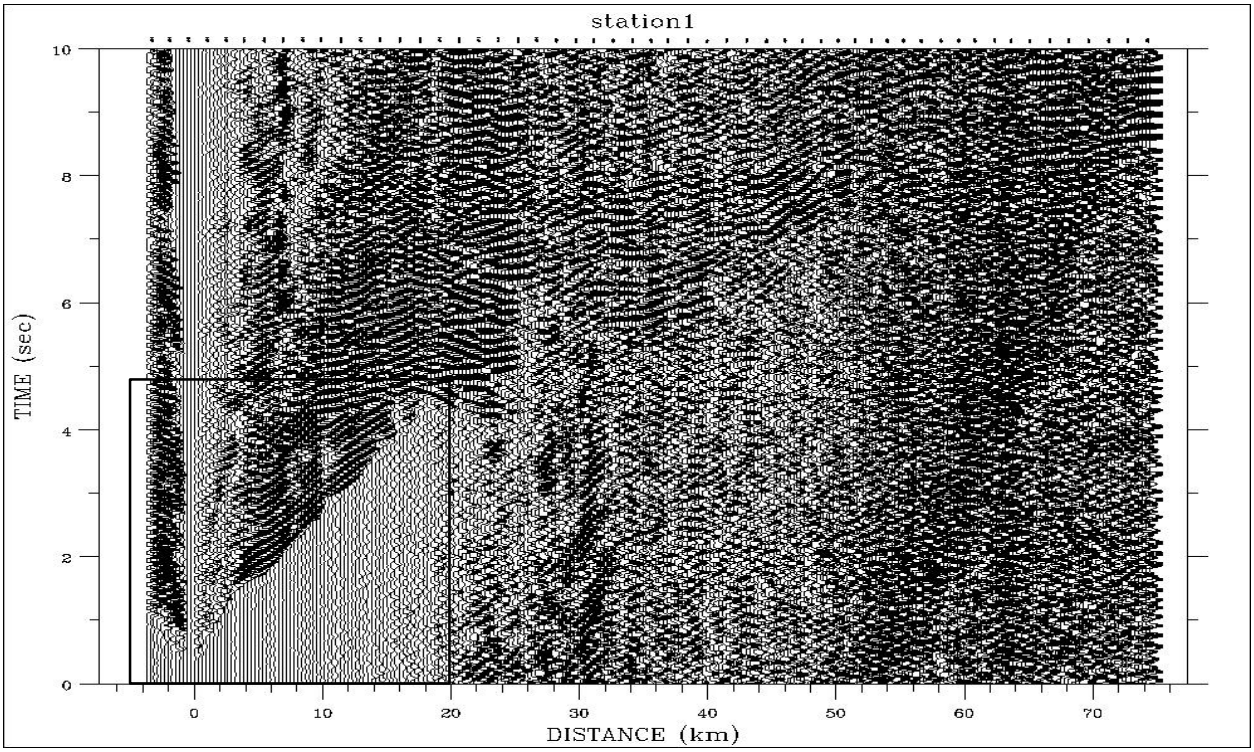

Figure D1 a) Vertical component record section for OBS 1 before any processing, b) Vertical component record section for OBS 1, after band pass filtered (4-10Hz) and applying coherency filter

a)

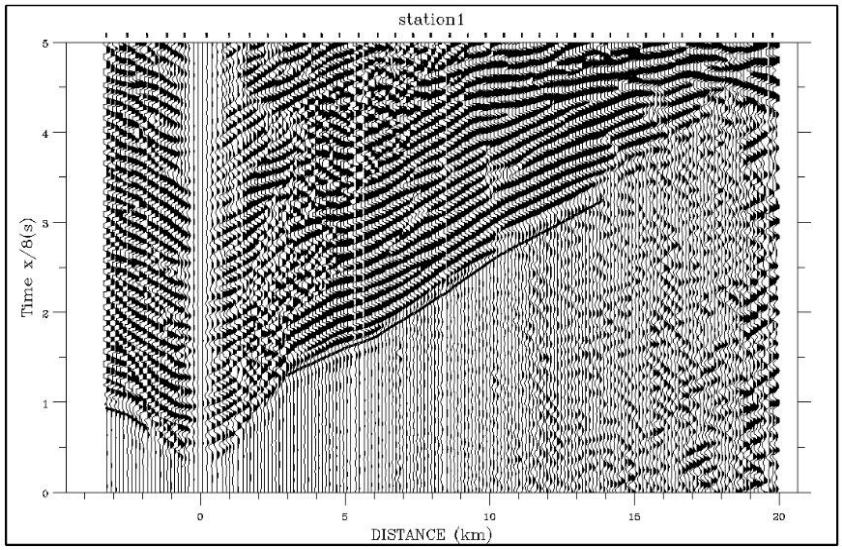

b)

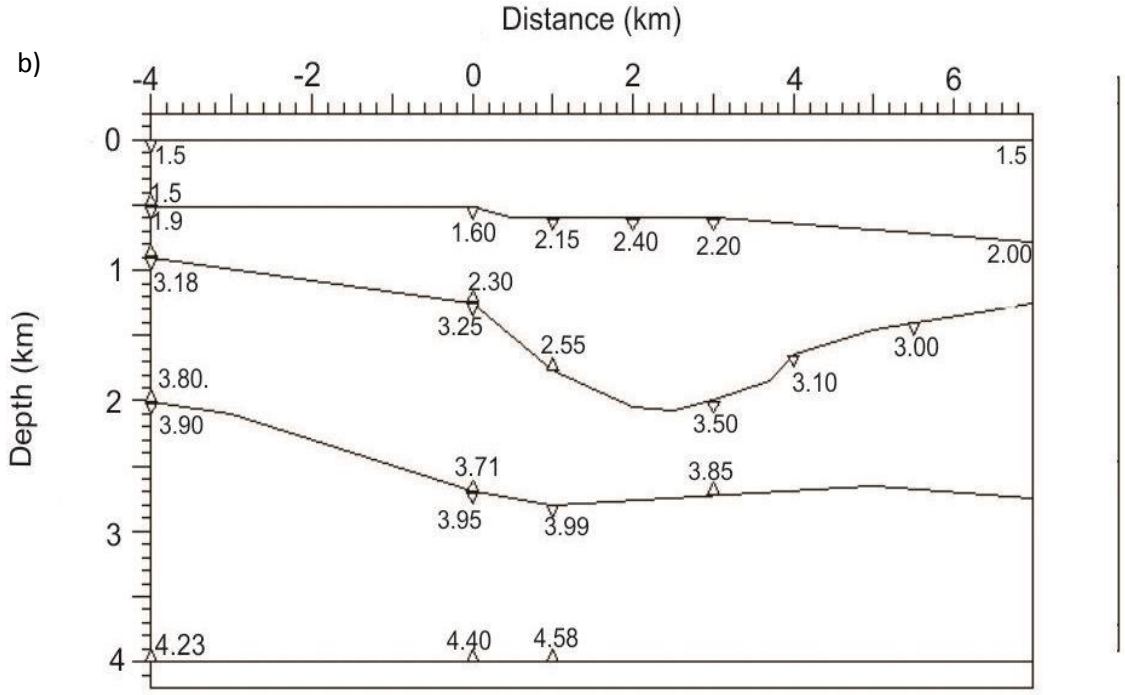

Figure D2 a) Close-up plot for the Short offset range (±20 km) of OBS 1 (indicated in D1b by rectangle), b) Short range shallow velocity model of OBS 1, the numbers indicate the assigned velocity values to each velocity node in the model

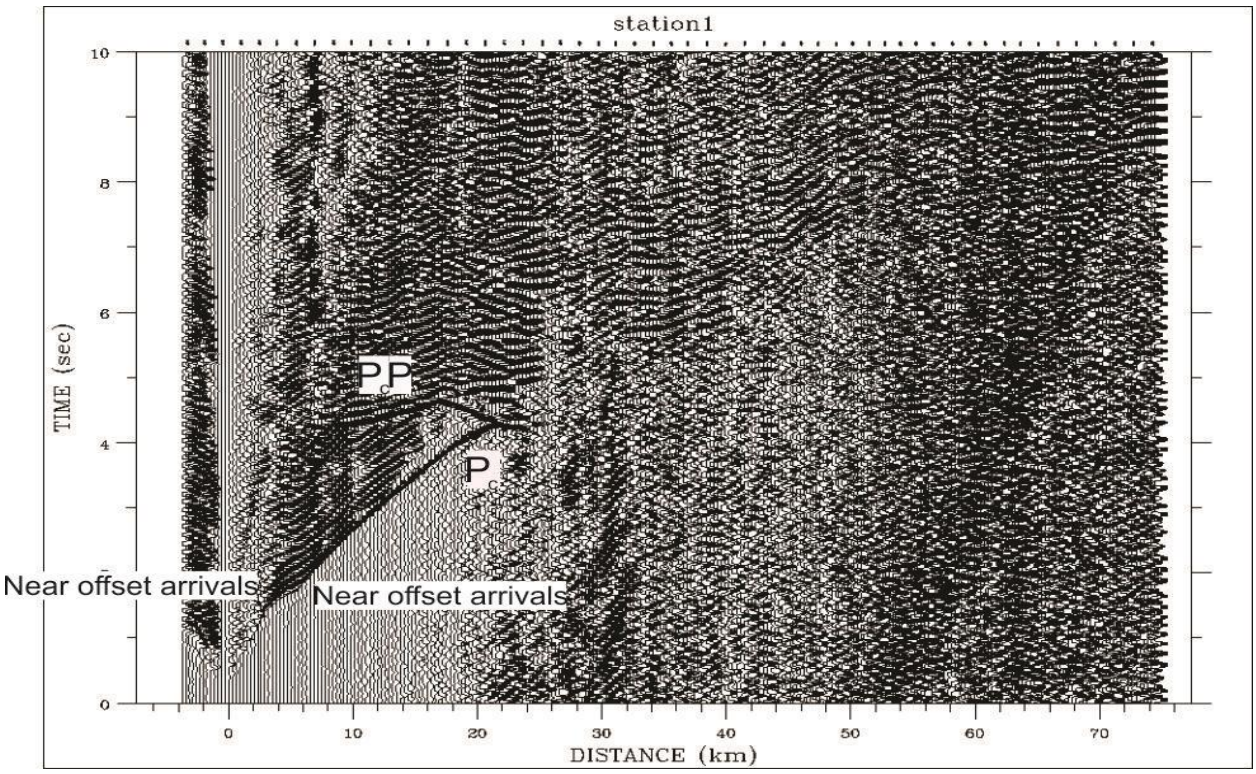

Figure D3 Vertical component record section for OBS 1 with computed travel times, P_cP = observed reflection arrival times and P_c= refraction travel times.

a)

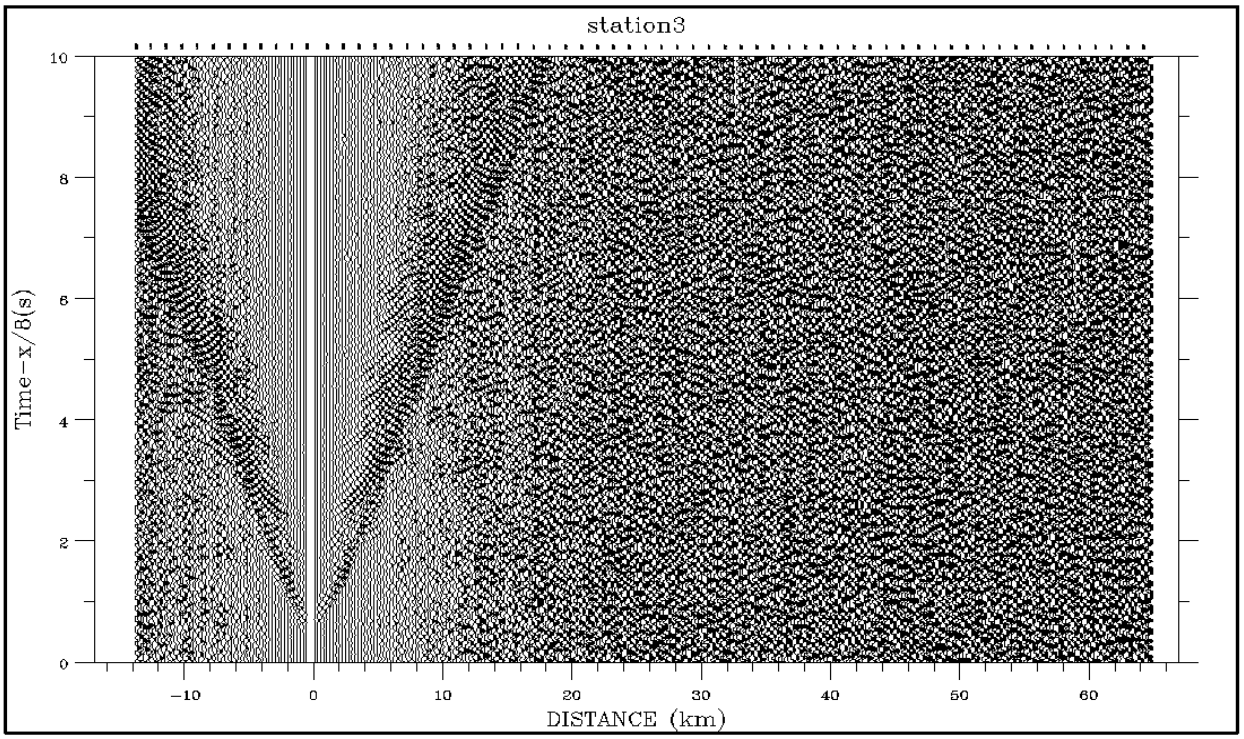

b)

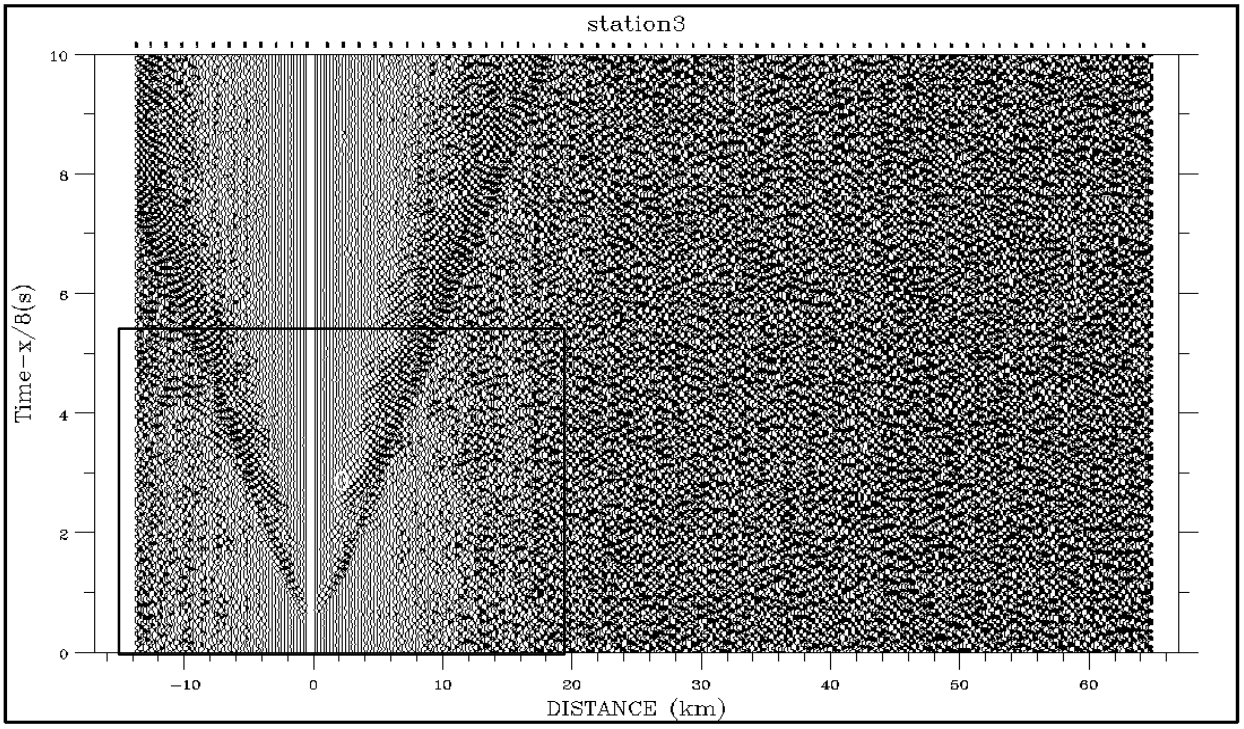

Figure D4 a) Vertical component record section for OBS 3 before any processing, b) Vertical component record section for OBS 3, after band pass filtered (4-10Hz) and applying coherency filter

a)

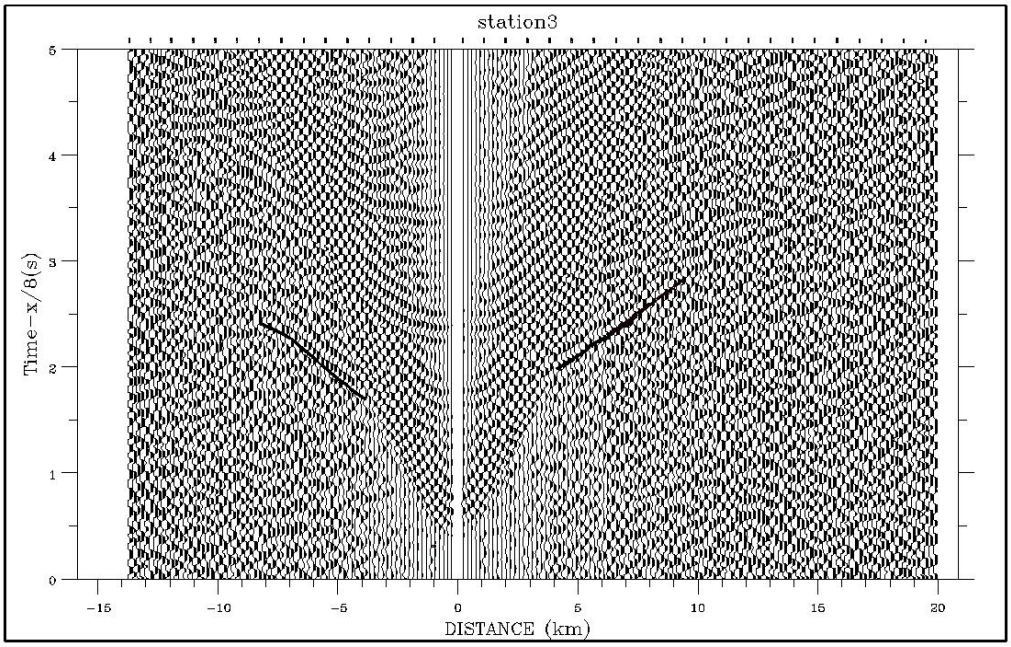

b)

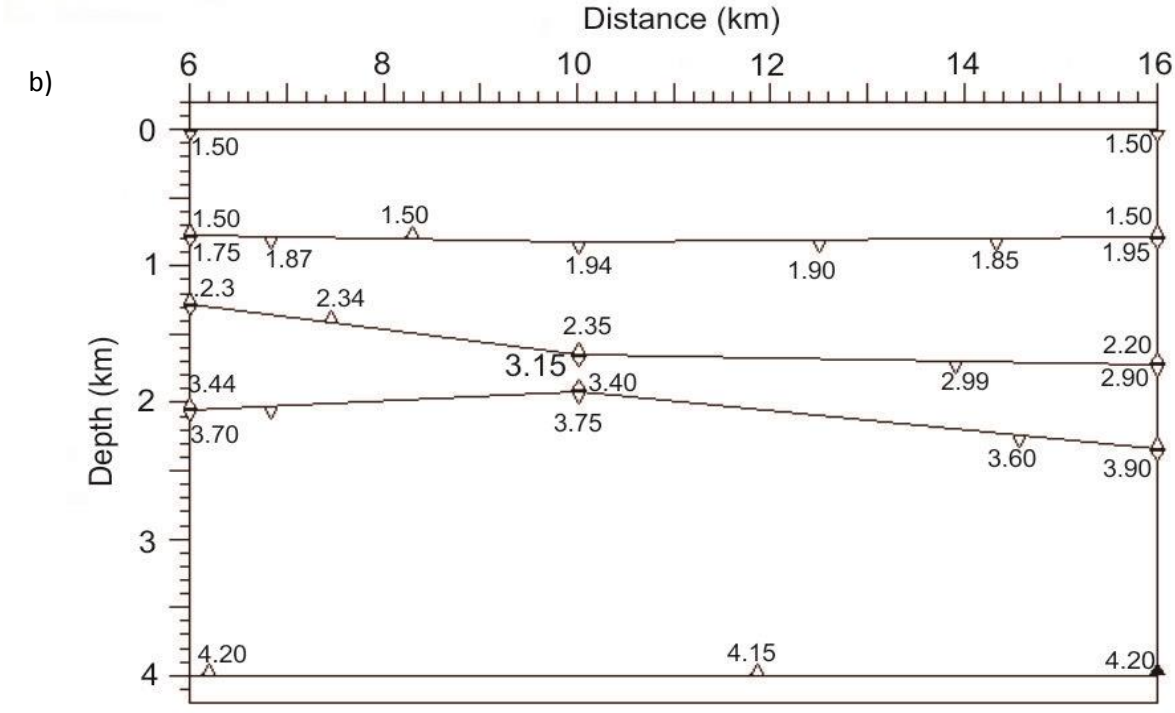

Figure D5 a) Close-up plot for the Short offset range (±20 km) of OBS 3 (indicated in D4b by rectangle), b) Short range shallow velocity model of OBS 3, the numbers indicate the assigned velocity values to each velocity node in the model

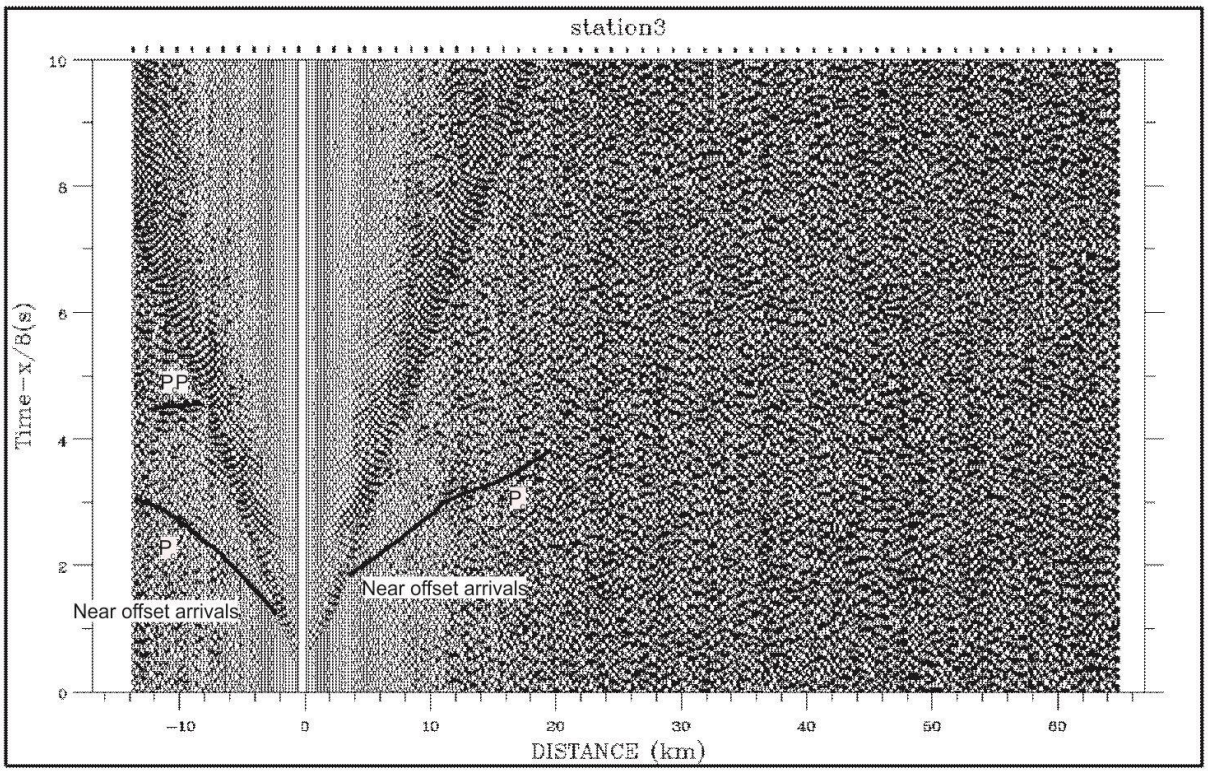

Figure D6 Vertical component record section for OBS 3 with computed travel times, P_cP = observed reflection arrival times and P_c= refraction travel times.

a)

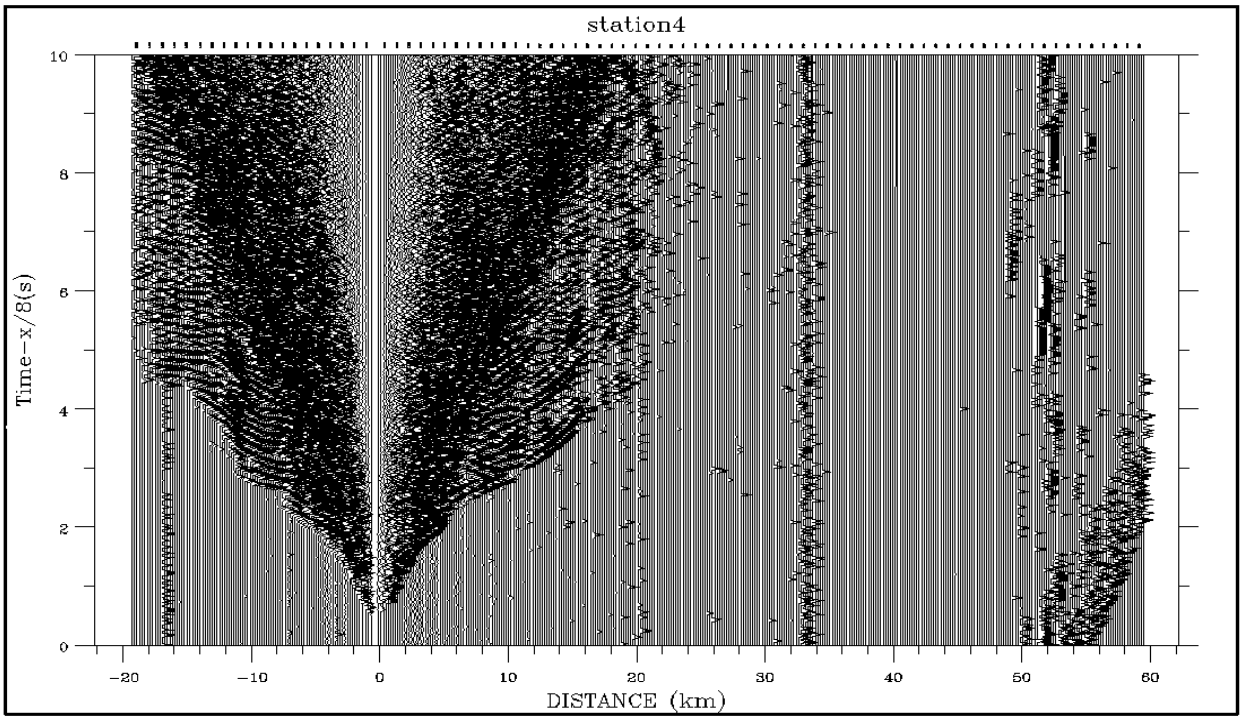

b)

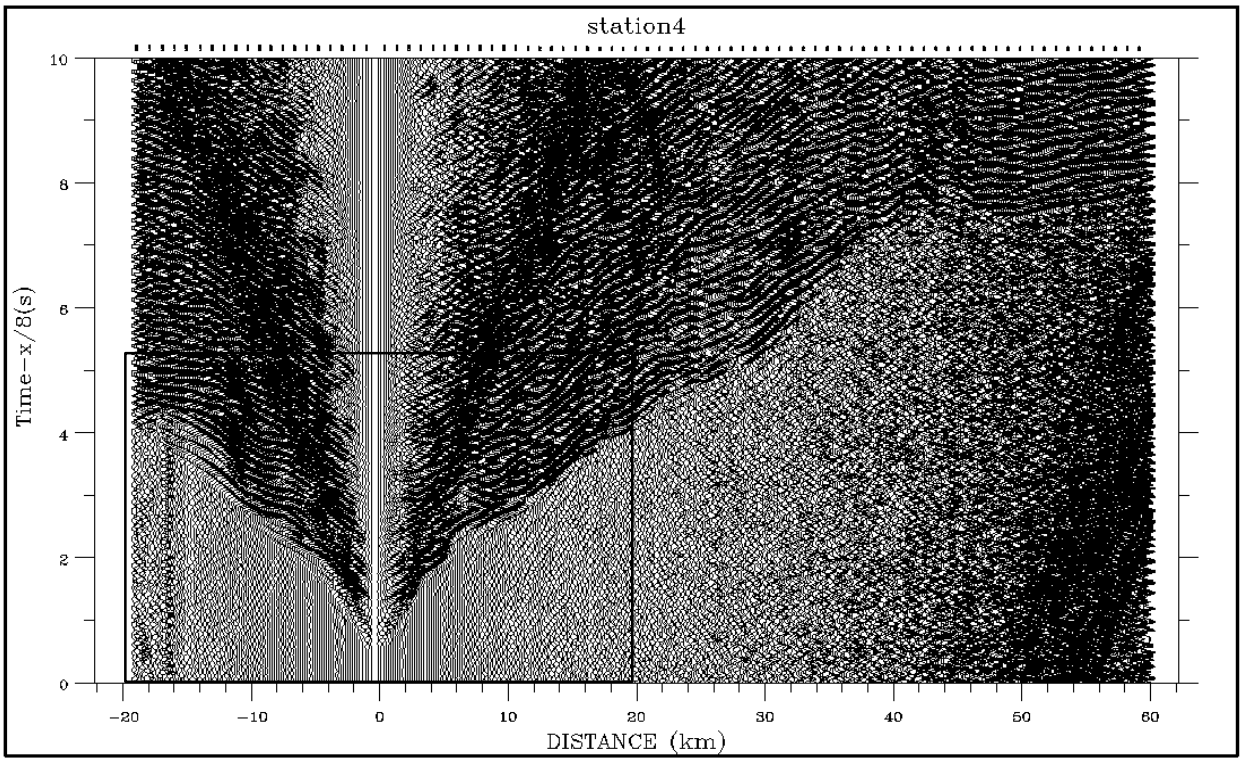

Figure D7 a) Vertical component record section for OBS 4 before any processing, b) Vertical component record section for OBS 4, after band pass filtered (4-10Hz) and applying coherency filter

a)

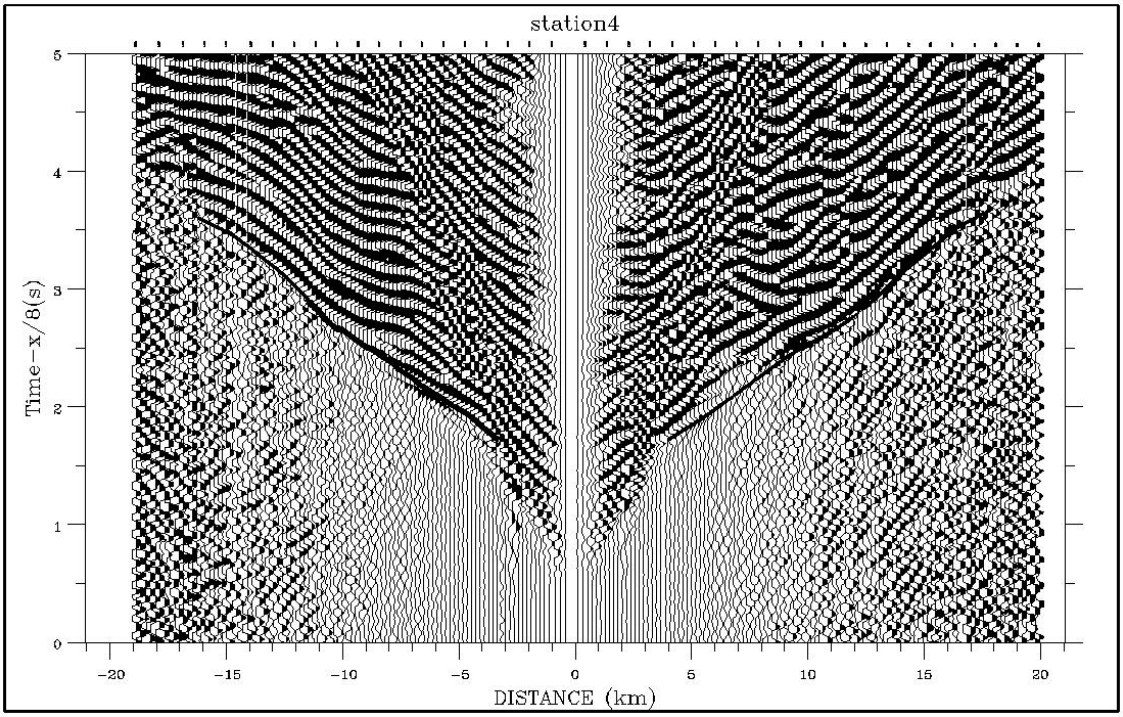

b)

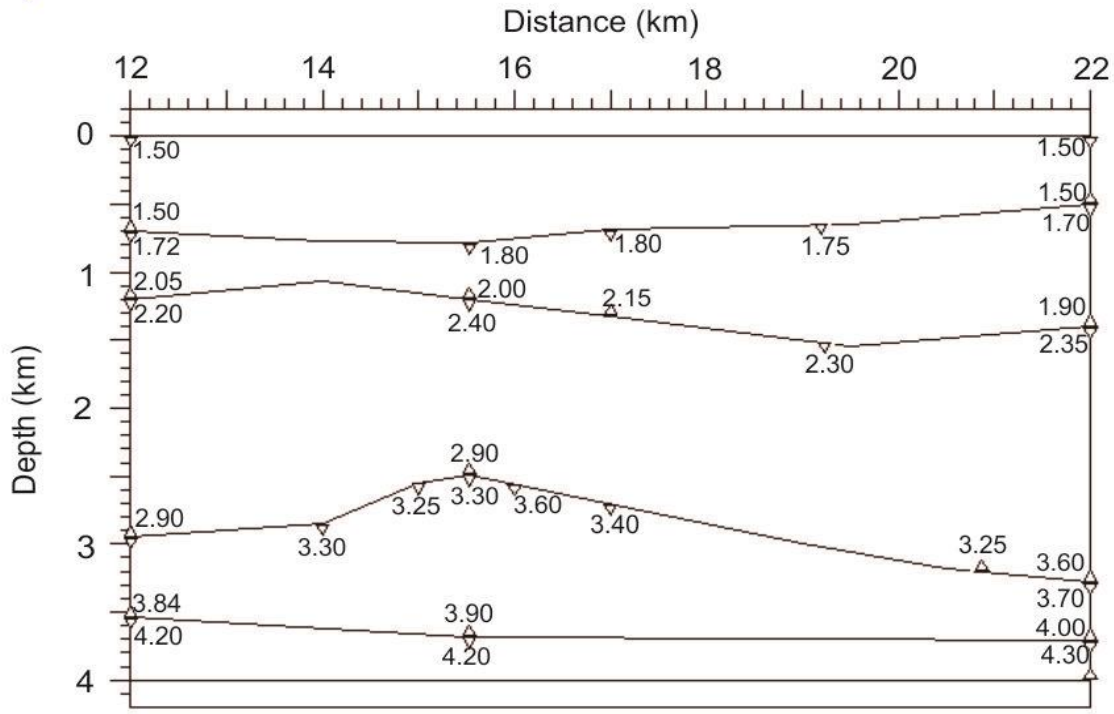

Figure D8 a) Close-up plot for the Short offset range (±20 km) of OBS 4 (indicated in D7b by rectangle), b) Short range shallow velocity model of OBS 4, the numbers indicate the assigned velocity values to each velocity node in the model

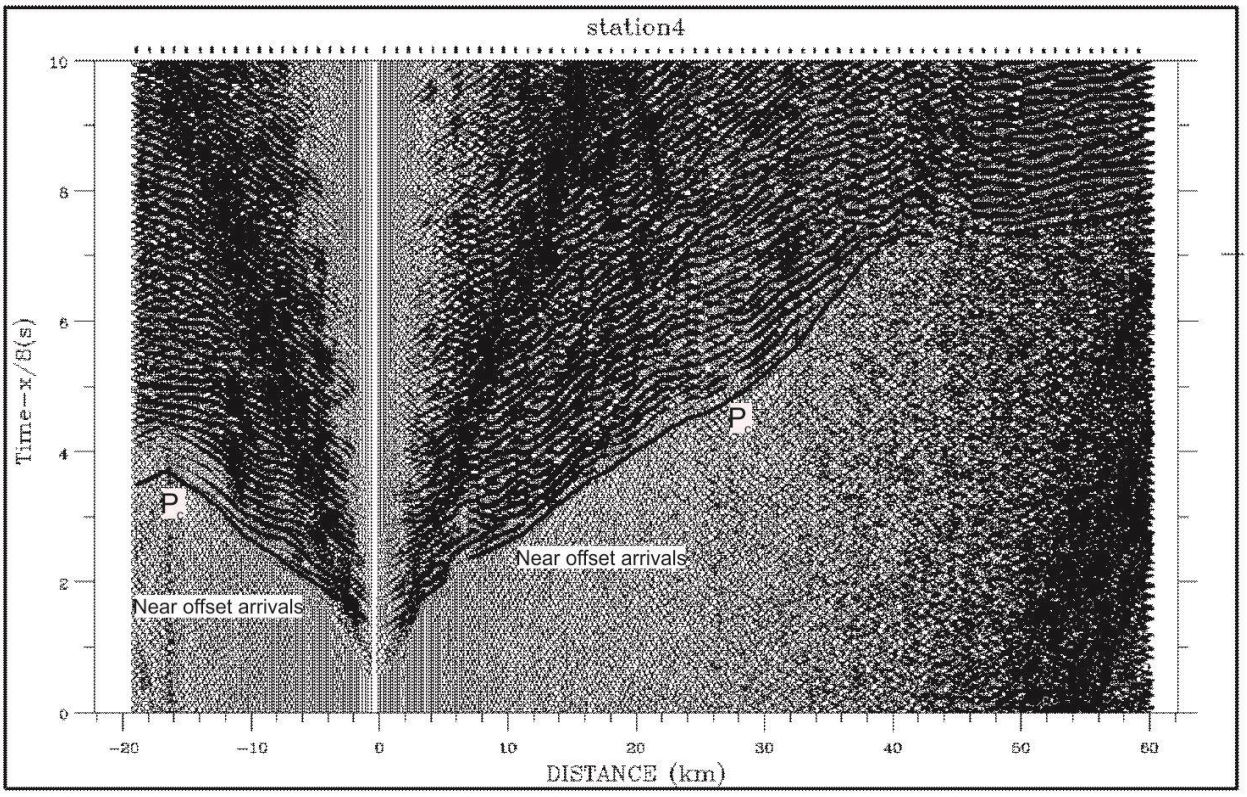

Figure D9 Vertical component record section for OBS 4 with computed refraction travel times (P_c)

a)

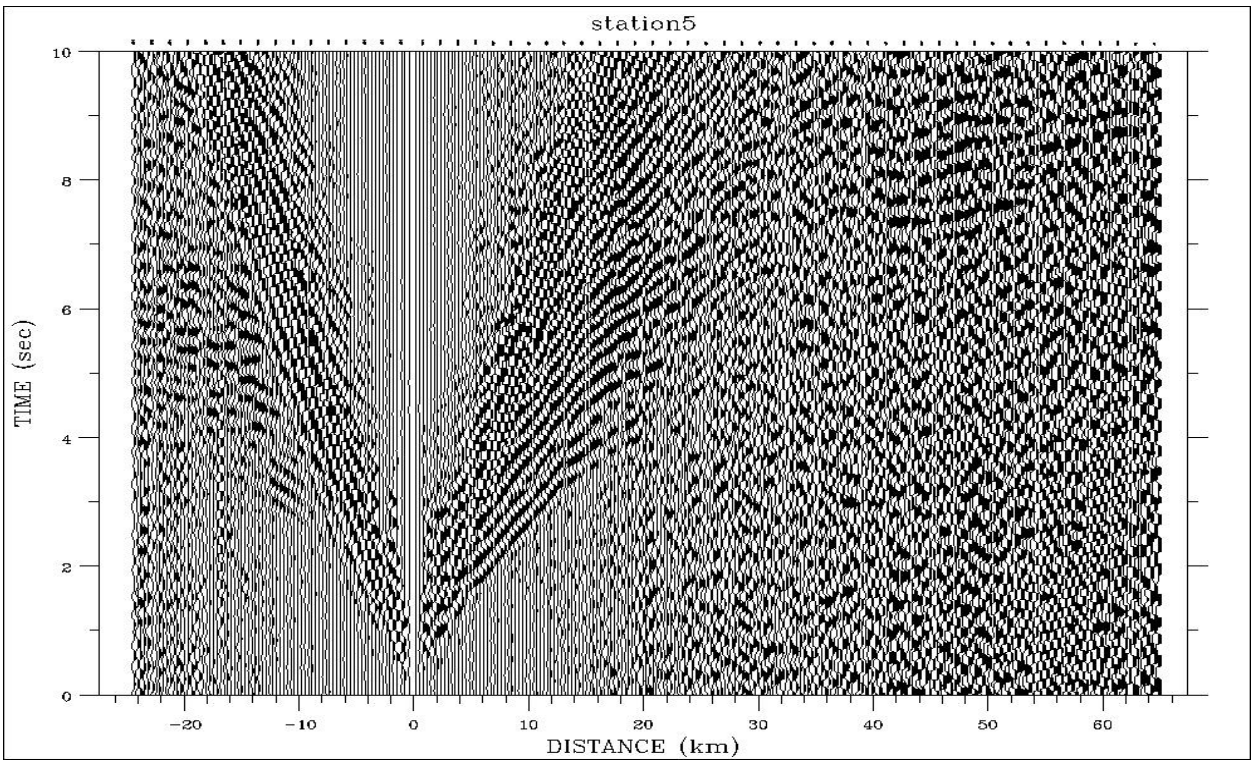

b)

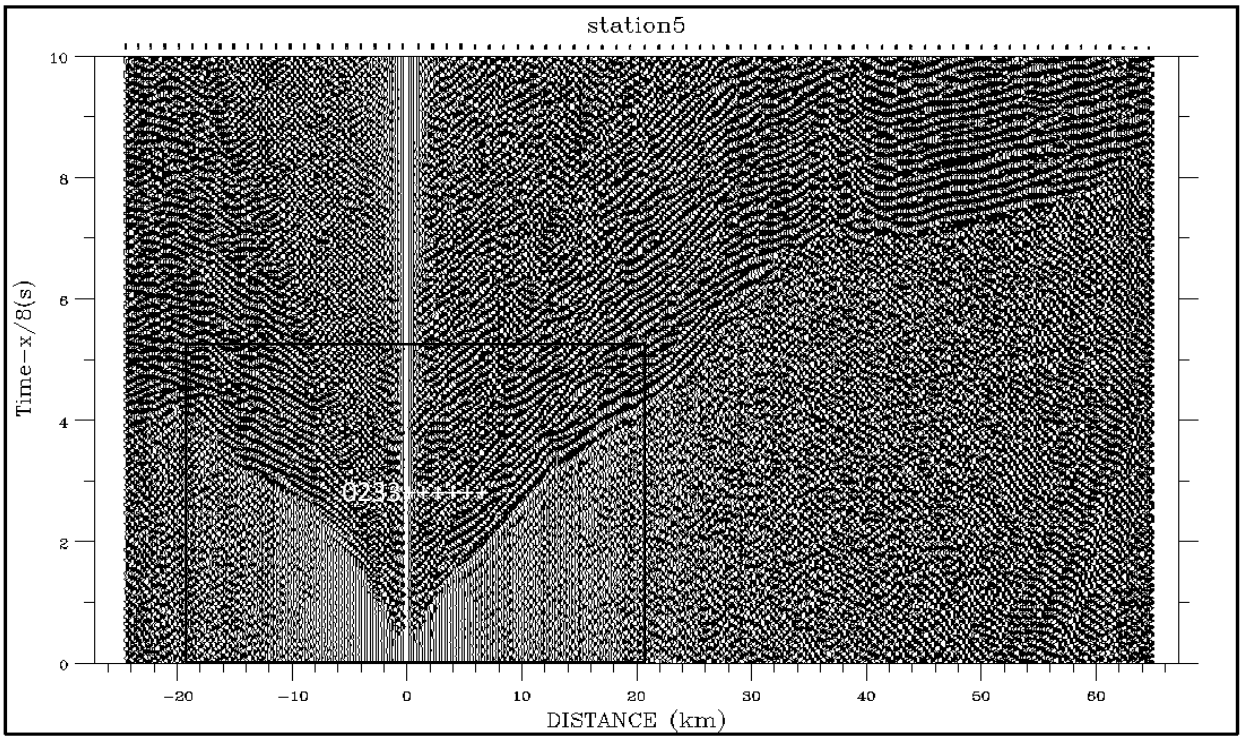

Figure D10 a) Vertical component record section for OBS 1 before any processing, b) Vertical component record section for OBS 1, after band pass filtered (4-10Hz) and applying coherency filter

a)

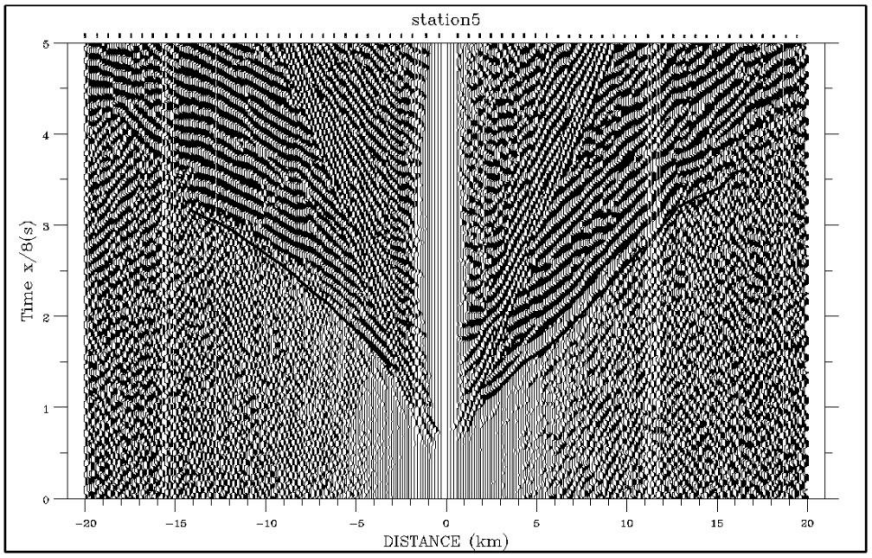

b)

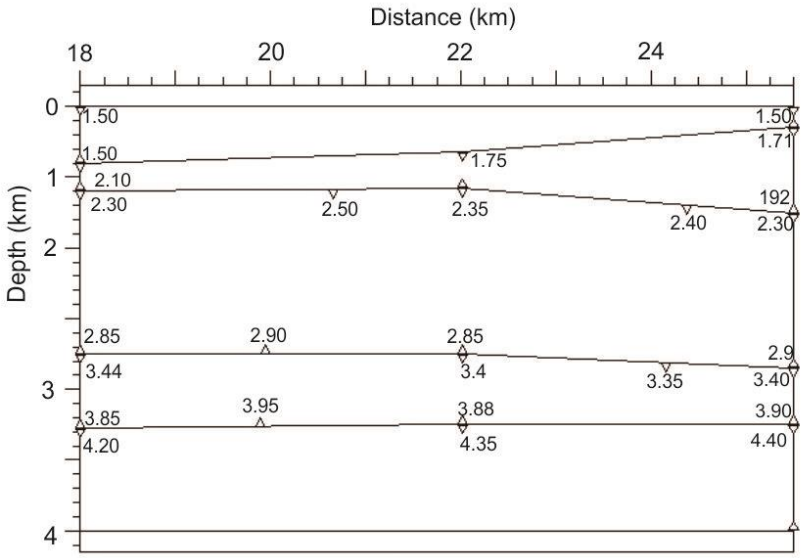

Figure D11 a) Close-up plot for the Short offset range ($\pm$20 km) of OBS 5 (indicated in D10b by rectangle), b) Short range shallow velocity model of OBS 5, the numbers indicate the assigned velocity values to each velocity node in the model

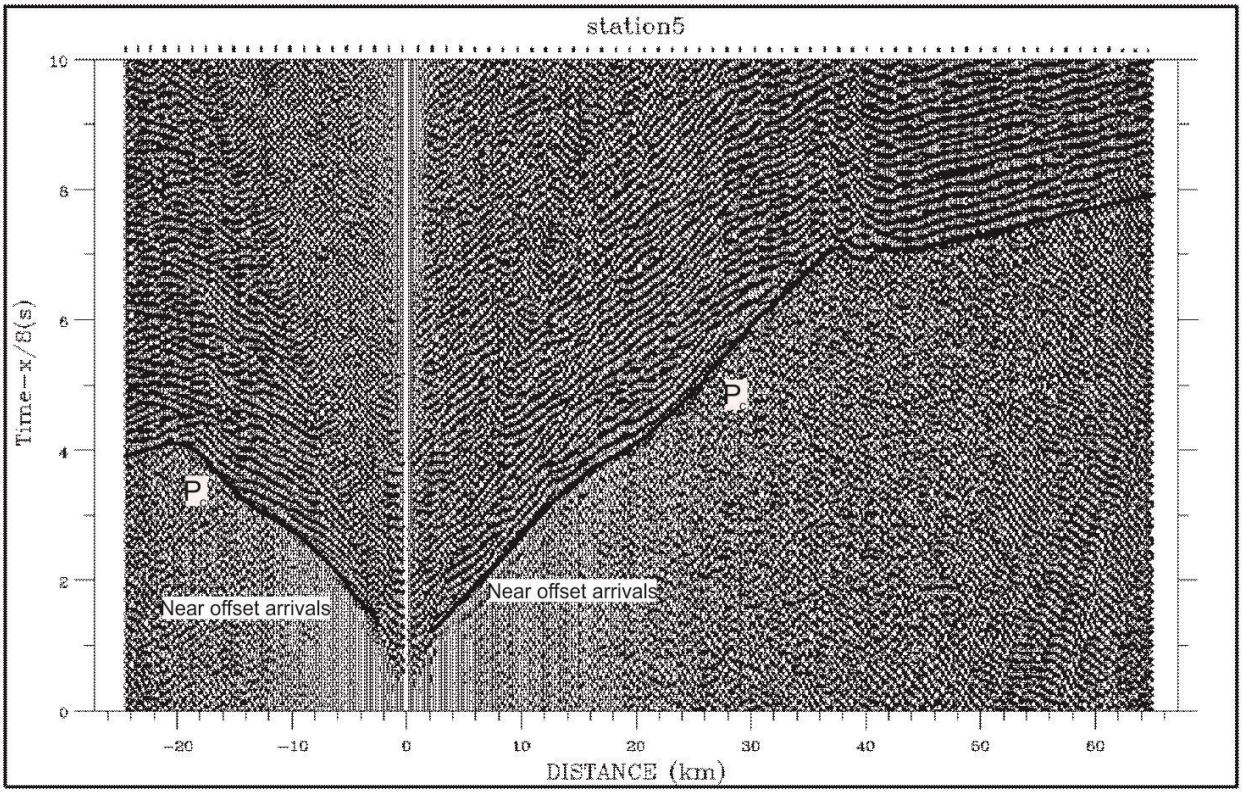

Figure D12 Vertical component record section for OBS 5 with computed refraction travel times (P_c)

a)

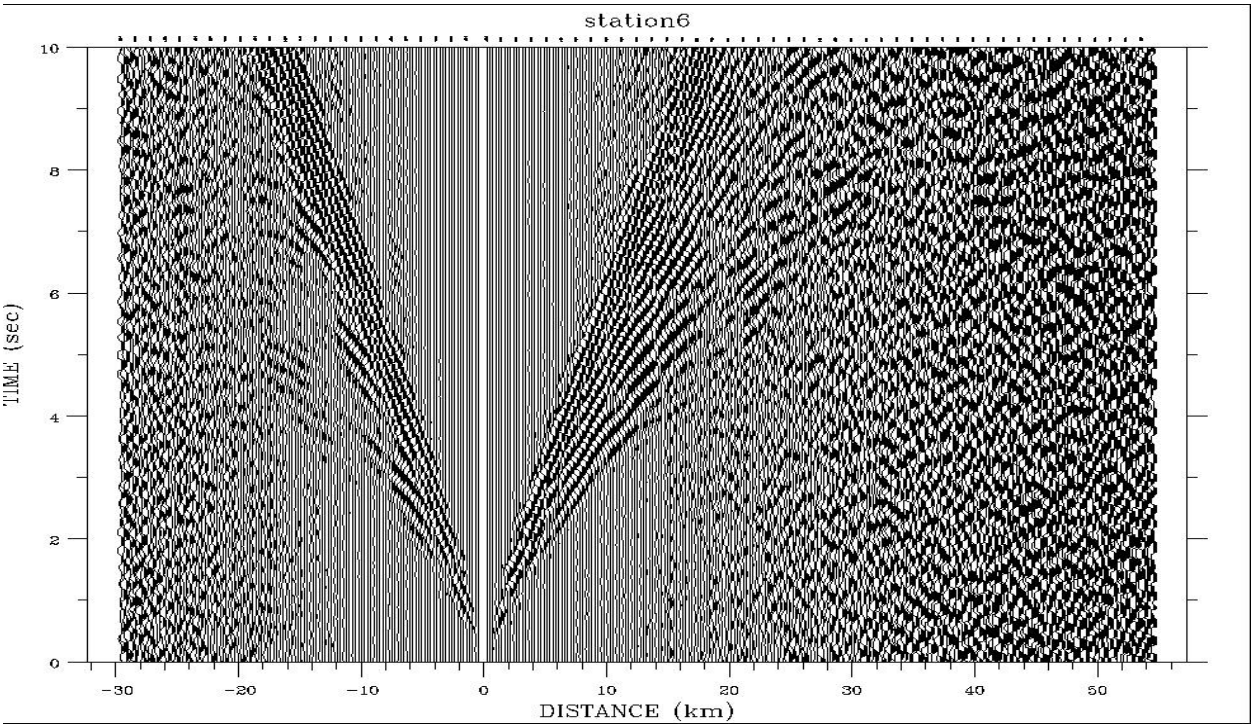

b)

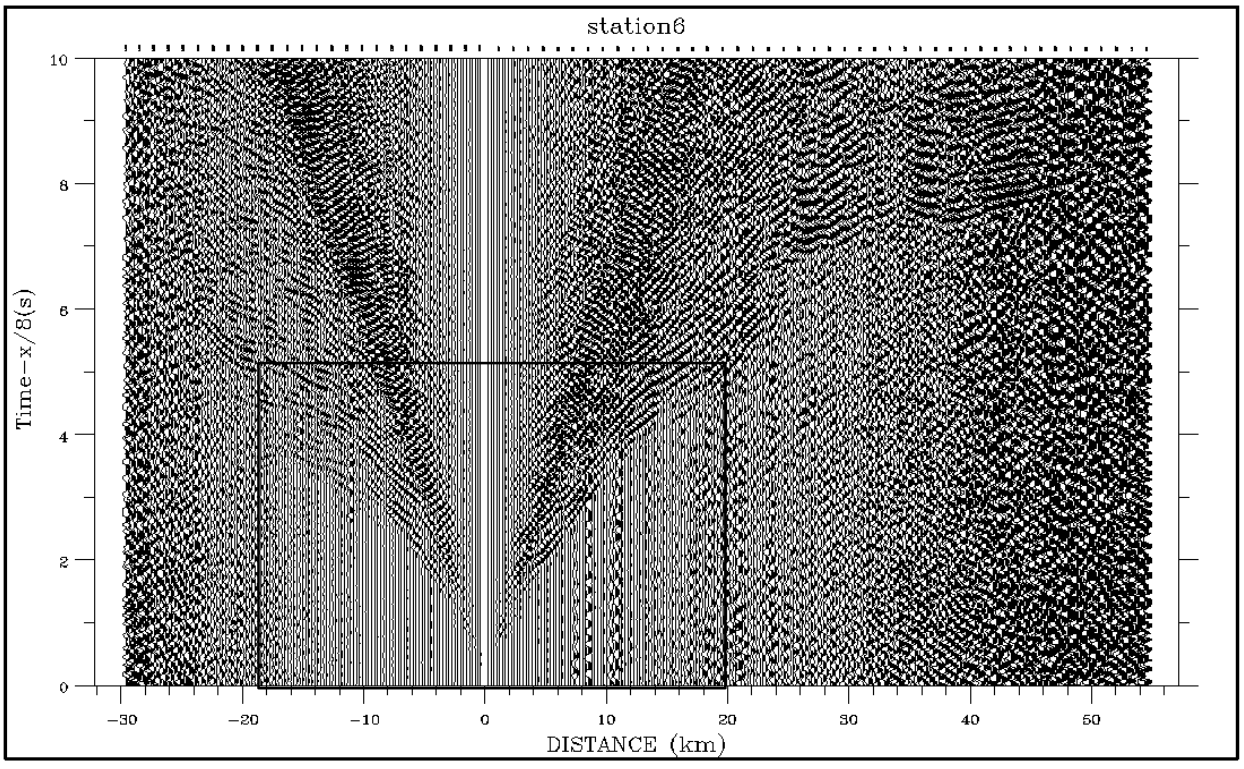

Figure D13 a) Vertical component record section for OBS 6 before any processing, b) Vertical component record section for OBS 6, after band pass filtered (4-10Hz) and applying coherency filter

a)

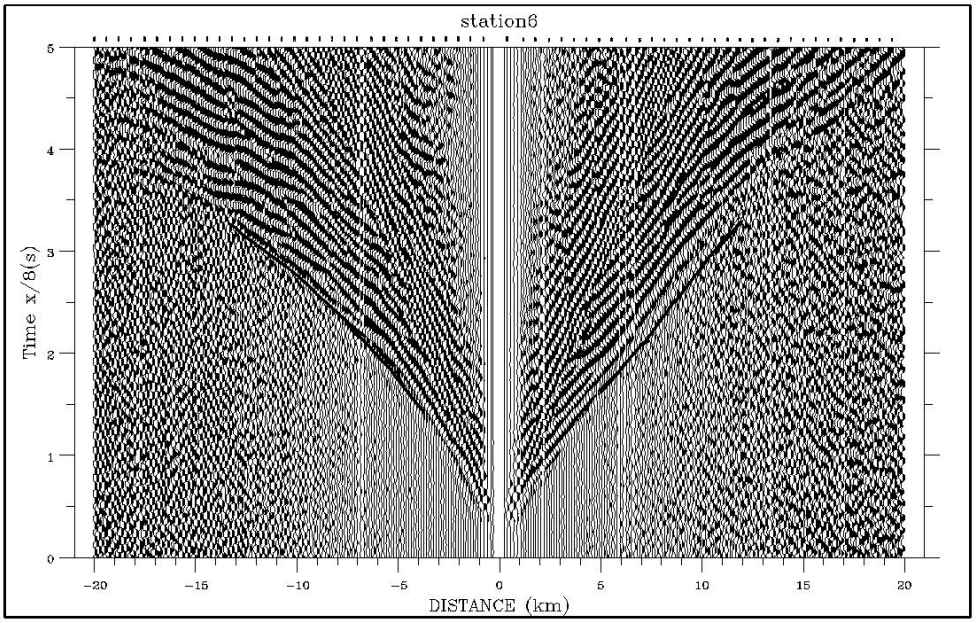

b)

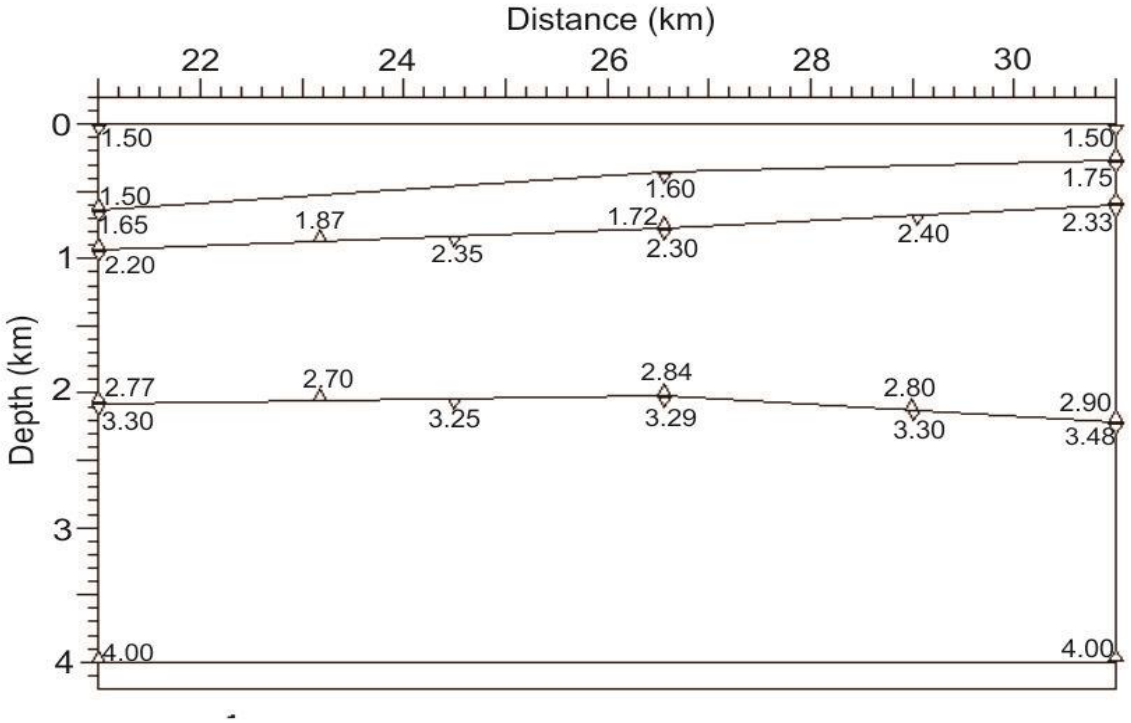

Figure D14 a) Close-up plot for the Short offset range ($\pm$20 km) of OBS 6 (indicated in D13b by rectangle), b) Short range shallow velocity model of OBS 6, the numbers indicate the assigned velocity values to each velocity node in the model

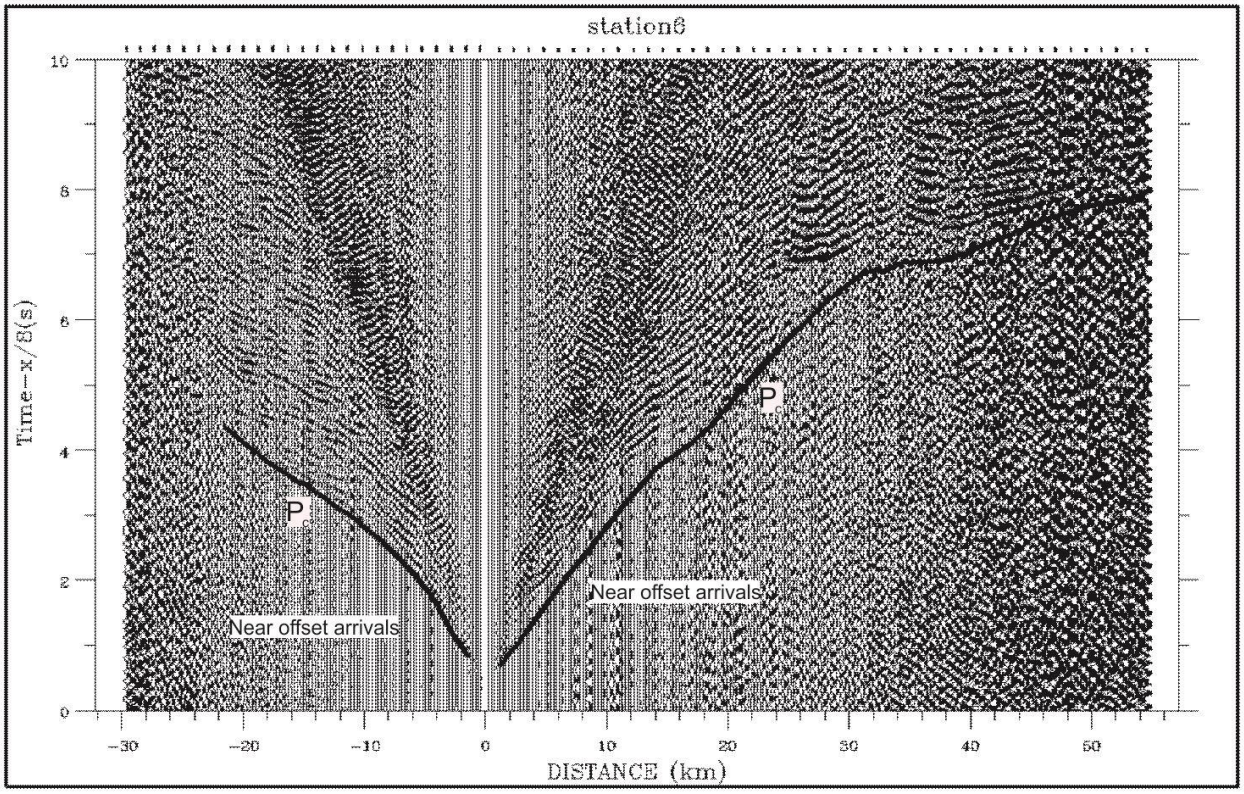

Figure D15 Vertical component record section for OBS 6 with computed refraction travel times (P_c)

a)

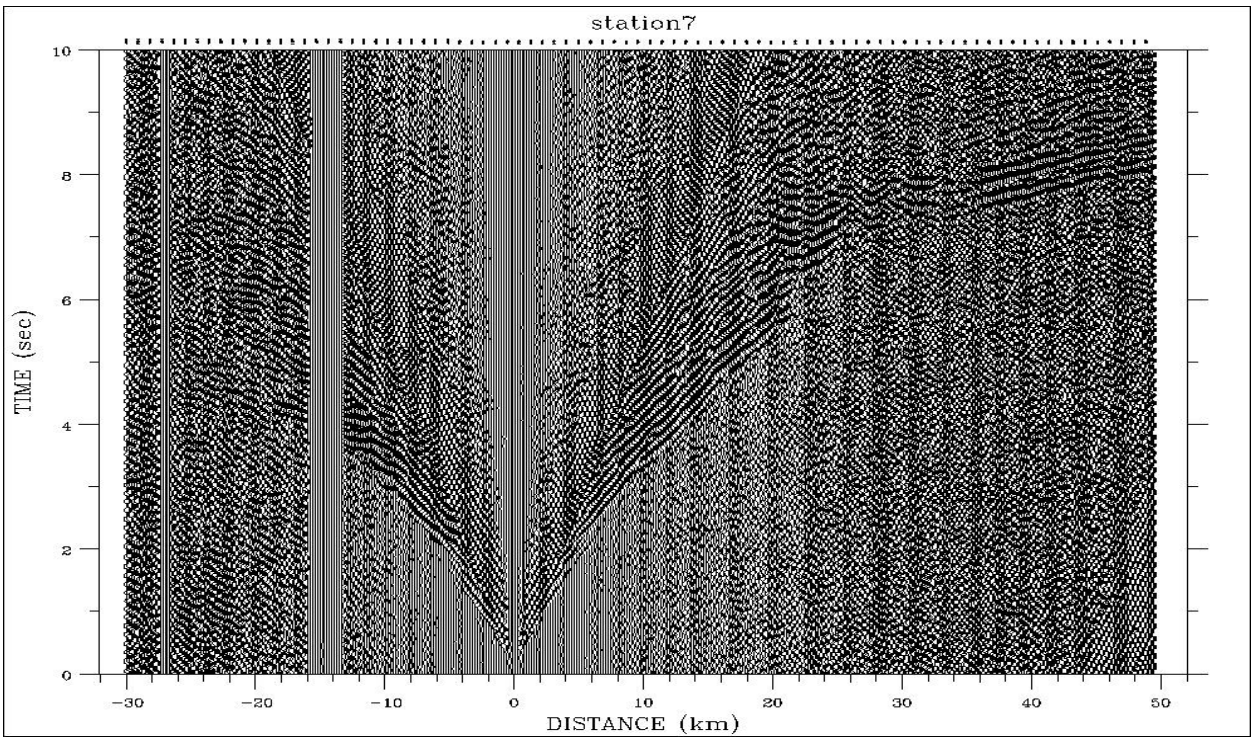

b)

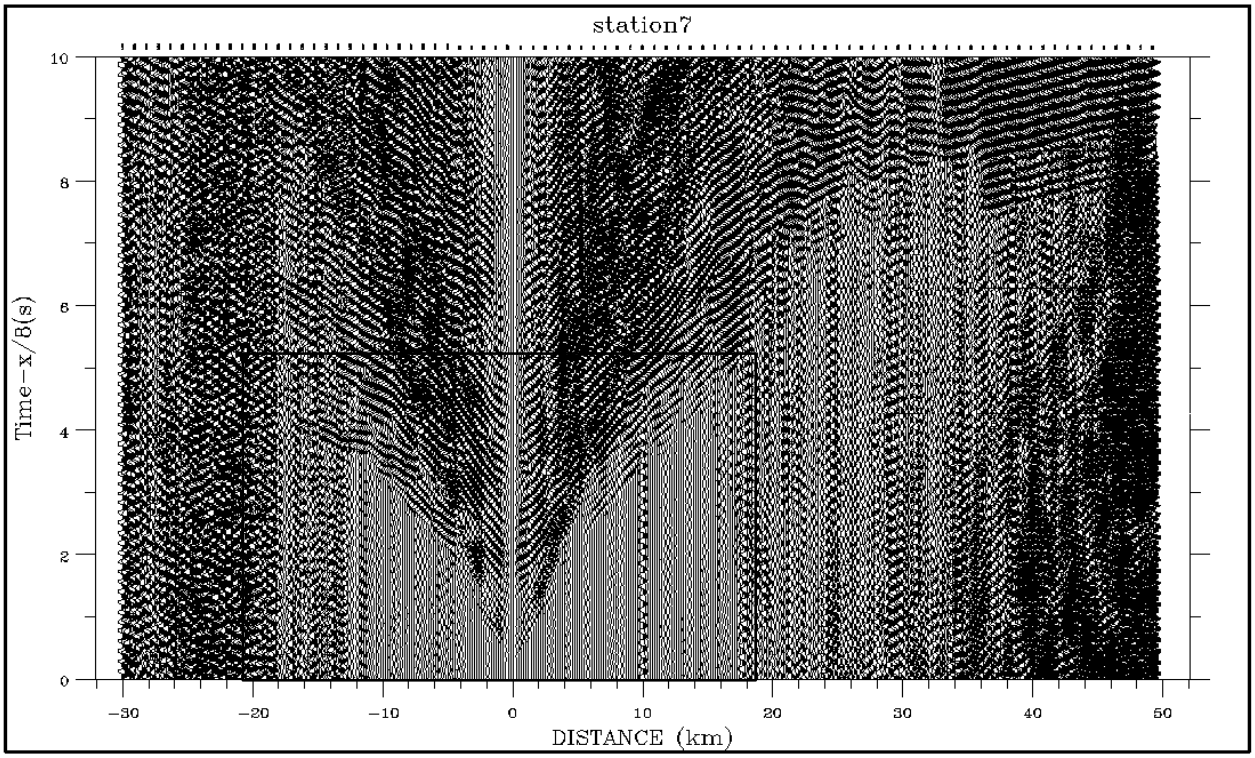

Figure D16 a) Vertical component record section for OBS 7 before any processing, b) Vertical component record section for OBS 7, after band pass filtered (4-10Hz) and applying coherency filter

a)

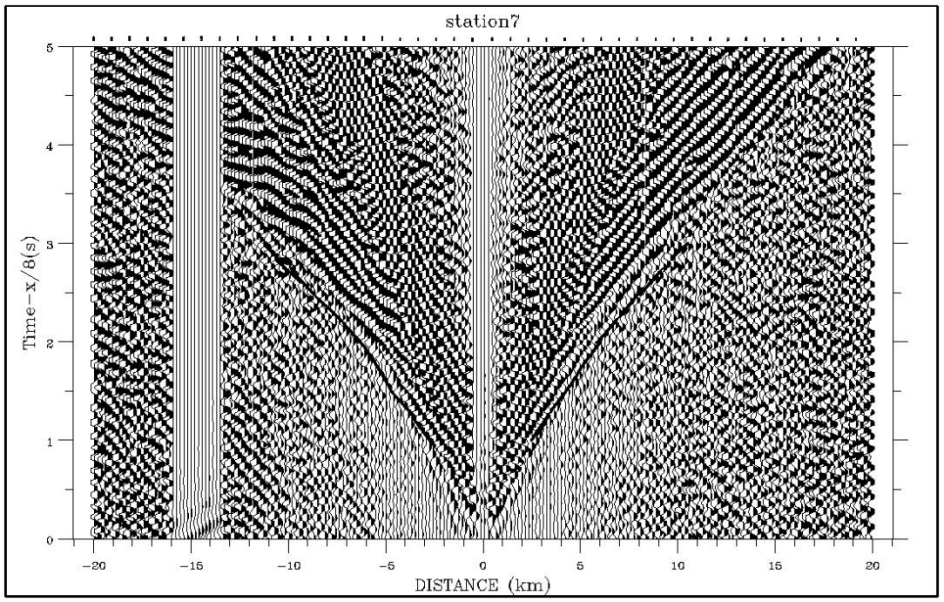

b)

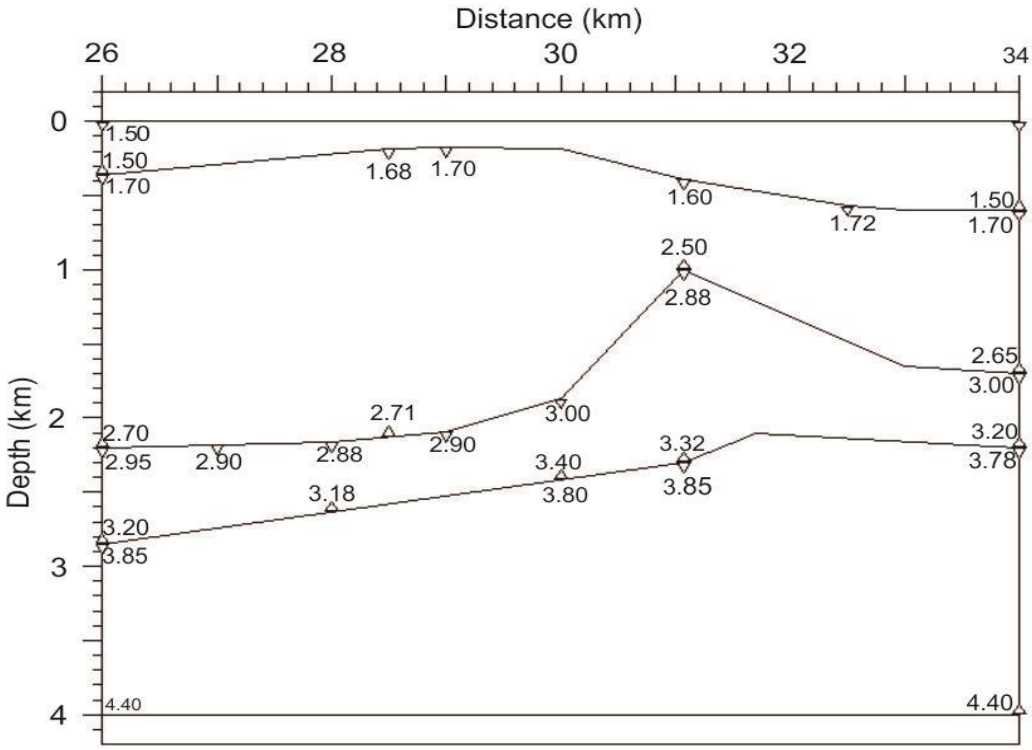

Figure D17 a) Close-up plot for the Short offset range ($\pm$20 km) of OBS 7 (indicated in D16b by rectangle), b) Short range shallow velocity model of OBS 7, the numbers indicate the assigned velocity values to each velocity node in the model

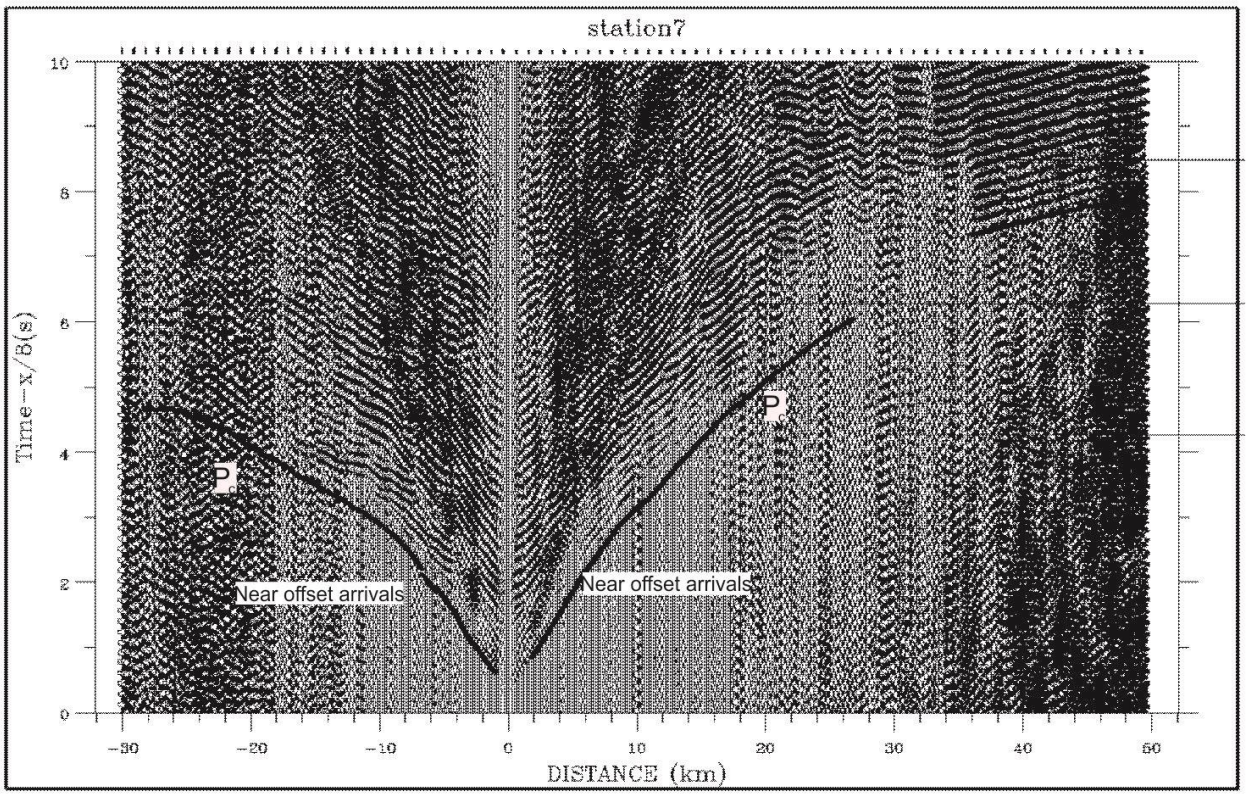

Figure D18 Vertical component record section for OBS 7 with computed refraction travel times (P_c)

a)

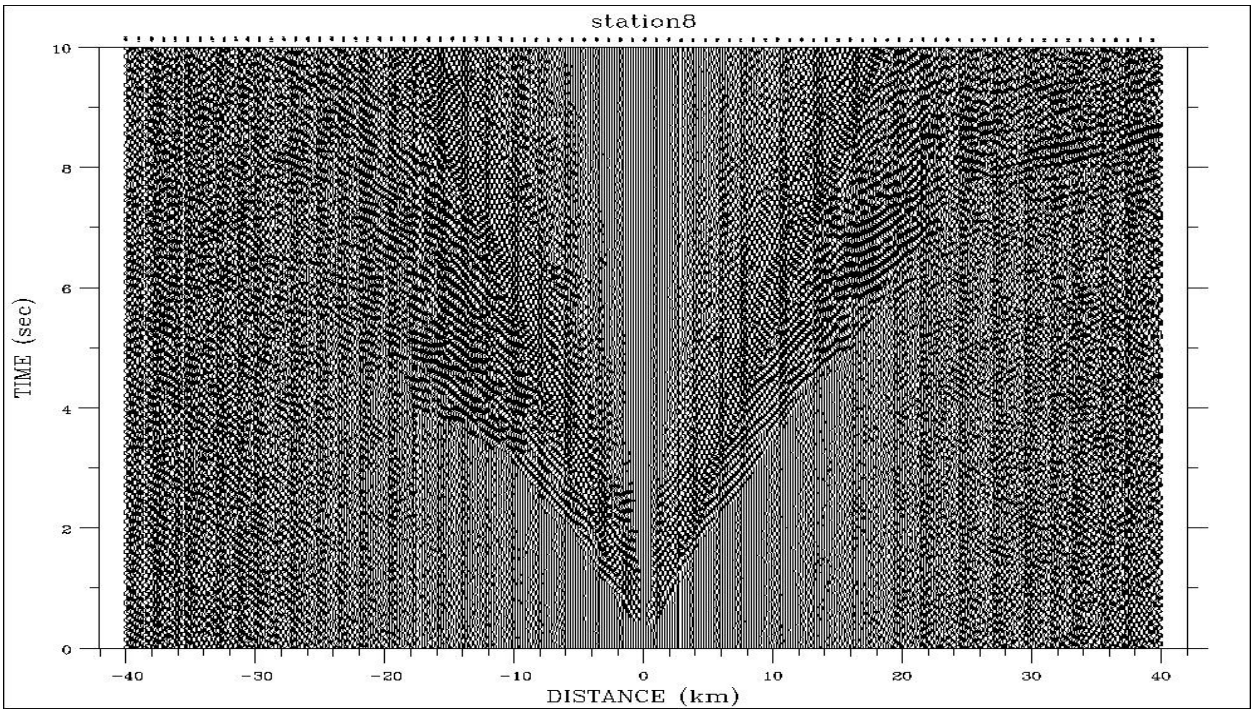

b)

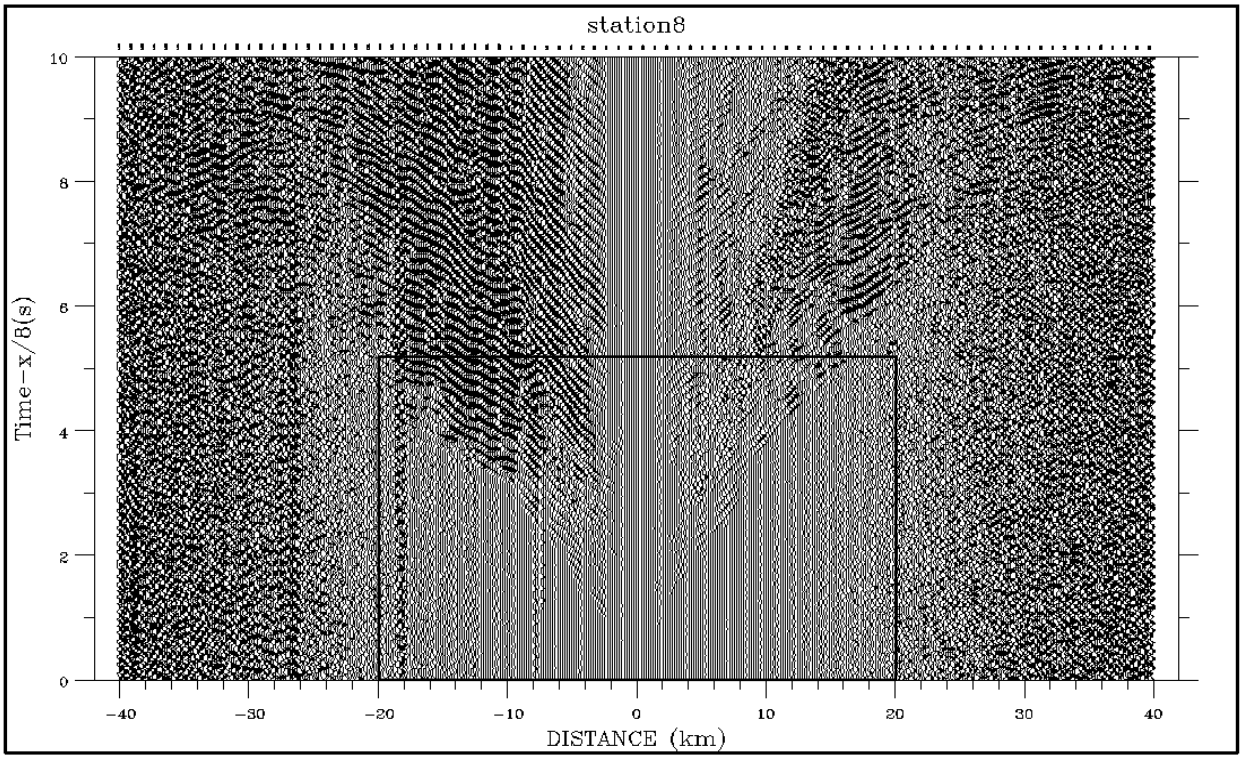

Figure D19 a) Vertical component record section for OBS 8 before any processing, b) Vertical component record section for OBS 8, after band pass filtered (4-10Hz) and applying coherency filter

a)

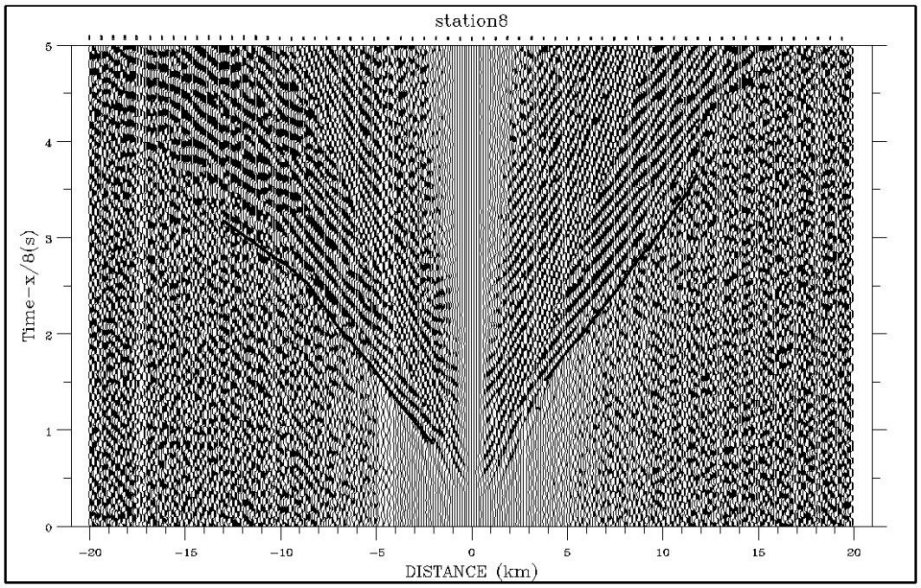

b)

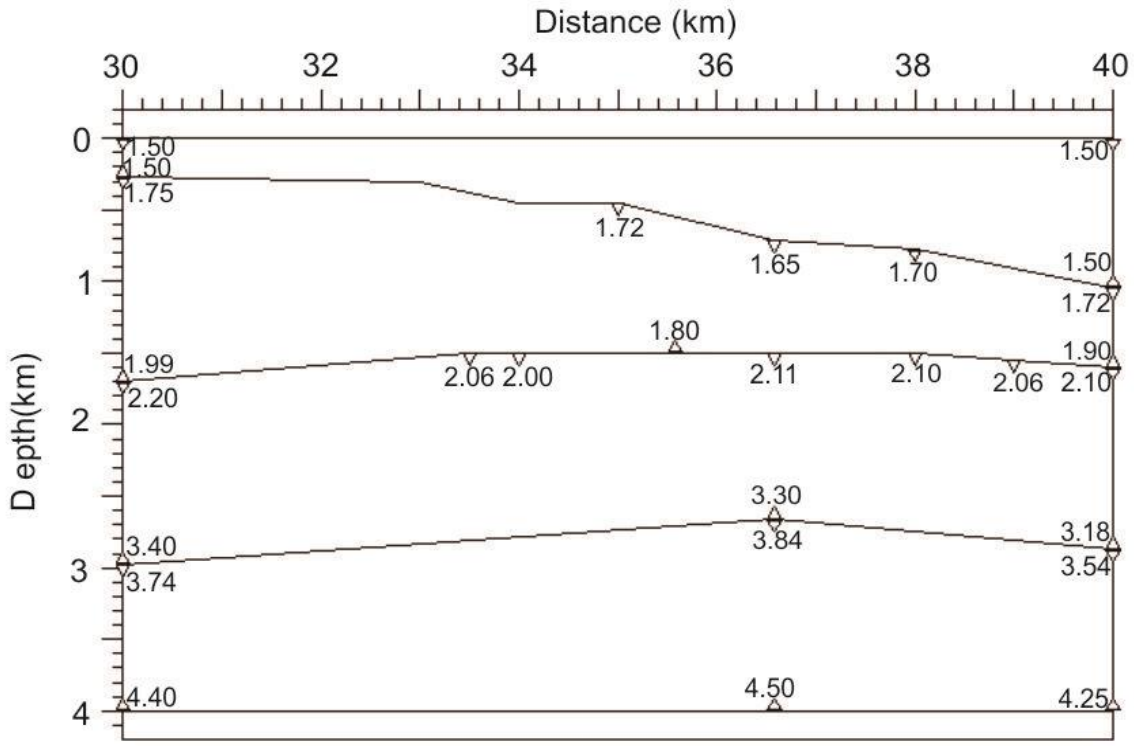

Figure D20 a) Close-up plot for the Short offset range ($\pm$20 km) of OBS 8 (indicated in D19b by rectangle), b) Short range shallow velocity model of OBS 8, the numbers indicate the assigned velocity values to each velocity node in the model

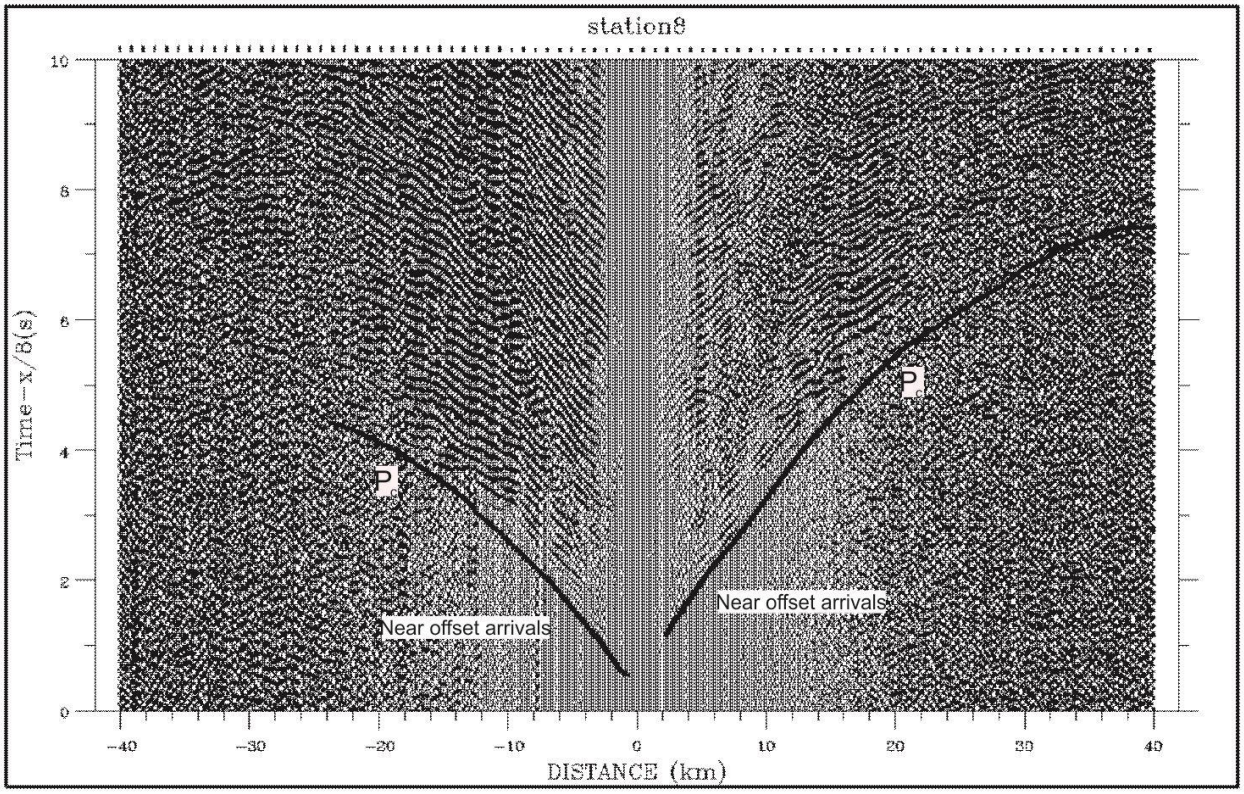

Figure D21 Vertical component record section for OBS 8 with computed refraction travel times (P_c)

a)

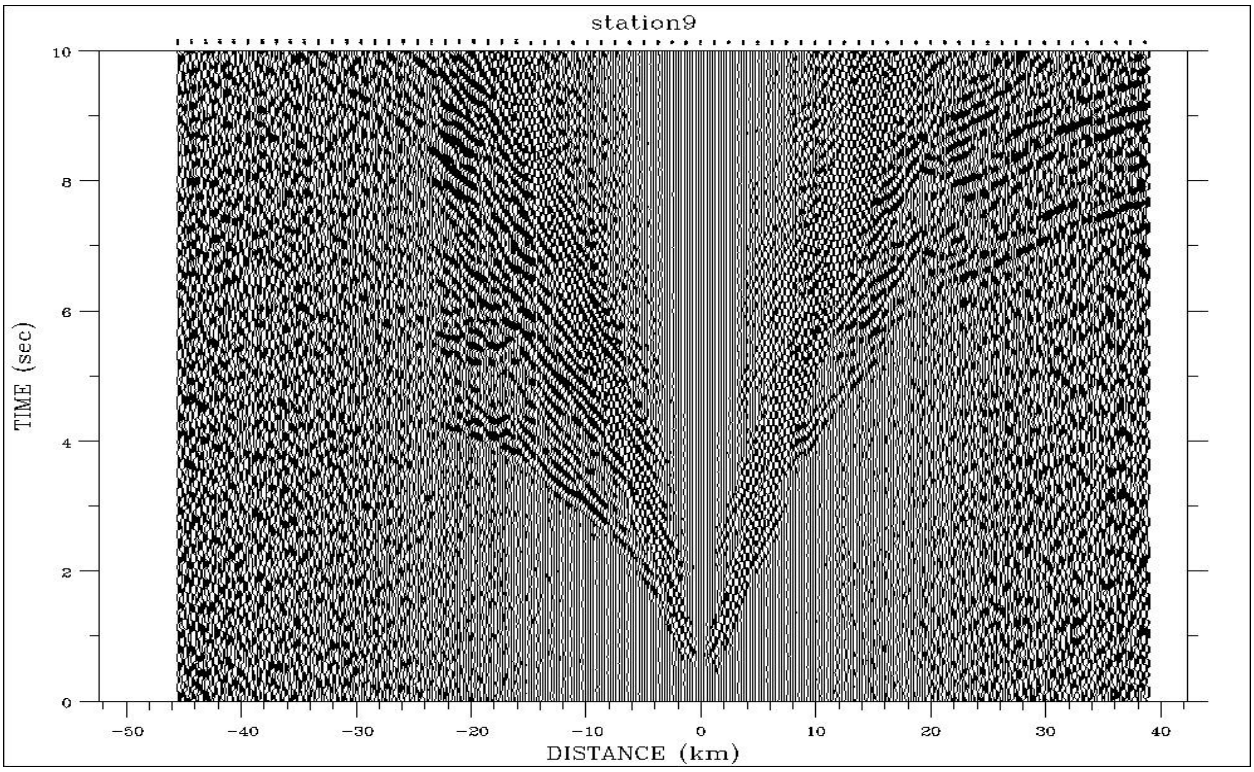

b)

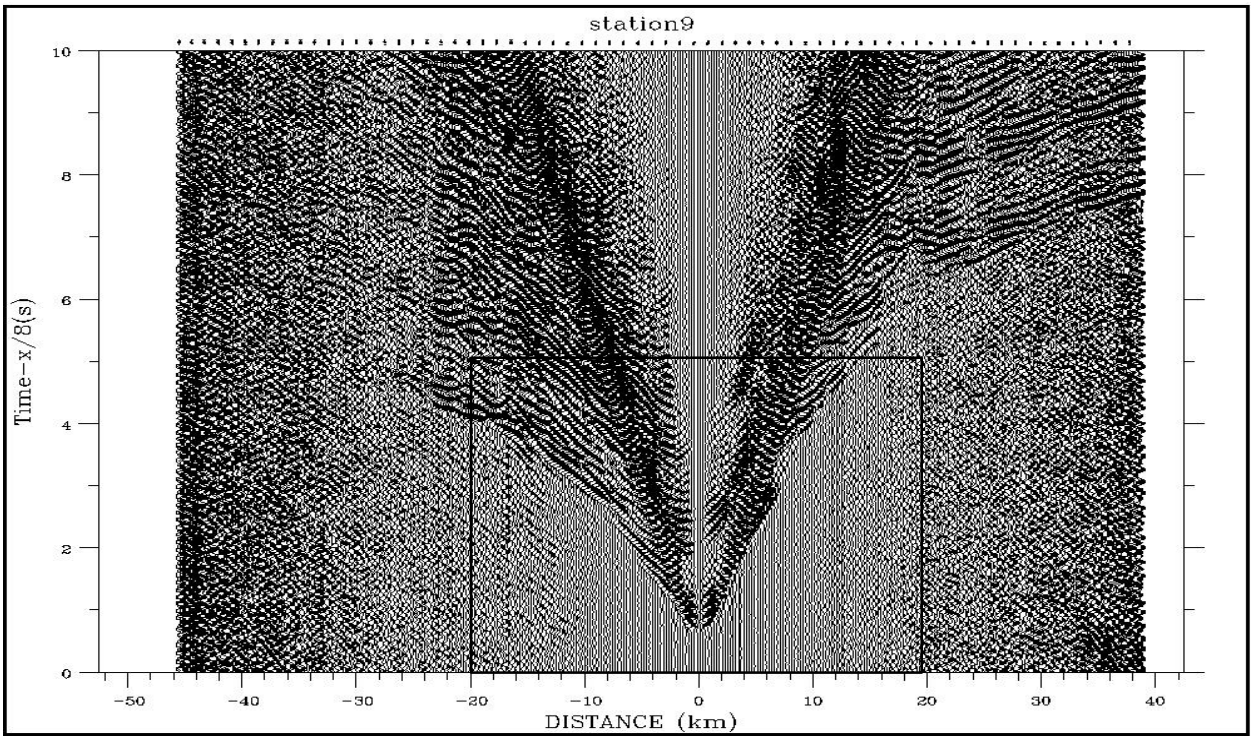

Figure D22 a) Vertical component record section for OBS 9 before any processing, b) Vertical component record section for OBS 9, after band pass filtered (4-10Hz) and applying coherency filter

a)

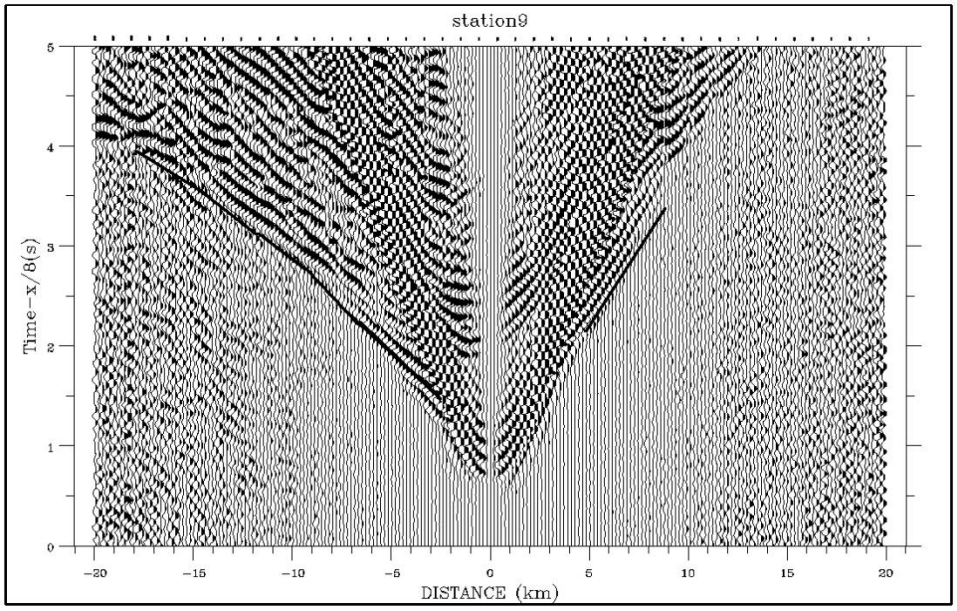

b)

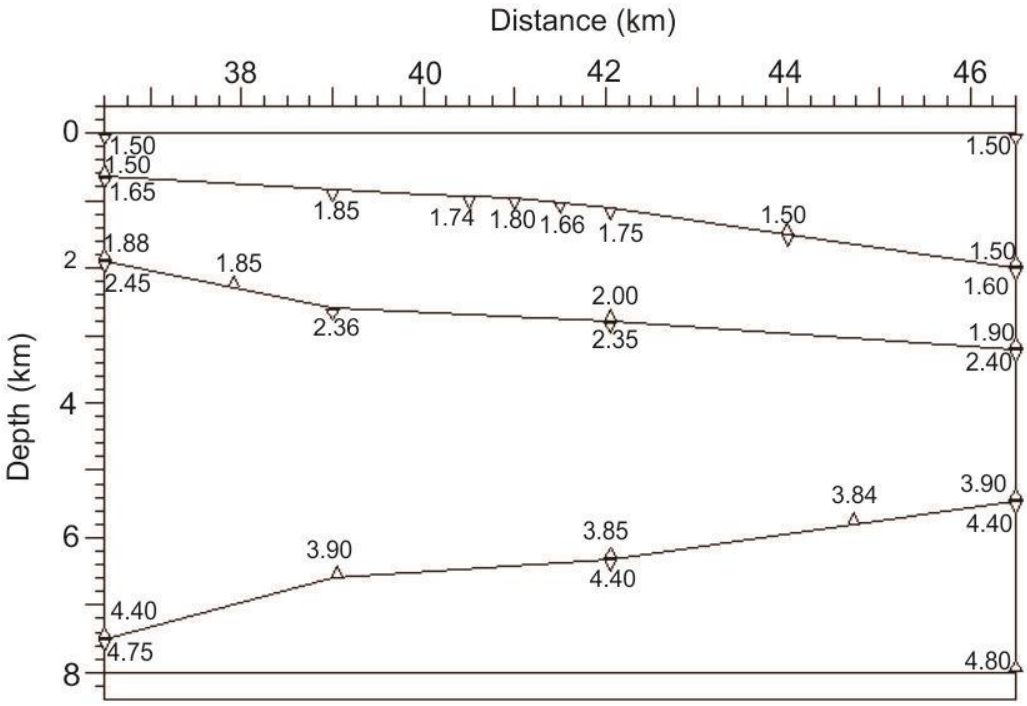

Figure D23 a) Close-up plot for the Short offset range ($\pm$20 km) of OBS 9 (indicated in D22b by rectangle), b) Short range shallow velocity model of OBS 9, the numbers indicate the assigned velocity values to each velocity node in the model

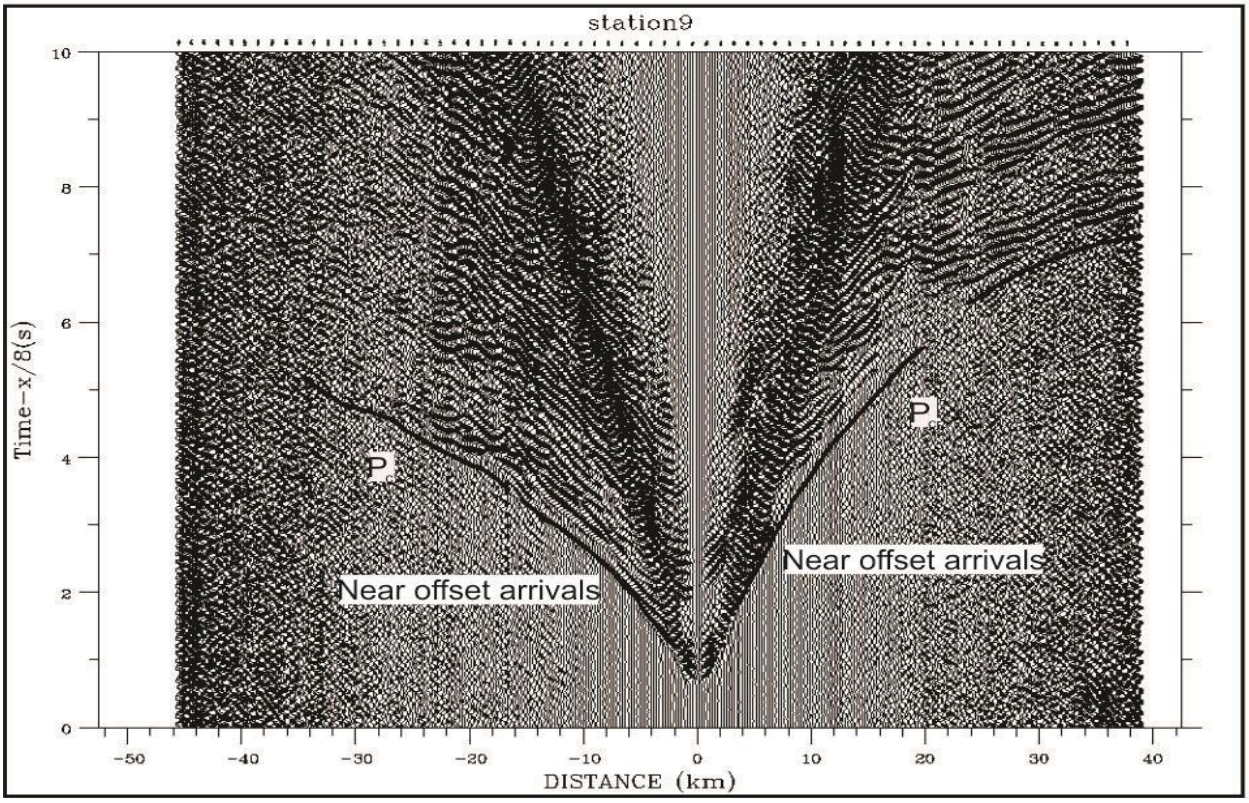

Figure D24 Vertical component record section for OBS 9 with computed refraction travel times (P_c)

a)

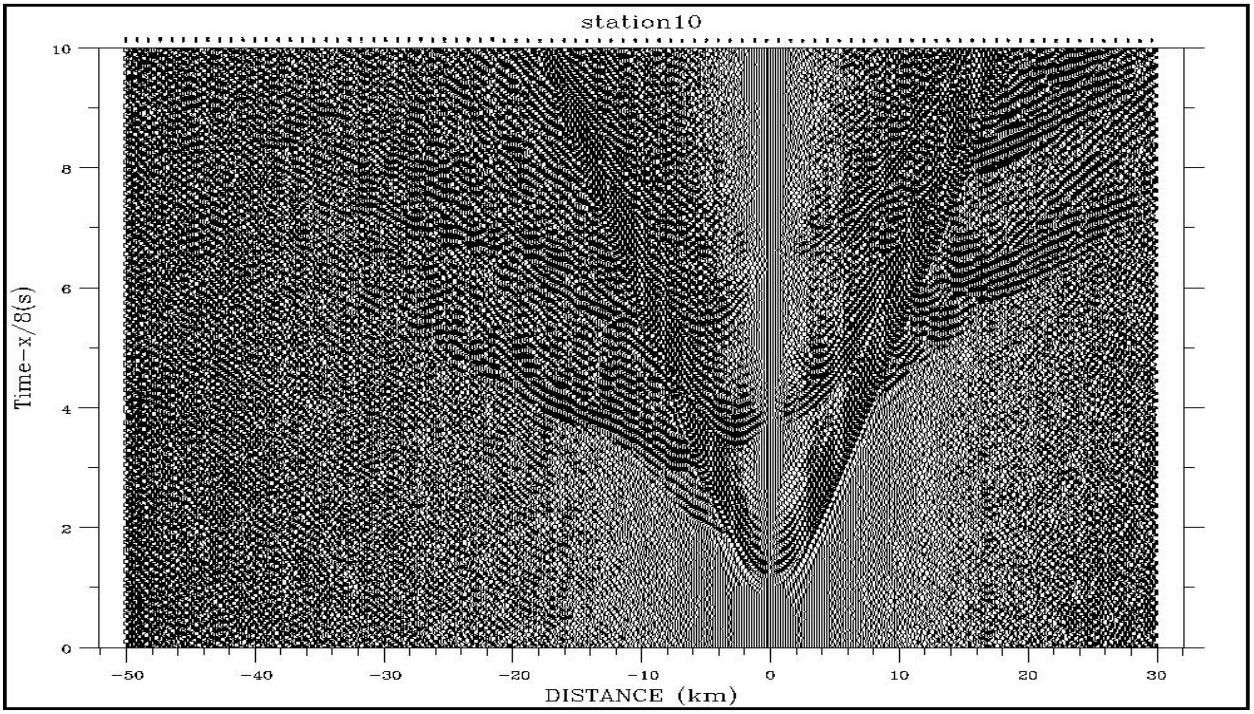

b)

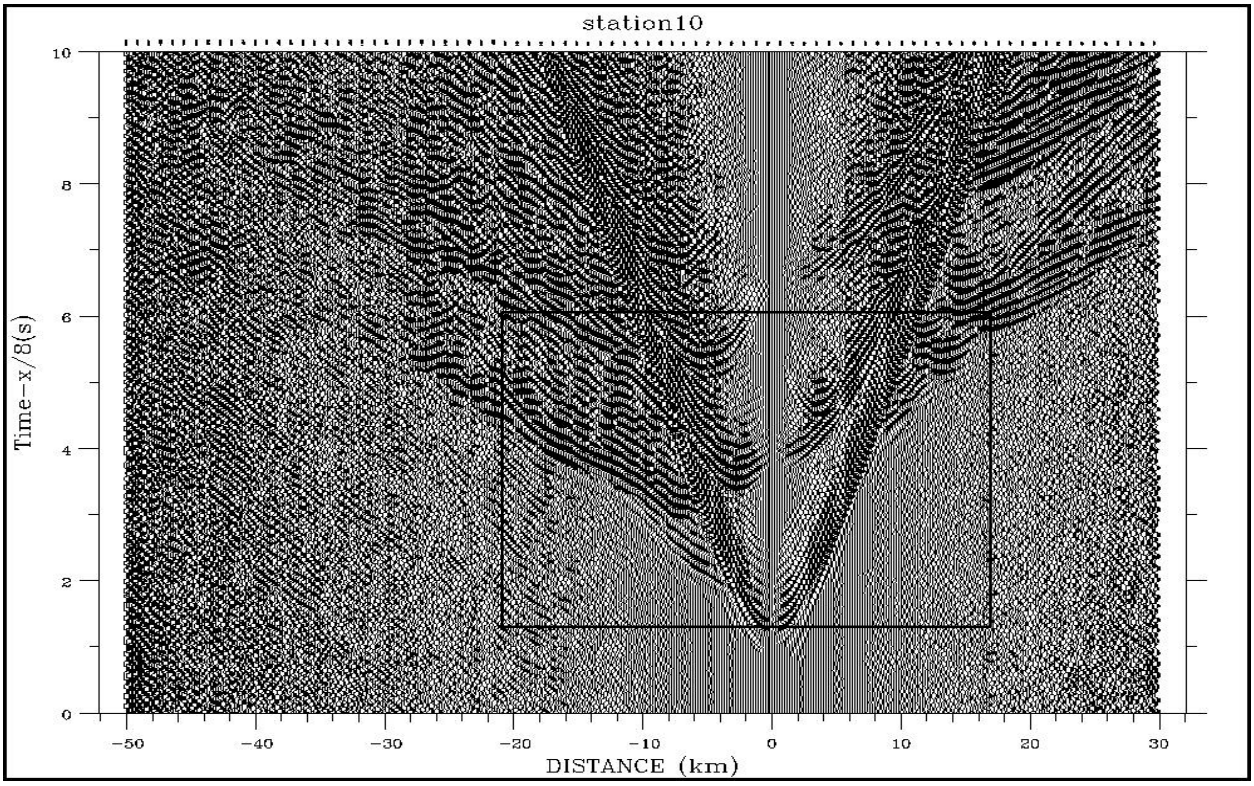

Figure D25 a) Vertical component record section for OBS 10 before any processing, b) Vertical component record section for OBS 10, after band pass filtered (4-10Hz) and applying coherency filter

a)

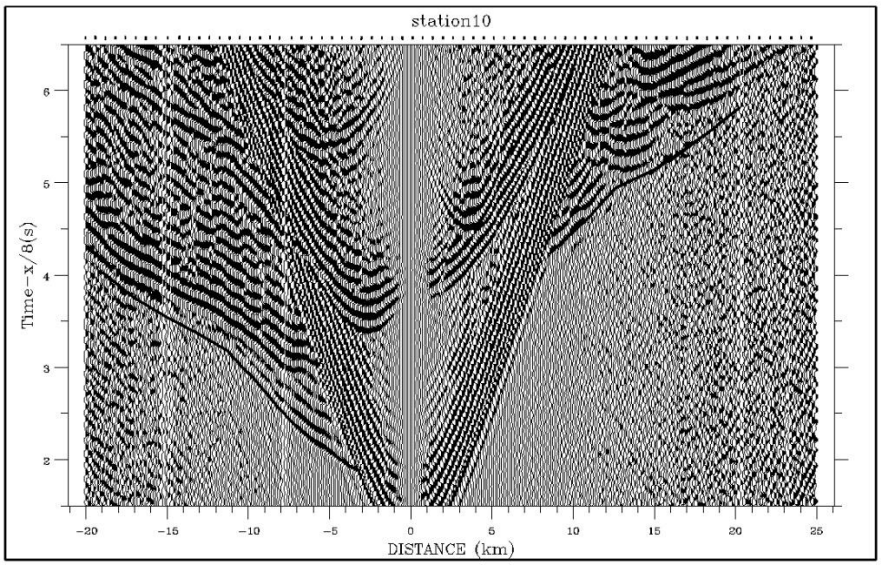

b)

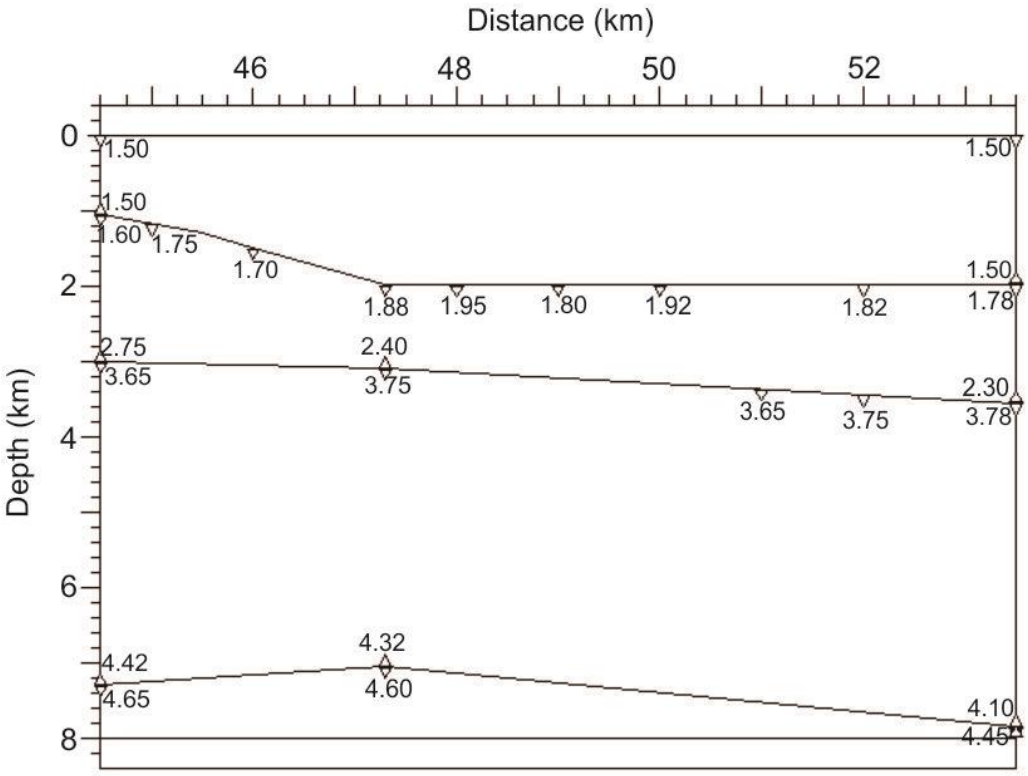

Figure D26 a) Close-up plot for the Short offset range of OBS 10 (indicated in D25b by rectangle), b) Short range shallow velocity model of OBS 10, the numbers indicate the assigned velocity values to each velocity node in the model

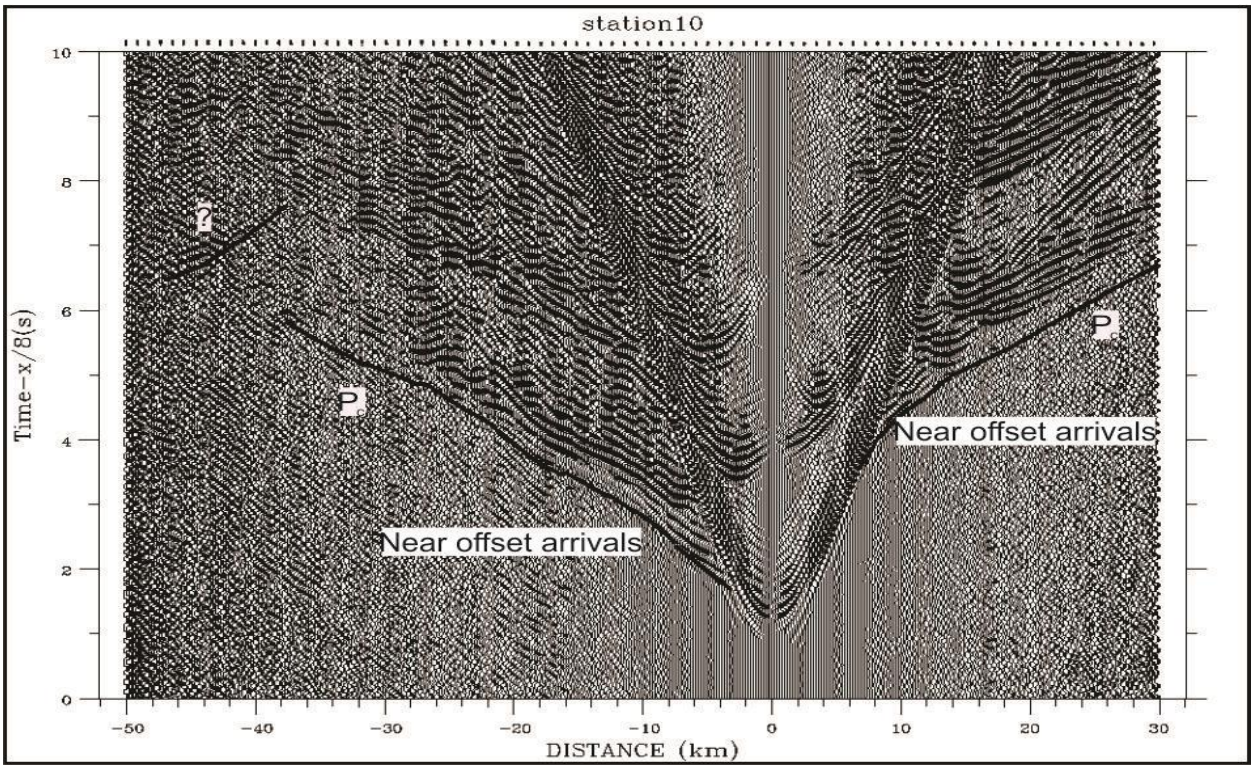

Figure D27 Vertical component record section for OBS 10 with computed refraction travel times (P_c), the phase marked with ? might be reflection from a discontinues reflector.

a)

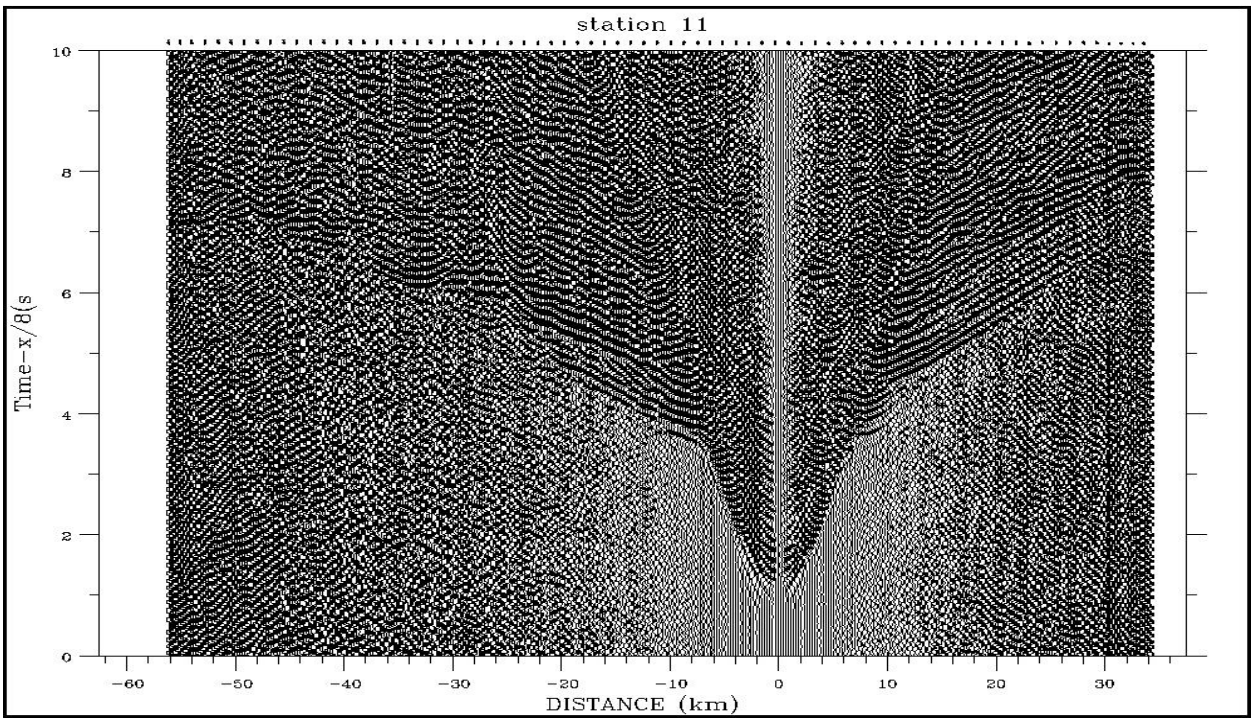

b)

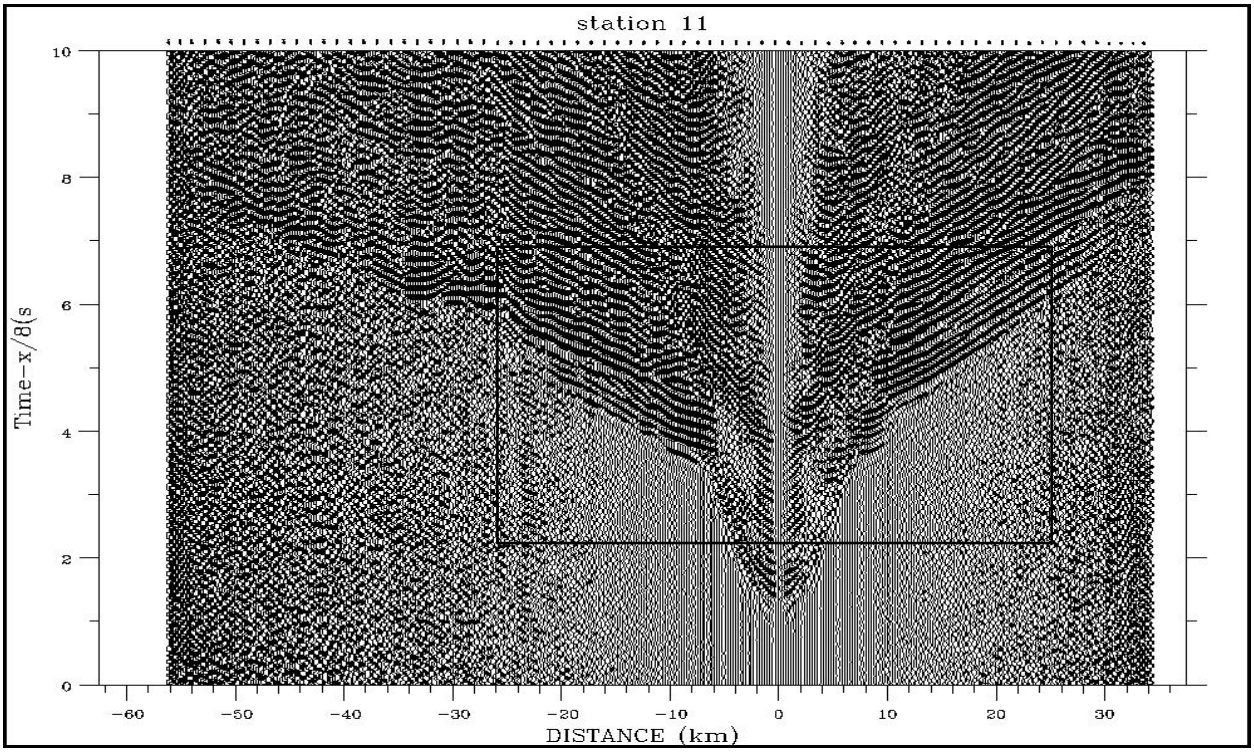

Figure D28 a) Vertical component record section for OBS 11 before any processing, b) Vertical component record section for OBS 11, after band pass filtered (4-10Hz) and applying coherency filter

a)

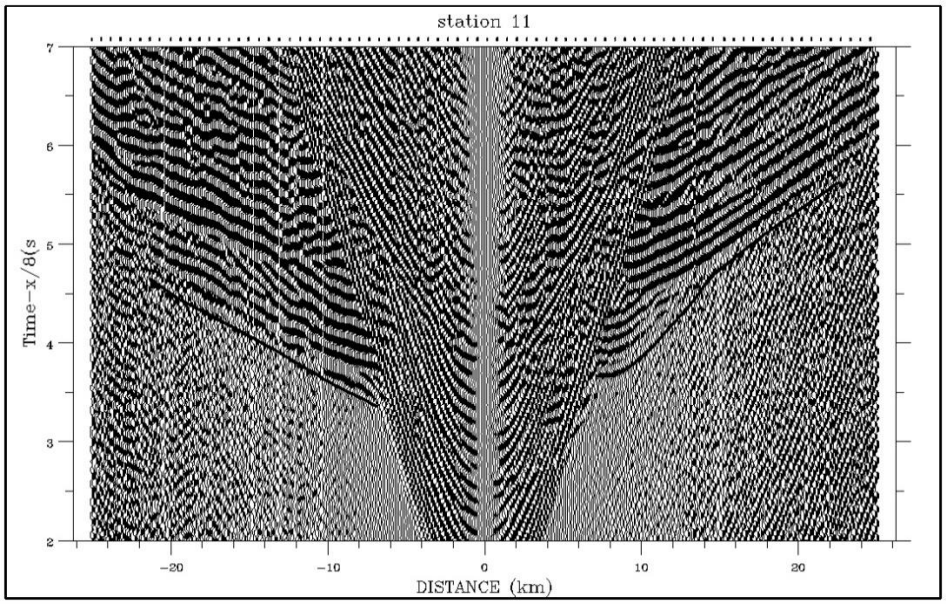

b)

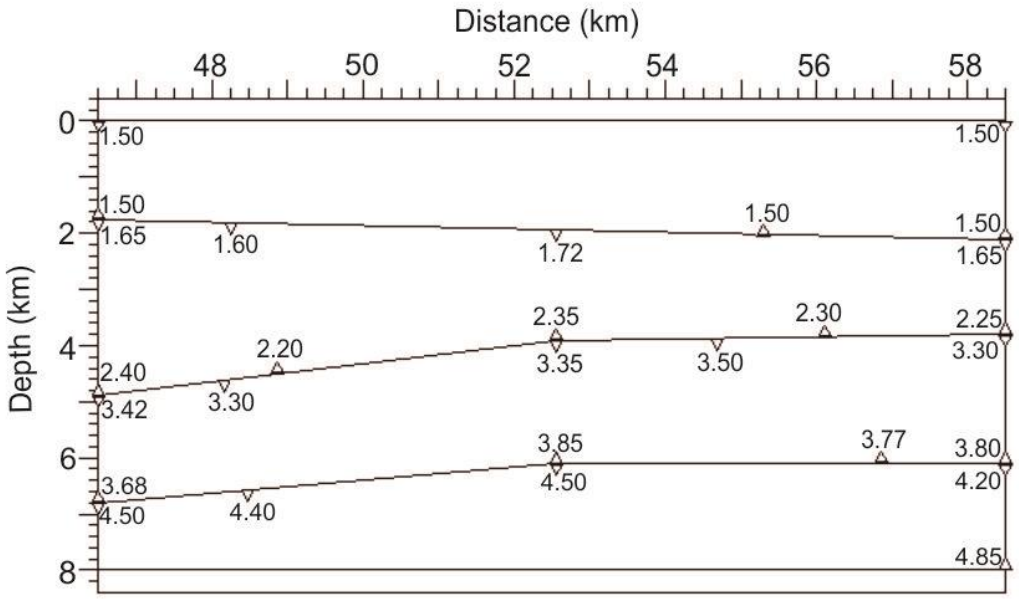

Figure D29 a) Close-up plot for the Short offset range of OBS 11 (indicated in D28b by rectangle), b) Short range shallow velocity model of OBS 11, the numbers indicate the assigned velocity values to each velocity node in the model

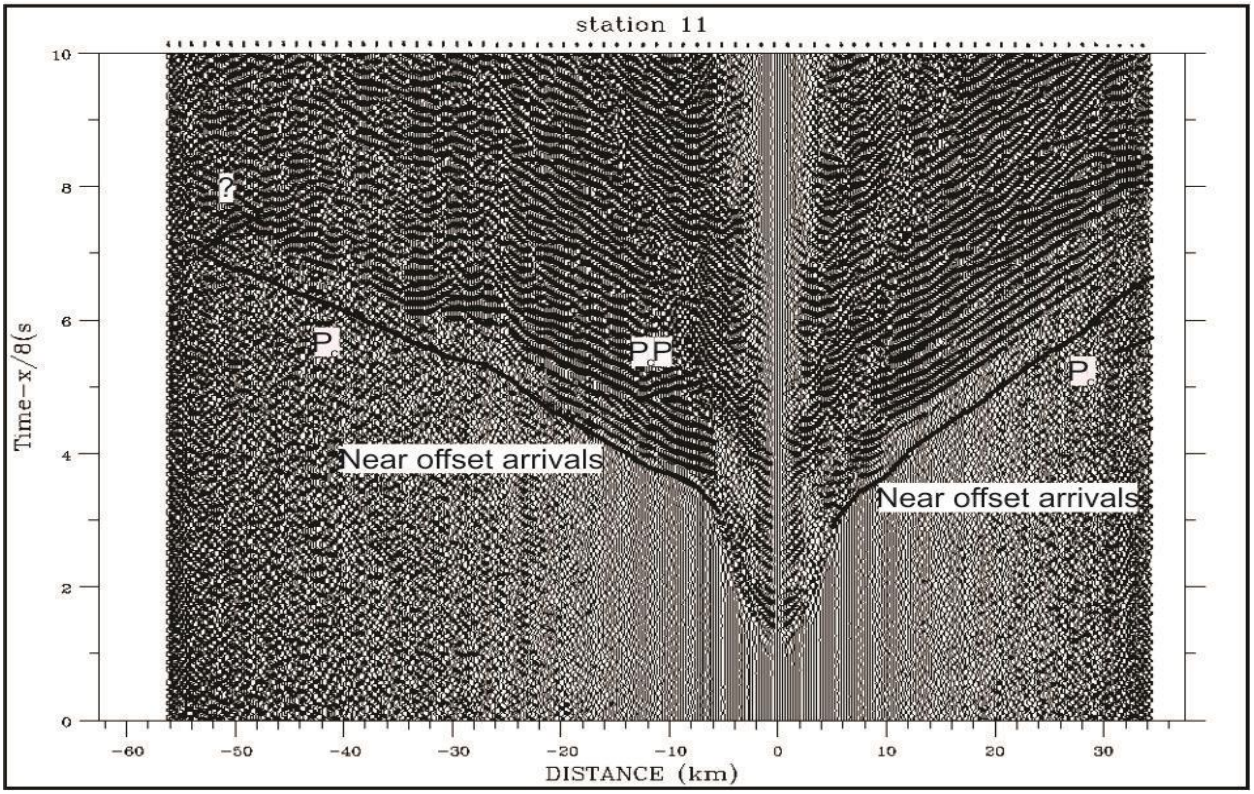

Figure D30 Vertical component record section for OBS 11 with computed refraction travel times (P_c) and reflection arrival times (P_cP) , the phase marked with ? might be reflection from a discontinues reflector

a)

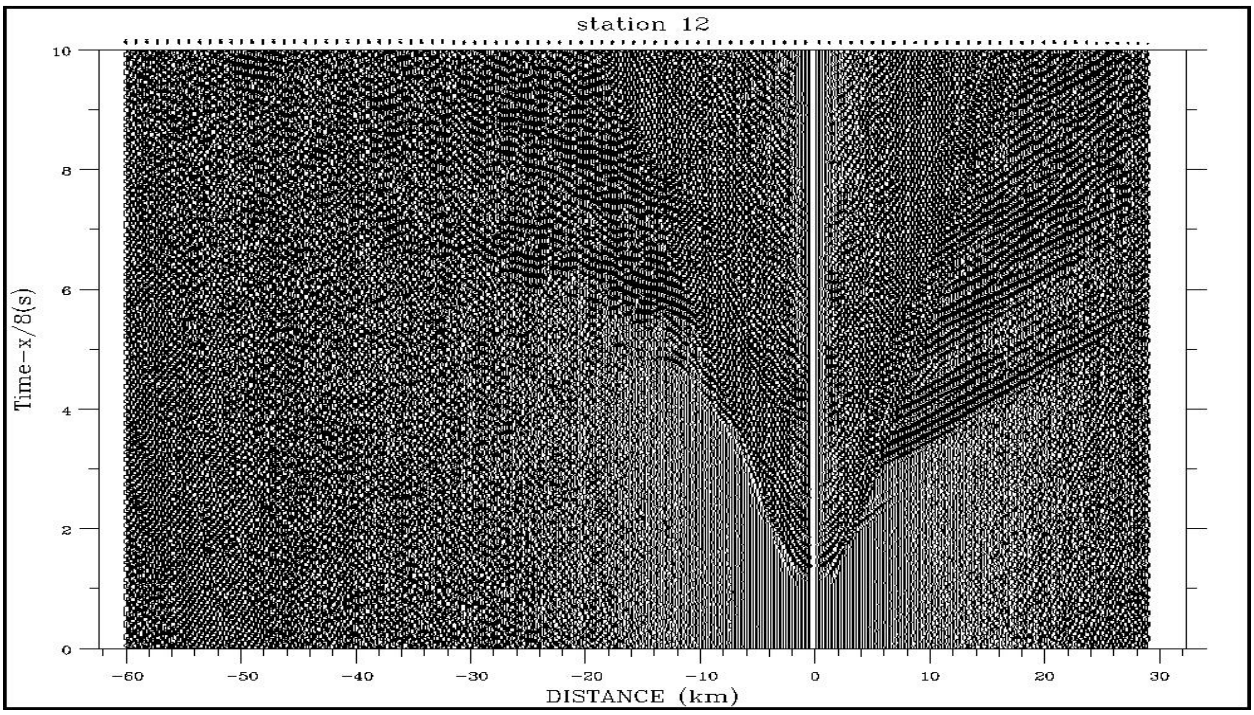

b)

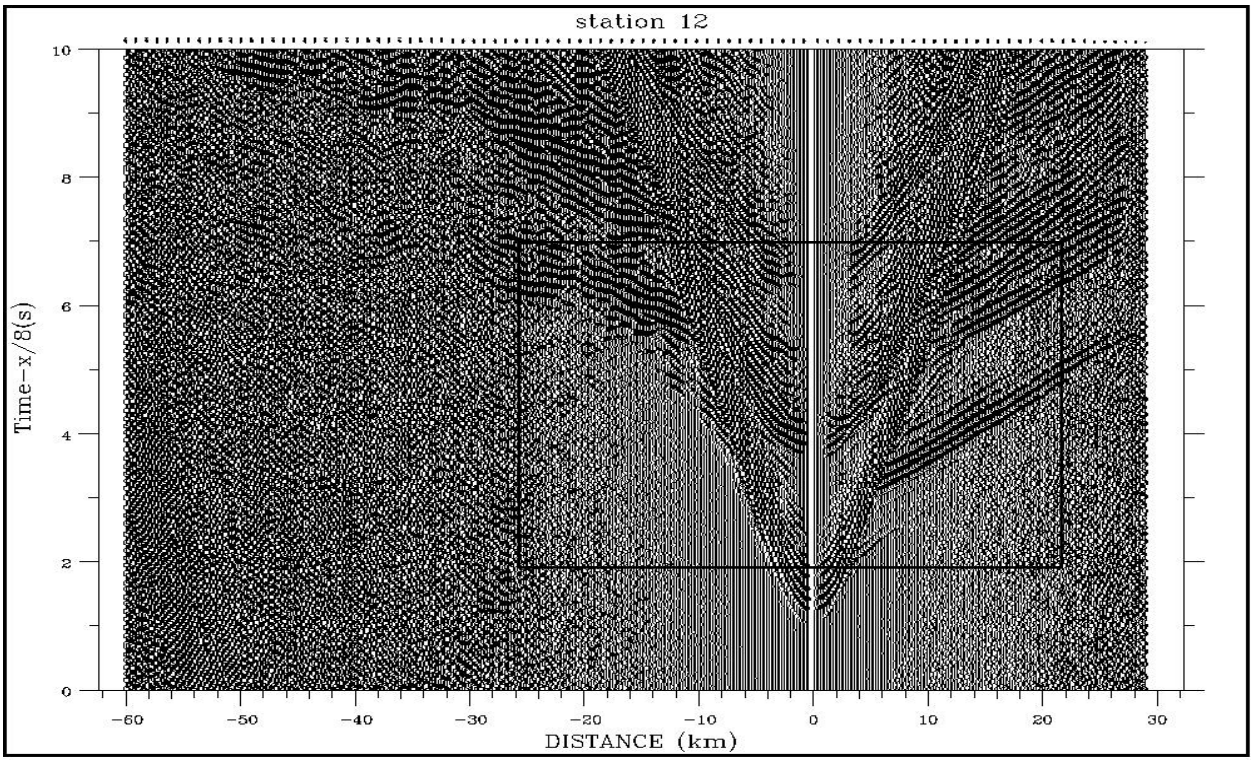

Figure D31 a) Vertical component record section for OBS 12 before any processing, b) Vertical component record section for OBS 12, after band pass filtered (4-10Hz) and applying coherency filter

a)

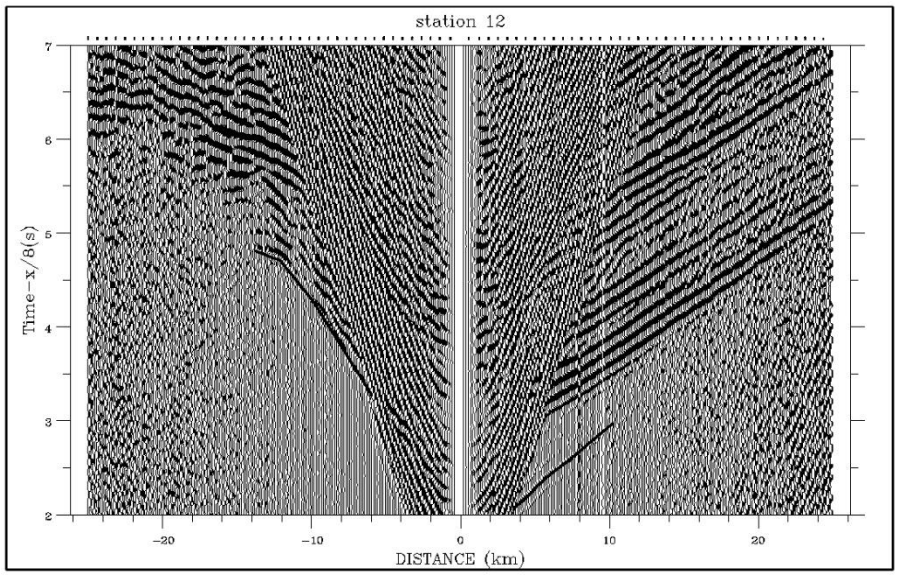

b)

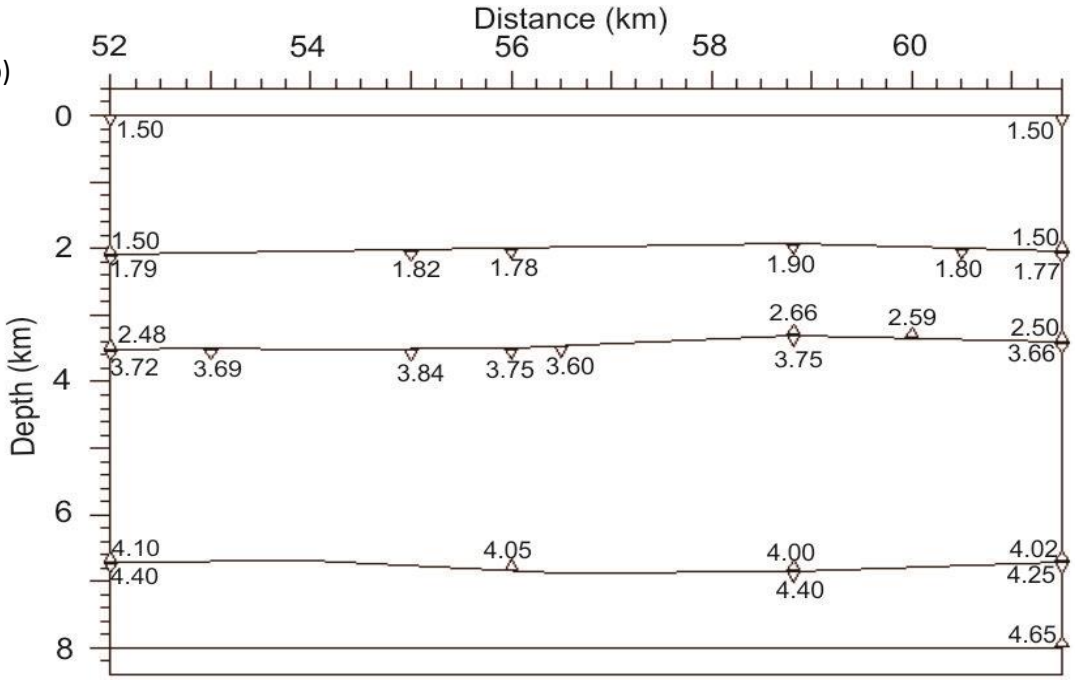

Figure D32 a) Close-up plot for the Short offset range of OBS 12 (indicated in D31b by rectangle), b) Short range shallow velocity model of OBS 12, the numbers indicate the assigned velocity values to each velocity node in the model

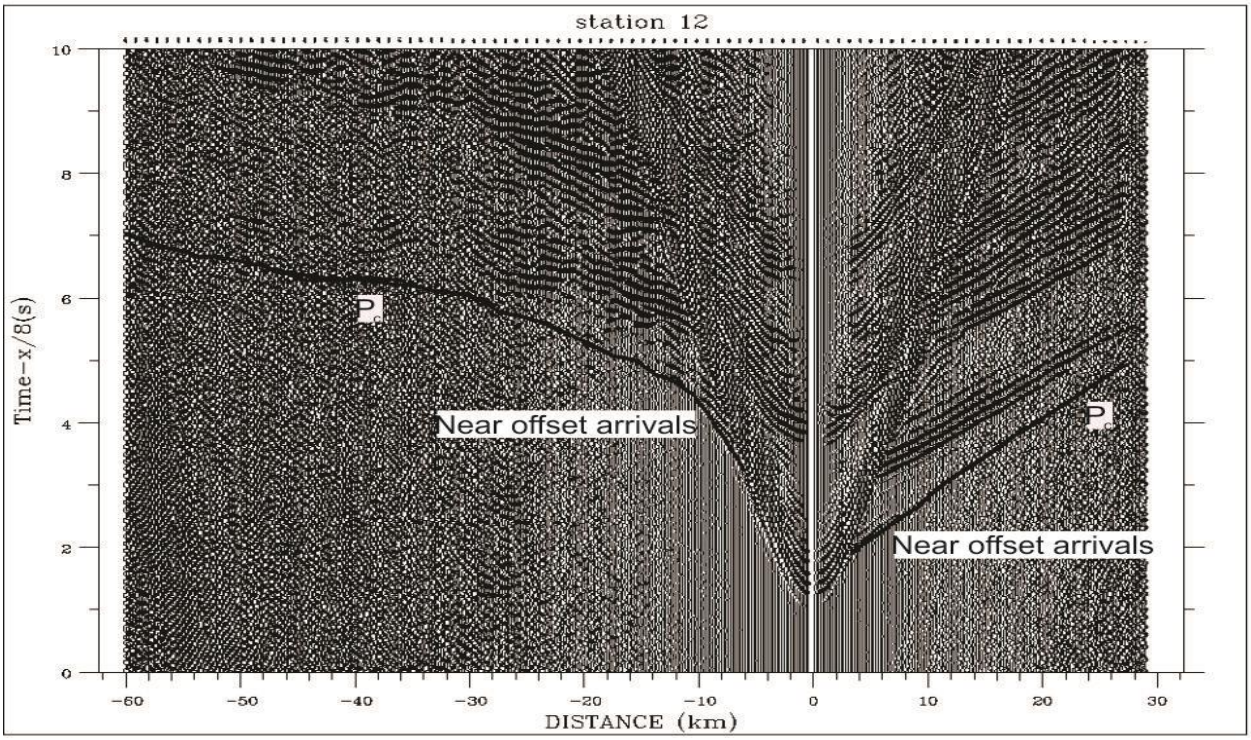

Figure D33 Vertical component record section for OBS 12 with computed refraction travel times (P_c).

a)

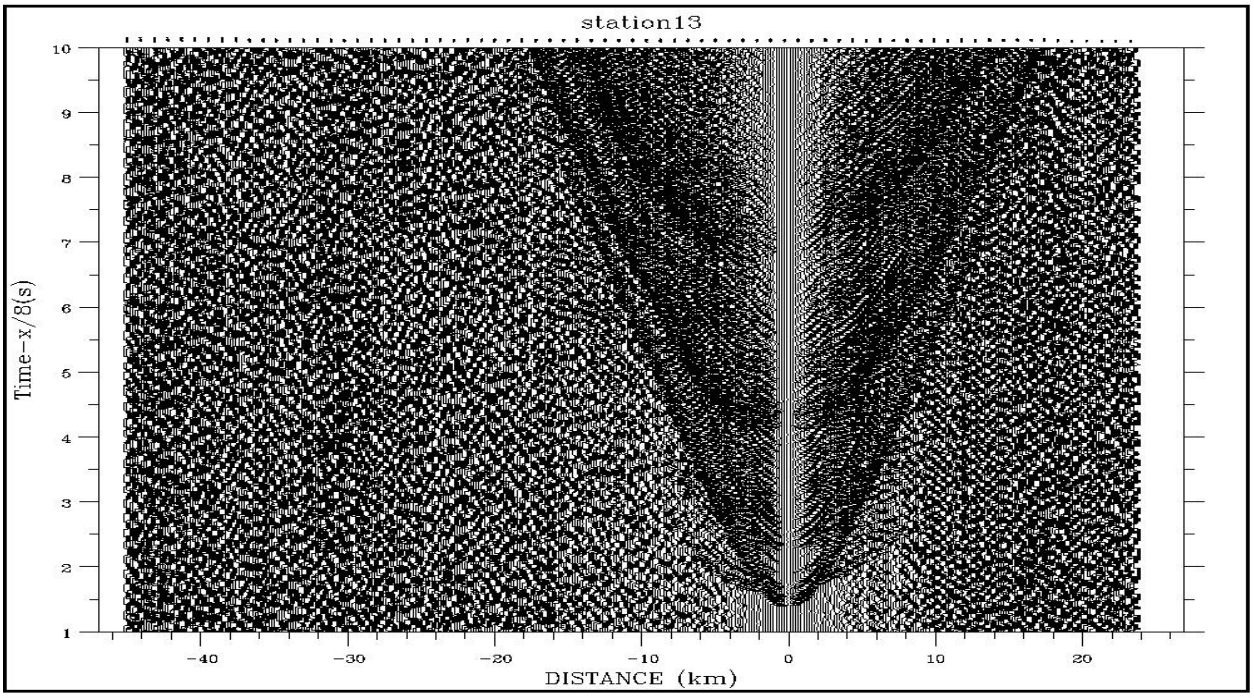

b)

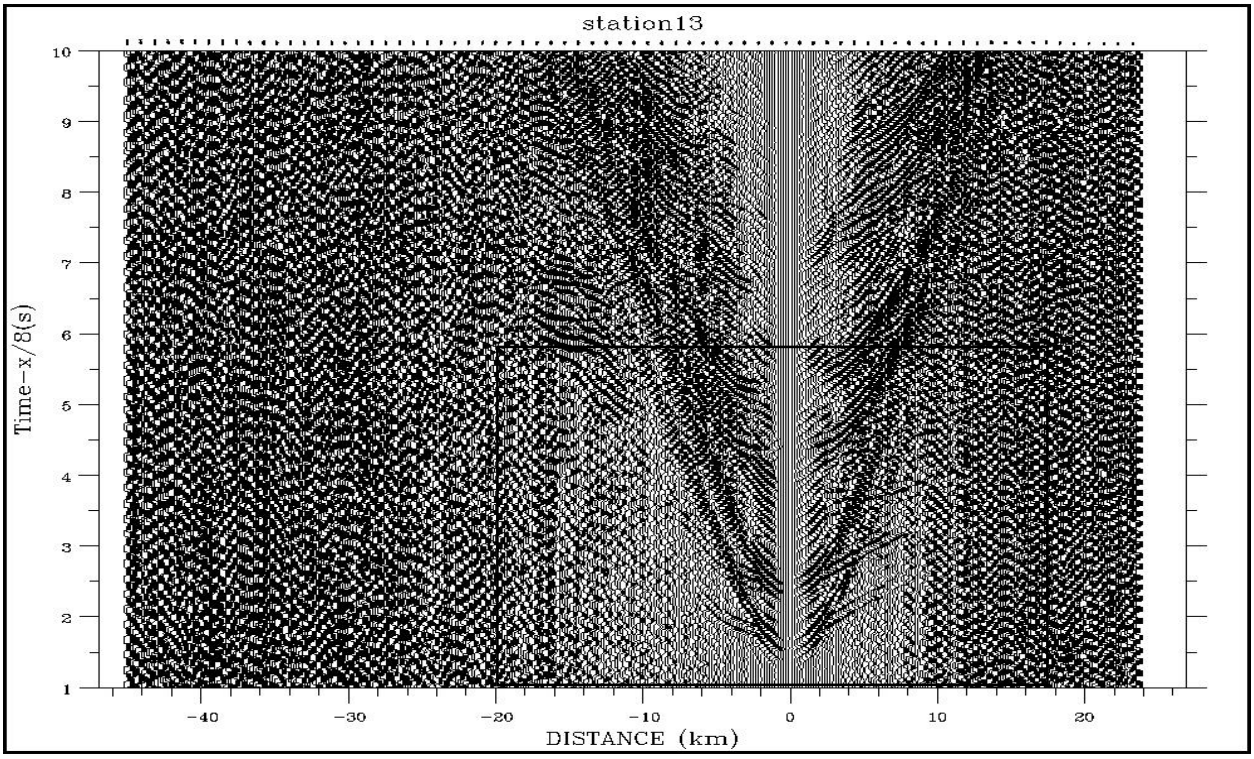

Figure D34 a) Vertical component record section for OBS 13 before any processing, b) Vertical component record section for OBS 13, after band pass filtered (4-10Hz) and applying coherency filter

a)

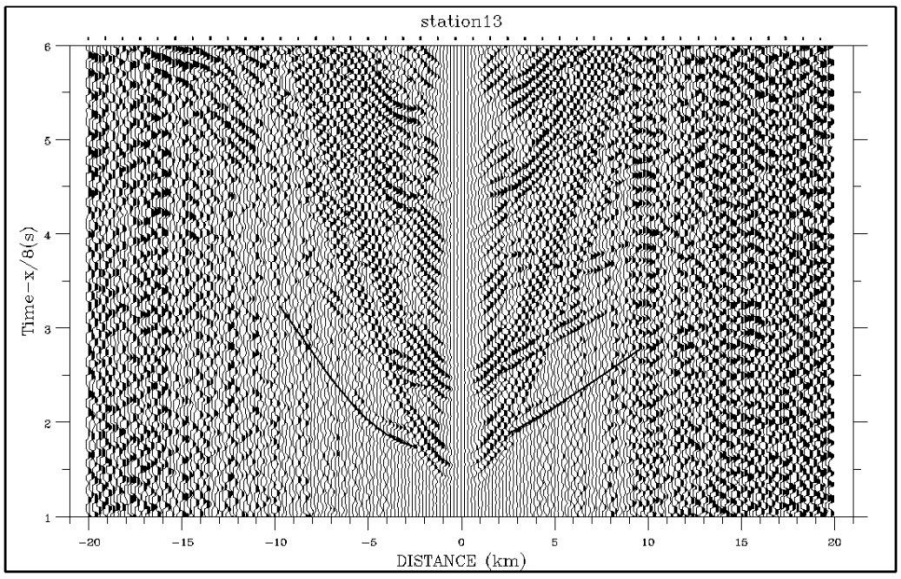

b)

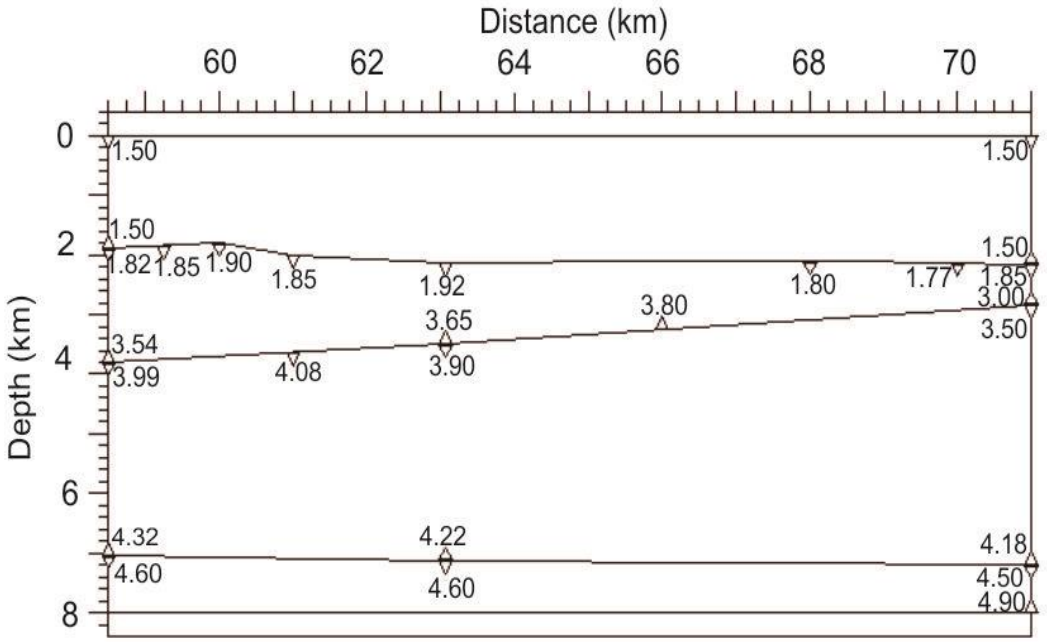

Figure D35 a) Close-up plot for the Short offset range of OBS 13 (indicated in D34b by rectangle), b) Short range shallow velocity model of OBS 13, the numbers indicate the assigned velocity values to each velocity node in the model

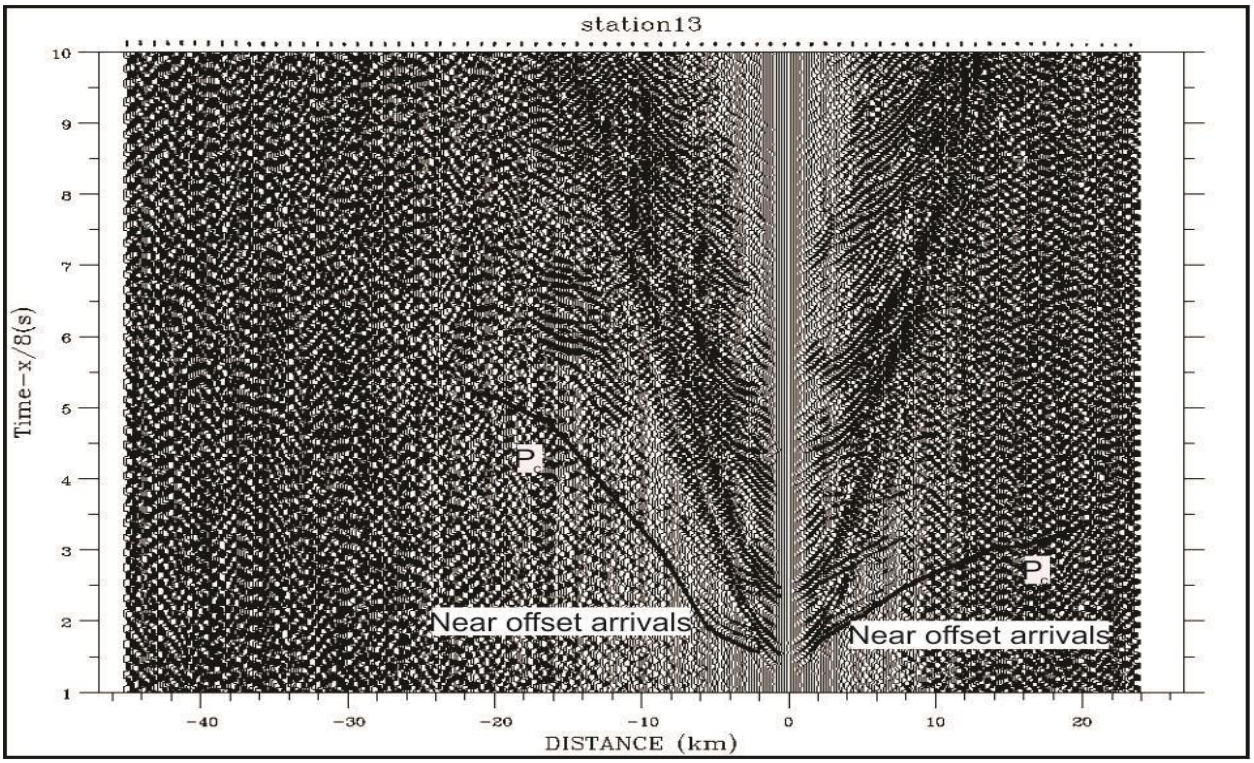

Figure D36 Vertical component record section for OBS 13 with computed refraction travel times (P_c).

a)

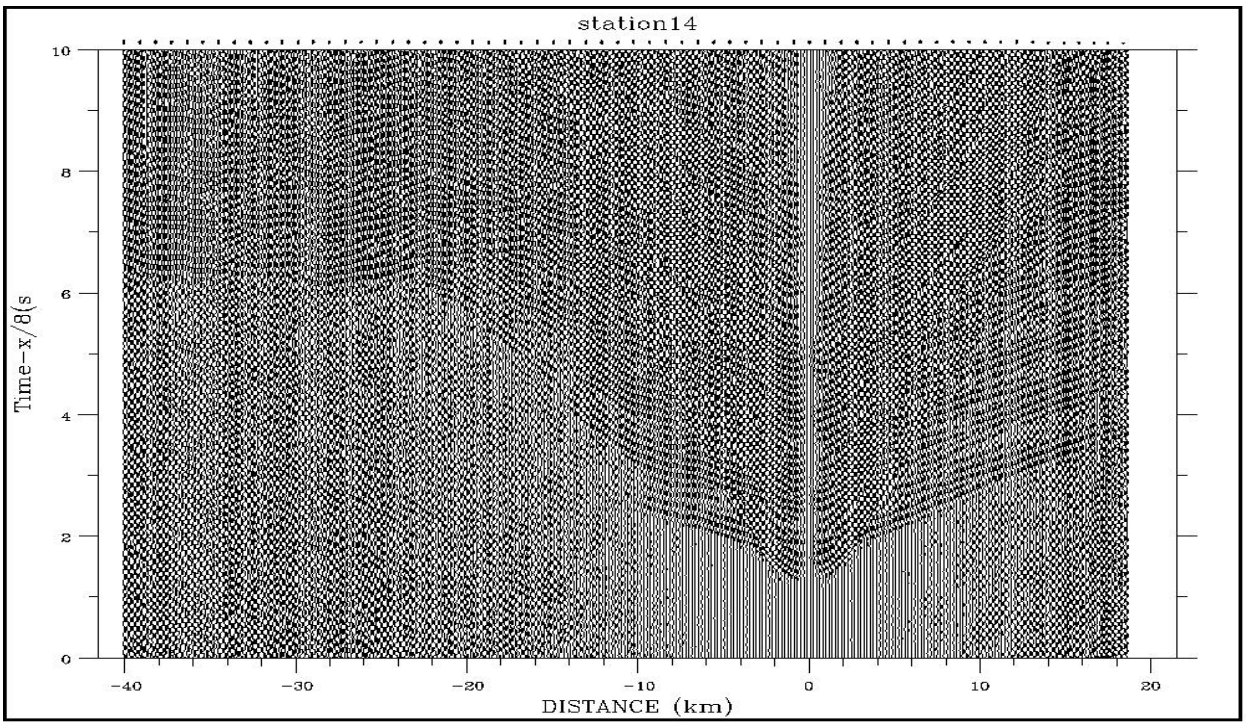

b)

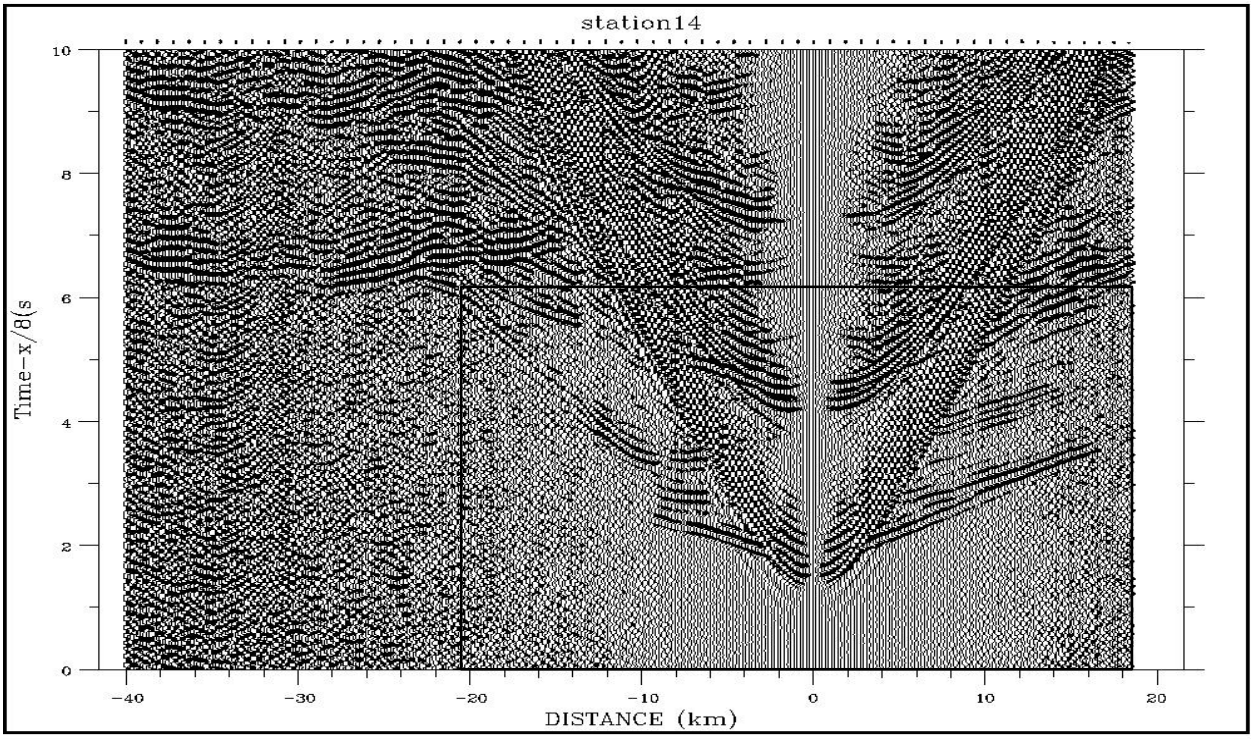

Figure D37 a) Vertical component record section for OBS 14 before any processing, b) Vertical component record section for OBS 14, after band pass filtered (4-10Hz) and applying coherency filter

a)

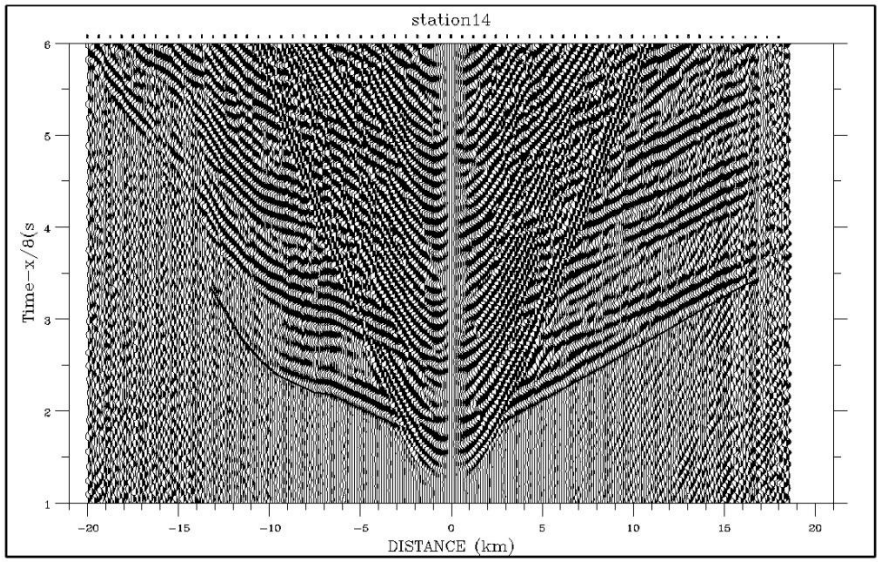

b)

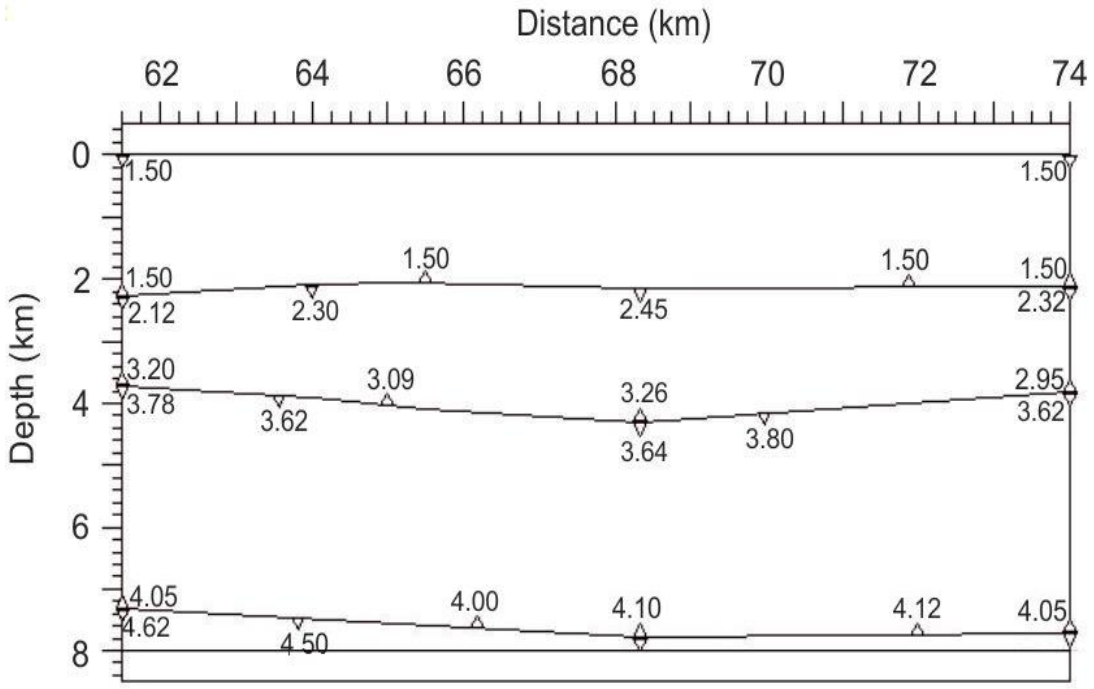

Figure D38 a) Close-up plot for the Short offset range (±20 km) of OBS 14 (indicated in D37b by rectangle), b) Short range shallow velocity model of OBS 14, the numbers indicate the assigned velocity values to each velocity node in the model

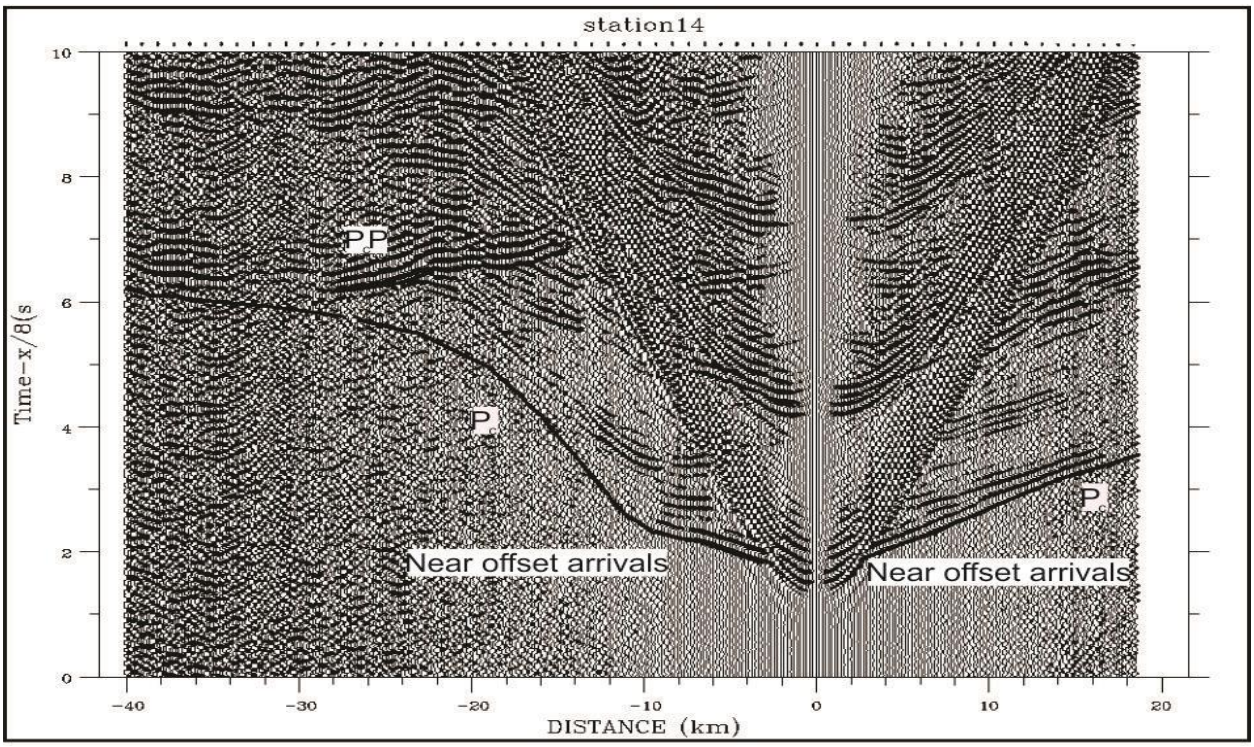

Figure D39 Vertical component record section for OBS 14 with computed travel times, P_cP = observed reflection arrival times and P_c= refraction travel times.

a)

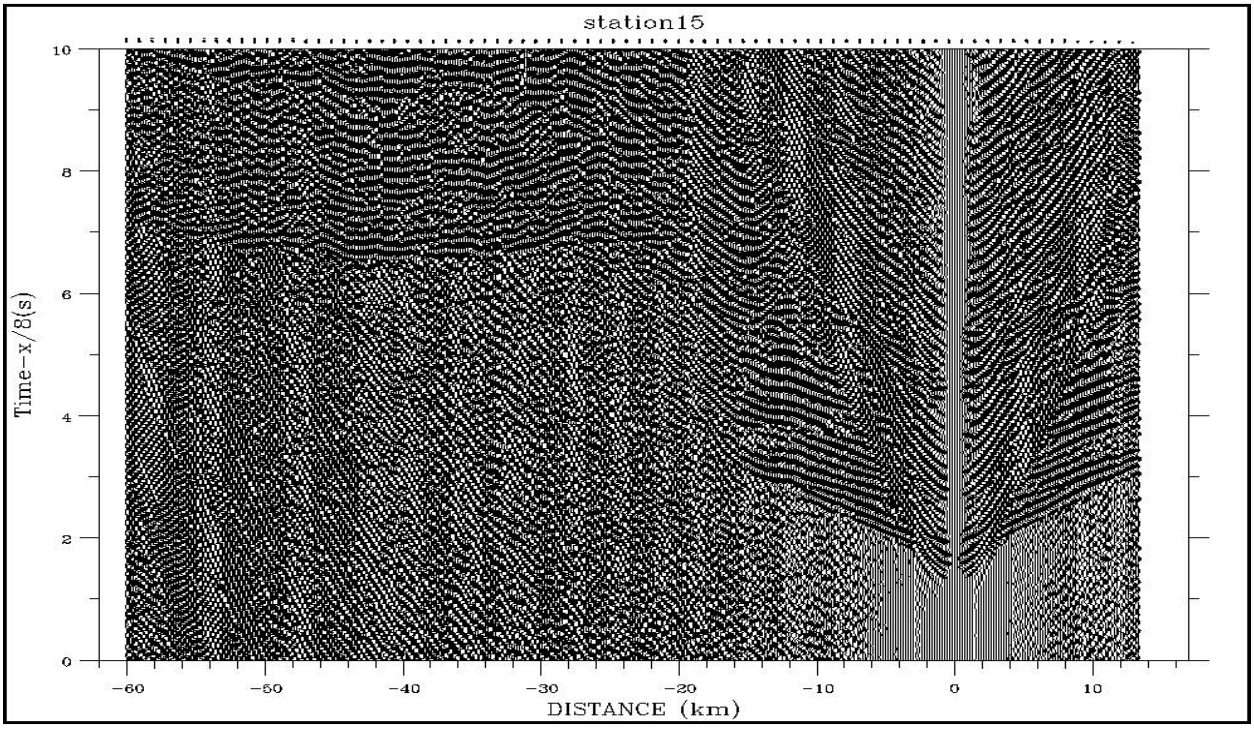

b)

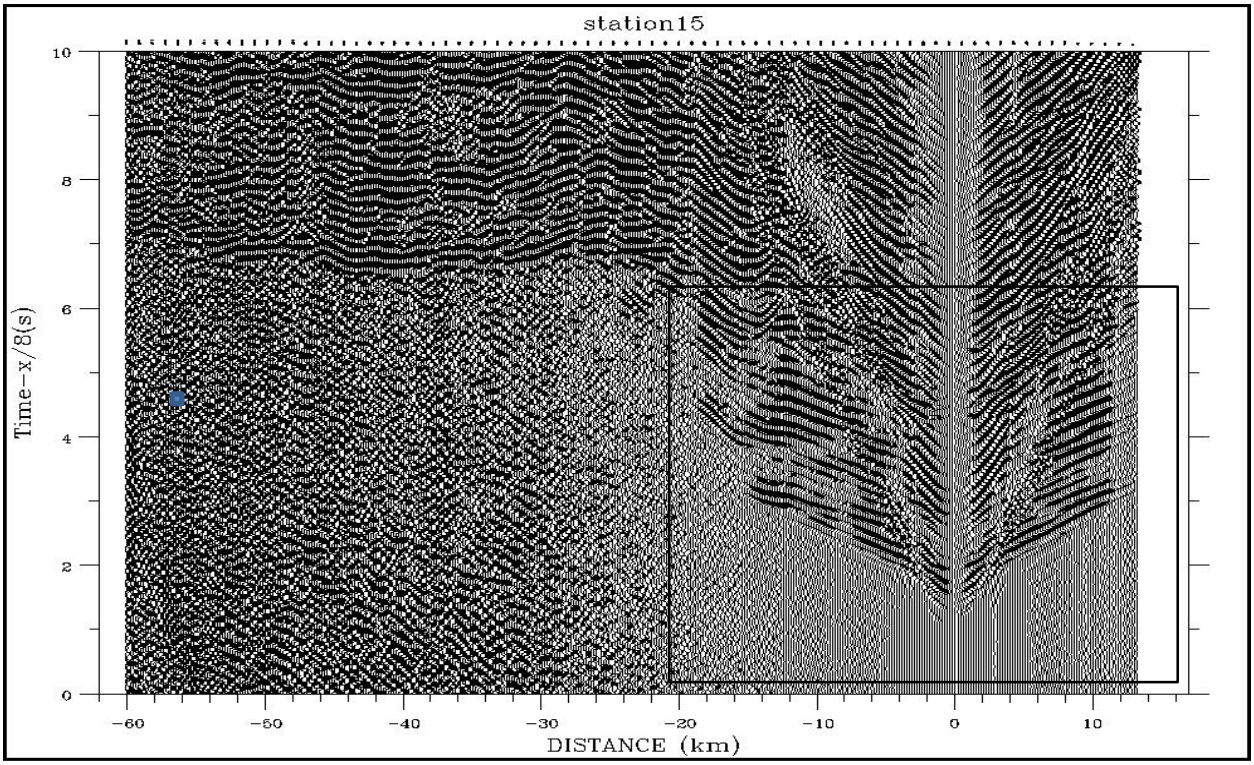

Figure D40 a) Vertical component record section for OBS 15 before any processing, b) Vertical component record section for OBS 15, after band pass filtered (4-10Hz) and applying coherency filter

a)

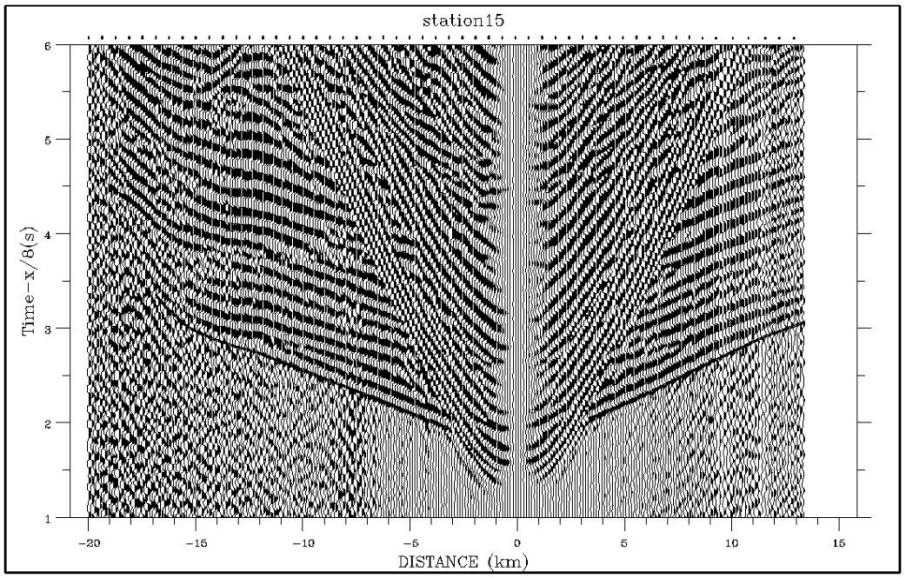

b)

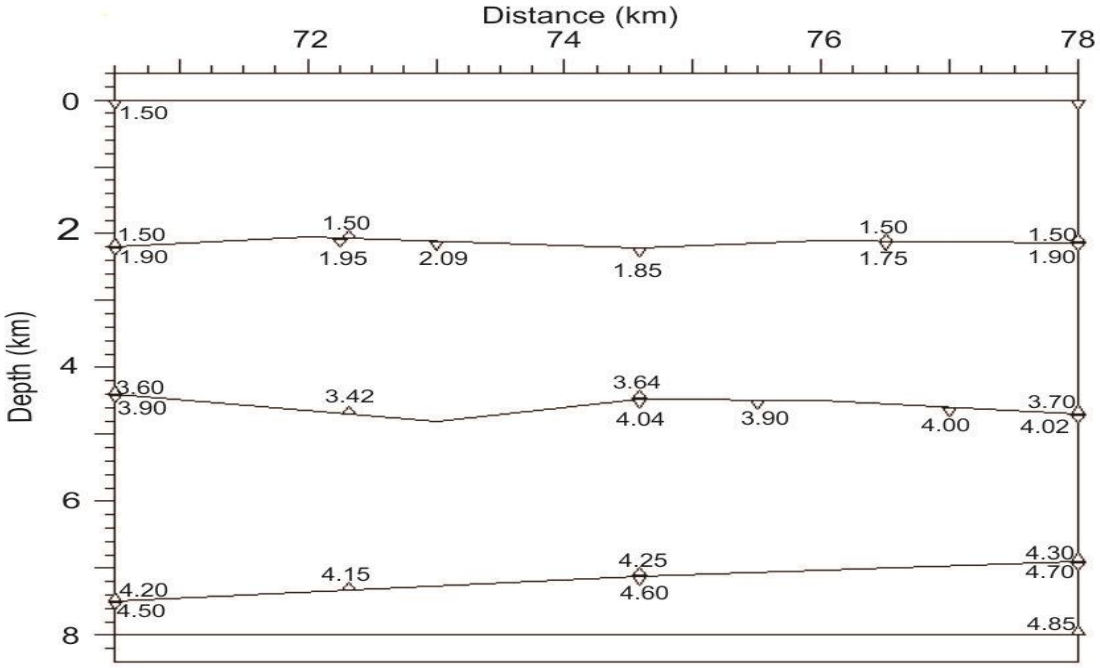

Figure D41 a) Close-up plot for the Short offset range ($\pm$20 km) of OBS 15 (indicated in D40b by rectangle), b) Short range shallow velocity model of OBS 15, the numbers indicate the assigned velocity values to each velocity node in the model

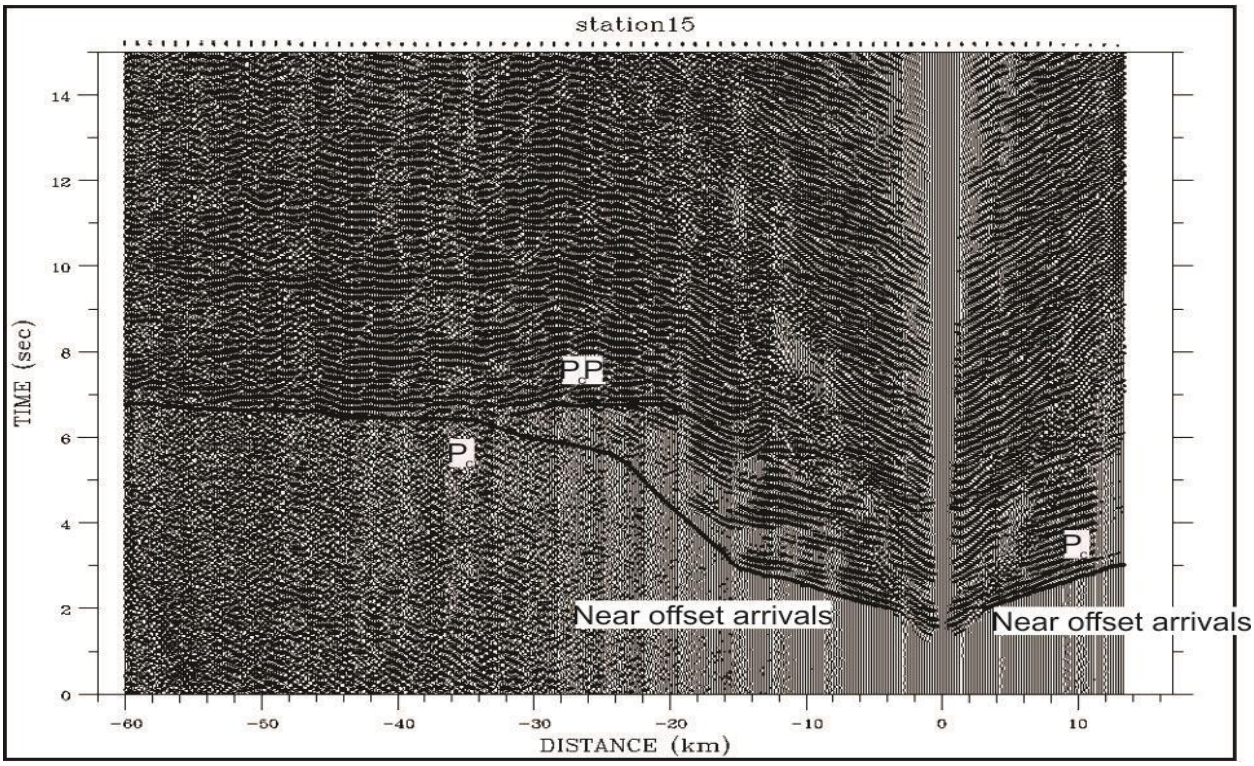

Figure D42 Vertical component record section for OBS 15 with computed travel times, P_cP = observed reflection arrival times and P_c= refraction travel times.